Amir Shoarian Sattari

Advances in Discrete Lattice Modeling of Cemented Geomaterials - Evolution and Application

Schriftenreihe des Lehrstuhls
Geomechanik und Geotechnik
Christian-Albrechts-Universität zu Kiel

10

Schriftenreihe des Lehrstuhls Geomechanik und Geotechnik
Christian-Albrechts-Universität zu Kiel
Heft 10

ISSN 2365-7162

Herausgeber:

Lehrstuhl für Geomechanik und Geotechnik

Christian-Albrechts-Universität zu Kiel

Prof. Dr.-Ing. habil. Frank Wuttke

Ludewig-Meyn-Straße 10

24118 Kiel

Telefon: ++49 – (0)431 – 880 1978

Telefax: ++49 – (0)431 – 880 4376

Internet: www.geotechnics.ifg.uni-kiel.de

Bezugsadresse:

Christian-Albrechts-Universität zu Kiel
Lehrstuhl für Geomechanik und Geotechnik

Advances in Discrete Lattice Modeling of Cemented Geomaterials - Evolution and Application

DISSERTATION

in fulfilment of the requirements for the degree
"Dr.-Ing."

of the Faculty of Mathematics and Natural Sciences
at Kiel University

submitted by
Amir Shoarian Sattari

Kiel, 2024

Gutachter:

1. Prof. Dr.-Ing. habil Frank Wuttke, Kiel University, Kiel, Germany
2. Prof. Dr. Marcelo Javier Sanchez Castilla, Texas A&M University, Texas, USA

Tag der mündlichen Prüfung: 23.01.2024
Zum Druck genehmigt: 29.01.2024

Der Dekan

Declaration of Authorship

I, Amir Shoarian Sattari, declare that apart from my supervisor's guidance, the content and design of this thesis titled "Advances in Discrete Lattice Modeling of Cemented Geomaterials - Evolution and Application" is all my own work and only using the sources listed. I confirm that:

- The thesis has not been submitted either partially or wholly as part of a doctoral degree to any other examining body, and it has not been published or submitted for publication.
- The thesis has been prepared in accordance to the Rules of Good Scientific Practice of the German Research Foundation.
- An academic degree of mine has never been withdrawn

Kiel, im Januar 2024
Amir Shoarian Sattari

Vorwort des Herausgebers

Die vorliegende Promotionsschrift von Herrn Dr.-Ing. Amir S. Sattari ist dem Forschungs- und Arbeitsgebiet Boden- und Geomechanik zuzuordnen. In dieser Dissertation wurde die Lattice-Element-Methodik zur Beschreibung von multiphysikalischen Zusammenhängen in granularen und zementierten Böden, für dynamische, thermo-hydro-mechanische und unzementierte Böden als Diskrete-Lattice-Element-Methodik (DLEM) zum Studium von mehrskaligen 2D und 3D Prozessen in diesen Böden weiterentwickelt. Für das Verständnis zum Verhalten von Geomaterialien in unterschiedlichen technischen Anwendungen wird eine gekoppelten thermo-hydromechanischen (THM) Beschreibung und Betrachtung immer wichtiger. Die Veränderung der THM-Eigenschaften von Geomaterialien bei gekoppelten Prozessen kann zu Störungen in Geosystemen, zum Versagen von Geostrukturen oder zur Kontamination der Umwelt führen. Um die auftretenden physikalischen Phänomene zu verstehen, müssen Studien von der Mikro- bis zur Makroskala durchgeführt werden. In dieser Dissertation wird die entwickelte Diskrete-Lattice-Methodik angewendet, um das Verhalten von Geomaterialien unter gekoppelten THM-Prozessen zu simulieren. Die Lattice-Element-Methode (LEM) ist in der Lage, eine stochastische Frack-Initiation während der THM-Simulation im Material zu simulieren. Diese Arbeit erweitert die konventionelle LEM, um komplexe multiphysikalische Problemstellungen auch unter großen Dehnungen zu simulieren. Das entwickelte Modell umfasst den instationären Wärmestrom, die Verwendung einer hydro-mechanischen Doppel-Vernetzung von Mechanik und Hydromechanik, mit der Berücksichtigung von Permeabilitätsänderung und der druckgetriebenen Fluidperkolation sowie der Wellengleichung zur Analyse der Wellenfeldstreuung in diskontinuierlichen und heterogenen Geomaterialien. Die entwickelten numerischen Modelle wurden an analytischen Lösungen und experimentellen Daten validiert. Schließlich werden verschiedene Anwendungen im Bereich untersucht, wie die Integrität von geologischen abdichtenden Deckgestein über nuklearen Endlagern oder CO2 oder anderen Speichern, das Verhalten von Gestein beim Frackingprozess, und das Versagen von verstärkten Mauerwerkswänden als Gesteinskomposit. Die DLEM hat sich als sehr effektiv für die Modellierung und Analyse von Materialveränderungen beim Übergang von der Mikro- zur Makroskala in komplexen anisotropen und heterogenen Geomaterialien erwiesen.

Kiel, im Januar 2024 Frank Wuttke

Acknowledgement

I would like to express my deepest appreciation to my supervisor Prof. Dr.-Ing. habil Frank Wuttke for his support, insightful comments, and inspiration during this study. I could not have undertaken this journey without his guidance and persistent help. I'm extremely grateful to the defense committee for their invaluable feedback and comments, who generously provided knowledge and expertise.

I would like to extend my sincere thanks to my colleagues at CAU Kiel for their support throughout my Ph.D. study. Special thanks to Zarghaam for his guidance and helpful discussions throughout the early stages of my study. I would like to extend my sincere thanks to Hem for providing the experimental data needed for the validation of the numerical model. Many thanks to Nima and Shadi for the long scientific discussions we had during the last couple of years.

I am also grateful to my parents for their unconditional support throughout my studies. This work would not have been possible without their support. Last but not least, I am deeply thankful to my wife, Annett, for her love and moral support during this process. Without her encouragement and motivation, I would not have been able to complete this journey. I would like to dedicate this thesis to my beloved son, Hugo Younes.

Amir Shoarian Sattari

Abstract

In Geo-Engineering applications, understanding the geomaterial's behavior under coupled therm-hydro-mechanical (THM) processes is imperative. The change of geomaterial's THM properties subjected to the coupled processes can lead to a decrease in the efficiency of the designed Geo-Systems (e.g. rock barriers), failure of the Geo-Structures, or even contamination of the environment. With the increase of computational power during the last decades, numerical methods are utilized as engineering tools not only to model large-scale problems but also to better comprehend the physical phenomena governing such a material behavior from micro- to macroscale perspective. In this contribution, the in-house developed discrete lattice method is applied to simulate the geomaterial's behavior under coupled THM processes.

The Lattice Element Method (LEM) is able to simulate a stochastic frack initiation and propagation in brittle or quasi-brittle materials, where small deformations are expected. In this study, the application of the conventional lattice method is extended to simulate complex Multiphysics problems. The developed Thermo-Mechanical lattice model is able to simulate the transient heat flux as well as the change in the effective thermal conductivity in heterogeneous domains under the coupled processes. With the implementation of the dual-lattice network, the Hydro-Mechanical lattice is considered to model the change of permeability and pressure-driven fluid percolation in discountinuum bodies. The dynamic lattice model is presented to investigate wavefield scattering in discontinuous and heterogeneous geomaterials.

The validation of the numerical results is carried out by comparing the lattice results with the analytical solutions and the experimental data. The theoretical developments presented in the field of Multiphysics are extended into practical applications, where the failure of reinforced masonry walls and the integrity of barrier rocks are studied. The LEM has been demonstrated to be an effective means of modeling and analyzing alterations in material behavior, even in complex anisotropic and heterogeneous geomaterials. As computational power increases and a transition from micro- to macroscale is put into practice, the lattice model can be used in large-scale engineering applications.

Zusammenfassung

Bei Geo-Engineering-Anwendungen ist das Verständnis des Verhaltens von Geomaterialien unter gekoppelten thermisch-hydromechanischen (THM) Prozessen von entscheidender Bedeutung. Die Veränderung der THM-Eigenschaften von Geomaterialien, die den gekoppelten Prozessen ausgesetzt sind, kann zu einer Verringerung der Effizienz der entworfenen Geosysteme (z. B. Felsbarrieren), zum Versagen der Geostrukturen oder sogar zur Kontamination der Umwelt führen. Mit der Zunahme der Rechenleistung in den letzten Jahrzehnten werden numerische Methoden als ingenieurtechnische Mittel nicht nur zur Modellierung großräumiger Probleme eingesetzt, sondern auch zum besseren Verständnis der physikalischen Phänomene, die ein solches Materialverhalten von der Mikro- bis zur Makroebene bestimmen. In diesem Beitrag wird die selbst entwickelte diskrete Lattice-Element-Methode (LEM) angewandt, um das Verhalten von Geomaterialien unter gekoppelten THM-Prozessen zu simulieren. Die LEM ist in der Lage, eine stochastische Rissinitiierung und -ausbreitung in spröden oder quasi-spröden Materialien zu simulieren, bei denen kleine Verformungen zu erwarten sind. In dieser Studie wird die Anwendung der konventionellen LEM erweitert, um komplexe Multiphysics-Probleme zu simulieren. Die entwickelte thermomechanische Methodik ist in der Lage, den instationären Wärmestrom sowie die Änderung der effektiven Wärmeleitfähigkeit in heterogenen Domänen unter den gekoppelten Prozessen zu simulieren. Mit der Implementierung der Doppel-Vernetzung wird die hydro-mechanische Vernetzung zur Modellierung der Permeabilitätsänderung und der druckgetriebenen Fluidperkolation in diskontinuierlichen Körpern berücksichtigt. Die dynamische LEM wird vorgestellt, um die Wellenfeldstreuung in diskontinuierlichen und heterogenen Geomaterialien zu untersuchen.

Die Validierung der Methodik erfolgt durch den Vergleich der numerischen Ergebnisse mit den analytischen Lösungen und den experimentellen Daten. Die auf dem Gebiet der Multiphysik vorgestellten theoretischen Entwicklungen werden auf praktische Anwendungen ausgedehnt, bei denen das Versagen von bewehrten Mauerwerken und die Integrität von Barrierefelsen untersucht werden. Die LEM hat sich als wirksames Modellierungs- und Analysemittel für Veränderungen im Materialverhalten erwiesen, selbst bei komplexen anisotropen und heterogenen Geomaterialien. Mit zunehmender Rechenleistung und dem Übergang von der Mikro- zur Makroskala kann die LEM in großtechnischen Anwendungen eingesetzt werden.

Contents

List of Figures

List of Tables

Nomenclature

List of Latin Symbols	|Definition|	|Unit|
$\ddot{\boldsymbol{u}}$	Acceleration of a nuclei	[m.s^{-2}]
$\dot{\boldsymbol{u}}$	Velocity of a nuclei	[m.s^{-1}]
$\boldsymbol{C_m}$	Damping matrix	[-]
$\boldsymbol{C_i}$	Stiffness tensor	[-]
$\boldsymbol{f_g}$	Force vector in global coordinate	[-]
$\boldsymbol{f_{con}}$	Contact force vector	[-]
$\boldsymbol{f_{ext}}$	External applied force vector	[-]
$\boldsymbol{F}$	Force vector	[-]
$\boldsymbol{J}$	Jacobian matrix	[-]
$\boldsymbol{K_e^f}$	Element hydraulic conductivity	[m.s^{-1}]
$\boldsymbol{K_g}$	Stiffness matrix in global coordinate	[-]
$\boldsymbol{K_l}$	Stiffness matrix in local coordinate	[-]
$\boldsymbol{K}$	Stiffness matrix	[-]
$\boldsymbol{M}$	Mass matrix	[-]
$\boldsymbol{p}$	Pore pressure	[Pa]
$\boldsymbol{u_g}$	Displacement vector in global coordinate	[-]
$\boldsymbol{u}$	Displacement of a nuclei	[m]
$\mathbf{g}$	Gravity	[m.s^{-2}]
$\mathbf{p}_{i'}$	Hydraulic pressure at conduit node of i'	[Pa]

E	Young's modulus	[Pa]
E^*	Effective elastic modulus	[Pa]
E_b	Young's modulus of an element	[Pa]
$E_{\mathbb{R}}$	Young's modulus of continuum	[Pa]
G	Shear modulus	[Pa]
$G_{\mathbb{R}}$	Shear modulus of continuum	[Pa]
K	Bulk modulus	[Pa]
K_f	Fluid bulk modulus	[Pa]
$K_{\mathbb{R}}$	Bulk modulus of continuum	[Pa]
q	Fluid flux	[$m.s^{-1}$]
A	Cross-sectional area of an element	[m^2]
A'	Cross-sectional area of the fluid channel	[m^2]
a_f	Hydraulic aperture	[m]
A_{con}	Contact intersection area	[m^2]
A_s	Shear surface area	[m^2]
c	Cohesion	[Pa]
c_i	Specific heat capacity of cell i	[$J.kg^{-1}.K^{-1}$]
$C_{\mathbb{R}}$	Continuum stiffness matrix	[-]
c_u	Undrained shear strength	[Pa]
D_{eff}	Equivalent effective diameter cell	[m]
e	Void ratio	[-]
e_0	Initial void ratio	[-]
f_a	Angular frequency	[ω]
f_d	Frequency	[Hz]
f_h	Hydraulic force	[N]
f_n	Normal contact force	[N]

f_t	Tangential contact force	[N]
f_x	Force in x-orientation	[N]
f_y	Force in y-orientation	[N]
f_{con}	Contact force between two unit cell	[N]
$f_{g,i}$	Gravity force	[N]
f_{S_r}	Saturation function	[-]
G	Strain energy release rate	[J.m^{-2}]
G_s	Relative density	[-]
h	Cross-section length of an element	[m]
$h_{i'}$	Hydraulic head at conduit node of i'	[m]
I	Principal moment of inertia	[kg.m^2]
I_i	Identity matrix	[-]
J_p	Polar moment of inertia	[m^4]
K	Stress intensity factor	[Pa.m$^{0.5}$]
K^f	Hydraulic conductivity	[m.s^{-1}]
k^f	Permeability	[m^2]
k_ϕ	Rotational stiffness	[N.m]
K_c	Fracture toughness	[Pa.m$^{0.5}$]
k_n	Normal stiffness	[N.m^{-1}]
K_r	Relative hydraulic conductivity	[m.s^{-1}]
k_s	Tangential stiffness	[N.m^{-1}]
k_X	Stiffness in X-orientation	[N.m^{-1}]
k_Y	Stiffness in Y-orientation	[N.m^{-1}]
l	Length of an element	[m]
l'	Length of a conduit elemen	[m]
l_{lev}	Lever arm	[m]

M	Moment	[N.m]
m_{eff}	Effective mass	[kg]
m_f	Fluid mass	[kg]
N_b	Total number of bonds for a unit cell	[-]
n_c	Total number of contacts of a unit cell	[-]
N_f	Total number of hydraulic nodes	[-]
n_f	Number of conduit elements	[-]
N_{DOF}	Total number of DOF	[-]
n_i	Unit normal vector	[-]
q_c	Heat loss	[W]
q_T	Heat flux	[W.m^{-2}]
q_{ave}	Average heat flux	[W.m^{-2}]
R_f	Flow resistance	[Pa.s.m^{-1}]
S	Softening ratio	[-]
S_r	Degree of saturation	[-]
$S_{r,res}$	Degree of residual saturation	[-]
t	Time	[s]
t^f	Height of the fluid channel	[m]
t_b	Height of an element	[m]
T_d	Period	[s]
t_f	Total duration of the evaporating process	[s]
T_i	Temperature of cell i	[K]
T_R	Temperature of a reference material	[K]
T_r	Torsion between two unit cell	[N.m]
T_{ave}	Average temperature	[K]
u_x	Displacement in x-orientation	[m]

u_y	Displacement in y-orientation	[m]
$U_{\mathbb{R}}$	Strain energy of a continuum	[J]
U_{Cell}	Strain energy of a Voronoi cell	[J]
U_{strain}	Strain energy	[J]
U_{total}	Total potential energy	[J]
V_c	Volume of virtual cavity	[m^3]
v_f	Fluid velocity	[$m.s^{-1}$]
v_p	P-wave velocity	[$m.s^{-1}$]
v_s	S-wave velocity	[$m.s^{-1}$]
$V_{\mathbb{R}}$	Continuum volume	[m^3]
$v_{rel,n}$	Relative velocity	[$m.s^{-1}$]
V_{RVE}	Volume of RVE	[m^3]
w	Water content	[-]
W_s	Section modulus	[m^3]

List of Greek Symbols	**|Definition|**	**|Unit|**
α'	Scaling parameter	[-]
α^T	Thermal expansion coefficient	[-]
α_r	Randomness factor	[-]
α_X^T	Thermal expansion coefficient in X-orientation	[-]
α_Y^T	Thermal expansion coefficient in Y-orientation	[-]
α_Z^T	Thermal expansion coefficient in Z-orientation	[-]
α_{sh}	Shrinkage coefficient	[-]
β	Newmark-β parameter	[-]
β_w	Shape factor	[-]
$\ddot{\theta}$	Angular acceleration	[$rad.s^{-2}$]

$\Delta \boldsymbol{F}$	Force increment vector	[-]
Δm_f	Fluid mass exchange	[kg]
Δt	Time step	[s]
$\dot{\theta}$	Angular velocity	[rad.s^{-1}]
γ	Newmark-β parameter	[-]
γ_n	Damping coefficient in normal direction	[-]
γ_t	Damping coefficient in tangential direction	[-]
λ	Thermal conductivity	[W.K^{-1}.m^{-1}]
λ'	Heat conductance	[W.K^{-1}]
λ_c	Heat convection coefficient	[W.m^{-2}.K^{-1}]
λ_l	Wavelength	[m]
λ_R	Thermal conductivity of a reference material	[W.K^{-1}.m^{-1}]
λ_w	Scale factor	[-]
λ_X	Thermal conductivity in X-orientation	[W.K^{-1}.m^{-1}]
λ_Y	Thermal conductivity in Y-orientation	[W.K^{-1}.m^{-1}]
λ_Z	Thermal conductivity in Z-orientation	[W.K^{-1}.m^{-1}]
ψ	Suction	[Pa]
μ_f	Dynamic viscosity	[Pa.s]
μ_{std}	Mean value	[-]
ν	Poisson's ratio	[-]
ν_f	Kinematic viscosity	[m^2.s^{-1}]
ϕ	Rotation	[°]
ϕ'	Friction angle	[°]
ρ	Density	[kg.m^{-3}]
ρ_f	Fluid density	[kg.m^{-3}]
σ_{p}	Peak stress	[Pa]

σ_c	Confinement stress	[Pa]
σ_h	Fluid pressure	[Pa]
σ_n	Normal stress	[Pa]
σ_s	Shear stress	[Pa]
σ_t	Tensile strength	[Pa]
$\sigma_{\mathbb{R}}$	Continuum stress	[Pa]
σ_{std}	Standard deviation	[-]
τ	Shear strength	[Pa]
τ_t	Hydraulic tortuosity	[-]
θ	Angular displacement	[rad]
ε	Strain	[-]
ε_{f}	Strain of an element at failure	[-]
ε_{p}	Peak strain	[-]
ε_m	Mechanical strain	[-]
ε_t	Thermal strain	[-]
$\varepsilon_{\mathbb{R}}$	Continuum strain	[-]
ε_{sh}	Shrinkage strain	[-]

List of Abbreviations	**|Description|**
AE	Acoustic Emission
AI	Artificial Intelligence
ANN	Artificial Neural Networks
BDEM	Bonded Discrete Element Method
BEM	Boundary Element Method
BIEM	Boundary Integral Equation Method
CCM	Cohesive Crack Model
CFD	Computational Fluid Mechanics

CMOD	Crack Mouth Opening Displacement
CTS	Compact Tension Specimen
DCB	Double Cantilever Beam
DDA	Discontinuous Deformation Analysis
DLEM	Discrete Lattice Element Method
DOF	Degree of Freedom
dynamiLEM	Dynamic Lattice Element Method
ED	Embedded Discontinuity
ESPI	Electronic Speckle Pattern Interferometry
ETC	Effective Thermal Conductivity
FDEM	Finite Discrete Element Method
FEM	Finite Element Method
FFM	Finite Fracture Mechanics
FPZ	Fracture Process Zone
GB	Generalized Beam
GSD	Grain Size Distribution
HAR	High Aspect Ratio
HM	Hydro-Mechanical
LDEM	Lattice Discrete Element Method
LEFM	Linear Elastic Fracture Mechanics
LEM	Lattice Element Method
MC	Mohr-Coulomb
MFT	Mesh Fragmentation Technique
microCT	Micro Computed Tomography
MLPG	Mesh-less Local Petrov-Galerkin
MPM	Material Point Method

NBS	Non-Binary Search
Pdf	Probability density function
PFC2D	Particle Flow Code 2D
PFEM	Particle Finite Element Method
PFF	Phase Field Fracture
PFM	Phase Field Method
PML	Perfectly Matched Layer
PSD	Pore Size Distribution
RBSN	Rigid-Body Spring Network
RVE	Representative Volume Element
SBT	Simple Beam Theory
SEM	Scanning Electron Microscope
SHM	Structural Health Monitoring
SPH	Smoothed Particle Hydrodynamics
SWCC	Soil Water Characteristic Curve
TDEM	Thermal Discrete Element Method
THM	Thermo-Hydro-Mechanical
TM	Thermo-Mechnical
UCS	Uniaxial Compressive Strength
VRL	Vectorizable Random Lattice
XFEM	Extended Finite Element Method

Chapter 1

Introduction

1.1 Background and motivation

In Geo-Engineering applications, the geomaterials are subjected to coupled Thermo-Hydro-Mechanical (THM) processes, in which the deformations and accumulated stresses can lead to the failure of the geomaterial body. Geo-Energy systems (Shao et al. 2016), energy storage facilitates (Ibrahim et al. 2008), underground natural gas reservoirs (Sedaee et al. 2019), underground CO_2 sequestration (Li and Yu 2020), hydraulic fracking processes (Wangen 2018), the storage of radioactive waste (Maßmann et al. 2011) and energy transport using underground power cables (Ocłoń et al. 2015) are some examples of Geo-Engineering applications where coupled THM processes are present. Grasping the manner in which geomaterials react to a combination of processes is a complex issue. Changes in geomaterials THM response can be attributed to multiple factors ranging from the micro- to macroscale. It is evident that a thorough examination of geomaterials on a microscale can provide us a better understanding of how even minor modifications to the THM properties at the particle-level can cause lasting changes to the effective properties of the material.

In order to simulate and visualize the coupled THM processes in geomaterials, various numerical approaches have been developed over the past decade. Continuous-based models, such as Finite Element Method (FEM) (Zheng 2018), Extended Finite Element Method (XFEM) (Jafari et al. 2023), Phase Field Method (PFM) (Wan and Chen 2022), are common numerical approaches that are considered to simulate coupled THM processes in Geo-Structures. These methods are well-established in engineering applications because of their large-scale simulation capabilities and computational performance. However, when dealing with the inherent heterogeneity of geomaterials and the present discontinuities on a microscale, these techniques are not as effective.

The inadequacies of continuum-based models led to the creation of discrete techniques, which are ideal for simulating discontinuities in heterogeneous media. Discontinuum-based models,

such as the Discrete Element Method (DEM) (Jing and Stephansson 2007) and the Lattice Element Method (LEM) (Rizvi 2019), are developed to address the aforementioned problems. The DEM is implemented to simulate and analyze the geomaterial behavior that evolves from the inter-particle contact mechanism. Lattice models are adopted to simulate the fracking process in cemented geomaterials, where small displacements are expected. The discrete lattice models are a robust numerical method to simulate the initiation and propagation of fracks in homogeneous or heterogeneous cemented geomaterials. Stress redistribution and concentration during the evolution of discontinuities are inherent in LEM. Due to the omission of the contact mechanism at the microscale, the LEM is computationally affordable compared to the DEM. The regularization of the lattice method, as well as the application of Multiscale scheme for the transition of micro- to macroscale properties, allows the model to simulate large-scale scenarios.

Compared to continuum-based numerical methods, the DEM is computationally costly, which is the main reason why this discountinuum-based method is less practical in applied engineering problems. The lattice solution neglects the complexity of the contact mechanism that exists in DEM and substantially reduces the simulation time. In lattice models, the discretized Representative Volume Element (RVE) is represented by a series of spring or beam elements. These bond elements represent the quality of contact between two adjacent unit bodies and transfer Thermo-Mechanical stresses between the generated nuclei. With the current developments in lattice approaches, the application of LEM is not limited to the simulation of mechanical fractures and complex Multiphysic problems can be studied. The lattice model offers a simpler yet effective solution to the problem, reducing computational costs while offering a precise solution.

1.2 Scope of the study

The purpose of this contribution is to develop and analyze a general discrete lattice model that can simulate the behavior of geomaterials when subjected to coupled THM processes. In the scope of this work, the following objectives are set to be studied:

- Develop a general lattice model to study the fracture progression in cemented geomaterials
- Apply a Thermo-Mechanical (TM) formulation to model the change of effective conductivity in heterogeneous geomaterials and account for developed thermal stresses
- Propose a new Hydro-Mechanical (HM) lattice model to simulate the pressure-driven fluid percolation and consider compressible fluid flow mechanism
- Extend the dynamic lattice model (dynamicLEM) into the study of the wavefields in heterogeneous and discontinuous domains and apply it in the field of Structural Health Monitoring (SHM) and defect localization
- Review of the developed lattice model in practical applications

- Explore the potential of the lattice model in the simulation of Multiphysics problems and outline its advantages and drawbacks

1.3 Outline of the thesis

The thesis is organized in six chapters, in which a detailed description of the theoretical background, implemented methodologies, validations of the numerical method, and discussion of the results are presented.

Chapter 1

The motivation and scope of this research are presented in the 1^{st} chapter. Here, the objectives of the conducted research study are outlined.

Chapter 2

In the 2^{nd} chapter of this thesis, the state of the art and review of continuum- and discontinuum-based numerical approaches are provided. In this regard, the application of numerical models to assess the geomaterial response under coupled THM processes is briefed.

Chapter 3

The methodology and mathematical formulation of the developed lattice model are presented in 3^{rd} chapter. Here, a detailed description of the discretization of the domain, the mathematical formulation of the mechanical model, the developed THM model, the application of the dynamic lattice model to wave propagation studies, as well as the extension of the lattice model in the discrete lattice model, are presented.

Chapter 4

This chapter includes numerical verifications of the lattice model by comparing the results with the analytical solutions and the experimental data. In addition, the parametric study of the THM lattice model is presented, and a discussion of the governing parameters is provided. In this chapter, the potential of the lattice model in the simulation of Multiphysic problems is outlined.

Chapter 5

The application of the developed lattice model to practical engineering problems is presented in the 5^{th} chapter. The lattice model is used to simulate the failure of reinforced masonry walls. Moreover, the lattice model is considered to investigate the integrity of geological barrier rocks. Within the scope of this research, the Hydro-Mechanical lattice model is considered to

model pressure-driven fluid percolation in rock bodies.

Chapter 6

In the final chapter, a thorough discussion of the implemented methodologies and simulation results and the applicability of the lattice model in Geo-Engineering problems are presented. Eventually, the advantages and shortcomings of the current state of research are clearly expressed, and possible future research works are proposed.

Chapter 2

State of the Art

2.1 Characteristics of geomaterials under the coupled THM processes

2.1.1 Introduction

Understanding the change in material properties under THM processes is complex matter. Changes in thermal properties, such as thermal conductivity or thermal expansion, are associated with mechanical properties. Similarly, hydraulic properties, such as fluid viscosity and pore pressure, are affected by thermal stresses. Specifically, the behavior of geomaterials subjected to THM processes alters drastically after the evolution of micro- to macroscale cracks (Liu et al. 2023). On the microscale, the development of fractures leads to an irreversible change in the mechanical stress-strain response of a geomaterial, the growth of fluid pathways, and the degradation of thermal conductivity. Eventually, any changes in the microscale are projected into the meso- and macroscale material behavior. Therefore, many studies have been conducted to investigate the uncertainties and obstacles during the transition from the micro- to the macroscale from a modeling and experimental perspective. From both numerical and experimental points of view, the heterogeneity and anisotropy that exist in the nano- and microscales lead to variation of the effective material property measured in the meso- and macroscale. In the scope of applied Geomechanics, the simplified coupled THM processes are presented in Fig.2.1, where the change in microscale properties will eventually affect the effective macroscale material behavior.

The crack growth on the microscale is summarized into a combination of three independent stress intensity factors (Irwin, 1957): (a) Mode I failure due to tensile stress, (b) Mode II failure as a result of shear stress applied perpendicular to the crack front, and (c) Mode III failure due to tearing and shear stress applied parallel to the crack front (Fig.2.2). Within the scope of fracture mechanics, the stress intensity factor at crack tip (K), fracture toughness (K_c), and strain energy release rate (G) are defined. The theory of Linear Elastic Fracture Mechanics

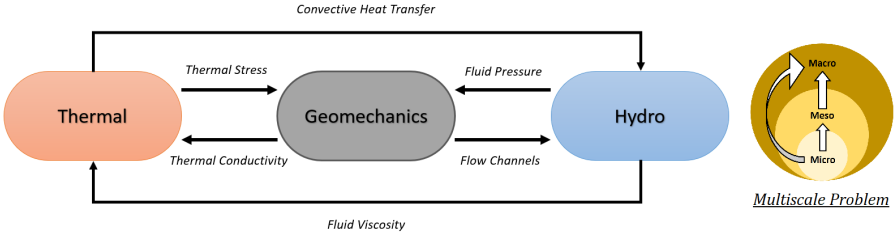

Figure 2.1: The simplified coupled THM processes in geomaterials

(LEFM) is developed based on crack development in linear elastic materials, where fracture toughness is defined to explore the resistance of brittle materials to the propagation of cracks (Lemaitre 2001). The theory of LEFM is implemented in different scientific works to study the fracture behavior of geomaterials. The size effect of fracture characteristics for propagation in anisotropic quasi-brittle geomaterials is investigated by Li et al. (2023). In an experimental work, the fracture toughness of semi-circular bend sample of rock is determined on a series of laboratory experiments (Kuruppu 2000). Similarly, the fracture toughness of Modes I and II of a rock sample is measured using disc-type specimens (Chang et al. 2002).

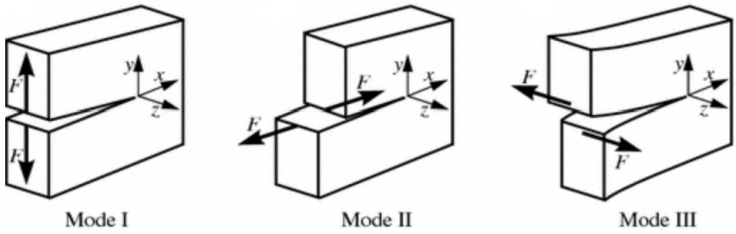

Figure 2.2: The failure modes in the scope of fracture mechanism (Richard and Sander 2016)

Constitutive models are used to explain the behavior of materials when subjected to various mechanical and/or thermal loading conditions. These models provide the stress-strain connections required to create the governing equations, as well as the conservation laws and kinematic relations. (Yang et al. 2013). The few examples of these models that are implemented in the study of geomaterial behavior are the following: Linear-Elastic (Lade and Nelson 1987), Hypo-Elastic (Hashiguchi 2017), Visco-Elastic (Maddalena and Ferrari 1995), Linear Elastic-Plastic (Chang and Hicher 2005), Hypo-Plastic (Kolymbas and Herle 1998, Stutz et al. 2017), Visco-Plastic (Cristescu 1994), and Visco-Hypo-Plastic models (Gudehus 2004). With the extension of the thermal formulation, constitutive models are implemented to study the TM behavior of geomaterials. The Thermo-Elastoplastic (Zhang et al. 2012), Thermoplastic/Viscoplastic (Zhou et al. 2011), and Thermo-Hyperelastic-Viscoplastic (Mähler et al. 2001) models are few examples of these constitutive models adopted to study the complex TM behavior of geomateirals. In

Geotechnical applications, the Mohr-Coulomb failure criterion is extensively studied to capture the material's pre- and post-failure behavior (Wang et al. 2012, Kok et al. 2009, Tian and Zheng 2023). The literature review of the material behavior of cohesive and non-cohesive soils as well as cemented geomateirals, such as rock and concrete, that are exposed to THM processes, is presented in this section.

2.1.2 Cohesive and non-cohesive soils

A wide range of experimental studies have been carried out to study the THM behavior of cohesive and non-cohesive soils. Sand, gravel and pure silt are known as non-cohesive soils that exhibit granular characteristics (Keaton 2018). Compared to cohesive soils, non-cohesive soils have higher hydraulic conductivity, higher confinement stiffness, and generally higher thermal conductivity as a result of the presence of quartz minerals. Chen (2008) investigated the application of an empirical equation to assess the thermal conductivity of four different types of sand. The experimental results indicate the dependence of the thermal conductivity on the porosity and water content of the sand samples. A similar conclusion was reached by Tokoro et al. (2016), who examined the effect of moisture on the thermal and electrical conductivities. As stated by Orsi and Sanfilippo (2020), the kinematic viscosity of water decreases with temperature. This results in lower hydraulic resistance in the pores, which eventually causes higher permeability values. The increase in the average diameter of the particles in granular soils also leads to higher permeability values (Shubber and Al-Saoudi 2018). This is due to growth in the dimensions of flow channels on the inter-particle scale. Feia et al. (2016) studied the changes in the permeability of Hostun sand (HN34) during the triaxial test. With the use of scanning electron microscopy (SEM) images, the authors observed the production of fine particles during the confinement and shearing processes.

Yao et al. (2019) studied the Thermo-Hydro-Mechanical behavior of poorly-graded sand using the suction-controlled thermo-mechanical method. In this setup, various temperatures and normal isotropic stresses are applied during the wetting and drying processes. The Soil Water Characteristic Curve (SWCC) indicates the increase in thermal conductivity during the wetting process at a constant temperature of 20°. The volume increase observed during the shear process in dense sand is due to interlocking of aggregates and lever motion. Simoni (2006) investigated the dilatancy of the sand-gravel mixture using the direct shear test procedure. Its shown that adding a gravel fraction to the sand mixture increases the porosity and, therefore, minimizes the dilatancy behavior. In another work by Wood et al. (2016), the effect of the addition of flexible fibers on the shear behavior of Hostun sand has been studied. The coupled Hydro-Mechanical processes also affect the dilatancy rate in non-cohesive soils. Fern et al. (2014) explored the effect of the presence of water on the shear strength and dilatancy of partially saturated sands using direct shear tests. The results indicate an improvement in critical-state strength, peak strength, and dilatancy rate with the presence of water on the

particle scale.

Clay is known as cohesive soil that exhibits plasticity and a strong cohesive bond at the inter-particle level (Gautam 2018). According to Mitchell and Soga (2015), the bond strength is due to cementation, adhesion, and valence bonding, as well as electrostatic and electromagnetic attractions. The swelling and shrinkage of the natural expansive clay soil during the wetting and drying processes was investigated by Basma et al. (1996). The results indicate gradual destruction of the contacts in the clay structure during the cyclic swelling process. The mechanical and hydraulic properties of clay soil, such as bond strength, micro crack initiation, and permeability, are altered during the swelling and shrinkage process. Aksu et al. (2015) investigated the swelling of montmorillonite pellets and its influence on the permeability of unconsolidated porous media using X-ray μ-computed tomography.

The mechanical properties of clay soil depend on the overconsolidation ratio (OCR), the loading rate, porosity, the grain size of the matrix, the clay content, and the degree of saturation. Stróżyk and Tankiewicz (2014) investigated the undrained shear strength (c_u) of the overconsolidated clay. The results indicate an increase of c_u under higher OCR values. The effect of porosity on the shear strength of sand-clay mixtures is studied by Vallejo and Mawby (2000). Laboratory results indicate the optimum porosity value, where shear strength is maximized. The plate-shaped aggregate geometry of clay minerals results in anisotropy and dependence of the THM properties on different orientations. Nishimura et al. (2007) reported the shear strength anisotropy of natural, highly overconsolidated London clay, where the rate of anisotropy increased with depth. The stress-dependent shear behavior of resedimented Boston blue clay is investigated by Abdulhadi et al. (2012). The outcome of the study indicates that the undrained secant Young's modulus ratio is stress-dependent, and its magnitude decreases with increasing consolidation stress. Mun et al. (2016) conducted the unconsolidated undrained (UU) triaxial tests on compacted clay soils with different values of water content while maintaining the constant void ratio. The results indicate a higher undrained shear strength with an increasing strain rate.

In a contribution by Ma et al. (2013), triaxial tests were performed under constant water content conditions on Yunnan red clay. The purpose of the research was to investigate the SWCC and the shear strength characteristics of the clay geomaterial. The osmotic suction method is used to apply suction values and determine SWCC. According to the results, the lower water content results in a higher shear strength and strain softening behavior. Heat transfer in moist clay with different water content has been investigated by Woodside and De Bruyn (1959). The outcome of the experimental study indicates the sensitivity of clay to water and moisture migration when subjected to a temperature gradient. The coupled Thermo-Mechanical and Thermo-Physicochemical behaviors of kaolinite and smectite are studied in the

thesis of Jefferson (1994). Here, the effect of temperature on the consolidation and permeability changes was studied. Cekerevac and Laloui (2004) investigated the impact of temperature on the mechanical behavior of Kaolin with a temperature-controlled triaxial apparatus. In this study, the effects of temperature on shear strength, critical state line, pre-consolidation pressure, compressibility index, and thermal volume change during the heating process were studied. The expelling of water leads to contraction of the soil, and the dilation ratio depends on the type of clay mineralogy. Paaswell (1967) studied the impact of temperature on clay soil consolidation. As a result, the higher the temperature, the more deformations are measured. The THM behavior of compacted unsaturated swelling clay is examined by Tang et al. (2008). Heating at constant pressure and suction values have been reported to induce swelling or contraction. When the temperature and suction values were kept constant, higher elastic and plastic compressibilities were recorded at lower suction values.

2.1.3 Cemented geomaterials

Compared to cohesive or non-cohesive soils, igneous, metamorphic, and sedimentary rocks exhibit greater stiffness, lower permeability, and greater strength. In many Geo-Engineering applications, rock formations are used to store or extract energy. As a result, the THM properties of cemented geomaterials have been subjected to various experimental studies. The fratcure toughness and strenght of rock materials have been widely investigated. The fracture toughness of Keochang Granite and Yeosan Marble under Mode I and Mode II failures was explored by Chang et al. (2002). In this experimental study, the size effect of samples with semicircular bend and a cracked chevron-notched Brazilian disc was studied. A series of three-point bending tests were conducted on Rockville granite to study the evolution of micro-cracks and the change in the fracture process zone with the size of the sample (Tarokh et al. 2017). According to the results, the length and width of the fracture process zone increases with the increase in the dimensions of the specimen. The experimental study of the fracture toughness of concrete samples on notched beam specimens is carried out by Hamoush and Abdel-Fattah (1996). It is shown that the fracturing criterion is independent of crack length and is only a function of the aggregate size and gradation. Similarly, the fracture toughness of fiber-reinforced concrete is explored (Gopalaratnam et al. 1991).

In a broad range of studies, the change in rock properties is reported under TM processes. Salt rock gypsum interlayers were subjected to high-temperature conditions in real time to investigate the alteration of Mode I fracture toughness in a coupled TM study (Li et al. 2020). The results indicate the degradation of the fracture toughness with increasing temperature. The experimental evaluation of the properties of rock samples subjected to high temperatures is investigated by Tiskatine et al. (2016). In this study, by conducting a Vickers hardness test, the compressive strength of rock samples is analyzed under thermal cyclic stresses. The dependency of thermal diffusivity on applied temperatures up to 300° is reported by

Mottaghy et al. (2008). Moreover, the change in the thermal conductivity of rock samples, such as sandstone, conglomerate, gypsum, and marble, under uniaxial and triaxial stresses is examined by Demırcı et al. (2004). In another study, the in-situ conditions are considered in laboratory experiments to study the effect of temperature on shale fracture properties and provide a correlation between temperature and fracture toughness (Li et al. 2023). Similarly, in-situ conditions are applied to determine the change in thermal conductivity of various rocks (Motra et al. 2020). The result of the experimental investigation shows that with increasing mechanical pressure with depth, the thermal conductivity of the rock samples increased. The effect of temperature on the mechanical properties of concrete samples has been widely investigated. The impact of low, high, and curing temperature on the strength of concrete samples, as well as the variation in fracture toughness with temperature, have been reported (Abdel-Fattah and Hamoush 1997, Elzohairy et al. 2020, Krishna et al. 2021).

The coupled THM processes that exist in Geo-Energy structures permanently can affect the material behavior of cemented geomaterials. Drop plate impact tests were performed on red sandstone samples with natural, dry, and saturated conditions to study the effect of the water content on the characteristic of the dynmaic fracture of the rock (Niu et al. 2020). According to the results, the speed of crack propagation was affected by the state of the water content of the samples. The water-rock interaction has been studied to investigate the change in rock strength with varying degrees of saturation (Zhang et al. 2023). The outcome of the experimental study illustrates the decrease in strength with different degrees of water content, immersion time, and wetting-drying cycles. Kodama et al. (2013) studied the influence of temperature and water content, as well as load rate, on the strength and failure process of frozen rocks. The strength of frozen rocks has been reported to be significantly affected by the water present and the loading rate. Under in-situ geological conditions (temperature, stress, and pore pressure), the mechanical behavior of the rock is investigated (Xie et al. 2021). The peak and residual strengths of the rock material have been reported under triaxial compression tests to be overestimated when the in-situ stress condition is restored. Pressure-driven fluid percolation in salt and clay rocks is experimentally and numerically investigated (Kolditz et al. 2021, Sattari et al. 2021). The principal stress configuration has been reported to influence the development of fluid pathways in salt rock. On the other hand, the embedded layering of clay rocks creates a weak interface, resulting in the development of flow channels (Glaß 2023). The effect of temperature and effective stresses on the evolution of permeability in sandstone formations was presented by Sun et al. (2016).

The intricacy of the interrelated THM characteristics of geomaterials is illustrated in this section. Numerical methods accompany experimental and field studies to investigate and model complex engineering problems. In the next section, the evolution of the numerical methods

and their application in the Geo-Engineering field of study to model the THM processes in geomaterials are briefed.

2.2 Application of the numerical methods in Multiphysics

2.2.1 Introduction

With the increase in computational power, the application of numerical methods to simulate complex Multiphysics problems has been comprehensively studied. In a general sense, the numerical methods are divided into two categories: (a) Continuum-based, or (b) discounituum-based models. The continuum-based models are subdivided into two different approaches: (a) Mesh-based, or (b) mesh-less models. The solutions of mesh-based models are typically Eulerian, whereas the mesh-less models are based on a Lagrangian formulation. In this section, the literature review of numerical methods developed to address the coupled THM processes in geomaterials is presented.

2.2.2 Continuum-based models

The Finite Element Method (FEM) is a powerful tool for solving a broad range of issues, including those involving nonlinearity, Multiscale, Multiphase, and Multiphysics. FEM is a widely used approach to numerically solve differential equations that arise in engineering and mathematical modeling. It is based on the concept of breaking down a domain into small elements (triangular elements) and approximating the solution of the problem within each element. The FEM solution of multi-dimensional two-phase flow through porous media was proposed by Jweeg et al. (2022). In a similar work, Juanes (2005) considered a variational Multiscale finite element method to simulate Multiphase flow in porous media. The application of FEM was extended to fully coupled Hydro-Mechanical processes and analyzing the behavior of unsaturated soil analysis under hydraulic and mechanical loads (Zhang et al. 2019). A fully coupled THM finite element method was applied to study the freezing process in porous media (Zheng 2018). One of the main issues with the FEM mesh is that it must fit the shape of the crack. Therefore, the mesh must be updated for each crack increment as the crack progresses. This can be challenging and computationally expensive, which makes the method less suitable for fracture simulations.

The Extended Finite Element Method (XFEM) is a numerical technique, derived from the FEM, that is specifically developed to address discontinuities. In XFEM, with the tracking of the crack path during the simulation, the positions of the crack surfaces were studied (Jenabidehkordi 2018). The application of XFEM was extended to simulate the deformable

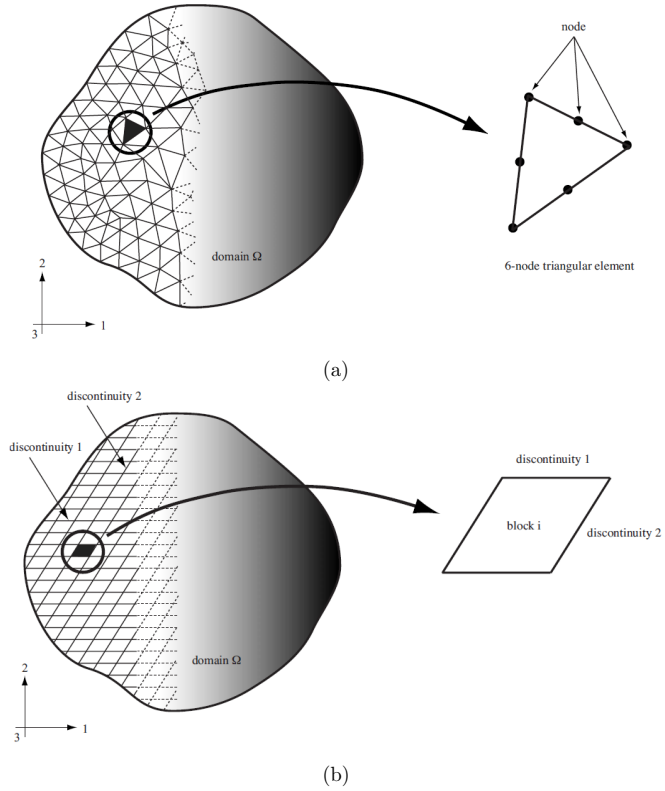

Figure 2.3: The discretization of the domain with (a) continuum-based, and (b) discountinuum-based models (Bobet et al. 2009)

fractured porous media (Xu et al. 2021). The implementation of XFEM in COMSOL multi-physics allows the simulation of Thermo-Hydro-Mechanical processes in discontinuous porous media (Jafari et al. 2023). In another contribution, the evolution of macroscale fracture during the hydraulic fracking process under coupled Thermal-Hydraulic conditions was explored by Zeng et al. (2020).

To avoid the need to trace the fracture surface, the Phase Field Method (PFM) is widely used to simulate fracture initiation and propagation in solid bodies. With the application of Phase Field Fracture (PFF) models, the quasi-static and dynamic fracture of brittle and quasi-brittle materials were modeled (Wu et al. 2019). A fully coupled thermo-mechanical PFM was used to model cracks with frictional contact by adopting the pressure-dependent thermal conductance model (Wan and Chen 2022). Furthermore, considering open source OpenGeoSys software, variational PFM was implemented to simulate the hydraulic fracture interaction with natural

discontinuities (Lepillier et al. 2020).

The Mesh Fragmentation Technique (MFT) has been implemented in FEM solver to avoid the necessity of crack-tracking schemes. In these methods, the interface between the finite elements is modified, where a solid finite element with a very high aspect ratio (HAR) is inserted. To study compressive fracture in concrete, the mesh fragmentation method was adopted (Gimenes et al. 2023). The formation of hydraulic fractures in rocks was studied with the application of MFT and consideration of HAR elements (Cleto et al. 2020). This numerical approach was also considered for studying soil desiccation cracks developed under laboratory and field conditions (Sánchez et al. 2014). Additionally, Multiscale coupling of the finite element method with the MFT was applied to simulate the failure of the reinforced steel fiber concrete (Bitencourt et al. 2018).

Due to the potential for mesh-distortion or complete detachment that can occur during large deformations, mesh-less continuum-based models have become increasingly popular. A few examples of the developed methods are Material Point Methods (MPM) (Wolper 2021), cracking particles method (Rabczuk and Belytschko 2004), Mesh-less Local Petrov-Galerkin (MLPG) (Lin and Atluri 2001), Particle Finite Element Method (PFEM) (Rodriguez et al. 2016), and Smoothed Particle Hydrodynamics (SPH) (Yu et al. 2021). SPH is a mesh-free approach that does not require a numerical mesh for the integration of governing equations. In the scope of computational fluid mechanics (CFD), SPH has been widely implemented to study fluid mechanics (Sibilla 2013). The heat conduction equations were integrated into the conventional SPH model to study the Thermo-Hydro-Mechanical damage processes within the rock structure (Yu et al. 2023). However, the definition of boundary conditions in SPH is relatively complex compared to mesh-based methods.

2.2.3 Discountinuum-based models

The conventional Discrete Element Method (DEM) considers the contact mechanics between interlocking discrete bodies to study THM problems in the discontinuous domain. Consequently, DEM was applied to simulate the mechanical behavior of granular materials (Yang and Wang 2012). To model the cohesive behavior of cemented soils or solids, the discrete cohesive element method was implemented, where the inter-particle bond was represented by a lattice element (D'Addetta 2004). The ability of DEM to simulate the continuous part of the material using a cohesive bond model was investigated by André et al. (2012). The study of fragmentation processes in geomaterials with discrete granular particle assembly was carried out by D'Addetta et al. (2008), where the beam elements represent the cohesive effects. In another contribution, two- and three-dimensional fracture analyzes in concrete under uniaxial compression were explored by Suchorzewski et al. (2018). Recognizing the discontinuous nature of fragmentation, fracture simulation was performed using the bonded discrete element method

(BDEM) (Lu et al. 2022). Moreover, the simulation of the reinforced concrete three-point bending test was carried out using the formulation of a circular rigid 2D discrete element (Azevedo et al. 2006).

With the implementation of a Hydro-Mechanical formulation in DEM, the hydraulic fracking process was simulated (Li and Zhang 2022). Particle Flow Code 2D (PFC2D) was used to simulate the interaction of hydraulic fractures and natural fractures in low permeable hard rock (Yoon et al. 2017). The interaction between hydraulic fracking and natural fracture was explored to predict fracture geometry and reservoir production (Basirat et al. 2019). In another contribution, a DEM was used to model the drying shrinkage and cracking of fine-grained soil (Peron et al. 2009). The swelling behavior of Na-montmorillonite, taking into account the forces of the inter-particles was carried out by (Anandarajah and Amarasinghe 2013). Additionally, the swelling behavior of expansive clay was simulated by calculating the adhesive force to capture the effect of water content on cohesion and inter-granular expansion (Xi et al. 2021). In another research work, a two-dimensional discrete model was proposed considering property change during the drying process and shrinkage kinetics (Lin et al. 2021).

To account for displacement discontinuities, different material interfaces, and the consideration of micro- and meso-scope heterogeneities, different authors extended the discrete element method (DEM) to simulate the heat transfer in granular assemblies and consider the contact quality factor in heat transmissions. The ETC of the granular RVE has been computed from the average heat flux and the average temperature gradient obtained from Thermal Discrete Element Method (TDEM) simulations taking into account the micro-scale structure. With the assumption of circular disk-shaped particles and conduction through solids in contact, heat transfer using TDEM was simulated (Feng et al. 2009). The thermal contact model can also consider the thermal resistance of rough surfaces in a DEM (Bahrami et al. 2004; 2006). In this regard, a DEM study was performed on the effective thermal conductivity of granular assemblies (Zhang et al. 2011). In 2016, an implicit 3D heat transfer model was derived to represent resolved heat conduction in spherical and non-spherical particles in the presence of a surrounding fluid (Oschmann et al. 2016).

The development of the numerical Lattice Discrete Element Method (LDEM) was based on the work of Nayfeh and Hefzy (1978), where the generated bars are assembled in a cubic arrangement with each cubic cell consisting of nine nodes. Nayfeh and Hefzy (1978) used such a unique arrangement to determine the properties of an orthotropic elastic medium. On the basis of this theoretical work, Riera (1984) developed the mathematical formulation under the LDEM. In LDEM, massless bar elements carry the axial load between nodal points. The mass is defined at nodal points with three DOF in the three orthogonal coordinated directions. Simulation of crack propagation in elastic solids using LDEM was explored by

Kosteski et al. (2012). Similarly, the study of reinforced concrete plates subjected to impact was presented by Kosteski et al. (2015). In a recent study, the effect of the scale on quasi-brittle material specimens was investigated and the results were analyzed with the theory of the fractal size effect (Kosteski et al. 2022). Similarly to the LEM method, LDEM was applied to the simulation of damage processes in quasi-brittle materials (Tanzi et al. 2023). Here, the LDEM was combined with the Acoustic Emission (AE) technique to analyze the damage. The coupling of LDEM with Abaqus/Explicit software was used to analyze failure processes and reduce computational costs (da Silva et al. 2020). The LDEM was also coupled with the FEM using the Abaqus environment to analyze failure processes and reduce computational costs (da Silva et al. 2020).

The transition from continuum to discontinuum during the fracture process resulted in the development of the combined Finite-Discrete Element Method (FDEM) (Munjiza et al. 2004). In FDEM, according to the equation of motion, the nodal coordinates are updated after each iteration step. The developed FDEM software, Y-Code, combines the FEM methodology with the concept of DEM (Munjiza et al. 2011). Furthermore, the 2D coupled FEM-DEM was developed to model the multi-fracture of beam structures (Paavilainen et al. 2009). The combination of a discrete crack and plastic deformation has been considered to simulate the fracture using FDEM (Rougier et al. 2020). The application of FDEM has been extended to cover multiphysics problems. In this manner, the hydraulic fracturing process was simulated using the FDEM by Yan et al. (2016). The 2D FDEM was used to account for moisture diffusion and simulate soil desiccation cracking (Yan et al. 2021). In a recent study, the combined FDEM model was implemented to simulate the coupled Thermo-Hydro-Mechanical processes of hydraulic fracking in deep reservoirs (Sharafisafa et al. 2023).

Due to the computational power needed to track the individual particles and determine the inter-particle contact forces, the application of DEM in large-scale models is limited. The Lattice Element Method (LEM) simplifies the discrete solution by neglecting the calculation of contact forces in time iterations. LEM is a numerical technique used in engineering and physics to solve problems related to structural mechanics and materials science. It involves dividing a structure into small interconnected elements, or lattices, and analyzing their behavior under different loading conditions. By applying the principles of matrix algebra and finite element analysis, the lattice element method can accurately predict stress, strain, and deformation in complex structures. In 1941, Hrennikoff used the regular triangular lattice to solve elasticity problems (Hrennikoff 1941). However, because of the inadequate computational power at the time, the model remained a theoretical approach. The initial application of the lattice model was to simulate the initiation and propagation of fractures in granular assemblies (Cundall and Strack 1979).

The lattice model discretized the domain with a series of 1D spring (Wong et al. 2015), bar, or beam elements (Nikolić et al. 2018). One of the main advantages of the LEM is its ability to simulate stress redistribution and concentration during the cracking process. The LEM is often used to simulate the fracturing process of the heterogeneous medium on micro- or mesoscale. Initially, LEM was used to solve elasticity problems and model progressive failure in a heterogeneous medium (Burt and Dougill 1977). Conductivity problems and simulations of brittle failure were studied by Herrmann and Roux (1990). Schlangen and Van Mier (1992) simulated the initiation and branching of cracks in cement concrete using truss elements as connecting links. In LEM, the heterogeneous medium is discretized with 1D lattice elements, and failure is modeled by removing elements that exceed the threshold strength locally based on defined failure models. In general, LEM deals with fracture analysis and crack initiation in concrete and other particle composites, where small particle movements or displacements are expected (Schlangen and Garboczi 1997, Topin et al. 2007, Liu et al. 2007, Snyder et al. 1993, Zhao et al. 2012, van Mier et al. 2002, Prado and van Mier 2003). The Generalized Beam (GB) lattice was introduced to reduce computational effort (Liu et al. 2007). In a GB element, the geometrical and material parameters of each beam are calibrated independently. The generalized beam lattice model, in which the properties of the mechanical bond-aggregate interface are implemented in a lattice element, was also used to simulate crack growth in concrete (Liu et al. 2009). The Timoshenko beam element theory was implemented to improve the accuracy of existing Euler-Bernoulli beams (Karihaloo et al. 2003). A lattice model with Embedded Discontinuity (ED) was developed to capture Mode I and II failures of the cohesive links (Nikolić et al. 2018). The Rigid-Body Spring Networks (RBSN) are also similar to lattice elements, representing the domain with a series of spring elements. In these methods, between each unit cell, three spring elements representing resistance against axial, tangential, and rotational displacements are considered (Bolander and Saito 1998, Hong and Yoshitake 2000, Rasmussen et al. 2018).

The initial step in the application of the lattice model is to grant the mesh-independence outcome of the simulations. In this regard, the embedded strong discontinuity is introduced into the lattice elements, resulting in mesh-independent computations of the failure response (Nikolić et al. 2018). In another approach, the correlation between the properties of a single element and a continuum is achieved using strain energy theory, where the strain energy stored in a unit cell is equal to the strain energy stored in a continuum (Ostoja-Starzewski 2002, Karihaloo et al. 2003). With the extension of the LEM to the 3D model, Liu (2001) studied the mechanical behavior of the short-fiber reinforced composites using 3D springs. Fracture growth was observed in three-phased concrete material using 3D beam elements (Lilliu and van Mier 2003). Under the uni-axial tension and with the implementation of 3D LEM, a fracture process of geomaterial with a pre-existing penny-shaped crack was modeled (Wong et al. 2015).

The crack simulation in lattice elements is performed by removing an element exceeding its strength threshold (brittle failure) or degrading the stiffness according to a bi-linear softening scheme. Failure of elements is defined based on the Mohr-Coulomb failure model with a tension cut-off (Liu et al. 2009, Bolander and Saito 1998) or based on the fracture mechanisms of Mode I and II, where a critical stress intensity factor has been used to calculate the strain energy release rate (Rizvi et al. 2019, Wong et al. 2015, Dong et al. 2016). A quasi-brittle geomaterial, such as rock, concrete, or mortar, discloses a strain softening behavior and progressively fails due to localization of stress and damage (Bolander and Kobashi 1995). Vervuurt (1997) studied the effect of size on the strength of plain concrete, implementing the stress softening of the matrix phase. van Vliet (2000) conducted research on fracture propagation in concrete while focusing on interface behaviors. Moreover, Ince et al. (2003) considered the effect of size and studied the tensile fracture of concrete and rock geomaterials. Similarly, spring networks and random lattice methods were implemented to simulate the onset and growth of fractures in cement mortar, cement composites, and concrete (Bolander et al. 2008, Kunhwi and Yun Mook 2011). In all the aforementioned studies, the focus was on the study of fracture propagation in materials.

In recent years, the application of the lattice element has been extended to simulate Multiphysic processes (Rizvi 2019). In 2010, Osama (2010) used the discrete lattice approach to model heat transfer, in which a one-dimensional governing partial differential equation for heat transfer was developed without considering contact quality and forces. Sattari et al. (2017) developed a mesoscale lattice model to simulate heat flow in the heterogeneous cemented geomaterial. This work was followed by the application of the numerical lattice model to predict the effective thermal conductivity of modified geomaterials (Rizvi et al. 2018) and unsaturated granular geocomposites (Shrestha et al. 2019). In 2019, a new lattice element method (LEM) with integrated interface elements was developed to determine the effective thermal conductivity of rock solids in thermo-mechanical processes (Sattari et al. 2019).

The application of the lattice model has been extended to model the fluid flow problems. Hydro-mechanical lattice models have been developed to simulate changes in flow and permeability in geomaterials (Grassl 2009, Grassl et al. 2013). The dual-lattice model was also implemented to investigate fluid-driven percolation and developed flow paths in salt and clay stone samples under anisotropic confining stresses (Kolditz et al. 2021). Few studies have been conducted to model the hydraulic phase and couple it with the conventional mechanical lattice model. The flow model in cracked concrete with the introduction of conduit elements along the Voronoi cell boundaries to carry the flow and the correlation between diffusion and fracture opening was explored by Grassl (2009). In another work by Grassl et al. (2013), liquid transport was modeled in the unsaturated cracked heterogeneous porous material. In another approach to model the behavior of unsaturated soil, the discrete cohesive link lattice model

based on inelastic Timoshenko beam elements with enhanced kinematics is applied in the axial and transverse directions. The coupling equations for the soil-pore fluid interaction are derived from Terzaghi's principle of effective stresses, Biot's theory of porous media, and Darcy's law for fluid flow through porous media (Hadzalic et al. 2018). In a recent work published by Yoshioka et al. (2022), the nucleation and propagation of flow pathways under variable stress conditions are simulated using the dual Hydro-Mechanical lattice model.

The extension of the mechanical formulation to simulate the dynamic wave field was initially carried out by Rizvi et al. (2018). Here, the dynamic LEM is used to simulate wave fields while considering a progressive fracking process in brittle and quasi-brittle material under dynamic loading. Moreover, dynamic LEM was applied to solve the problem of mechanical waves in the rock mass or cemented granular material under dynamic loadings (Rizvi et al. 2020). The simulation of crack propagation under dynamical forces using an embedded strong discontinuity approach was also implemented by Nikolić et al. (2018). The simulation results of the dynamicLEM were used to train the artificial neural network (ANN) model to detect and localize discontinuities and defects (Wuttke et al. 2021). In a recent contribution by Sattari et al. (2022), wavefield scattering and dispersion due to inherent heterogeneity and discontinuity of geomaterials have been simulated using dynamicLEM.

Furthermore, the lattice method is coupled with continuum- and discontinuum-based numerical methods to study fracture processes. The coupled lattice and finite element method (FEM) is developed to study fracture in composite concrete pavements (Khazanovich 2012). The lattice element has been combined with the discrete element method (DEM), known as the cohesive discrete element method, to simulate fracture problems. D'Addetta (2004) studied the application of discrete models for cohesive frictional geomaterials using the cohesive discrete element method, where the bond between grains is represented with a lattice spring or beam element. The 3D commercial hydraulic fracturing model (XSite) is developed based on the combined discrete lattice method and synthetic rock mass (SRM) to address the hydraulic fracturing process, where the lattice domain is separated into two coarse and fine meshes (sub-lattice) to reduce computational costs and enhance the accuracy (Damjanac et al. 2020).

Chapter 3

Methodology of the developed discrete lattice model

3.1 Framework of the lattice model

The mathematical formulation and application of the lattice element method (LEM) for the simulation of micro- to mesoscale material behavior under the coupled THM processes are presented in this chapter. To begin with, the domain discretization techniques within the scope of the lattice model are introduced. Next, the introduction of a micro- to macroscale heterogeneity scheme on the discretized domain is explained. The mathematical formulation of the mechanical lattice model that is used to simulate the pre- and post-failure response of geomaterials is provided. Afterward, the mechanical model is extended with the thermo- and hydro-solutions to solve the heat and fluid flow problems. Finally, the lattice model is extended to simulate wave propagation in a damaged or heterogeneous domain using the dynamic lattice model. Fig.3.1 illustrates the flow chart of the lattice models developed in the scope of this study.

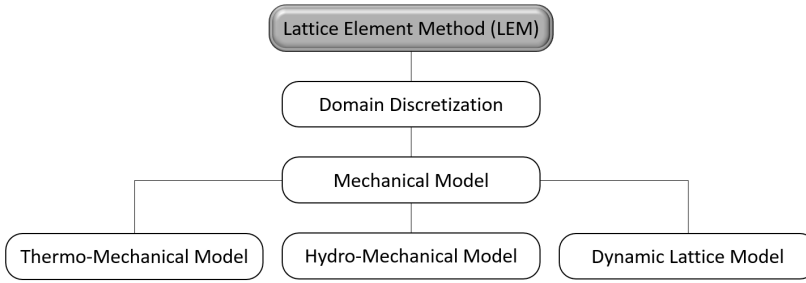

Figure 3.1: The flowchart of the developed lattice models

3.2 Domain discretization and stochastic irregularity

The initial step in any numerical study is to discretize the domain with a series of elements, nodes, or discrete bodies. In the lattice element method, different approaches could be considered to generate and distribute the numerical nodes. The two main algorithms for generating meshes adopted in LEM are the Vectorizable Random Lattice (VRL) (Moukarzel and Herrmann 1992) and the Poissonian random lattice (Rizvi 2019). The generated mesh based on these two models each has its own advantage and disadvantages. In VRL, which is implemented in this study, the generated heterogeneity is controlled by a parameter known as the randomness factor (α_r). Based on the predefined magnitude of α_r, the domain could be regular or moderately irregular. Therefore, the simulated results are to some extent affected by this parameter, for example, the frack propagation path. However, due to the defined randomness factor, the irregularity ratio is controlled, and regularization of the lattice approach is possible. On the other hand, in a Poissonion lattice, the mesh nuclei are randomly generated. In this method, to avoid numerical difficulties that can arise due to small element lengths (beam elements), a minimum element length is defined as a threshold. The mesh generated with this method is more irregular compared to the VRL method. But, on the other hand, the results are stochastic, and the outcomes of the simulations are greatly affected by the mesh choice. Fig.3.2 compares the irregularity of the generated mesh with the VRL with the maximum randomness factor (α_r=1) and the Poissonian lattice. The number of generated mesh nodes is kept constant for both simulations.

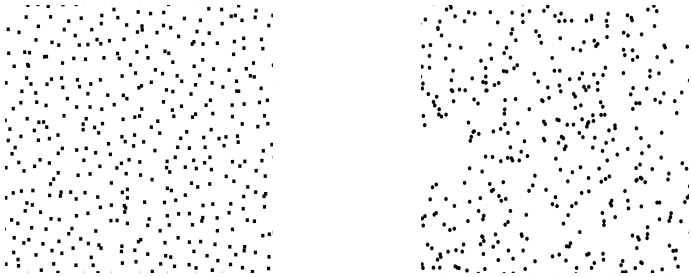

(a) (b)

Figure 3.2: Discretization approach in LEM: (a) vectorizable random lattice with α_r=1 and (b) Poissonion lattice

In this work, the VRL is adopted due to its capability to control the mesh irregularity. This leads to the development of a more accurate regularization scheme and reduces the mesh dependency of the results. As mentioned before, in the implemented VRL method, the generated irregularity of a mesh is controlled using the defined randomness factor (α_r), where $\alpha_r = 1$ provides the maximum irregularity and $\alpha_r = 0$ generates a regular mesh. Initially, based on the predefined

mesh size, the medium is divided into squares (or cubes in 3D) with a side length of D_{Mesh}. Based on the predefined α_r, inside each one of these squares, a second square of side length D_{Node} is generated (D_{Node}=$D_{Mesh} \times \alpha_r$). A single nucleus (n_i) is then randomly generated within each of the smaller inner squares (Fig.3.3).

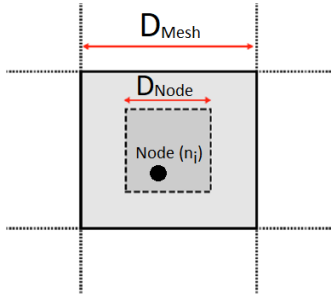

Figure 3.3: The generated nodes using VRL and with the defined α_r

According to the coordinates of the generated nuclei, the Voronoi tessellation is considered to discretize the domain into polygons. A Voronoi diagram is a division of a plane into regions close to each of a given set of objects (Pokojski and Pokojska 2018). The shape of the polygons is strongly affected by the chosen (α_r). Fig.3.4 illustrates three Voronoi tessellation outcomes with different values of the randomness factor. To flatten the boundary surfaces, a regular distribution of nuclei ($\alpha_r \approx 0$) in the surrounding boundaries is adopted. To do so, auxiliary points outside of the domain are generated. The importance of Voronoi tessellation in LEM is for better visualization of the simulation results, determination of contact areas (or cross-section of the elements) as well as the definition of flow channels in the hydro-lattice model (Sect.3.6). On the other hand, in DLEM, the shape of the polygons does represent the micro-scale particle shapes. The magnitude of contact forces, sliding, and rolling of polygons is affected by the shape of the polygons. Voronoi tessellation is performed using the available Matlab function *"voronoin"*, which generates the polygons and defines the index number of all vertices, as well as their Cartesian coordinates (X, Y, and Z).

The last step in domain discretization is to define the connectivity of polygons (cells) with lattice elements, where generated 1D elements connect two adjacent nodes. The properties of these elements can be later assigned as spring, bar or beam elements. In order to generate the lattice elements, the Delaunay triangulation theory is implemented here. Delaunay triangulation maximizes the minimum of all angles of the triangles in the triangulation (Lee and Schachter 1980). The MATLAB function *"delaunayTriangulation"* is utilized to generate all triangles, where each triangle consists of three 1D lattice elements. The irregularity in length and orientation of the generated lattice elements depends on the predefined randomness factor. Fig.3.5 illustrates three different discretized domains with different randomness factors. In the

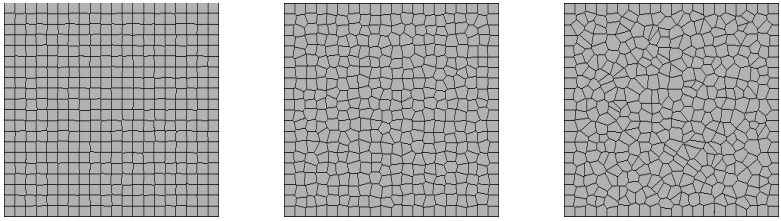

(a) (b) (c)

Figure 3.4: The Voronoi tessellation in LEM with different α_r values: (a) $\alpha_r = 0.1$, (b) $\alpha_r = 0.5$, and (c) $\alpha_r = 0.9$ (Sattari et al. 2017)

conventional lattice element model, there is no load or heat transmission through the contact area of Voronoi cells. Only the lattice elements transmit mechanical and thermal loads from one node to another.

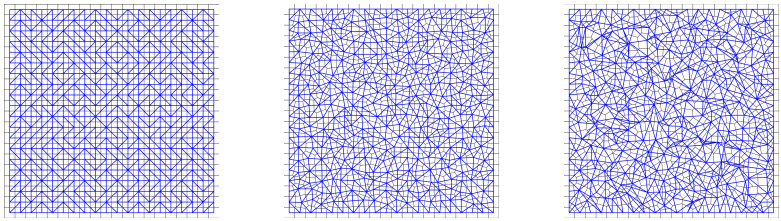

(a) (b) (c)

Figure 3.5: The generated lattice elements (blue) in LEM with different α_r values: (a) $\alpha_r \approx 0$, (b) $\alpha_r = 0.5$, and (c) $\alpha_r = 1$

The in-house code developed is also extended to account for circular or cylindrical domains with smooth surfaces. To do so, the generated vertices of each Voronoi cell located outside of the circular domain are re-positioned as demonstrated in Fig.3.6a. The result of this relocation is a smooth circular surface (Fig.3.6b). The methodology mentioned above is also extended to a 3D lattice model, where, with the generation of nodes using VRL in 3D space, Voronoi tessellation and Delaunay tessellation are considered to discretize the domain, as shown in Fig.3.7.

In order to decrease the number of elements in large simulations and reduce the computational costs, two different approaches are considered in this study. First, the mesh refinement algorithm is implemented in the model as depicted in Fig.3.8a. Here, the element size increases with the distance to the refinement nucleus. The circular refinement is carried out by subdiving a circle around the refinement mesh into multiple segments. Then a random nucleus is generated inside each segment. The other simplified version is to mesh the domain with different mesh intervals. Here, two or more mesh intervals can be used to discretize the domain (Fig.3.8b). It is noticed that, to avoid numerical difficulties, it is preferable to reduce the mesh interval to not more

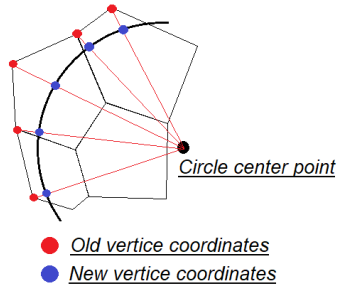

(a)

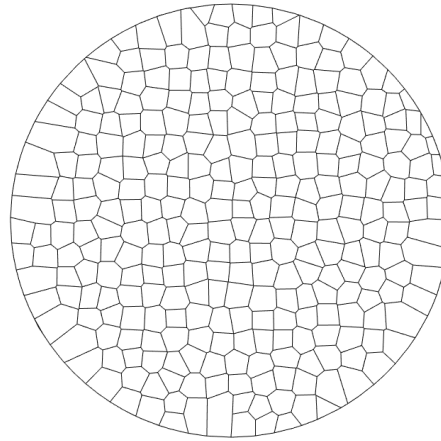

(b)

Figure 3.6: Circular domain discretization scheme in LEM: (a) repositioning of the outer vertices on boundaries, and (b) the resulted mesh in 2D with $\alpha_r = 0.5$

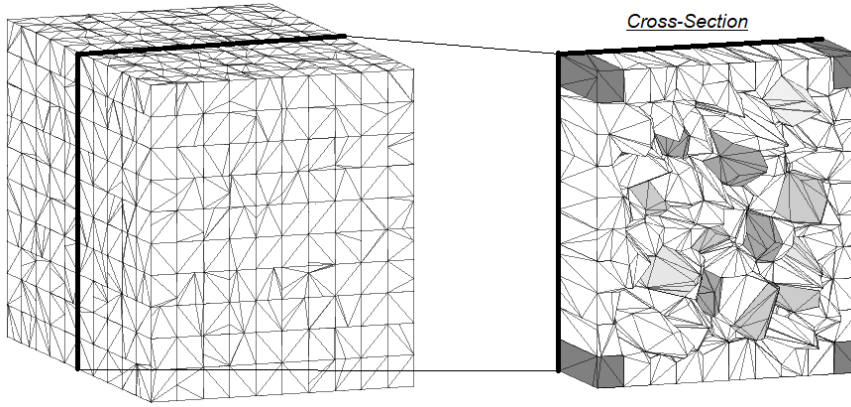

Figure 3.7: The generated 3D lattice model with $\alpha_r = 1$

than half of the adjacent mesh interval. This minimizes the errors that could develop by the regularization scheme presented in Sec.3.4.3.

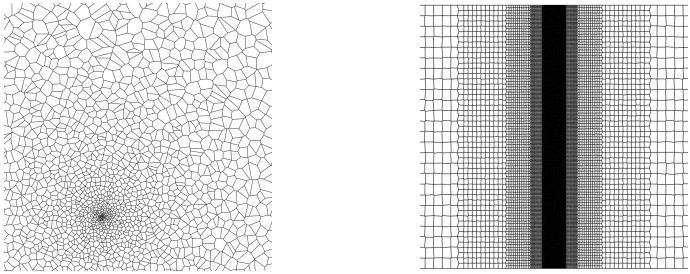

(a) (b)

Figure 3.8: Implemented mesh refinement scheme in LEM: (a) circular refinement, and (b) partitioned refinement with five different mesh intervals, where $\alpha_r = 0.1$

3.3 Introduction of heterogeneity and discontinuity

In the lattice model, heterogeneity and discontinuity could be defined from micro- to macroscale. In addition to the mesh irregularity that was discussed in the previous section (Sec.3.2), the heterogeneity of geomaterials on the microscale leads to a change of effective material properties on the macroscale. Examining closely, we can observe that all geomaterials found in nature are heterogeneous. This could be as simple as the porosity of the materials or as complicated as different mineral compositions in a rock sample. The effective material response, which is measured during lab-scale (mesoscale) or field-scale (macroscale) tests, is driven by micro- to nanoscale material behavior of every single component of the structure. For example, the dimension, distribution, and amount of porous volume in a geomaterial have influence on the effective parameters measured in the laboratory scale.

Heterogeneity has been introduced into the discretized domain in different schemes. The simplest approach would be to stochastically distribute heterogeneity with a known composition ratio. In a random manner, a property of any node or Voronoi cell could be assigned to any particular mineral or void. The lattice element connecting to an identical node property would represent that specific mineral or void. On the other hand, an element connecting two different node properties would be assigned as an interface element between two different compositions. So in the lattice element method, an interface has a thickness as only 1D elements are considered in this approach. Fig.3.9 depicts the generated domains with a predefined porosity of 10% as well as a cross-section of the rock sample with four different minerals randomly distributed.

In another approach, the heterogeneity is distributed according to the particle size distribution data. For instance, for a concrete sample with a known grain size distribution (GSD) circular or spherical grains are randomly generated on top of the Voronoi cells. The Voronoi cells intersecting the circles or spheres are assigned as granular domains. With the known pore size distribution (PSD) in the concrete sample, the voids are distributed. The remaining Voronoi

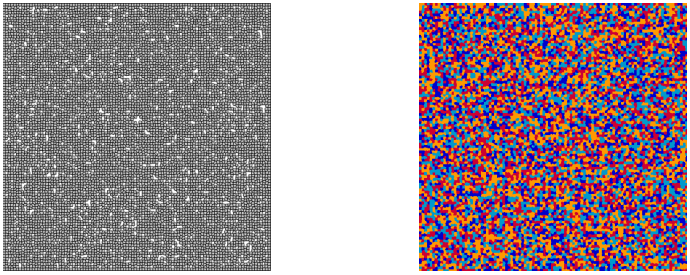

(a) (b)

Figure 3.9: Random distribution of heterogeneity in LEM: (a) porous medium with 10% porosity, and (b) rock sample with four different minerals shown with different colors (Sattari et al. 2022)

cells are defined as the cement matrix. The LEM representing a concrete sample with a uniform grain size distribution ranging from 0.5 to 2 [mm], pore size distribution from 0.05 to 0.02 [mm], and a porosity of 1% is shown in Fig.3.10. In this figure, the assigned material properties to the lattice elements representing the grains (yellow), the cement (blue), and the grain-cement interfaces (red) are illustrated.

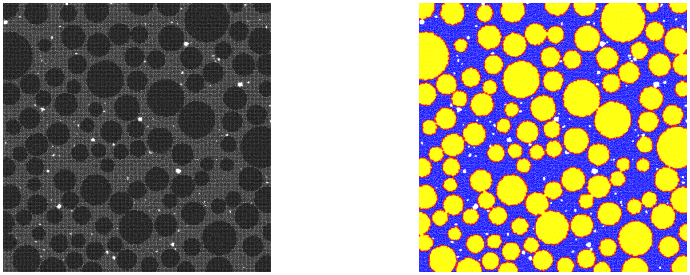

(a) (b)

Figure 3.10: Distribution of heterogeneity based on GSD and PSD in LEM: (a) generated concrete-like domain with sand, cement, and porosity of 1%, and (b) transmitted heterogeneity to the lattice elements (Blue=gains, yellow=cement, and red=interface)

In LEM, the embedded layering of the geomaterials is also represented by assigning different material properties in different orientations and lengths. The Opalinus clay rocks (Fig.3.11) are known for their embedded layering heterogeneity (Wenk et al. 2009, Glaß 2023, Schumann 2019, Bergmann 2019), which results in a great anisotropy behavior. This approach is similar in defining bi-material properties, where based on the length and orientation of the layering, different material properties are assigned to Voronoi cells. The heterogeneities are then transmitted to the lattice elements, representing different layering, as well as the interface elements for inter-domain transmission.

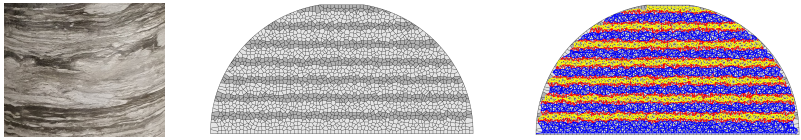

(a) (b) (c)

Figure 3.11: Defined embedded layering in LEM: (a) Opalinus claystone sample from Mont-Terri in Switzerland, (b) generated Voronoi cells and defined heterogeneity, and (c) transmitted heterogeneity to the lattice elements (Blue=Layer1, yellow=Layer2, and red=interface)

A more precise assessment of heterogeneity is achieved when an image processing of 2D cross-section or 3D microCT (micro Computed Tomography) of a geomaterial is performed. Conducting image processing in MATLAB using the *"imtool"* function results in exact 2D or 3D reconstruction of a simulated domain. On the basis of the RGB values of each pixel or voxel, it is possible to identify and categorize different domains. With respect to known mineralogy and element composition of the domain, the material properties are assigned to the lattice elements. The processed image is mapped on top of the Voronoi cells to define the material properties. However, the most challenging task is to experimentally assess the properties of THM material on a microscale, which eventually will be assigned to the individual elements. Fig.3.12 depicts the reconstructed heterogeneity of a cross-section of a rock specimen in the lattice model.

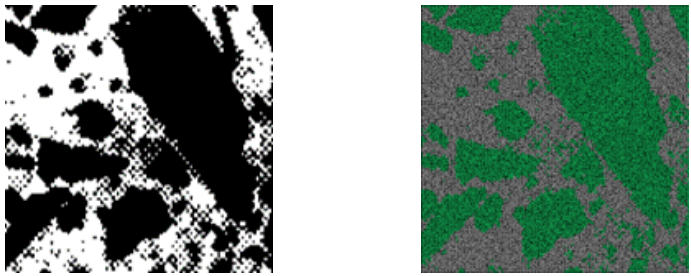

(a) (b)

Figure 3.12: Reconstruction of heterogeneity in LEM using image processing: (a) microscope image of a thin cut from rock, and (b) reconstructed lattice domain after image processing (Sattari et al. 2017)

In 3D simulations, heterogeneity is introduced similarly into the lattice model. Randomly distributed mineralogy, embedded layered heterogeneity, as well as spherical grain distribution, are all implemented into the lattice model. Fig.3.13 shows a concrete sample generated with 3375000 Voronoi cells, where only the grains and the cement matrix are visualized and the pore volume is set to zero.

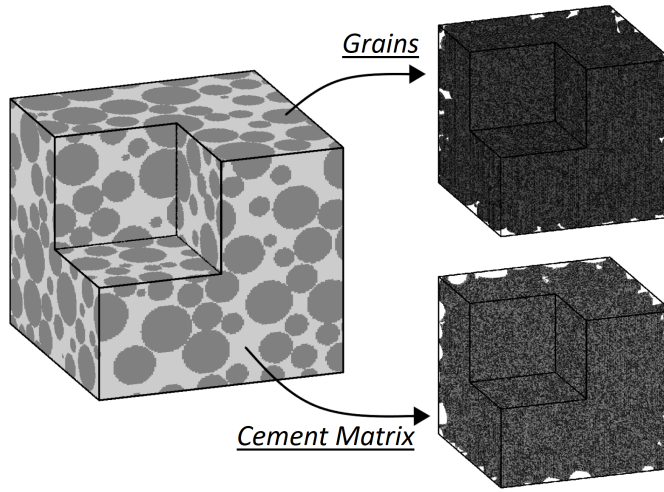

Figure 3.13: The generated 3D concrete domain with 3375000 Voronoi cells and $\alpha_r = 0.5$

In order to distribute the heterogeneity and irregularity of the material at the particle level, probability distribution methods can be considered. The Gaussian function is used to normally distribute the strength and stiffness of the elements in the lattice model. The Gaussian distribution (*"bell curve"*) of the element's tensile strength (σ_t) is performed using the probability density function (Pdf) of normally distributed strengths as

$$\text{Pdf}(\sigma_t(r)) = \frac{1}{\sigma_{std}\sqrt{2\pi}} \exp\left(-\frac{1}{2}\frac{(r-\mu_{std})^2}{\sigma_{std}^2}\right), \tag{3.1}$$

where σ_{std} is the standard deviation, r is the strength range with defined minimum and maximum values, and μ_{std} is the mean value. Fig.3.14b shows the distribution of the tensile strength between the lattice elements using the Gaussian density function, where $\sigma_{std} = 1$ and $1 \leq r \leq 10$. Similarly, the Weibull distribution is implemented to compare the simulation results. According to the Weibull probability density function, the tensile strength of elements (σ_t) is randomly distributed according to

$$\text{Pdf}(\sigma_t(r)) = \frac{\beta_w}{\lambda_w}\left(\frac{r}{\lambda_w}\right)^{\beta_w - 1} e^{-(r/\lambda_w)^{\beta_w}}, \tag{3.2}$$

where λ_w is the scale factor and β_w is the shape factor. The result of the tensile strength distribution using the Weibull distribution approach for $\lambda_w = 5$, $\beta_w = 1$ and the strength range of $1 \leq r \leq 10$ is depicted in Fig.3.15. Changing the shape factor significantly affects the distribution function. In both distribution techniques, the total number of generated elements is 2581 elements. Similarly, the stiffness of the elements can be randomly distributed. Depending on the random or anticipated strength and rigidity of a geomaterial, any of the

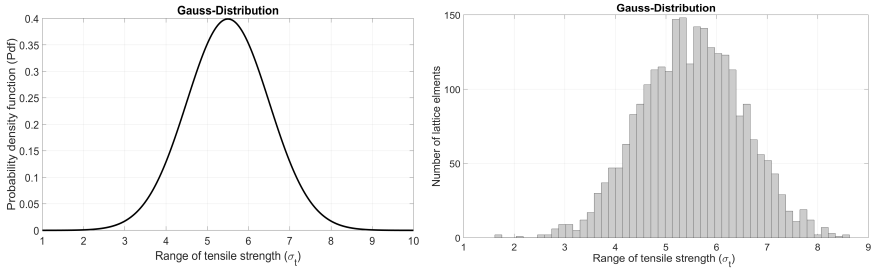

(a) (b)

Figure 3.14: The distribution of materials tensile strength using normalized Gaussian function ($\sigma_{std} = 1$): (a) probability density function, and (b) the total number of elements for each strength value

approaches mentioned above can be used to introduce heterogeneity into the lattice model.

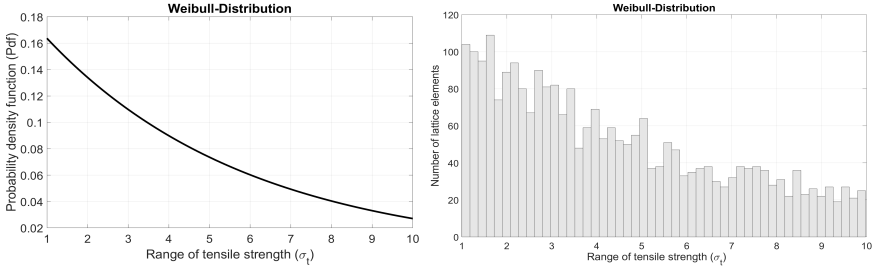

(a) (b)

Figure 3.15: The distribution of materials tensile strength using Weibull density function ($\lambda_w = 5$ and $\beta_w = 1$): (a) probability density function, and (b) the total number of elements for each strength value

Discontinuity that exists on micro- to macroscale can be defined using the lattice approach. The discontinuity is introduced by removing Voronoi cells and eliminating the lattice bond. The zero thickness crack path does not exist in standard LEM, and the minimum crack opening dimension is the pre-assigned mesh size of the domain (Fig.3.16a). When the Voronoi cells are removed, a better visualization of the predefined notch is possible, as shown in Fig.3.16b for a three-point bending test with a predefined notch width. In a discrete lattice model (DLEM), where a single Voronoi cell presents a grain body, it is possible to model a zero-thickness discontinuity. In DLEM, the lattice elements represent the cohesive bond between the grain bodies.

The length and orientation of each fracture network could also be generated based on existing field or experimental data. It is also possible to stochastically generate and map the discontinu-

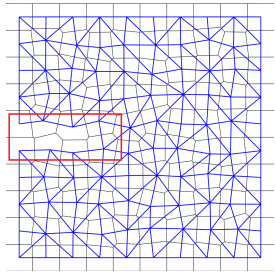

(a)

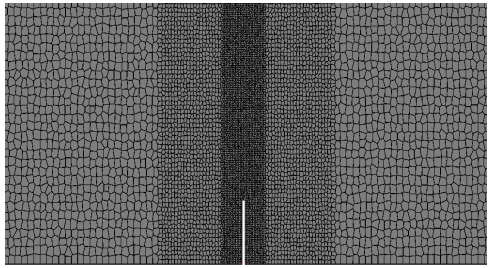

(b)

Figure 3.16: The introduction of discontinuity in LEM: (a) removal of solely lattice elements, and (b) representation of pre-defined notch with the removal of Voronoi cells

ities on top of the generated domain (Fig.3.17a). The lattice elements intersecting these fracture networks are then removed from the domain. Generally, in the lattice element models, the crack propagation path is developed by removing or softening (damage scheme) the elements that exceed the predefined stress thresholds. The lattice element model is a great tool for simulating and studying discontinuities in any domain. It is possible to investigate crack initiation, crack propagation path, crack branching, crack bridging, and change of material behavior during the fracking process. A similar approach is implemented to generate and model discontinuities in a 3D lattice model (Fig.3.17b).

(a)

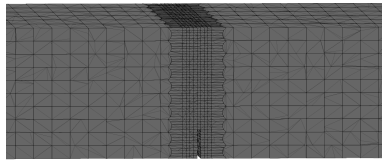

(b)

Figure 3.17: The introduction of discontinuity in LEM: (a) randomly generated discontinuities, and (b) 3D lattice model with a predefined notch

3.4 Implementation of mechanical lattice model

3.4.1 Introduction

The in-house developed 2D and 3D mechanical lattice model involves the following measures. After the model discretization described in the previous section, the characteristic of each lattice element (spring or beam properties) is defined and according to the materials behavior (brittle or quasi-brittle) and the considered fracture mechanism, the crack initiation and propagation as well as change of the mechanical properties of the materials are simulated. Similar to any modeling technique, besides the mechanical input properties, such as Young's modulus and Poisson's ratio, model parameters are also pre-defined. For the mechanical model, these parameters are as follows: Randomness factor (α_r) and softening ratio (S), which are both input parameters of the model. The flowchart of the developed mechanical lattice algorithm is presented in Fig.3.18.

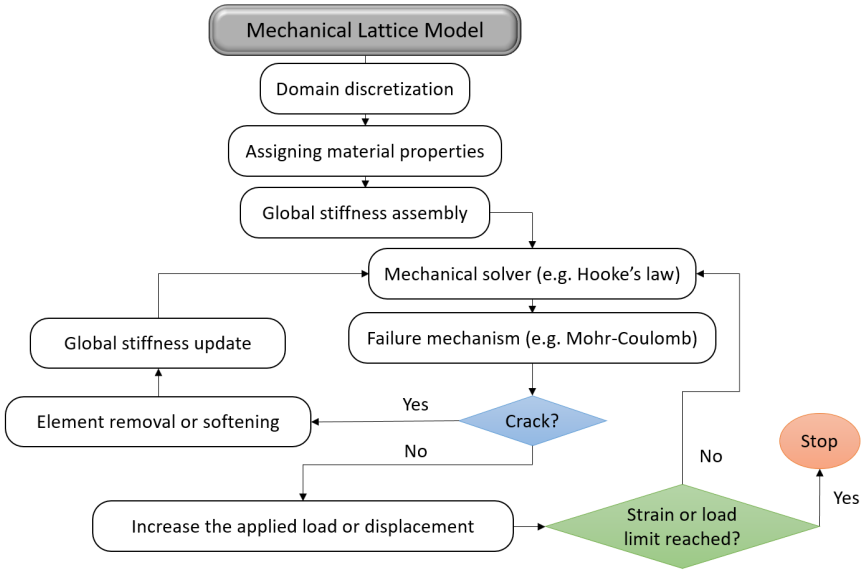

Figure 3.18: Flowchart of the mechanical model and the developed lattice algorithm

3.4.2 Element properties

In LEM, the domain is represented by a series of lattice elements in the form of spring or beam elements. In comparison to DEM, in LEM, there is no contact search or contact force calculation required. This reduces the computational costs of LEM, in which large domains

with a great number of elements can be simulated. In LEM, with the generation of multiple spring or beam elements, Mode I (tensile) and Mode II (shear) failures are realized.

Spring Model In the simplest approach, each lattice element is a 1-Mode normal spring element with axial deformation. Therefore, failure of the elements only in Mode I is feasible, and simulation of shear failure and the development of shear bands is not possible. The model can easily extend to 2-Mode lattice elements with representing each bond between two Voronoi cells with two spring elements. In this case, the first normal spring is activated under axial forces and displacements, whereas the second shear spring operates under shear forces. Similarly, a rotation spring element can also be considered between two neighboring nodes to model the rotation of the elements. In a 2D domain, for a 1-, 2- and 3-Mode spring lattice elements, 2, 2, and 3 degrees of freedom (DOF) in each node in global coordinates are considered, respectively. Similarly, in a 3D domain, for a 1-, 2- and 3-Mode spring lattice elements, 3, 3, and 6 degrees of freedom in each node are considered, respectively.

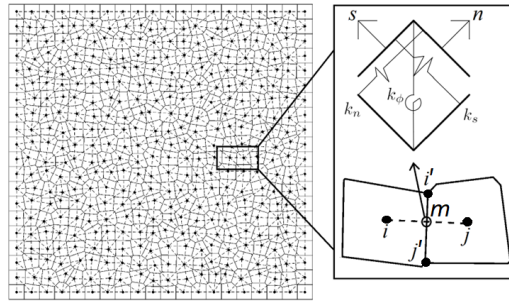

Figure 3.19: The 3-Mode lattice element in 2D domain with three DOF in each node in global coordinates (Sattari et al. 2022)

In another approach, the normal, tangential and rotational springs are located at the interface between two Voronoi cells. The model is known as the rigid body-spring network (RBSN), in which, in a 3D model, 6 springs with their specific stiffnesses $(k_n, k_s, k_t, k_{\phi n}, k_{\phi s}, k_{\phi t})$ are considered as a bond between two neighboring cells.

The spring model implemented in this study is shown in Fig.3.19. In a 2D domain, each neighboring cell is connected to each other with 3-Mode spring elements.

$$k_n = E\frac{A}{l}, \qquad k_s = G\frac{A}{l}, \qquad k_\phi = k_n\frac{h^2}{12}, \tag{3.3}$$

where k_n is the normal stiffness, k_s is the tangential stiffness, k_ϕ is the rotational stiffness, E is Young's modulus, G is the shear modulus, h is the cross-sectional length of the elements, l

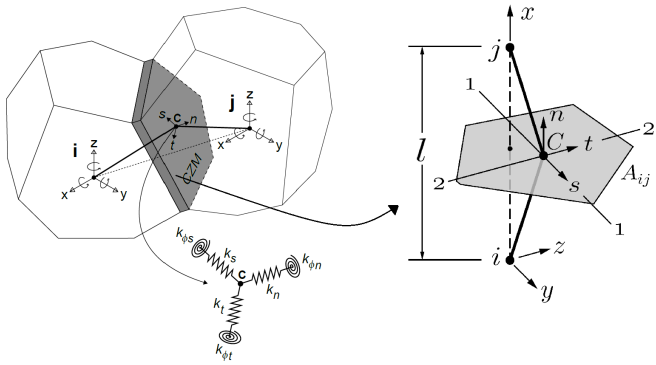

Figure 3.20: The 3D RBSN model with six springs on the Voronoi interfaces (Rasmussen et al. 2018, Berton and Bolander 2006)

is the length of elements or the Euclidean distance between nuclei, and A is the cross-sectional area ($A = t_b \times h$). With the assumption of linear elasticity and according to Hooke's law:

$$\boldsymbol{f_g} = \boldsymbol{K_g u_g}, \qquad \boldsymbol{K_g} = \boldsymbol{T}^T \boldsymbol{K_l T}, \tag{3.4}$$

where $\boldsymbol{f_g}$ is the vector of forces, $\boldsymbol{K_g}$ is the stiffness matrix, $\boldsymbol{u_g}$ is the vector of displacements in the global Cartesian coordinate, $\boldsymbol{T}$ is the transformation matrix, $\boldsymbol{T^T}$ is the transpose of the transformation matrix and $\boldsymbol{K_l}$ is the stiffness matrix in local coordinates. With the direct stiffness method, the system equilibrium equations are constructed and solved. In RBSN, a geometric transformation matrix $\boldsymbol{B}$ is defined to account for irregularities in geometry.

$$\boldsymbol{u_l} = \boldsymbol{B u_g}, \qquad \boldsymbol{K_g} = \boldsymbol{B}^T \boldsymbol{K_l B}, \tag{3.5}$$

where $\boldsymbol{u_l}$ is the vector of displacements in the local coordinate. For a 2D domain with 3-Mode lattice elements (Fig.3.19), $\boldsymbol{B}$ is given as (Sofianos and Koumousis 2017)

$$\boldsymbol{B} = \frac{1}{h} \times \begin{bmatrix} y_h & -x_h & (-x_h \times x_{mi} - y_h \times y_{mi}) & -y_h & x_h & (x_h \times y_{mj} + y_h \times y_{mj}) \\ x_h & y_h & (y_h \times x_{mi} - x_h \times y_{mi}) & -x_h & -y_h & (-y_h \times x_{mj} + x_h \times y_{mj}) \\ 0 & 0 & -h & 0 & 0 & h \end{bmatrix} \tag{3.6}$$

$$x_h = x_{j'} - x_{i'}, \qquad y_h = y_{j'} - y_{i'}, \qquad x_{mi} = \frac{x_{j'} + x_{i'} - 2 \times x_i}{2},$$

$$y_{mi} = \frac{y_{j'} + y_{i'} - 2 \times y_i}{2}, \qquad x_{mj} = \frac{x_{j'} + x_{i'} - 2 \times x_j}{2}, \qquad y_{mj} = \frac{y_{j'} + y_{i'} - 2 \times y_j}{2}$$

In a 3D domain and with 3-Mode lattice elements, six DOF is permitted in each node at global coordinates. The stiffnesses of the normal, tangential, and rotational springs are defined as (Berton and Bolander 2006)

$$k_n = \mathrm{E}\frac{A}{l}, \qquad k_s = k_t = \mathrm{G}\frac{A}{l}, \qquad k_{\phi n} = \mathrm{E}\frac{J_p}{l}, \qquad k_{\phi s} = \mathrm{E}\frac{I_{11}}{l}, \qquad k_{\phi t} = \mathrm{E}\frac{I_{22}}{l}, \tag{3.7}$$

where I_{11}, I_{22} are the two principal moments of inertia of the facet area, and J_p is the polar moment of inertia of the facet area. For a 3D RBSN model, the geometric transformation matrix $\boldsymbol{B}$ with a dimension of 6×12 is defined as

$$\boldsymbol{B} = \begin{bmatrix} -I_i & B_1 & I_i & B_2 \\ 0 & -I_i & 0 & I_i \end{bmatrix}, \tag{3.8}$$

where I_i is an identity matrix of size 3 (3×3), 0 is a zero matrix of size 3 (3×3). B_1 and B_2 are defined according to Fig.3.20 as

$$\boldsymbol{B_1} = \begin{bmatrix} 0 & -z_c & y_c \\ z_c & 0 & -\frac{l}{2} \\ -y_c & \frac{l}{2} & 0 \end{bmatrix}, \qquad \boldsymbol{B_2} = \begin{bmatrix} 0 & z_c & -y_c \\ -z_c & 0 & \frac{l}{2} \\ y_c & -\frac{l}{2} & 0 \end{bmatrix}, \tag{3.9}$$

where l is the Euclidean distance between the nuclei i and j, y_c, and z_c are the offsets of the centroid of the facet area c from the y and z axes of the element, respectively.

Beam Model The lattice elements can also be represented with Euler-Bernoulli or Timoshenko beam elements in 2D and 3D domains. In the 2D domain, the Euler-Bernoulli beam element has 3 DOF in each node that acts in normal, tangential, and rotational directions. In order to increase the accuracy of the model and overcome numerical difficulties arising from short beam elements, Timoshenko beam elements are widely used in LEM. In the 2D domain, the Euler-Bernoulli beam element considered in Fig.3.21 has 3 DOF in global coordinates (X,Y) on each node. In local coordinates (x,y), the elements bear axial forces (f_x), shear forces (f_y) and momentum (M), which correspond to axial displacement (u_x), tangential displacement (u_y) and rotation (ϕ), respectively.

For a Euler-Bernoulli beam, the local stiffness matrix $\boldsymbol{K_l}$, is as given:

$$\boldsymbol{K_l} = \frac{\mathrm{E}}{l}\begin{bmatrix} A & 0 & 0 & -A & 0 & 0 \\ 0 & \frac{12I}{l^2} & \frac{6I}{l} & 0 & -\frac{12I}{l^2} & \frac{6I}{l} \\ 0 & \frac{6I}{l} & 4I & 0 & -\frac{6I}{l} & 2I \\ -A & 0 & 0 & A & 0 & 0 \\ 0 & -\frac{12I}{l^2} & -\frac{6I}{l} & 0 & \frac{12I}{l^2} & -\frac{6I}{l} \\ 0 & \frac{6I}{l} & 2I & 0 & -\frac{6I}{l} & 4I \end{bmatrix}, \tag{3.10}$$

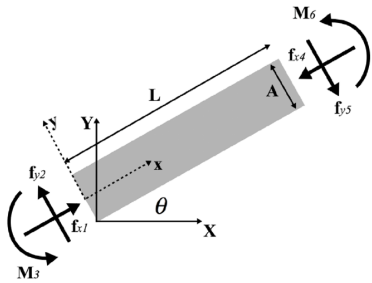

Figure 3.21: The 2D Euler-Bernoulli beam element in LEM and assigned DOF (Sattari et al. 2017)

where A is the cross-sectional area, l is the length, I is the moment of inertia, and E is Young's modulus of beam elements. The global stiffness matrix ($\boldsymbol{K_g}$) is calculated with Eq.3.4, where the transformation matrix ($\boldsymbol{T}$) is defined accordingly as

$$\boldsymbol{T} = \begin{bmatrix} cos(\theta) & sin(\theta) & 0 & 0 & 0 & 0 \\ -sin(\theta) & cos(\theta) & 0 & 0 & 0 & 0 \\ 0 & 0 & 1 & 0 & 0 & 0 \\ 0 & 0 & 0 & cos(\theta) & sin(\theta) & 0 \\ 0 & 0 & 0 & -sin(\theta) & cos(\theta) & 0 \\ 0 & 0 & 0 & 0 & 0 & 1 \end{bmatrix} \tag{3.11}$$

With the direct stiffness method, the global forces are then calculated with

$$\begin{bmatrix} F_{X1} \\ F_{Y2} \\ M_3 \\ F_{X4} \\ F_{Y5} \\ M_6 \end{bmatrix} = \boldsymbol{K_{g(6\times6)}} \times \begin{bmatrix} u_{X1} \\ u_{Y2} \\ \phi_3 \\ u_{X4} \\ u_{Y5} \\ \phi_6 \end{bmatrix} \tag{3.12}$$

In order to solve the system of equations with unknown displacements and forces at each node, minimizing the potential energy of the system is considered (Topin et al. 2007). The potential energy of an elastic body (U) is equal to the strain energy (U_{strain}) minus the loading potential energy ($U_{loading}$). For the Euler-Bernoulli beam, the strain energy (U_{strain}) is the sum of the axial (U_A), shear (U_S) and momentum (U_M) energies as:

$$U_{Strain}(x) = U_A(x) + U_S(x) + U_M(x) = \frac{1}{2}\int_0^l ((\frac{f_x(x)^2}{\mathrm{E}A}) + (\frac{f_y(x)^2}{\mathrm{G}A}) + (\frac{M(x)^2}{\mathrm{E}I}))\, dx \tag{3.13}$$

With the assumption of a linear function along the length of an element (l):

$$U_A = \frac{f_x^2 l}{2\mathrm{E}A}, \qquad U_S = \frac{f_y^2 l}{2\mathrm{G}A}, \qquad U_M = \frac{M^2 l}{2\mathrm{E}I} \tag{3.14}$$

The total strain energy of the domain is the sum of all individual strain energies of the elements. The total potential energy (U_{total}) is then calculated from the total strain energy minus the potential load energy. To determine the displacements in global coordinates, the total potential energy is minimized. Minimizing the potential energy is reached when the first order of derivative of dU_{total} based on each unknown is equal to zero.

$$\begin{bmatrix} \frac{dU_{total}}{du_{X1}} = 0 \\ \frac{dU_{total}}{du_{Y2}} = 0 \\ \frac{dU_{total}}{du_{\phi 3}} = 0 \\ \vdots \\ \frac{dU_{total}}{du_{\phi N_{DOF}}} = 0 \end{bmatrix}, \tag{3.15}$$

where N_{DOF} is the total number of DOF. The displacements on each node are calculated by solving the system of the above-mentioned equations using the Newton-Raphson Jacobin approach. After the third iteration loop, the error threshold ($error = 10 \times e^{-10}$) between two subsequent results has been reached, and the iteration process has stopped. In a 3D domain, the 3D Euler-Bernoulli beam elements have six DOF on each node in global coordinates. The stiffness matrix in Eq.3.10 is then extended to the 3D model as

$$\boldsymbol{K_l} = \frac{1}{l}\begin{bmatrix}
\mathrm{E}A & 0 & 0 & 0 & 0 & 0 & -\mathrm{E}A & 0 & 0 & 0 & 0 & 0 \\
0 & \frac{12\mathrm{E}I}{l^2} & 0 & 0 & 0 & \frac{6\mathrm{E}I}{l} & 0 & -\frac{12\mathrm{E}I}{l^2} & 0 & 0 & 0 & \frac{6\mathrm{E}I}{l} \\
0 & 0 & \frac{12\mathrm{E}I}{l^2} & 0 & -\frac{6\mathrm{E}I}{l} & 0 & 0 & 0 & -\frac{12\mathrm{E}I}{l^2} & 0 & -\frac{6\mathrm{E}I}{l} & 0 \\
0 & 0 & 0 & \mathrm{G}J_p & 0 & 0 & 0 & 0 & 0 & -\mathrm{G}J_p & 0 & 0 \\
0 & 0 & -\frac{6\mathrm{E}I}{l} & 0 & 4\mathrm{E}I & 0 & 0 & 0 & \frac{6\mathrm{E}I}{l} & 0 & 2\mathrm{E}I & 0 \\
0 & \frac{6\mathrm{E}I}{l} & 0 & 0 & 0 & 4\mathrm{E}I & 0 & -\frac{6\mathrm{E}I}{l} & 0 & 0 & 0 & 2\mathrm{E}I \\
-\mathrm{E}A & 0 & 0 & 0 & 0 & 0 & \mathrm{E}A & 0 & 0 & 0 & 0 & 0 \\
0 & -\frac{12\mathrm{E}I}{l^2} & 0 & 0 & 0 & -\frac{6\mathrm{E}I}{l} & 0 & \frac{12\mathrm{E}I}{l^2} & 0 & 0 & 0 & -\frac{6\mathrm{E}I}{l} \\
0 & 0 & -\frac{12\mathrm{E}I}{l^2} & 0 & \frac{6\mathrm{E}I}{l} & 0 & 0 & 0 & \frac{12\mathrm{E}I}{l^2} & 0 & \frac{6\mathrm{E}I}{l} & 0 \\
0 & 0 & 0 & -\mathrm{G}J_p & 0 & 0 & 0 & 0 & 0 & \mathrm{G}J_p & 0 & 0 \\
0 & 0 & -\frac{6\mathrm{E}I}{l} & 0 & 2\mathrm{E}I & 0 & 0 & 0 & \frac{6\mathrm{E}I}{l} & 0 & 4\mathrm{E}I & 0 \\
0 & \frac{6\mathrm{E}I}{l} & 0 & 0 & 0 & 2\mathrm{E}I & 0 & -\frac{6\mathrm{E}I}{l} & 0 & 0 & 0 & 4\mathrm{E}I
\end{bmatrix}, \tag{3.16}$$

where J_p is the polar moment of inertia. Similarly, the transformation matrix ($\boldsymbol{T}$) with a dimension of 12×12 is extended into the 3D domain as

$$\boldsymbol{T} = \begin{bmatrix} \boldsymbol{R_1} & \boldsymbol{0} & \boldsymbol{0} & \boldsymbol{0} \\ \boldsymbol{0} & \boldsymbol{R_1} & \boldsymbol{0} & \boldsymbol{0} \\ \boldsymbol{0} & \boldsymbol{0} & \boldsymbol{R_1} & \boldsymbol{0} \\ \boldsymbol{0} & \boldsymbol{0} & \boldsymbol{0} & \boldsymbol{R_1} \end{bmatrix}, \qquad \boldsymbol{R_1} = \begin{bmatrix} a_1 & a_2 & a_3 \\ \frac{a_2}{b_1} & \frac{a_1}{b_1} & 0 \\ \frac{a_1 \times a_3}{b_1} & \frac{a_2 \times a_3}{b_1} & b_1 \end{bmatrix}, \tag{3.17}$$

$$a_1 = \frac{X_j - X_i}{l}, \qquad a_2 = \frac{Y_j - Y_i}{l}, \qquad a_3 = \frac{Z_j - Z_i}{l}, \qquad b_1 = \sqrt{a_1^2 + a_2^2},$$

where X, Y, Z are the global coordinates of the element nodes i and j, $\mathbf{0}$ is the zero matrix of 3×3, and eventually the global stiffness is calculated according to Eq.3.4. In addition to the Euler-Bernoulli beam elements, it is possible to consider the Timoshenko beam theory. The Timoshenko theory is applied to shear-dominated beams or short beams (short span length). On the other hand, the Euler-Bernoulli beam theory is considered to model the behavior of flexure-dominated beams or long beams. Timoshenko beam considers the deflection of the cross-section of the beam with shear forces. In Euler-Bernoulli, the cross-section remains perpendicular to the neutral axis even after deformation. Similarly to the Euler-Bernoulli beam, in 2D domain, the Timoshenko beam has three DOF on each node in global coordinates. In local coordinates, the stiffness of the Timoshenko beam is

$$\boldsymbol{K_l} = \frac{\mathrm{E}I}{l^3(1+\phi^T)} \begin{bmatrix} \frac{Al^2(1+\phi^T)}{I} & 0 & 0 & -\frac{Al^2(1+\phi^T)}{I} & 0 & 0 \\ 0 & 12 & 6l & 0 & -12 & 6l \\ 0 & 6l & l^2(4+\phi^T) & 0 & -6l & l^2(2-\phi^T) \\ -\frac{Al^2(1+\phi^T)}{I} & 0 & 0 & \frac{Al^2(1+\phi^T)}{I} & 0 & 0 \\ 0 & -12l & -6l & 0 & 12l & -6l \\ 0 & 6l & l^2(2-\phi^T) & 0 & -6l & l^2(4+\phi^T) \end{bmatrix}, \tag{3.18}$$

where $\phi^T = \frac{12\mathrm{E}I}{GA_sL^2}$ and A_s is the shear area. The stiffness matrix can also be extended into the 3D domain with six DOF on each node in global coordinates. The implementation of the lattice element method was extended to model the concrete-type geomaterial with three different material properties: Aggregate, cement matrix, and aggregate-cement interface (Fig.3.22). In a novel approach known as the generalized beam (GB) lattice model, the equivalent stiffness matrix of a Timoshenko beam element in interfaces has been driven. In this approach, the aggregate-cement interface element is composed of three smaller beam elements: An aggregate beam, a cement beam, and a short beam among them to represent the interface. Therefore, the length of the interface element is reduced to any predefined value. This is possible with the assumption of Timoshenko beams, as the approach results in extremely short beam elements. This approach eliminates the need to generate additional nodes to represent the interface element, which is computationally expensive. The formulation that exists for the GB lattice model is based on the regular lattice model, where the stiffness of the equivalent GB element is driven in 2D and 3D domains.

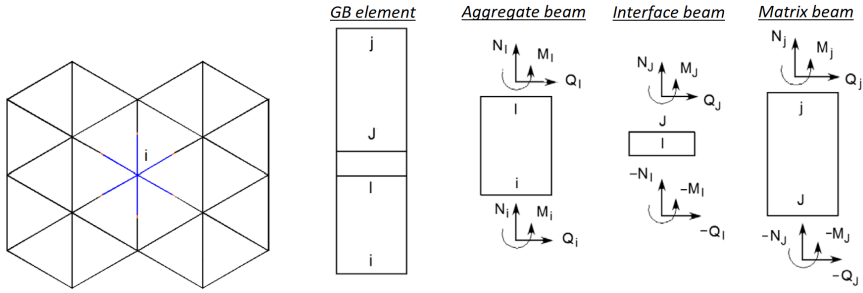

(a) (b)

Figure 3.22: The generalized beam (GB) lattice model for concrete composite with (a) equivalent hexagonal lattice, and (b) the composition of an aggregate-cement interface beam element (Liu et al. 2007)

Interface Lattice Model For simulation of thermal strains, shrinkage, and swelling in geomaterials, it is essential to consider an interface element between each two neighboring Voronoi cells (Sattari et al. 2019). As shown in Fig.3.23b, a swelling (an increase of the Euclidean distance between two nuclei) of a domain in a conventional lattice model results in tensile stress on the element. On the contrary, swelling should increase the confinement pressure on the contact area. Similarly, during the shrinkage process (decrease of the Euclidean distance between two nuclei), the confinement pressure increases in the contact area, which is opposite to what is observed in geomaterials. In order to overcome this drawback of the conventional lattice model and accurately simulate thermal strains, an additional interface element is generated in each contact area ($Element_{12}$) shown with a blue line in Fig.3.23b). This element then represents only the bond stiffness between two Voronoi cells.

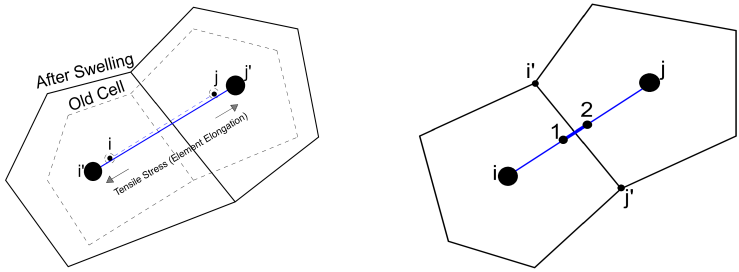

(a) (b)

Figure 3.23: The interface lattice model in 2D domain: (a) swelling and elongation of lattice element in conventional LEM, and (b) the interface lattice model solution with generated interface element ($Element_{12}$)

Therefore, a single element in a conventional LEM ($Element_{ij}$) is divided into three elements: $Element_{i1}$, $Element_{12}$ and $Element_{2j}$. To avoid short beam numerical difficulties, spring elements with 1-, 2- or 3-Mode degrees of freedom are assigned to the interface elements ($Element_{12}$). The mathematical formulation remains similar to the spring model. However, the computational cost increases substantially, as the number of generated elements is approximately 3× greater. The advantage of this model over the GB lattice is that a single element will solely present the interface domain, and the numerical error, which evolves from an extreme short beam element, could be eliminated.

3.4.3 Regularization of lattice model

It is essential to eliminate or minimize the mesh dependency of lattice results. Similar to FEM, the mechanical response of the material obtained from LEM should be independent of the mesh size or the irregularity of the mesh of a discretized domain. In LEM, the irregularity of the mesh, which is introduced with the so-called randomness factor in Sec.3.2, grants irregular crack paths and surfaces. The effect of this parameter on the stress-strain, strength, or material's stiffness should be diminished. The stiffness, strength, or general THM properties of a continuum should be assessed using microscale models such as the lattice or discrete element method. Therefore, regularization of a lattice element to represent the continuum properties is vital. For instance, for a lattice model with regular elements, the continuum stiffness of an isotropic domain is different from the assigned microscale stiffnesses on the elements. The aim of a regularization technique is to determine the correlation between the continuum and the properties of the elements.

In order to determine the stiffness correlation between the properties of a continuum and the elements, the stored strain energy of a continuum, $U_{\mathbb{R}}$, is set equal to the stored strain energy in each single Voronoi cell, U_{Cell}. For lattice models with regular discretized meshes, such as triangular or square-shaped forms, this approach leads to unique correlation values for spring or beam elements.

$$U_{Cell} = U_{\mathbb{R}} \tag{3.19}$$

The U_{Cell} stored in each Voronoi cell depends on the number of lattice elements, the orientation of the elements, the shape of the unit cell, and the type of lattice element (spring or beam). For a 1-Mode spring element in the 2D domain, the strain energy stored in a unit cell depends on the total number of bonds in each cell (N_b), the response force of the elements (F_b) and the response displacement (u_b). On the other hand, for a continuum, the stored energy depends on the continuum stresses ($\sigma_{\mathbb{R}}$) and the continuum strains ($\varepsilon_{\mathbb{R}}$) throughout the continuum volume ($V_{\mathbb{R}}$).

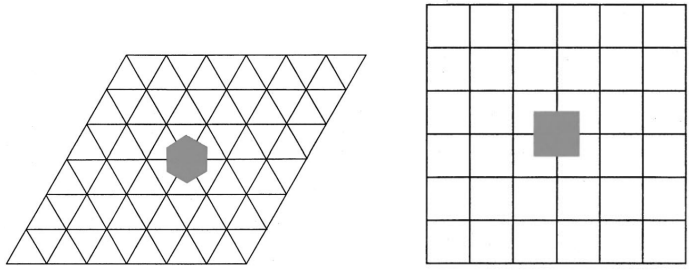

(a) (b)

Figure 3.24: The regularization of regular lattice: (a) triangular lattice with hexagonal unit cell, and (b) square lattice with square unit cell (Ostoja-Starzewski 2002)

$$U_{Cell} = \frac{1}{2}\sum_{b=1}^{b=N_b} F_b.u_b, \qquad U_{\mathbb{R}} = \frac{1}{2}\int_{V_{\mathbb{R}}} \sigma_{\mathbb{R}}.\varepsilon_{\mathbb{R}}.dV \tag{3.20}$$

In the case of in-plane elasticity and planar continuum, the isotropic Hooke's law is

$$\boldsymbol{\sigma_{i,j}} = \boldsymbol{C_{i,j,k,m}}.\boldsymbol{\varepsilon_{k,m}}, \qquad i,j,k,m = 1:2, \tag{3.21}$$

where $\boldsymbol{C_{i,j,k,m}}$ is the stiffness tensor. For a triangular spring lattice (regular mesh) with central interactions and two DOF on each node, the stored strain energy in a unit cell is calculated based on the length of the elements (l), the first stiffness coefficient (R') and the orientation of the unit normal vector ($n_{i,j,k,m}$).

$$U_{\text{cell}} = \frac{1}{2}\sum_{b=1}^{b=N_b} l_b^2 \left(R'\, n_i\, n_j\, n_k\, n_m\, \varepsilon_{ij}\, \varepsilon_{km}\right)_b \tag{3.22}$$

The stored strain energy of a continuum is determined on the basis of

$$U_{\mathbb{R}} = \frac{1}{2}\varepsilon_{\mathbb{R}}\, C_{\mathbb{R}}\, \varepsilon_{\mathbb{R}}, \tag{3.23}$$

where $C_{\mathbb{R}}$ is a continuum stiffness matrix. For instance, for a regular square lattice network (Fig.3.24b), orthotropic medium, and anti-plane elasticity conditions, the component of stiffness tensor are

$$C_{11} = \frac{k_X}{2}, \qquad C_{22} = \frac{k_Y}{2}, \qquad C_{12} = C_{21} = 0, \tag{3.24}$$

where k_X and k_Y are the spring constants in the X and Y orientations. On the other hand, for a triangular Euler-Bernoulli beam lattice in 2D, the curvature strain ($\kappa_{i,j}$), curvature stiffness ($D_{i,j}$), stiffness matrix ($C_{i,j,k,m}$) and second stiffness coefficient (R'') are related as

$$U_{\mathbb{R}} = \frac{V}{2}\varepsilon_{ij}C_{ijkm}\varepsilon_{km} + \frac{V}{2}\kappa_i D_{ij}\kappa_j, \tag{3.25}$$

$$C_{ijkm} = \sum_{b=1}^{b=N_b}(n_i.n_k\,(n_j.n_m.R') + n_j.n_m.R''))_b \tag{3.26}$$

Eventually, a relation between the continuum and element properties for isotropic or anisotropic regular lattice has been driven. In the case of triangular elements, isotropic medium, and in-plane elasticity, the relation between Young's modulus of the Euler-Bernoulli beam (E_b) and spring constant (k_n) with continuum properties ($\mathrm{E}_{\mathbb{R}}, \nu$) are

$$\mathrm{E}_b = \frac{\mathrm{E}_{\mathbb{R}}}{\sqrt{3}(1-\nu)\sqrt{\frac{1-3\nu}{1+\nu}}}, \qquad k_n = \frac{\mathrm{E}_{\mathbb{R}}}{\sqrt{3}(1-\nu)} \tag{3.27}$$

For an irregular lattice network, it is not feasible to drive a generalized equation similar to that for regular lattices. Any individual mesh network with different randomness factor values leads to a unique relation between continuum and element properties. In an irregular lattice for a representative volume element (RVE), the stored strain energy is set to be equal to the continuum. Eventually, similar to the regular lattice, a correlation between continuum properties such as Young's modulus ($\mathrm{E}_{\mathbb{R}}$), shear modulus ($\mathrm{G}_{\mathbb{R}}$) and bulk modulus ($\mathrm{K}_{\mathbb{R}}$), with lattice element properties (E, G), is driven. The irregularity of the generated mesh (α_r) has an influence on the correlated ratios (α_1, α_2).

$$\frac{\mathrm{E}_{\mathbb{R}}}{\mathrm{E}} = \alpha_1, \qquad \frac{\mathrm{G}_{\mathbb{R}}}{\mathrm{G}} = \alpha_2 \tag{3.28}$$

The regularization process in an irregular lattice is summarized in the following steps:

- The domain with a pre-defined mesh size and randomness factor is generated.
- The continuum properties or so-called target properties are pre-assigned.
- The strain energy of the spring or beam elements is calculated.
- The calibration factor between the continuum and RVE values is determined.
- According to the determined ratio, the properties of the elements are correlated.

3.4.4 Fracture model

The main advantage of LEM is to simulate crack initiation and propagation in materials while accounting for domain irregularity, anisotropy, and heterogeneity. In the lattice models, it is possible to simulate the crack bridging, branching, development of traction-free as well as stress concentration on crack tips or the so-called fracture process zone (FPZ). The crack representation is done by removing a lattice element or softening a stiffness based on a damage

function to capture ductile material behavior. The fracture mechanism considered in this work is based on Mode I and Mode II fracture modes. In Mode I, the tensile failure of the elements is permitted and in Mode II, the shear failure or sliding failure is captured. In the literature, various fracture mechanisms are considered for lattice models, which consider only Mode I or a combination of Mode I and Mode II failures.

In the majority of scientific contributions, Mode I fracture is examined when subjected to tension. In these methods using the 1-Mode, 3-Mode spring lattices, or beam elements, the inner forces and moments in each lattice element are calculated.

$$\sigma_{\mathrm{t}} = \frac{f_X}{A} - \alpha' \frac{\max(|M_i|, |M_j|)}{W_s}, \tag{3.29}$$

where $f_X = f_n$ is the normal force, A is the cross-sectional area or length of the element ($A = t_b \times h$), $M_{i,j}$ are the bending moments in node i and j, α' is a scaling parameter equal to 0.005 (Ince et al. 2003), and W_s is the section modulus (for a rectangle $W_s = \frac{t_b h^2}{6}$). In recent applications of lattice models, the tensile cut-off Mohr-Coulomb failure criteria have been considered for fracture studies. The failure envelope is presented in Fig.3.25, where normal stress (σ_{n}) is plotted against shear strength (σ_{s}). Furthermore, the cohesion (c), friction angle (ϕ'), tensile strength (σ_{t}) and confinement strength (σ_{c}) are highlighted.

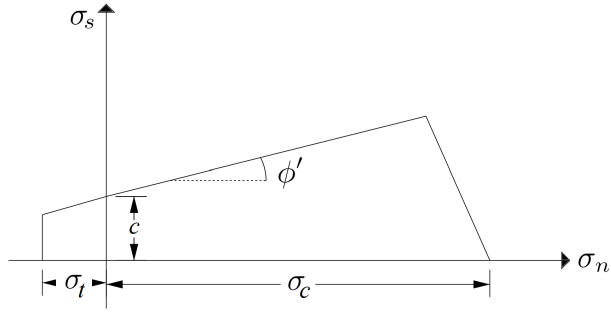

Figure 3.25: Mohr-Coulomb failure envelop with tension cut-off (Sattari et al. 2022)

$$\sigma_{\mathrm{s}} = \sigma_{\mathrm{n}} \cdot \tan(\phi') + c \tag{3.30}$$

The Linear Elastic Fracture Mechanics (LEFM) approach is used to simulate the failure mechanism. According to LEFM, the material under load has an elastic behavior. This approach is based on the stress intensity factor (K), where K_{I}, K_{II} and K_{III} are the Mode I, II and III stress intensity factors, respectively. The critical stress intensity factor (K_c), known as fracture toughness, is considered a parameter of engineering design. Similarly, three fracture toughness values (K_{Ic}, K_{IIc} and K_{IIIc}) for three different Modes (I, II and III) exist. For a crack in an infinite plate under Mode I loading or a penny-shaped crack in an infinite domain, the analytical

solution for the magnitude of the fracture toughness has been driven. Based on the values of the stress intensity factor (K) and Young's modulus (E), the strain energy release rate (G) can be determined in different modes (G_{I} and G_{II}). For plane stress,

$$G_{\mathrm{I}} = K_I^2(\frac{1}{\mathrm{E}}), \qquad G_{\mathrm{II}} = K_{\mathrm{II}}^2(\frac{1}{\mathrm{E}}), \tag{3.31}$$

and for the plane strain condition the G_{I} and G_{II} are

$$G_{\mathrm{I}} = K_{\mathrm{I}}^2(\frac{1-\nu^2}{\mathrm{E}}), \qquad G_{\mathrm{II}} = K_{\mathrm{II}}^2(\frac{1-\nu^2}{\mathrm{E}}) \tag{3.32}$$

The LEFM is an ideal failure model to capture the behavior of brittle materials. In all of the above-mentioned failure mechanisms, until the failure point, linear elastic behavior is assumed. In the case of an elastic-brittle 1-Mode spring bond, the total strain energy is released when the element breaks. Hence,

$$\frac{1}{2.}k_n \cdot u_x = G_{\mathrm{Ic}} \cdot A \qquad \rightarrow \qquad \sigma_t = \sqrt{\frac{2G_{\mathrm{Ic}}\mathrm{E}}{l}}, \tag{3.33}$$

which gives the relation between the tensile strength and the Mode I fracture toughness value. The lattice properties are neither microscopic nor engineering material characteristics. The calibration or multi-scaling of properties to match macroscopic geomaterial properties such as tensile strength and stiffness could be performed as studied by Damjanac et al. (2020). To do so, two scale transition parameters are defined: R is the resolution factor, and α_k is the stiffness calibration factor. Similarly to the regularization approach explained in Sec.3.4.3, the normal stiffness of a spring element (k_n) is correlated to the effective stiffness of a bulk (k_e) with,

$$k_n = k_e \cdot \alpha_k \cdot R \tag{3.34}$$

Similarly, the tensile strength of a lattice element ($\sigma_t^{Element,S}$ and $\sigma_t^{Element,K}$) is correlated with the macro-scale tensile strength of the material (σ_t^e) and the fracture toughness (K_{Ic}^e).

$$\sigma_t^{Element,S} = \alpha_t \cdot \sigma_t^e \cdot R^2, \qquad \sigma_t^{Element,K} = \alpha_K \cdot K_{\mathrm{Ic}}^e \cdot R^{\frac{3}{2}}, \tag{3.35}$$

where α_t and α_K are the calibration factors of tensile strength and fracture toughness. The calibration parameters (α_k, α_t, α_K) depend on the arrangement of the lattice elements (randomness factor, α_r), similar to the regularization approach. On the microscale, the tensile, shear, or compressive strength of the elements are calibrated to the macroscale engineering strengths. When the element size is set to match the grain sizes, the fracture toughness could also be used for simulations. However, in macroscale simulations, considering the grain-size elements results in a tremendous amount of elements and increases the computational costs drastically. Therefore, in order to simulate the macro-setup and consider larger elements (to decrease the computational costs), a rescaling of the fracture toughness corresponding to the tensile strength (macro strengths) is required.

$$R = (\frac{K_{\mathrm{Ic}}^{e}}{\sigma_{t}^{e}})^{2} \tag{3.36}$$

When the element tensile strength is calculated from the macroscale, the strengths and fracture toughness values are equal: $\sigma_t^{Element,S} = \sigma_t^{Element,K}$. For example, for a rock geomaterial with a resolution (R) of 1 [cm] or less, the lattice matches both the tensile strength and the fracture toughness. This resolution corresponds to the internal length scale of the rocks. If the lattice is up-scaled (higher resolution, which means larger element sizes than the internal length scale) and the tensile strength of the element is matched to the macroscopic tensile strength (used $\sigma_t^{Element,S}$ for the failure mechanism), then the fracture toughness of the material (K_{Ic}^{e}) will be overestimated. On the other hand, if the tensile strength of the element is calibrated according to the fracture toughness value (used $\sigma_t^{Element,K}$ for the failure mechanism), the tensile strength of the material (σ_t^{e}) is underestimated, resulting in a higher safety factor.

The simulation of crack initiation and propagation in geomaterials with brittle behavior is carried out by removing the element (or multiple elements) in which the determined inner stresses exceed the defined strengths or fracture toughness thresholds. However, the behavior of geomaterials is not only limited to brittle behavior. To capture the softening behavior of geomaterials after failure (quasi-brittle behavior), the bi-linear stiffness softening scheme has been adopted. The ductile behavior of the Geomaterial after failure (elastoplastic) is modeled with the definition of new parameters, such as the peak stress (σ_{p}), the peak strain (ε_{p}), the strain of an element at failure (ε_{f}) and a softening ratio (S). Similarly to the damage model (damage matrix), the initial stiffness of the elements will be degraded during the mechanical iterations until the strain of the elements (ε) is greater than ε_{f}. When the strain of the element surpasses ε_{f}, the element is removed and its stiffness is set to zero.

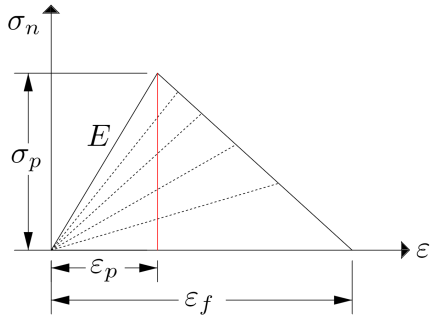

Figure 3.26: The bi-linear softening scheme to simulate quasi-brittle material behavior (Sattari et al. 2022)

$$\mathrm{E}_{new} = \frac{\sigma_\mathrm{p}}{\varepsilon_\mathrm{f} - \varepsilon_\mathrm{p}} \left(\frac{\varepsilon_\mathrm{f}}{\varepsilon} - 1 \right), \qquad S = \frac{\varepsilon_\mathrm{f}}{\varepsilon_\mathrm{p}}, \tag{3.37}$$

where E_{new} is Young's modulus of an element calculated according to the defined softening ratio. The softening scheme is implemented in the lattice model solely by the defined S value ($S = 1$ is a brittle response). According to the secant modulus of elasticity, in every load step, the initial setup with degrading Young's modulus is evaluated. Therefore, cumulative strains are not considered. Therefore, during the unloading process, the plastic deformations will be equal to zero. The tangential modulus, where deformations after each load iteration are transmitted into the next iteration (cumulative strains are calculated and stored), results in a slightly different stress-strain response compared to the secant modulus (Fig.3.27). The tangential modulus of elasticity results in smoother stress-strain curves and accumulative strains. On the negative side, the computational costs are greater. In the secant modulus of elasticity, the stiffness matrix ($\boldsymbol{K}$) is assembled only for the first computational cycle and updated according to the failure of elements.

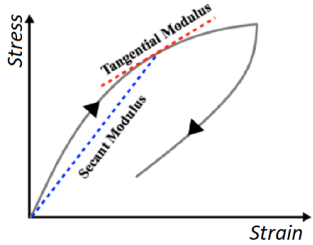

Figure 3.27: Secant and tangential modulus of elasticity

$$\boldsymbol{K}_{n+1,i} = \boldsymbol{K}_{n,i} - \Delta\boldsymbol{K}_{n,i}, \tag{3.38}$$

where n is the mechanical iteration step and $\Delta\boldsymbol{K}$ is the reduction in stiffness due to the softening behavior of the element i. In the brittle case, $\Delta\boldsymbol{K}_{n,i} = \boldsymbol{K}_{n,i}$ and when the element i is not damaged $\Delta\boldsymbol{K}_{n,i} = 0$. For an applied load of $\boldsymbol{F}$ from the boundaries of RVE (load-control scheme), the following equation is valid.

$$[\boldsymbol{K}_n][\boldsymbol{\delta}_n] = [\boldsymbol{F}_n], \tag{3.39}$$

where $\boldsymbol{\delta}_n$ is the displacement matrix in n^{th} iteration. In the case of the tangential modulus of elasticity, when an initial applied load of $\boldsymbol{F}_0$ results in the displacement matrix of $\boldsymbol{\delta}_0$, the load increment of $\Delta\boldsymbol{F}$ results in $\Delta\boldsymbol{\delta}$.

$$[\boldsymbol{K}_n] \cdot ([\boldsymbol{\delta}_{n-1}] + [\Delta\boldsymbol{\delta}_n]) = [\boldsymbol{F}_n] \qquad \rightarrow \qquad [\boldsymbol{K}_n] \cdot [\Delta\boldsymbol{\delta}_n] = [\boldsymbol{F}_n] - [\boldsymbol{K}_n] \cdot [\boldsymbol{\delta}_{n-1}] \tag{3.40}$$

3.4.5 Summary

The theoretical framework and mathematical formulation of the developed mechanical lattice model are presented in this section. In this study, the VRL method is considered to discretize the domain. Different approaches, such as image processing techniques or random assignment of properties, are utilized to define the heterogeneity and discontinuity of the simulated domain. The mathematical formulation of the element properties ranging from single normal lattice elements to more advanced interface lattice elements is provided. In particular, considered fracture models based on the Mohr-Coulomb theory and LEFM are discussed. Eventually, the bi-linear softening scheme to capture the ductile material response is explained. Depending on the problem framework, a unique approach is selected (e.g. spring or beam element; brittle or quasi-brittle behavior; Mohr-Coulomb or fracture toughness theory) to simulate the geomaterials response under the THM processes. The validation of the mechanical lattice model with the analytical solution (double cantilever beam) is provided in Sec.4.1. Comparison of numerical and analytical solutions exhibits the accuracy of the developed lattice model. Furthermore, in Sec.4.1, a parametric study of the developed lattice model is carried out and the lattice results are compared with the experimental data.

3.5 Development of the Thermo-Mechanical (TM) lattice model

3.5.1 Introduction

Over the last few decades, Thermo-Mechanical discrete element models (TDEM) have been implemented in the simulation of heat transfer in the particulate medium (Feng et al. 2009). These models are extended to the lattice element simulations to account for cemented geomaterials (Sattari et al. 2017). The in-house developed TM lattice model is composed of the following numerical steps: Simulation of steady heat transfer in cemented and particulate geomaterials in 2D and 3D, simulation of transient heat transfer, and calculation of thermal conductivity change under coupled processes. The mechanical lattice elements, which are discussed in Sec.3.2, are used to transfer heat between the Voronoi nodes. The thermal properties of the elements are extracted from the properties of the underlying material assigned to each Voronoi cell in Sec.3.3. The flowchart of the developed TM lattice algorithm is presented in Fig.3.28.

3.5.2 Steady heat transfer

The lattice model considers the heat conduction within particles (unit cell), through particle-to-particle contact surface, particle-fluid-particle conduction, and heat convection within fluid and air. Fig.3.29 depicts the heat conduction, convection, and radiation in a particulate geomaterial. In the lattice model, heat radiation is neglected. The method developed here simulates heat

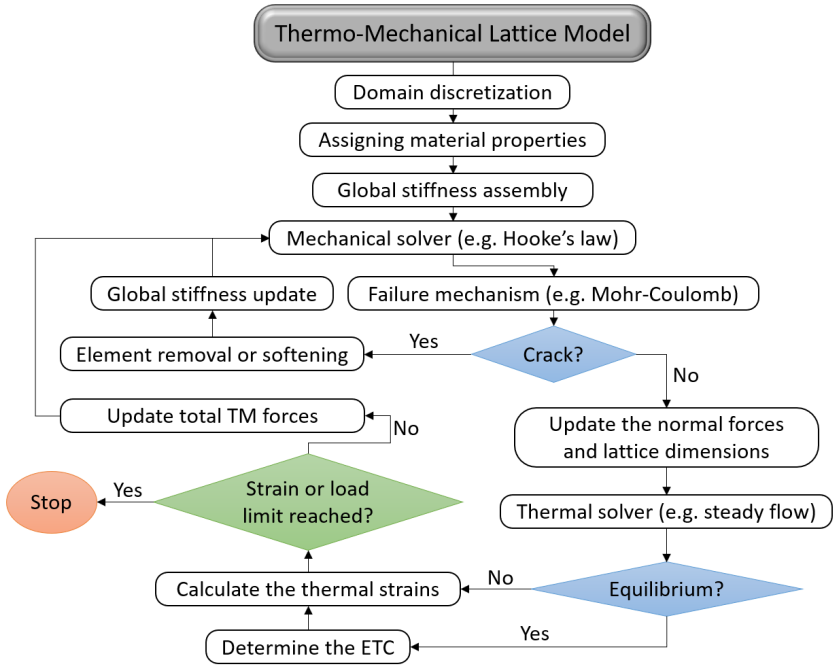

Figure 3.28: Flowchart of the Thermo-Mechanical model and the developed lattice algorithm

transfer in heterogeneous granular assemblies, taking into account smooth contact surfaces. The advantage of the thermal lattice model over TDEM is the consideration of the contact area or surface between the particles. In TDEM, only a contact point for heat transfer between two adjacent particles is considered, where, based on the Hertzian contact theory, the heat conductance (λ') [WK^{-1}] between two particles is determined (Zhang et al. 2011). Nonetheless, in the lattice, the contact surface (3D) or the length (2D) for the heat transfer between two polygons (unit cells) is considered. To develop the TM lattice model, the contact length is a function of the normal contact force and Young's modulus. By adopting this methodology for thermal conduction, the heat transfer using LEM is modeled (Sattari et al. 2017).

The Hertzian contact theory considers the change in contact area or surface of an elastic sphere (circle) with a downward force of P on a half-plane. Surface deformations (δ) and increase in contact area ($2a$) are shown in Fig.3.30. The elastic modulus of a sphere is E_1, and for a half-plane, the elastic modulus is E_s, where the sphere has a radius of R_1. The change in contact length depends on the applied normal force P, the radius of the sphere (R_1), and the effective elastic modulus (E^*).

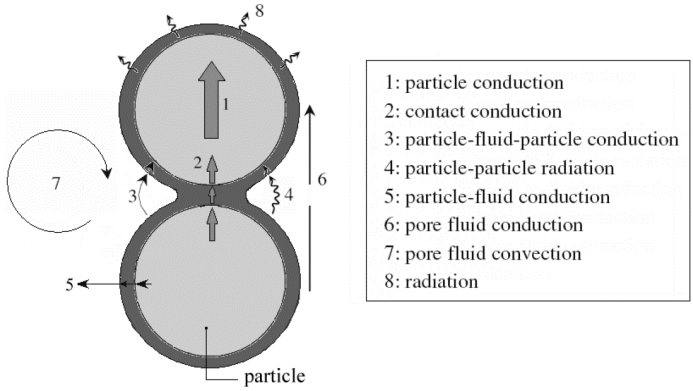

Figure 3.29: The mechanisms of heat flow in particulate granular medium (Dehdezi 2012)

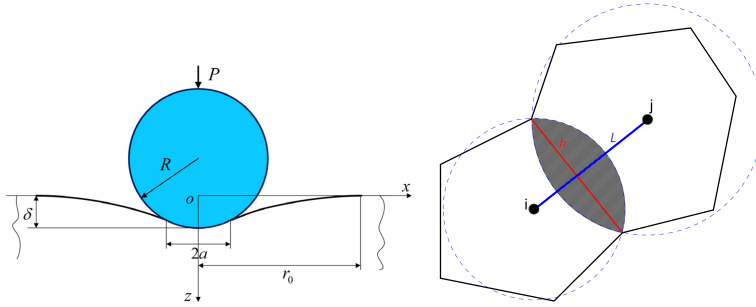

(a) (b)

Figure 3.30: The Hertzian contact theory and increase of contact area in 2D for (a) sphere and a half plane (Long et al. 2012), and (b) two Voronoi cells

$$a = \sqrt[3]{\frac{3PR_1}{4E^*}}, \qquad \delta = \frac{a^2}{R_1}, \qquad \frac{1}{E^*} = \frac{1-\nu_1^2}{E_1} + \frac{1-\nu_s^2}{E_s} \tag{3.41}$$

For two spheres in contact, the equation remains similar. Additionally, the effective radius (R^*) and the effective elastic modulus (E^*) are calculated based on the radius of two spheres (1 and 2).

$$\frac{1}{R^*} = \frac{1}{R_1} + \frac{1}{R_2}, \qquad \frac{1}{E^*} = \frac{1-\nu_1^2}{E_1} + \frac{1-\nu_2^2}{E_2} \tag{3.42}$$

In LEM, for two polygons connected to each other with a lattice element, a similar approach has been considered. The confinement force between the two unit cells (i, j) is the normal axial force (f_n). The length of the lattice is equivalent to two times the effective radius ($l \approx 2 \times R^*$). Therefore, the change in contact area (Δh) is as given.

$$\frac{\Delta h}{2} = \sqrt[3]{\frac{3f_n(\frac{l}{2})}{4\mathrm{E}^*}}, \qquad \frac{1}{\mathrm{E}^*} = \frac{1-\nu_i^2}{\mathrm{E}_i} + \frac{1-\nu_j^2}{\mathrm{E}_j} \tag{3.43}$$

Eventually, the total contact surface or length (h) between two unit cells under an axial force of f_n is given as

$$h = h_0 \pm 2 \times \sqrt[3]{\frac{3f_n(\frac{l}{2})}{4\mathrm{E}^*}}, \tag{3.44}$$

where h_0 is the initial contact length without considering the external force. The governing heat conduction equation for particle i is,

$$\rho_i c_i \frac{dT_i}{dt} - \nabla.(\lambda \nabla T_i) - \rho_i \dot{q}_i = 0, \tag{3.45}$$

where ρ_i is the density, c_i is the specific heat capacity, t is time, T_i is the temperature, λ is the thermal conductivity and $\dot{q}_i$ is the heat density. For TM simulations with LEM, the particles are considered to have only one temperature DOF and there is no heat source within the particle, so $\dot{q}_i(t) = 0$. In the case of steady heat transfer, the temperature gradient is equal to zero ($\frac{dT_i}{dt} = 0$), and the temperature of each particle in steady heat transfer ($T_i(X, Y, t)$ in 2D $T_i(X, Y, Z, t)$ in 3D) must satisfy Eq.3.46. In the steady case, the sum of heat flow (q_i) into and out of the particle i is equal to zero.

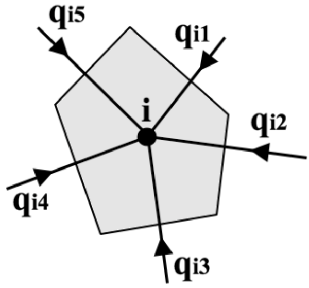

Figure 3.31: Schematic view of heat flow channels into a unit cell of i (Sattari et al. 2017)

$$\nabla.(\lambda \nabla T_i) = \sum_{j=1}^{n} q_{i,j} = 0, \tag{3.46}$$

where n is the total number of neighboring cells (in Fig.3.31, $n = 5$). The heat flow exchange between particle i and j is equal to,

$$q_{ij} = \lambda'_{ij}(T_i - T_j), \tag{3.47}$$

where λ' is the heat conductance [WK^{-1}], T_i and T_j are the temperatures of the particles i and j, respectively. The modified analytical solution of heat conductance, λ'_{ij}, based on Hertzian contact theory for perfectly smooth surfaces, is

$$\lambda'_{ij} = \lambda \times h, \tag{3.48}$$

where λ is the thermal conductivity [$\mathrm{WK}^{-1}\mathrm{m}^{-1}$] and h is the contact length according to Eq.3.44. In Eq.3.44, when two particles are in tension, a negative sign is used (contact reduction), and when they are in compression, a positive sign is considered. Fig.3.32 depicts a generated 2D domain with heat flow in and out from a unit cell of i. In total, six Voronoi cells have contact with the reference unit cell.

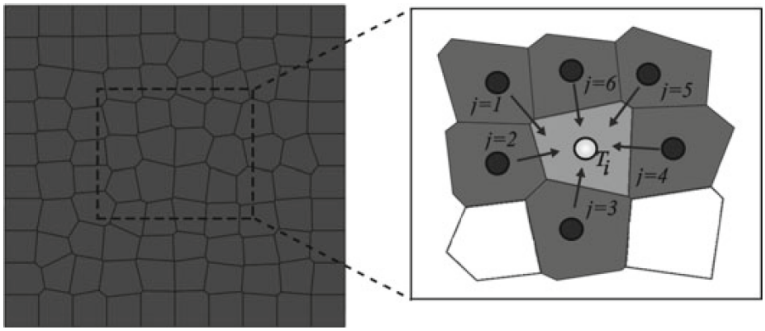

Figure 3.32: The heat flow into a unit cell i from surrounding boundaries (Kolditz et al. 2021)

So eventually, for each nuclei the following equation has been solved:

$$f_i^{eq} = \sum_{j=1}^{n} \lambda_{ij} \cdot (h_{0,ij} \pm 2 \times \sqrt[3]{\frac{3f_{n,ij}(\frac{l_{ij}}{2})}{4\mathrm{E}^*_{ij}}}) \cdot (T_i - T_j) = 0 \qquad for \qquad i = 1 : N \tag{3.49}$$

where N is the total number of Voronoi cells generated in RVE. To solve the matrix of multiple unknown temperatures ($\boldsymbol{T}$), the Newton-Raphson Jacobian approximation is used. When the maximum difference between two subsequent unknowns ($\max|\boldsymbol{T}_{new} - \boldsymbol{T}_{old}|$) is less than the error tolerance ($10 \times e^{-10}$), the Newton-Raphson iteration process is aborted.

$$\boldsymbol{T}_{new} = \boldsymbol{T}_{old} - \boldsymbol{J}^{-1}(\boldsymbol{T}_{old}) \cdot \boldsymbol{F}^{\boldsymbol{eq}}(\boldsymbol{T}_{old}), \tag{3.50}$$

where the $\boldsymbol{F}^{\boldsymbol{eq}}(\boldsymbol{T}_{old})$ matrix is

$$\boldsymbol{F}^{\boldsymbol{eq}}(\boldsymbol{T}_{old}) = \begin{bmatrix} f_1^{eq} & f_2^{eq} & \dots & f_{i=N}^{eq} \end{bmatrix}^T,$$

the Jacobin matrix $\boldsymbol{J}(\boldsymbol{T}_{old})$ is

$$\boldsymbol{J}(\boldsymbol{T}_{old}) = \begin{bmatrix} \frac{\partial f_1^{eq}}{\partial T_1} & \frac{\partial f_1^{eq}}{\partial T_2} & \cdots & \frac{\partial f_1^{eq}}{\partial T_N} \\ \frac{\partial f_2^{eq}}{\partial T_1} & \frac{\partial f_2^{eq}}{\partial T_2} & \cdots & \frac{f_2^{eq}}{T_N} \\ \vdots & \vdots & \ddots & \vdots \\ \frac{\partial f_N^{eq}}{\partial T_1} & \frac{\partial f_N^{eq}}{\partial T_2} & \cdots & \frac{\partial f_N^{eq}}{\partial T_N} \end{bmatrix},$$

and $\boldsymbol{T}_{old}$ is the temperature profile from the previous iteration step. The error threshold is reached after three iteration steps. In the lattice model, the material heterogeneity and its effect on the heat profile informs of randomly distributed heterogeneity, image processing, or multiple material layering can also be considered.

Regularization In order to simulate anisotropic heat transport, regularization of the thermal lattice properties is essential, where thermal conductivities in various flow orientations are different ($\lambda_X \neq \lambda_Y \neq \lambda_Z$). Again, this process depends on the meshing technique and the defined randomness factor (α_r). According to Rizvi (2019), in a 2D domain, for a 1D spring or bar element, the effective thermal conductivity of the domain is

$$\lambda_{mk} = \frac{1}{A} \sum_{b=1}^{N} \lambda'_{mk} \cdot l_b \cdot n_m \cdot n_k \qquad m, k = 1:2, \tag{3.51}$$

where A is the contact cross-sectional area, N is the total number of cells generated, l_b is the lattice length of element b, and $n_{m,k}$ are the normal unit vectors. In a 3D domain, the volume of the unit cell is considered instead of the cross-sectional area. The effective thermal conductivity matrix is equal to

$$\boldsymbol{\lambda} = \begin{bmatrix} \lambda_{XX} & \lambda_{XY} \\ \lambda_{YX} & \lambda_{YY} \end{bmatrix}, \tag{3.52}$$

where X and Y are the principal directions. In a 3D domain,

$$\boldsymbol{\lambda} = \begin{bmatrix} \lambda_{XX} & \lambda_{XY} & \lambda_{XZ} \\ \lambda_{YX} & \lambda_{YY} & \lambda_{YZ} \\ \lambda_{ZX} & \lambda_{ZY} & \lambda_{ZZ} \end{bmatrix} \tag{3.53}$$

3.5.3 Transient heat conduction

For a transient heat transport, $\frac{dT_i}{dt} \neq 0$, and without no heat source within the particle. the governing heat equation for a unit cell of i is

$$\sum_{i=1}^{n} q_i = \rho_i c_i v_i \frac{dT_i}{dt}, \tag{3.54}$$

where v_i is the volume of unit cell. For each Voronoi cell ($i = 1 : N$), the following condition should be satisfied:

$$f_i^{eq} = \sum_{j=1}^{n} \lambda_{ij} \cdot (h_{0,ij} \pm 2 \times \sqrt[3]{\frac{3 f_{n,ij}(\frac{l_{ij}}{2})}{4 \mathrm{E}_{ij}^*}}) \cdot (T_i - T_j) - \rho_i c_i v_i \frac{dT_i}{dt} = 0, \tag{3.55}$$

where the rate of temperature change ($\frac{dT_i}{dt}$) in each time step is calculated. To solve the matrix of unknown temperatures ($\boldsymbol{T}$), the Newton-Raphson Jacobian approximation in each time step is implemented. The convergence of the approximation approach (Newton-Raphson) depends on the pre-defined magnitude of the time step (Δt). It is essential to consider small time steps ($\Delta T_i = T_{t_2} - T_{t_1}$) so that thermal disturbances do not progress further than their neighboring cells. The value of Δt depends on the dimension and number of Voronoi cells generated in the RVE. The Δt should also not be so small, as this measure increases computational costs. For the lattice models and with the try and error approach, it is found that for coarse mesh sizes, $\Delta t = 10^{-1}$ [s] is satisfactory. In finer mesh sizes, a smaller time step is required.

Assessment of the thermal conductivity The thermal conductivity of a geomaterial can be determined with the following equation when there is a 1D heat transfer.

$$\lambda = \frac{\lambda_R * H}{\left(\frac{T_2 - T_1}{T_R - T_1}\right) \; H_{R1} - H_R}, \tag{3.56}$$

where T_1 and T_2 are applied thermal boundaries, T_R is the measured temperature in a reference material with known thermal conductivity of λ_R, H is the sample height and H_R is the height of the reference material, and H_{R1} is the distance between the measurement height in the reference material (T_R) and the upper boundary (T_1), as shown in Fig.3.33. In order to calculate the thermal conductivity using the above-mentioned approach, the material should reach the temperature equilibrium, so that the steady heat condition is valid. The 1D heat flow is present when the effect of the surrounding boundary on a temperature gradient is negligible. This condition could be present in an isolated material or, when considering lab-scale slender samples, in which the length-to-height ratio is great. A numerical investigation could be conducted to investigate the effect of the sample height-length ratio on a 1D heat flow.

The assessment of thermal conductivity with the above-mentioned approach requires a 1D heat flow condition, steady heat flow, as well as the measurement values of temperature in the reference material (T_R) with a known thermal conductivity value (λ_R). Comparison of the numerical results with the experimental data could be used to validate the developed numerical method. In a transient case or when a 1D heat flow is not present, the thermal conductivity of the homogeneous or heterogeneous geomaterial could also be determined using LEM. The simplified approach in DEM and LEM is based on the calculation of the heat flux (q_T) and the temperature gradient (∇T). This eliminates the need to solve the complex Fourier's law of heat conduction. The constitutive relation between ∇T and q_T is

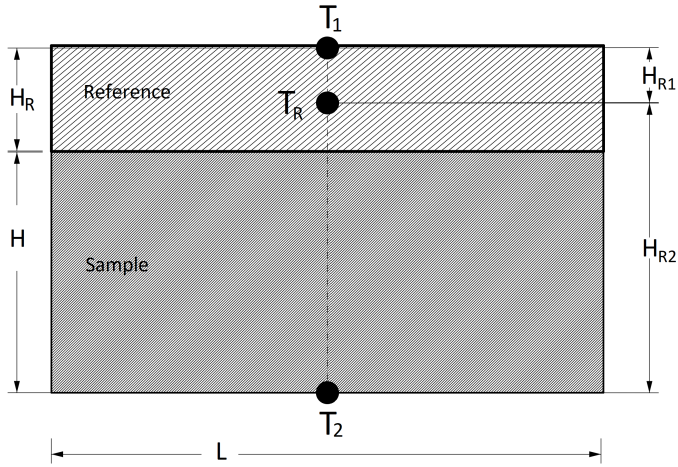

Figure 3.33: The 1D heat flow and measurement of thermal conductivity

$$q_T = -\lambda \cdot \nabla T \tag{3.57}$$

The thermal conductivity can be calculated when the system is in equilibrium, where no change in TM properties occurs. The temperature gradient can be determined based on the relative temperature of the unit cell ($\hat{T}_i$) and the average temperature (T_{ave}).

$$\hat{T}_i = \nabla T \cdot \hat{C}_i, \qquad \hat{T}_i = T_i - T_{ave}, \tag{3.58}$$

where $\hat{C}_i$ is the relative coordinate of each unit cell as

$$\hat{C}_i = C_i - C_{ave}, \tag{3.59}$$

C_i is the Cartesian coordinate of each unit cell (X, Y, Z in the 3D domain), and C_{ave} is the average value. Regarding the fluctuation of the temperature and its distribution within the geomaterial, the relative temperature cannot be computed directly from Eq.3.58. Therefore, with the minimization scheme, ∇T can be determined as a solution of linear equations as follows.

$$\sum_{i=1}^{N} C_i \cdot (\hat{T}_i - \nabla T \cdot C_i) = 0 \tag{3.60}$$

According to the average-volume technique, the average heat flux of RVE is

$$q_{ave} = \frac{\int_{RVE} q_b \, dV}{V_{RVE}}, \tag{3.61}$$

where q_b is the heat flux through the boundaries of RVE and V_{RVE} is the volume of RVE. In LEM, the average heat flux (q_{ave}) is determined with respect to the amount of heat exchange in the unit cells located on the thermal boundaries (q_b).

$$q_{ave} = \frac{\sum_{i=1}^{n_b} q_{b_i} \cdot \hat{C}_i}{V_{RVE}}, \tag{3.62}$$

where n_b is the number of cells located on the boundaries of RVE. Finally, Eq.3.57 is solved, and the effective thermal conductivity of the domain in different orientations has been computed.

$$[\boldsymbol{\lambda}] = [\boldsymbol{q}]^{-1} \cdot [\nabla \boldsymbol{T}] \tag{3.63}$$

Heat loss by convection Heat loss by convection occurs when the body of the unit cell is in contact with moving molecules such as air or liquid. In the case of not isolated boundaries, the heat lost through convection from boundaries has a huge impact on the total amount of heat flux. This is due to the large surface area that is exposed to air or fluid. The basic relationship for heat transfer by convection is

$$q_c = \lambda_c A_c (T_i - T_c), \tag{3.64}$$

where q_c is the amount of heat loss [W], λ_c is the heat convection coefficient [$\mathrm{Wm^{-2}K^{-1}}$], A_c is the area of contact between the solid and air or fluid [$\mathrm{m^2}$], T_i is the temperature of the solid and T_c is the temperature of the air or fluid in contact with the solid body. To implement the heat convection loss in the lattice model, additional lattice elements on the boundaries between the solid body (unit cells) and surrounding (atmosphere) is created. The surface contact area (A_c) is calculated based on the dimensions of the unit cells located on the boundaries. The heat convection coefficient [$\mathrm{Wm^{-2}K^{-1}}$] of air is dependent on the velocity of air (v) in [$\mathrm{ms^{-1}}$], which can be determined with an empirical equation as follows.

$$\lambda_c(air) = 12,12 - 1,16v + 11,6v^{0,5} \tag{3.65}$$

Therefore, similar to Eq.3.46, the amount of heat flow out and in for the unit cell of i subjected to air or fluid on the boundaries is

$$\sum_{j=1}^{n} q_{ij} - q_{ci} = 0, \tag{3.66}$$

where q_{ci} is the heat loss through the unit cell i (red elements in Fig.3.34). The negative sign corresponds to the heat outflow from a unit cell of i toward neighboring cells (j) and the loss of heat through convection.

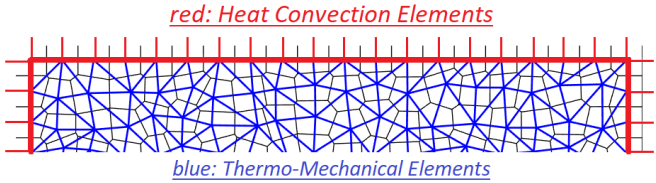

Figure 3.34: The convection heat loss from the boundaries of RVE

3.5.4 Thermal expansion

The change of heat flow and thermal conductivity with external mechanical loads and the internal contact forces developed in the lattice elements are discussed in previous sections. To complete the TM coupling process, the effect of thermal stresses on the mechanical properties should be studied. The rise in temperature in RVE results in thermal stress and a change in the contact forces between the particles. The total strain under thermo-mechanical conditions is

$$\varepsilon = \varepsilon_m + \varepsilon_t, \tag{3.67}$$

where ε_t is the thermal strain. The linear thermal strain can be calculated using the thermal expansion coefficient (α^T). For an anisotropic material and in the 3D domain: $\alpha_X^T \neq \alpha_Y^T \neq \alpha_Z^T$.

$$\varepsilon_t = \alpha^T \Delta T, \tag{3.68}$$

where ΔT is the temperature difference. For a lattice element between the unit cell of i and j, the thermal strain is equal to

$$\varepsilon_{t,ij} = \alpha_{ij}^T (T_{t+\Delta t,ij} - T_{t,ij}), \tag{3.69}$$

where t is the time and Δt is the time step. The element's elongation or contraction can be computed based on the temperature difference between the two succeeding time steps. The elongation of the element as a result of thermal expansion increases the confinement pressure at contact points or surfaces. On the other hand, the shrinkage of an element results in tensile forces between unit cells. Thermal stresses are converted to thermal forces along the axis of the lattice elements. The resultant normal force of thermal expansion or shrinkage (f_n^t) is then equal to

$$f_n^t = k_n u_t = \mathrm{E} A \varepsilon_t \tag{3.70}$$

The normal force calculated for each element due to the change in temperature is transferred to the mechanical iteration algorithm, and the weak TM coupling scheme has been completed (Fig.3.28). To correctly simulate thermal expansion and thermal cracks, it is essential to use

the interface lattice model (Sec.3.4.2). As shown in Fig.3.23, the standard lattice element is not able to project the elongation of the elements with increasing confinement pressure between the unit cells. The reasons for this are that the discretized inter-particle domain is only represented with a single lattice element, and the Voronoi unit cells do not have physical properties. For an interface lattice model, the element $i1$ only represents the unit cell i (Fig.3.23).

$$\varepsilon_{t,i1} = \alpha^T_{i1}(T_{t+\Delta t,i1} - T_{t,i1}) \tag{3.71}$$

Here, $T_{t+\Delta t,i1}$ and $T_{t,i1}$ represent the temperature change of a unit cell i instead of the lattice element ij as previously described. The magnitude of the thermal expansion coefficient depends on the temperature. Therefore, for any existing empirical relation that can be found in the literature, the temperature-dependent values of α^T are considered.

The initiation and propagation of the crack for total TM strains are based on the fracture mechanism described in Sect.3.4.4. When the lattice element is removed, no contact between the unit cells (two solid bodies) exists. Therefore, the assumption of heat conduction between solids is no longer valid. The heat conduction is then converted to solid-fluid or solid-air in a geomaterial. The thermal conductivity of air is considered to be 0.02 [$\mathrm{Wm^{-1}K^{-1}}$], and the thermal conductivity of water is 0.598 [$\mathrm{Wm^{-1}K^{-1}}$] at 20°.

3.5.5 Summary

The theoretical framework and mathematical formulation of the developed Thermo-Mechanical lattice model are presented in this section. The lattice elements carry both mechanical and thermal loads between the adjacent cells. Initially, the mathematical formulation of the developed steady and transient heat flow in heterogeneous cemented geomaterials is explained. It is shown that the thermal lattice model is capable of simulating heat conduction and convection through the boundaries. With the calculation of the thermal deformations using the thermal expansion coefficient, the thermal forces are calculated and transferred to the mechanical solver. After the removal of any element, the heat conduction between solids is broken. To visualize the thermal expansion of the domain and assess the contact forces, the application of the novel interface lattice model is proposed. The parametric study and validation of the TM lattice model are provided in Sec.4.2. Comparison of numerical and analytical solutions exhibits the accuracy of the developed TM lattice model. Furthermore, in Sec.4.2, the simulation results are compared with the experimental data obtained in the Geomechanical laboratory of CAU Kiel.

3.6 New Hydro-Mechanical (HM) lattice model

3.6.1 Introduction

The aim of this development is to develop a new coupled Hydro-Mechanical (HM) lattice model, where the coupled processes, such as hydraulic fracking, fluid and gas flow in cemented geo-material, shrinkage and swelling under the imposed humidity boundary condition, could be simulated and studied. Crack initiation and propagation under humidity change, developed fluid pathways, as well as the change of mechanical properties, such as deformations and stiffness of domain, are captured using the lattice model. In this section, a detailed description of the algorithm developed to simulate coupled HM processes is presented. In this regard, the discretization of the domain, the generation of conduit elements, the discretization of the governing differential flow equations, the fracking process and the developed 3D model are explained. The flowchart of the developed HM lattice algorithm is presented in Fig.3.35.

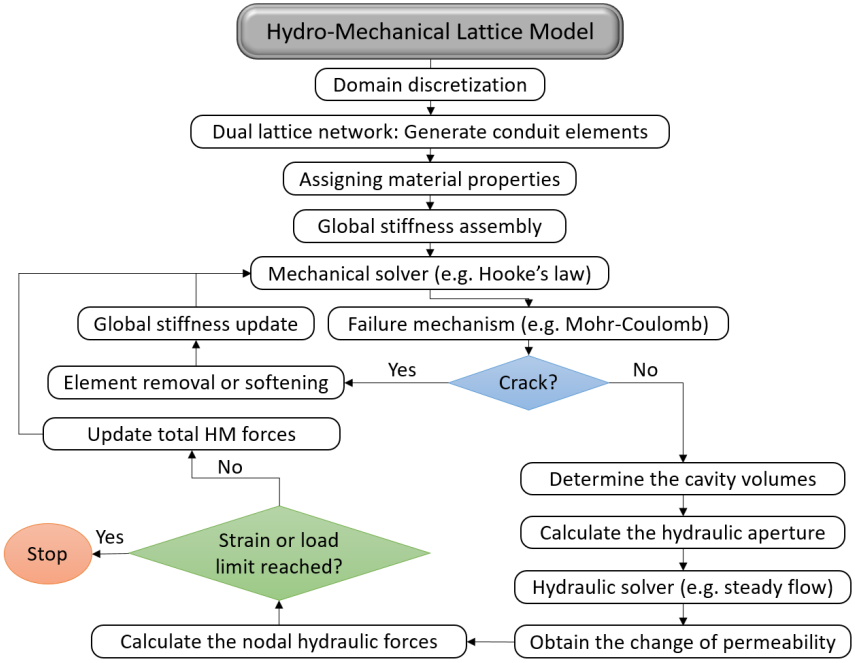

Figure 3.35: Flowchart of the Hydro-Mechanical model and the developed lattice algorithm

3.6.2 Dual lattice model

The developed HM lattice model is based on the assumption of a dual lattice network (Grassl 2009, Grassl et al. 2013). The TM lattice elements transfer heat and forces between the two adjacent unit cells. On the other hand, the hydraulic flow pathways (so-called conduit elements) are defined on the circumference of the Voronoi cells. Therefore, no fluid flow through the unit cell (solid body) is simulated with LEM. As a result, the flow pathways are the interconnected flow channels surrounding the unit cells. The dual-lattice term indicates the two independent meshing layers, where the hydraulic mesh is separated from the TM mesh. The vertices of the Voronoi cells are defined as the hydraulic nodes. Fig3.36 depicts the implemented dual lattice model in a 2D domain for the simulation of coupled HM problems.

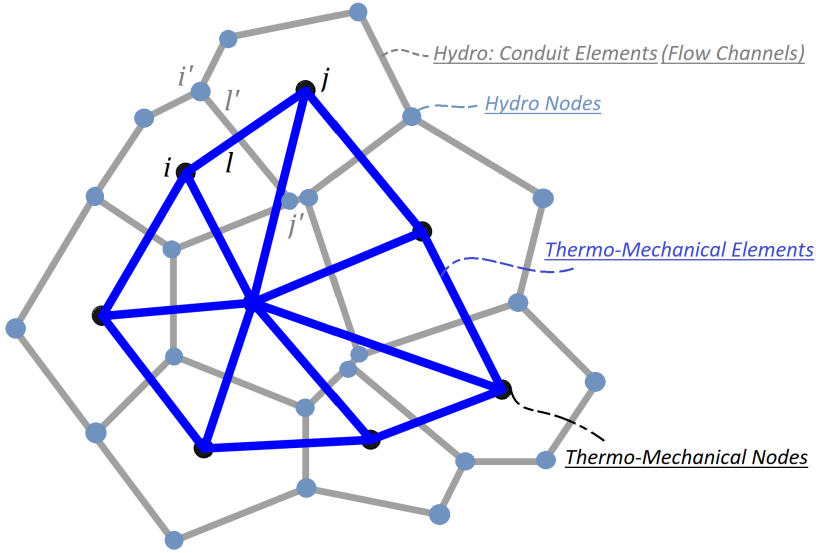

Figure 3.36: Schematic sketch of implemented dual lattice model for the coupled Hydro-Mechanical processes

The developed HM lattice model is under the assumption of laminar flow. The Navier-Stokes equations consider the conservation of mass as well as the conservation of momentum for Newtonian fluids. The Navier-Stokes momentum equation is driven in the form of the Cauchy momentum equation as follows:

$$\rho(\frac{\partial \mathbf{v_f}}{\partial t} + \mathbf{v_f} \cdot \nabla \mathbf{v_f}) = -\nabla \mathbf{p} + \nabla \cdot \boldsymbol{\tau} + \rho\, \mathbf{g}, \tag{3.72}$$

where ρ is the density, $\mathbf{v_f}$ is the fluid velocity, $\mathbf{p}$ is the pressure, $\nabla\cdot$ is the divergence, τ is the deviatoric stress tensor of order two and $\mathbf{g}$ is gravity. With no deviatoric stress, the Cauchy equations transform to the Euler equations, and in the case of conservation of mass,

$$\frac{\partial \rho}{\partial t} + \nabla \cdot (\rho\, \mathbf{v_f}) = 0 \tag{3.73}$$

With homogenization methods, Dracy's flow law for laminar flows has been driven from the Navier-Stokes equations. The flow, according to Darcy's law, is based on the hydrostatic condition, where the pressure gradient results in the flow of pressure from high pressure toward low pressure. The Darcy flux (q) is equal to

$$\mathrm{q} = -\frac{k^f}{\mu_f} \times \frac{\partial \mathbf{p}}{\partial \chi}, \qquad \chi = X, Y, \mathrm{or} Z, \tag{3.74}$$

where k^f is the permeability, $\frac{\partial \mathbf{p}}{\partial \chi}$ is the pressure gradient in the χ direction and μ_f [Pa.s] is the dynamic viscosity of the fluid. Kinematic viscosity (ν_f) [$\mathrm{m^2 s^{-1}}$] is related to dynamic viscosity (μ_f) with $\mu_f = \rho_f \nu_f$, where ρ_f is the density of the fluid. For an anisotropic porous 3D domain, the vector of fluid flux ($\vec{\mathrm{q}}$) is:

$$\vec{\mathrm{q}} = -\begin{bmatrix} K^f_{XX} & K^f_{XY} & K^f_{ZX} \\ K^f_{YX} & K^f_{YY} & K^f_{ZY} \\ K^f_{ZX} & K^f_{ZY} & K^f_{ZZ} \end{bmatrix} \begin{bmatrix} \frac{\partial h}{\partial X} \\ \frac{\partial h}{\partial Y} \\ \frac{\partial h}{\partial Z} \end{bmatrix}, \tag{3.75}$$

where K^f_{XX} is the hydraulic conductivity in the XX orientation, K^f_{XY} is the hydraulic conductivity in the mixed XY orientation, and $\frac{\partial h}{\partial X}$ is the hydraulic gradient in the X orientation. For an isotropic porous medium, the above-mentioned equation is simplified as

$$\vec{\mathrm{q}} = -K^f \begin{bmatrix} \frac{\partial h}{\partial X} \\ \frac{\partial h}{\partial Y} \\ \frac{\partial h}{\partial Z} \end{bmatrix} \tag{3.76}$$

In this study, the change in hydraulic conductivity and permeability is determined using the cubic flow law (Ghassemi et al. 2020), where a correlation is driven between the hydraulic aperture (defined as the width of the conduit channels) and the magnitude of permeability and conductivity for laminar flows. According to the cubic flow law and the defined flow channels in the dual lattice model, as shown in Fig.3.37, the hydraulic conductivity is equal to

$$K^f = \frac{\mathbf{g} a_f^2}{12 \nu_f}, \tag{3.77}$$

where a_f is the hydraulic aperture equal. With the assumption of linear variation of the hydraulic aperture between the hydraulic nodes, a_f is equal to

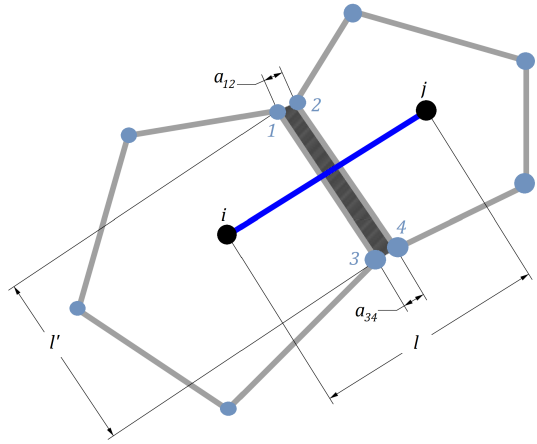

(a)

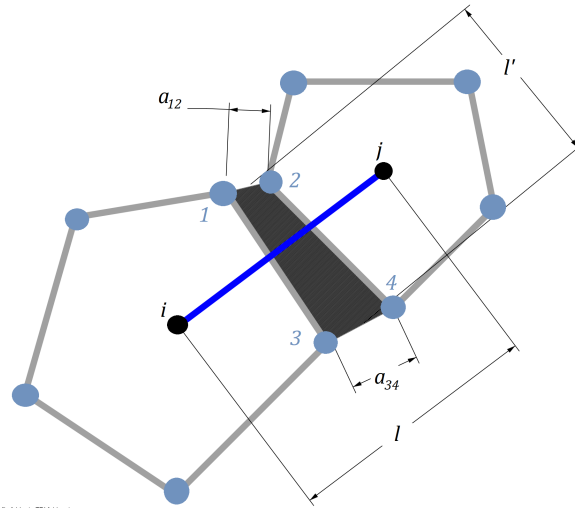

(b)

Figure 3.37: The schematic sketch of flow channels (a) before deformation, and (b) after deformation

$$a_f = \sqrt[3]{\frac{2(a_{12} \times a_{34})^2}{a_{12} + a_{34}}} \tag{3.78}$$

The flow resistance (R_f) of a conduit channel is calculated with the assumption of cubic law (parallel-plate flow) as

$$R_f = \frac{12\nu_f l'}{a_f^3} \tag{3.79}$$

3.6.3 Discretization of the differential flow equation

Different discretization methods of the differential equation of the non-stationary flow could be found in the literature. The governing fluid flow relation in the HM lattice model developed by Grassl (2009) is based on the element conductivity ($\boldsymbol{K_e^f}$) and the capacity matrix ($\boldsymbol{C_e}$) as well as the flow potential ($\boldsymbol{\theta_f}$).

$$\boldsymbol{K_e^f \theta_f} + \boldsymbol{C_e}\frac{\partial \boldsymbol{\theta_f}}{\partial t} = \boldsymbol{F_f}, \tag{3.80}$$

where $\boldsymbol{F_f}$ are the fluxes of the external fluids. For a conduit element shown in Fig.3.36, the conductivity matrix as well as the capacity matrix are defined as follows,

$$\boldsymbol{K^f_{e,i'j'}} = \frac{l_{ij}K^f_{i'j'}}{l'_{i'j'}}\begin{bmatrix} 1 & -1 \\ -1 & 1 \end{bmatrix}, \qquad \boldsymbol{C_{e,ij}} = \frac{l'_{i'j'}l_{ij}}{12}\begin{bmatrix} 2 & 1 \\ 1 & 2 \end{bmatrix}, \tag{3.81}$$

where l_{ij} and $l'_{i'j'}$ are the mechanical and conduit elements shown in Fig.3.36, respectively. Conductivity of the conduit element ($K^f_{i'j'}$) is equal to the initial conductivity of the element (K^f_0) plus the change in conductivity with deformations and crack paths (K^f_c). According to the cubic flow law, the change in hydraulic conductivity is determined with Eq.3.77.

The implementation of coupled Discontinuous Deformation Analysis (DDA) in finite element mesh for simulation of the hydro-mechanical continuum-discontinuous problems has been considered by Choo et al. (2016). Similarly, a fully-coupled HM solution has been developed by Lisjak et al. (2017) to simulate the fracturing processes using the FDEM. Here, the implementation of the formulation that exists for DDA-FEM and FDEM solutions is extended to the lattice element method. The developed methodology is applicable to a compressible fluid taking into account the linear fluid compressibility model (Lisjak et al. 2017). Based on the principle of mass conservation, the mass of fluid in a single element is equal to the fluid influx minus the source/sink and outflux flows. For an infinitesimally small element volume, the equilibrium of fluid mass is

$$\frac{\partial q_\chi}{\partial \chi} = \frac{r(\chi,t)}{\rho_f} - S_r(\frac{\Delta h}{\Delta t}) = 0, \qquad \chi = X, Y, \text{or} Z, \tag{3.82}$$

where $r(\chi,t)$ is the source/sink function based on the flow distance in the direction of χ and time (t), Δh is the hydraulic head difference, q_χ is the flow rate in the direction of χ and S_r is the degree of saturation of a joint. For a 2D domain, the flow rate and flow velocity in the direction of χ, according to Darcy's law, are equal to

$$q_\chi = -\mathbf{v}_{f_\chi}.a_{f_\chi}, \qquad v_{f_\chi} = K^f.\frac{\partial h_\chi}{\partial \chi} \tag{3.83}$$

Eventually, based on the cubic flow law (Eq.3.77), the equilibrium for the inflow and outflow fluxes from a hydraulic node of (i') and its adjacent joints (j') is

$$\sum_{j'=1}^{n_f} \frac{\partial}{\partial \chi_{i'j'}}\left(\frac{\mathbf{g}(a_{f,i'j'})^3}{12\nu_f}\cdot\frac{h_{j'}-h_{i'}}{\partial \chi_{i'j'}}\right)+\frac{r(\chi_{i'},t)}{\rho_f}-S_r\left(\frac{\Delta h}{\Delta t}\right)=0, \tag{3.84}$$

where n_f is the number of conduit elements interconnected to a hydraulic node of i' and $\chi_{i'j'}$ is the distance between i' and j'. The iterative approximation method is implemented to determine the hydraulic head of all the hydraulic nodes ($h_{i'}$) in every time step (t). Therefore, the Newton-Raphson Jacobian approach explained in Sec.3.5.2 is implemented for this purpose. After determining the hydraulic heads in each conduit node, the hydraulic pressures (pore pressures) ($\mathbf{p}_{i'}$) are calculated as

$$\mathbf{p}_{i'} = \rho_f \mathbf{g}(h_{i'} - Y_{i'}), \tag{3.85}$$

where $Y_{i'}$ is the elevation of the conduit node i' with respect to the fixed predefined reference point. With the assumption of a linearly distributed force along the flow channel of $i'j'$ the hydraulic forces on the conduit nodes (f_h) are calculated as

$$f_{h,i'} = \frac{l'}{2}\left(\frac{2\mathbf{p}_{j'}}{3}+\frac{\mathbf{p}_{i'}}{3}\right), \tag{3.86}$$

where $\mathbf{p}_{i'}$ and $\mathbf{p}_{j'}$ are the pore pressures in the conduit nodes i' and j', respectively. In the lattice model, and in order to reduce the number of nodes for the mechanical solver, the hydraulic nodes are separated from the mechanical nodes. However, the transformation of pore pressures and forces into a mechanical solver is essential to complete the coupling process. The equilibrium of forces and moments in a system is considered ($\sum F_X = \sum F_Y = \sum F_Z = \sum M = 0$) to transform the fluid forces into the mechanical solver. Fig.3.38 illustrates the fluid forces between two Voronoi cells and the hydraulic forces calculated in the conduit element of $i'j'$, which is deformed to the irregular quadrilateral flow channel between the conduit nodes 1234.

$$f_{h,13} = f_{h,24} = \frac{l'}{2}\cdot(\mathbf{p}_1+\mathbf{p}_3) \tag{3.87}$$

The distance between the resultant hydraulic force along the flow channel and the Voronoi node (mechanical node) is determined, and the resultant forces and moments in the Voronoi cell i and j are calculated. Deformation of the mechanical nodes results in a change in the flow pathways and the dimension of the hydraulic aperture (a_f), which changes the hydraulic conductivity of the conduit elements. On the other hand, the hydraulic pressures are converted to the local forces applied to the mechanical nodes, resulting in deformations and hydraulic

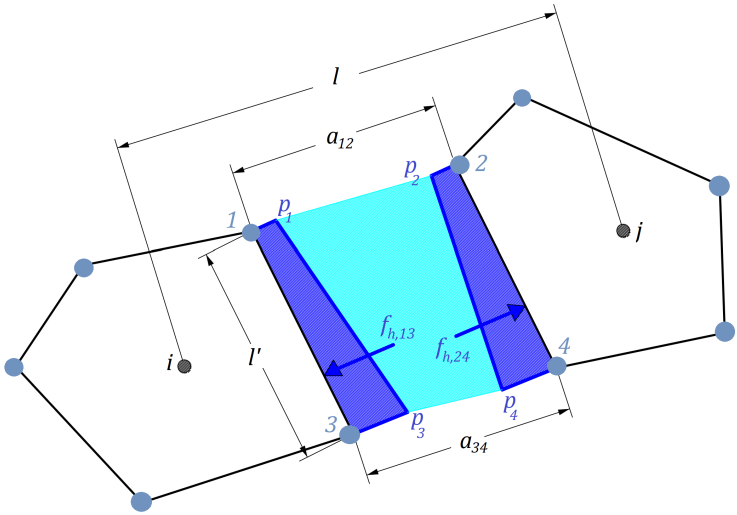

Figure 3.38: Schematic sketch of the hydraulic forces and their transformation into mechanical solver

frack initiation.

In the developed HM lattice model, the continuity equation and the conservation of fluid mass are considered, where the fluid mass (m_f) in the conduit node i' in a given time step (m^{t+1}) is equal to the fluid mass in the previous time step (m^t) plus the fluid mass (Δm_f) exchange between the conduit node i' and its neighboring nodes j'.

$$m_{f,i'}^{t+1} = m_{f,i'}^{t} + \Delta m_{f,i'}, \qquad \Delta m_{f,i'} = \sum_{j'=1}^{n_f} \Delta m_{f,i'j'} \tag{3.88}$$

In addition to the pore cavities, virtual cavities are defined in each hydraulic node. The volume of each virtual cavity (V_c) is calculated based on the volume of the conduit channels (V_f) connected to the node.

For a virtual cavity of i' and according to Fig.3.39 and Fig.3.38 the volume is equal to

$$V_{f,i'j'} = \frac{A'_{i'j'} \cdot (a_{12} \cdot a_{34})_{i'j'}}{2}, \qquad A'_{i'j'} = l'_{i'j'} \cdot t^f_{i'j'}, \qquad V_{c,i'} = \sum_{j'=1}^{n_f} \frac{V_{f,i'j'}}{2}, \tag{3.89}$$

where A' is the cross-sectional area of the fluid channel and t^f is the depth of the channel. The volume of the real pore is calculated on the basis of the dimension of the defined Voronoi cell,

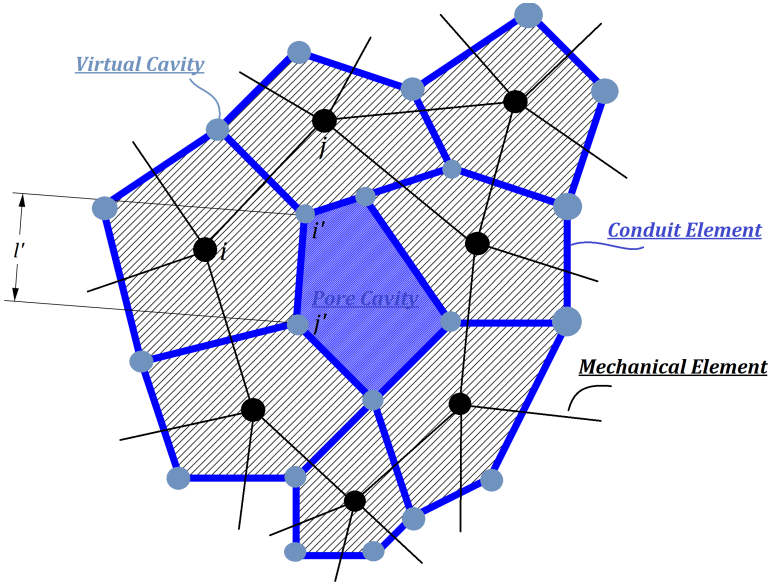

Figure 3.39: The definition of virtual cavities on hydraulic nodes

as shown in Fig.3.39. According to Darcy's law, the flow rate through a conduit channel ($i'j'$) for a viscous (Newtonian) laminar flow is

$$q_{f,i'j'} = \frac{dm_f}{dt} = -\frac{\mathbf{p}_{i'} - \mathbf{p}_{j'} - \rho_f \mathbf{g}(Y_{i'} - Y_{j'})}{R_{f,i'j'}}, \tag{3.90}$$

where R_f is the flow resistance of the conduit channel. The fluid mass flowing from the conduit node i' to j' in a time step of Δt is determined with the application of an explicit temporal integration scheme,

$$\Delta m_{f,i'j'} = -f_{S_r} \frac{\mathbf{p}_{i'} - \mathbf{p}_{j'} - \rho_f \mathbf{g}(Y_{i'} - Y_{j'})}{R_{f,i'j'}} \Delta t, \qquad \Delta m_{f,j'i'} = -\Delta m_{f,i'j'}, \tag{3.91}$$

where f_{S_r} is the saturation function defined as (Lisjak et al. 2017)

$$f_{S_r} = S_r^2 \cdot (3 - 2S_r), \qquad 0 \leq f_{S_r} \leq 1$$

The flow resistance is determined according to Eq.3.79, in which the hydraulic aperture (a_f) for the flow channel is calculated from Eq.3.78. Convergence of the explicit scheme is dependent on the defined hydraulic time step (Δt). The volume of the virtual cavities (V_c), fluid density (ρ_f), flow resistance (R_f) as well as the bulk modulus of the fluid (K_f) have an effect on the considered time step.

$$\Delta t = min(\frac{\rho_f V_{c,i'}}{\mathrm{K}_f \sum_{j'=1}^{n_f} \frac{1}{R_{f,j'}}}), \qquad i' = 1 : N_f, \tag{3.92}$$

where N_f is the total number of hydraulic nodes. For a cavity (virtual or pore), the amount of the fluid mass is determined based on its saturation degree and its volume.

$$m_{f,i'}^t = S_{r,i'}^t V_{c,i'}^t \rho_f (1 + \frac{P_{i'}^t}{\mathrm{K}_f}), \tag{3.93}$$

where for a dry cavity $m_{f,i'}^t = 0$ and for a partially saturated cavity $m_{f,i'}^t = S_{r,i'}^t V_{c,i'}^t \rho_f$. Eventually, with the help of Eq.3.88, Eq.3.91 and Eq.3.93, the total amount of fluid mass ($\Delta m_{f,i'}^{t+1}$) flowing in or out of all cavities is calculated. For the calculation of fluid pressures (pore pressures) in cavities, the linear fluid compressibility model is considered. In this model, which is not applicable to a partially saturated flow process, the amount of fluid pressure is calculated with respect to the fluid flux into a cavity.

$$\mathbf{p}_{f,i'}^{t+1} = \begin{cases} 0, & \text{if} \quad S_r < 1 \\ \mathbf{p}_{f,i'}^t + \dfrac{\mathrm{K}_f \Delta m_{f,i'}}{\rho_f V_{c,i'}}, & \text{if} \quad S_r \geq 1 \end{cases} \tag{3.94}$$

In each iteration step, the degree of saturation of the cavities is determined and in case $S_r \geq 1$, the excessive fluid mass resulting in $S_r \geq 1$ is computed. This excessive fluid mass results in pore pressure in a cavity. Therefore, for dry, partially saturated cavities, the fluid pressure is equal to zero.

$$S_{r,i'}^t = \frac{m_{f,i'}^t}{\rho_f V_{c,i'}} \tag{3.95}$$

As a saturation degree greater than 1 does not have physical meaning, the saturation degree is set to 1. After determining the fluid pressures in each virtual cavity, the nodal forces are calculated as shown in Fig.3.38. For a 3D domain, the implementation of dual lattice and generation of the hydraulic nodes on all Voronoi vertices are computationally expensive. To reduce the number of hydraulic nodes and generated flow channels, between each two Voronoi cells in contact, a conduit node is generated as shown in Fig.3.40. The connectivity of the generated flow channels in the 3D domain is based on each Voronoi cells neighboring contacts.

With the transformation of the fluid pressures into the mechanical nodes, the change in hydraulic conductivity with deformations and the fracking process as well as the diffusion of pore pressure can be simulated. The flow simulation is implemented under both pressure- and flow-rate-controlled boundary conditions.

For flow in unsaturated geomaterial and when the soil water characteristic curve (SWCC) is available, the correlation between hydraulic conductivity, capillary pressure, and air entry

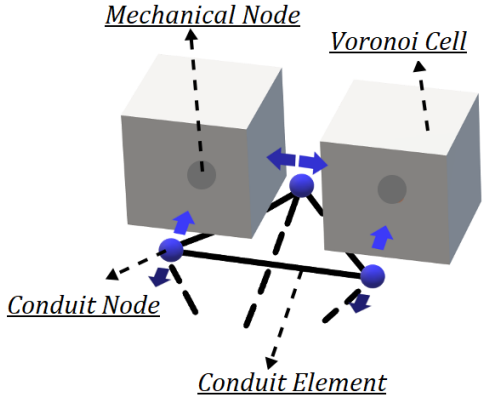

Figure 3.40: The schematic sketch of dual lattice model in 3D domain (Kolditz et al. 2021)

pressure value is made (Grassl et al. 2013). To do so, a relative conductivity (K_r) is defined, which is a function of the effective degree of saturation. Similarly, the roughness of the crack surface can be implemented in the cubic law formulation with a tortuosity factor (ξ_t). According to Xiao et al. (2013) and Vervoort and Cattle (2003), for a surface tortuosity (τ_s) of 1, the hydraulic conductivity and tortuosity (τ_t) are equal to

$$K^f = \frac{1}{\xi_t}\frac{\mathbf{g}a_f^2}{12\nu_f}, \qquad \xi_t = \tau_t^2 = (\frac{L_e}{L_f})^2, \qquad \xi_t \geq 1, \tag{3.96}$$

where L_e is the effective flow pathway and L_f is the shortest straight flow pathway. In LEM, the tortuosity factor (ξ_t) depends on the randomness factor and the defined irregularity of the mesh.

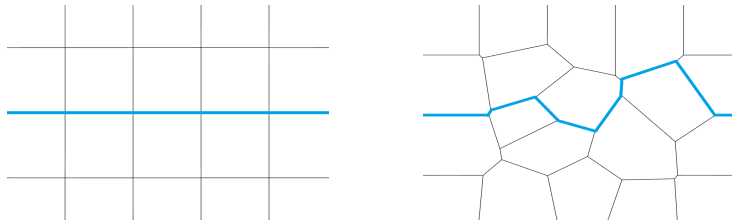

(a) (b)

Figure 3.41: The tortuosity and flow pathway (shown with blue line) in LEM: (a) regular mesh ($\alpha_r \approx 0$), and (b) irregular mesh ($\alpha_r = 1$)

3.6.4 Shrinkage and desiccation induced cracking

The discrete element models have been developed to study the behavior of clay subjected to swelling and shrinkage. For the simulation of the shrinkage process, the data from SWCC is used to correlate the water content (saturation degree) and evaporation rate with time and suction values. Bolander and Berton (2004) used the RBSN model discussed in Sec.3.4.2 to simulate the shrinkage in cemented composites. To do so, the shrinkage strain of the lattice elements is determined on the basis of the shrinkage coefficient (α_{sh}) and the moisture gradient.

$$\varepsilon_{sh} = \alpha_{sh} \cdot \Delta H, \tag{3.97}$$

where H is the relative humidity of a pore. Therefore, the shrinkage model is developed according to the simulated flow and humidity profile in the domain. The α_{sh} is calculated from drying tests of different compounds at different relative humidities. The shrinkage and expansion model considered in this study is extended from the formulation that exists in discrete models. As a result, drying shrinkage is simulated at the aggregate level with an explicit correlation between the size of the lattice elements and time (Sima et al. 2014). In lattice elements, Voronoi cells and lattice elements (spring or beam elements) are subjected to drying kinetics.

$$l_t = l_{t=0} \cdot \exp(-\alpha_{sh} \frac{t}{t_f}), \tag{3.98}$$

where t is the time, t_f is the total duration of the evaporating process, and l is the length of lattice elements. The water content of the domain can be used to reformulate the shrinkage relation mentioned above.

$$l_t = l_{t=0} \cdot \exp(-\alpha_{sh} \frac{w_0 - w}{w_0 - w_f}), \tag{3.99}$$

where w_0 is the initial water content, w_f is the final water content at time $t = t_f$ and w is the water content at any given time step. The value of α_{sh} depends on the shrinkage phase. In a saturated condition, the decrease in volume during the shrinkage process is proportional to the water loss. Therefore, the value of α_{sh} is constant.

$$\alpha_{sh} = -\frac{1}{3} \ln (1 - \frac{G_s(w_0 - w_f)}{1 + e_0}), \tag{3.100}$$

where e_0 is the initial void ratio. During the residual shrinkage phase, the value of α_{sh} can be determined from

$$\alpha_{sh} = -\frac{1}{3} \ln (1 - \frac{e_0 - e_f}{1 + e_0}), \tag{3.101}$$

where e_f is the final void ratio at time $t = t_f$. When $\alpha_{sh} = 0$, no shrinkage is expected. The input of the shrinkage algorithm is the SWCC model. This could be determined directly from experimental data or can be approximated using numerical (Sattari and Toker 2016, Sattari

et al. 2020) or empirical (Azmi et al. 2019) methods. In the above-mentioned methods, the shrinkage or elongation of the lattice elements results in drying forces which are transformed into the mechanical solver. In the mechanical solver, then, the fracture initiation and propagation due to the drying process has been modeled. In these methods, it is not required to simulate the flow in the partially saturated domain to simulate the desiccation cracking.

In addition to the discrete and aggregate shrinkage models mentioned above, shrinkage and desiccation cracking can be solved by simulating the flow in the partially saturated domain, where no shrinkage factor (α_{sh}) needs to be defined (Vo et al. 2017). The governing equation is defined as

$$\boldsymbol{\sigma} = \boldsymbol{C} : \boldsymbol{\varepsilon} - S_r \boldsymbol{p}\boldsymbol{\delta}, \tag{3.102}$$

where $\boldsymbol{\sigma}$ is the stresses, $\boldsymbol{C}$ is the elasticity tensor, $\boldsymbol{\varepsilon}$ is the strain, S_r is the degree of saturation in the time step t, $\boldsymbol{p}$ is the pore pressure and $\boldsymbol{\delta}$ is the identity matrix. At any time step, the pore pressure is solved using Eq.3.94. The saturation degree can be extracted from the experimental results of SWCC or using empirical equations such as Van Genuchten model (Ghanbarian et al. 2010).

$$\frac{S_r - S_{r,res}}{1 - S_{r,res}} = \frac{1}{(1 + (m_1\psi)^{m_2})^{m_3}}, \tag{3.103}$$

where $S_{r,res}$ is the degree of residual saturation, ψ is the suction value, m_1, m_2, and m_3 are parameters of the Van Genuchten model. Additionally, the hydraulic conductivity (K_f) depends on the degree of saturation of the medium. As a result, during the drying process, the value of K_f decreases. According to the cubic flow law and when considering the drying process, the hydraulic conductivity is equal to

$$K_f = K_{f,s_r=1} \cdot (\frac{S_r - S_{r,res}}{1 - S_{r,res}})^3 = \frac{1}{\xi_t} \frac{\mathbf{g} a_f^2}{12\nu_f} \cdot (\frac{S_r - S_{r,res}}{1 - S_{r,res}})^3 \tag{3.104}$$

In addition to hydraulic conductivity, the strength and stiffness of the domain depend on the degree of saturation and the water content. For example, according to Sima et al. (2014), for Romainville clay, the following empirical relations for Young's modulus (E) and tensile strength (σ_t) have been driven.

$$\mathrm{E} = 3 \times 10^7 \cdot (\exp(-0.177 \cdot w)), \qquad \sigma_t = 3729 \cdot (\exp(-0.083 \cdot w)) - 25.21, \tag{3.105}$$

where w is the water content (%) in time step of t. Similarly, the swelling process can be simulated when the wetting path of the SWCC curve is available. The weak coupling scheme to simulate desiccation cracking using the flow equation is based on the determination of the pore pressures (in the partially saturated domain) in the hydraulic model and the recalculation

of mechanical stresses. The coupling weak scheme for simulating the desiccation cracking using the aggregate model can be summarized as:

- Run the mechanical lattice solver
- Calculate the shrinkage factor (α_{sh}) with respect to saturation degree and water content at time t (SWCC results)
- Determine the element's shrinkage or elongation
- Compute the strains and element's normal forces due to the shrinkage process
- Repeating the mechanical process with the consideration of shrinkage forces
- Fracture simulation with the defined fracture mechanism
- Abort the mechanical solver if no additional element fails
- Time step increment with the defined Δt and recalculation of element's normal forces due to the shrinkage process
- Return to the mechanical solver and repeat the above-mentioned steps

3.6.5 Summary

The theoretical framework and mathematical formulation of the developed Hydro-Mechanical lattice model are presented in this section. In order to simulate the flow in the lattice model, the dual lattice concept is implemented in this study. Next, with the discretization of the differential flow equation, the evolution of fluid pressure is determined in the generated flow channels and hydraulic nodes. The calculated hydraulic forces are then transmitted to the mechanical nodes. Afterward, the mechanical solver is used to simulate the deformations and determine the inner lattice stresses. Deformations lead to crack initiation and deformation of the flow channels, which alter the hydraulic properties of the simulated domain. Additionally, the mathematical formulation of the lattice model is proposed to simulate the shrinkage process in cemented geomaterials. The parametric study and validation of the HM lattice model are provided in Sec.4.3. Comparison of numerical and analytical solutions exhibits the accuracy of the developed HM lattice model. Moreover, in Sec.4.3, the evolution of the effective stresses during hydraulic fracking is studied. Eventually, in Sec.5.3, the application of the developed HM lattice model is presented in the simulation of pressure-driven fluid percolation in barrier rocks.

3.7 Wave propagation with dynamic lattice model (dynamicLEM)

3.7.1 Introduction

The developed dynamic lattice model is implemented to capture the scattering and disturbance of wave fields in heterogeneous and discountinuum domains. The discrete lattice model is an ideal tool for simulating microscale heterogeneities (Rizvi et al. 2020), and with the extension of the model into the SHM field, the detection and localization of discontinuities are feasible. In this section, the extension of the conventional lattice model into a dynamic analysis is presented. The equation of motion is solved using the Newmark-β method with the incremental formulation. Finally, the system of nonlinear equations is solved using the Newton-Raphson Jacobin method to determine the acceleration, velocity, and displacement of the cell nucleus.

3.7.2 Mathematical formulation

The equation of motion of forced vibration is solved to simulate the dynamic wave propagation in geomaterials. In the methodology implemented, the accelerations ($\ddot{\boldsymbol{u}}$), velocities ($\dot{\boldsymbol{u}}$) and displacements ($\boldsymbol{u}$) of the nodes in each time step (t) are calculated according to the applied external forces. The contact forces in the dynamic lattice method, in contrast to discrete element models, are equal to zero, as no contact search between the elements is required. This reduces the computational costs of dynamic lattice models. The damping matrix ($\boldsymbol{C_m}$) is also specified, although contact damping is neglected here. The stiffness matrix ($\boldsymbol{K_g}$) of the lattice elements (spring or beam) is assembled as explained in Sec.3.4.2.

$$\boldsymbol{M}\ddot{\boldsymbol{u}}(t) + \boldsymbol{C_m}\dot{\boldsymbol{u}}(t) + \boldsymbol{K_g}\boldsymbol{u}(t) = \boldsymbol{f_{ext}}(t), \qquad t = t_{\mathrm{p}} + \Delta t, \tag{3.106}$$

where $\boldsymbol{f_{ext}}$ is a vector of external dynamic loads and Δt is the time step. The mass matrix ($\boldsymbol{M}$) can be assembled based on the mass of elements (beam or truss) or with respect to the mass of Voronoi cells (similar to discrete element methods). For a truss element (bar) in the planar domain, the consistent mass matrix ($\boldsymbol{M}$) and the lumped mass matrix of the element ($\boldsymbol{M_l}$) are evenly distributed on the nodes of the element (ij)(Jweeg et al. 2022).

$$\boldsymbol{M} = \frac{\rho_{ij} A_{ij} l_{ij}}{6} \begin{bmatrix} 2 & 0 & 1 & 0 \\ 0 & 2 & 0 & 1 \\ 1 & 0 & 2 & 0 \\ 0 & 1 & 0 & 2 \end{bmatrix}, \qquad \boldsymbol{M_l} = \frac{\rho_{ij} A_{ij} l_{ij}}{2} \begin{bmatrix} 1 & 0 & 0 & 0 \\ 0 & 1 & 0 & 0 \\ 0 & 0 & 1 & 0 \\ 0 & 0 & 0 & 1 \end{bmatrix}, \tag{3.107}$$

where ρ_{ij} is the density, A_{ij} is the cross-sectional area, and l_{ij} is the length of the element ij. For a two-dimensional beam element

$$\boldsymbol{M} = \frac{\rho_{ij} A_{ij} l_{ij}}{420} \begin{bmatrix} 140 & 0 & 0 & 70 & 0 & 0 \\ 0 & 156 & 22l_{ij} & 0 & 54 & -13l_{ij} \\ 0 & 22l_{ij} & 4l_{ij}^2 & 0 & 13l_{ij} & -3l_{ij}^2 \\ 70 & 0 & 0 & 140 & 0 & 0 \\ 0 & 54 & 13l_{ij} & 0 & 156 & -22l_{ij} \\ 0 & -13l_{ij} & -3l_{ij}^2 & 0 & 0 & 4l_{ij^2} \end{bmatrix}, \boldsymbol{M_l} = \frac{\rho_{ij} A_{ij} l_{ij}}{2} \begin{bmatrix} 1 & 0 & 0 & 0 & 0 & 0 \\ 0 & 1 & 0 & 0 & 0 & 0 \\ 0 & 0 & \frac{l_{ij}}{12} & 0 & 0 & 0 \\ 0 & 0 & 0 & 1 & 0 & 0 \\ 0 & 0 & 0 & 0 & 1 & 0 \\ 0 & 0 & 0 & 0 & 0 & \frac{l_{ij}}{12} \end{bmatrix} \tag{3.108}$$

When considering the mass of the Voronoi cell for the mass matrix assembly, the mass of each Voronoi cell is calculated similarly to that of the discrete element method. Therefore, the mass of each Voronoi cell is determined based on its volume and the density of representative material. The damping matrix ($\boldsymbol{C_m}$) is a diagonal matrix with components of normal (c_n), tangential (c_t), and rotational damping (c_r) coefficients. For a beam element in 2D domain, the acceleration ($\ddot{\boldsymbol{u}}$), velocity ($\dot{\boldsymbol{u}}$) and displacement ($\boldsymbol{u}$) matrices are as follows.

$$\ddot{\boldsymbol{u}} = \begin{bmatrix} \ddot{u}_{X1} \\ \ddot{u}_{Y2} \\ \ddot{\phi}_3 \\ \ddot{u}_{X4} \\ \ddot{u}_{Y5} \\ \ddot{\phi}_6 \end{bmatrix}, \qquad \dot{\boldsymbol{u}} = \begin{bmatrix} \dot{u}_{X1} \\ \dot{u}_{Y2} \\ \dot{\phi}_3 \\ \dot{u}_{X4} \\ \dot{u}_{Y5} \\ \dot{\phi}_6 \end{bmatrix}, \qquad \boldsymbol{u} = \begin{bmatrix} u_{X1} \\ u_{Y2} \\ \phi_3 \\ u_{X4} \\ u_{Y5} \\ \phi_6 \end{bmatrix} \tag{3.109}$$

where X and Y are the axis of Cartesian coordinates and ϕ is the rotation angle. Different explicit and implicit methods can be used to solve the equation of motion, such as the central difference method, the implicit linear acceleration method, and Newmark-β method with the incremental formulation. In this paper, the equation of motion of forced vibration is solved using the Newmark-β method with an incremental formulation as given below.

$$\delta\ddot{\boldsymbol{u}} = \frac{1}{\beta\Delta t^2}\delta\boldsymbol{u} - \frac{1}{\beta\Delta t}\dot{\boldsymbol{u}} - \frac{1}{2\beta}\ddot{\boldsymbol{u}}, \qquad \delta\dot{\boldsymbol{u}} = \frac{\gamma}{\beta\Delta t}\delta\boldsymbol{u} - \frac{\gamma}{\beta}\dot{\boldsymbol{u}} + \Delta t(1 - \frac{\gamma}{2\beta})\ddot{\boldsymbol{u}}, \tag{3.110}$$

$$\delta\ddot{\boldsymbol{u}} = \ddot{\boldsymbol{u}}(t) - \ddot{\boldsymbol{u}}(t_\mathrm{p}), \qquad \delta\dot{\boldsymbol{u}} = \dot{\boldsymbol{u}}(t) - \dot{\boldsymbol{u}}(t_\mathrm{p}), \qquad \delta\boldsymbol{u} = \boldsymbol{u}(t) - \boldsymbol{u}(t_\mathrm{p}), \tag{3.111}$$

where γ, β are the Newmark-β parameters and $\delta\boldsymbol{u}$, $\delta\dot{\boldsymbol{u}}$, $\delta\ddot{\boldsymbol{u}}$ are the increments of displacement, velocity, and acceleration, respectively. The incremental formulation of Newton's second law is given as

$$\boldsymbol{M}\delta\ddot{\boldsymbol{u}} + \boldsymbol{C_m}\delta\dot{\boldsymbol{u}} + \boldsymbol{K_g}\delta\boldsymbol{u} = \boldsymbol{\delta} f_{ext}. \tag{3.112}$$

The incremental formulation of the equation of motion can be solved under the assumption of different γ and β parameters. When $\beta = \frac{1}{4}$ and $\gamma = \frac{1}{2}$, the Newmark method is unconditionally

stable and implicit. If $\beta = \frac{1}{6}$ and $\gamma = \frac{1}{2}$, the Newmark method is similar to the linear acceleration method. Under the assumption of $\beta = 0$ and $\gamma = \frac{1}{2}$ the Newmark method is identical to the central difference method (Humar and Wright 2011). The Newton-Raphson Jacobian is implemented here to solve the system of nonlinear equations with multiple variables.

$$\delta \boldsymbol{u}_{n+1} = \delta \boldsymbol{u}_n - \boldsymbol{J}^{-1}(\delta \boldsymbol{u}_n)\boldsymbol{F}(\delta \boldsymbol{u}_n), \tag{3.113}$$

where n is the numerical iteration number and $\boldsymbol{J}^{-1}$ is the inverse of the Jacobian matrix, which is equal to the derivative of $\boldsymbol{F}(\delta \boldsymbol{u}_n)$ with respect to each unknown node displacement.

$$\boldsymbol{F}(\delta \boldsymbol{u}_n) = \boldsymbol{M}\delta \ddot{\boldsymbol{u}} + \boldsymbol{C_m}\delta \dot{\boldsymbol{u}} + \boldsymbol{K_g}\delta \boldsymbol{u} - \boldsymbol{\delta} f_{ext} \tag{3.114}$$

The convergence of the dynamic lattice method in the time domain depends on the wavelength and length of the lattice elements. Higher frequencies lead to smaller wavelengths, which require smaller element sizes and eventually increase computational costs. The correlation between time step, frequency, length of elements and wavelength could be driven to avoid divergence of the numerical method. The wavelength of λ_l for a sinusoidal waveform traveling through a uniform medium (constant speed) is equal to

$$\lambda_l = \frac{v_{phase}}{f_d}, \qquad f_d = \frac{1}{T_d}, \qquad f_a = \frac{w_d}{2\pi}, \tag{3.115}$$

where v_{phase} is the phase velocity, f_d is the frequency, T_d is the period, f_a is the angular frequency and w_d is the rate of change of the angular displacement. The distortion of the wave field in heterogeneous and porous mediums is simulated using the dynamic lattice model (Sattari et al. 2022). Analytical and empirical equations can be used to obtain the wave velocity in a porous medium (Diaz and Ezziani 2009). The developed dynamic lattice method also considers the Sommerfeld radiation conditions for infinite domains by using Perfectly Matched Layer (PML) (Komatitsch and Tromp 2003, Azizia et al. 2017) to absorb the wave energy at the boundaries and avoid boundary reflections if necessary. With the lattice simulations, it is possible to observe and detect the P-wave (v_p), S-wave (v_s) (body waves) as well as surface waves as shown in Fig.3.42, where a single Ricker wavelet is excited in a homogeneous domain.

Wave propagation and distortion using dynamicLEM can also be used to detect and identify the orientation, length, and location of discontinuities in a geomaterial. On the basis of the arrival time of the initial and secondary waves in the reference sensors, the discontinuities can be localized. The wave velocities are correlated with the elastic constants with

$$v_p = \sqrt{\frac{\mathrm{E}(1-\nu)}{\rho(1+\nu)(1-2\nu)}}, \qquad v_s = \sqrt{\frac{\mathrm{G}}{\rho}}, \tag{3.116}$$

where ν is the Poisson's ratio and ρ is the density. The above-mentioned equation is valid for an elastic, non-porous, isotropic, and uniform domain. Using the neural network and artificial

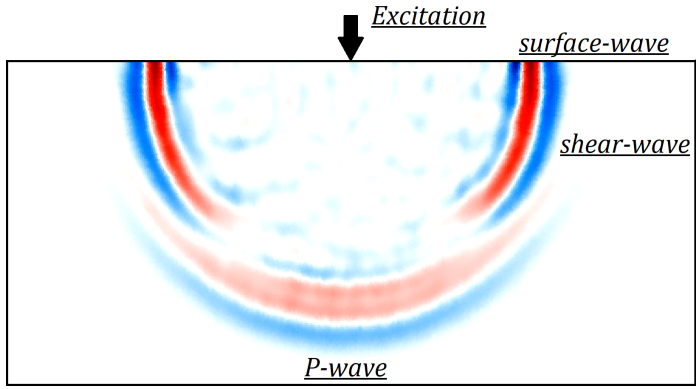

Figure 3.42: The dynamic wave (Ricker wavelet) propagation in homogeneous domain using the dynamicLEM

intelligence (AI) and training the algorithm with the results of the dynamicLEM, the identification and localization of discontinuities have been reported by Wuttke et al. (2021). In this research, the simulation of dynamic crack propagation is not covered.

3.7.3 Summary

The mathematical formulation of the developed dynamic lattice model is presented in this section. In order to simulate the P and S-wave propagation in a heterogeneous and discontinuous geomaterial, the equation of motion is solved. In Sec.4.4, the validation of the dynamicLEM with the analytical solution is carried out. Moreover, in Sec.4.4, a numerical study is conducted to illustrate the distortion of the wave fields in discontinuous and heterogeneous domains using dynamicLEM. In this manner, rock and concrete cantilever beam bodies are subjected to dynamic excitation, and receiver sensors are used to detect and analyze the arriving wave fronts.

3.8 Extension of LEM to discrete lattice model (DLEM)

3.8.1 Introduction

In the lattice model described in Sec.3.4, the generated Voronoi cells do not represent the solids. Therefore, the contact forces between the unit bodies have been neglected. The advantage of the lattice model is to simulate small displacements and frack progression in cemented geomaterials. Moreover, the lattice model is computationally efficient than discrete element methods, as no extra computational process for computing the contact possibilities and forces is required. But this leads to the main disadvantage of the lattice models, as they are not developed to simulate large displacements. The contact forces, the effect of the particle's shape, friction, sliding,

rotating, and slipping of the particles cannot be investigated directly with the lattice model. Therefore, in this study, the implementation of the discrete lattice model in the simulation of crack initiation and propagation is presented, where in addition to the discrete Voronoi cells, a cohesive bond (lattice elements) in the inter-particle scale is generated. This approach is also known as the cohesive discrete element method. The discretization of the domain, mesh generation, particle shape factor, mechanical discrete lattice model, as well as calculation of the contact forces are presented in this section. The flowchart of the developed discrete-lattice algorithm is presented in Fig.3.43.

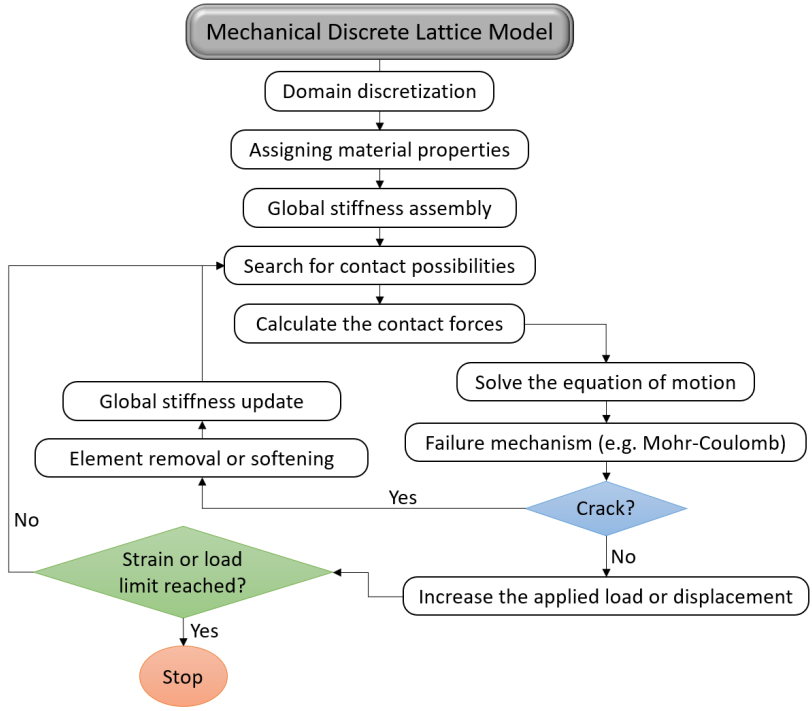

Figure 3.43: Flowchart of the discrete lattice model and the developed lattice algorithm

3.8.2 Model framework

Similarly to the lattice model, the discretization of the domain is achieved using the vectorizable random lattice (VRL) and the defined randomness factor (α_r). Additionally, in DLEM, the shape of the Voronoi cells represents the form of the particles or defined clusters. Therefore, the output of the mechanical stress deformations is dependent on the shape factor. When considering the 2D domain, the shape of Voronoi cells differs from regular square ($\alpha_r \approx 0$) to irregular

angular polygonal particles ($\alpha_r = 1$). In order to investigate the circular (or spherical in 3D) particle shapes, a packing algorithm according to the particle size distribution is implemented. The placement of circular or spherical particles in the representative volume element is reached by solving the equation of motion or a packing algorithm (Sattari and Toker 2016, Sattari et al. 2020), where based on porosity and GSD, the domain with circular and spherical particles is generated. Fig.3.44 depicts the generated 2D domain using circular and polygonal packings with regular and irregular meshing approaches. The circular packing coherently includes the porous structure, which can be controlled using the contact damping coefficient within the packing algorithm.

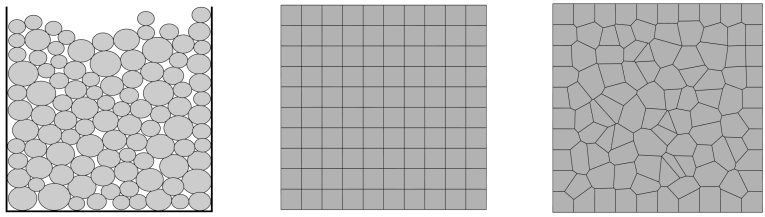

(a) (b) (c)

Figure 3.44: The generated domain in DLEM with (a) circular disks, (b) VRL with $\alpha_r \approx 0$, and (c) VRL with $\alpha_r = 1$

In order to define the porous structure in VRL, two approaches can be considered. The simplest approach, which was also explained in Sec.3.3, is to randomly assign the pore properties to the generated Voronoi cells (Fig.3.9). This approach can lead to an overestimation of the void size. Therefore, to overcome this issue, the dimension of the generated Voronoi cell should be representative of the pore structure, which leads to a computationally expensive model. An alternative approach, which is also considered in this study, is to resize the generated polygonal with different scaling factors and then implement the packing algorithm based on the equation of motion. This gives realistic pore sizes, even for larger Voronoi cells, and is better suited for the simulation of particulate granular material. Fig.3.45 depicts the 2D domain, which is packed using the equation of motion. Here, the generated Voronoi cells are re-scaled, randomly rotated, and packed to generate porosity and reduce contact lengths (or area in 3D) between the Voronoi cells in the domain.

When solving the equation of motion (discussed later in Sec.3.8.3) to determine the position and rotation of the Voronoi cells, it is essential to generate a contact matrix. The search for possible contact possibilities can then be limited to the neighboring cells that surround the reference cell (Fig.3.46). This is computationally efficient and eliminates the need to search for contact possibilities between a reference cell and all the particles generated. The non-binary search (NBS) contact detection algorithm could be implemented to optimize the contact search process and decrease computational costs (D'Albano et al. 2017). In the case of small

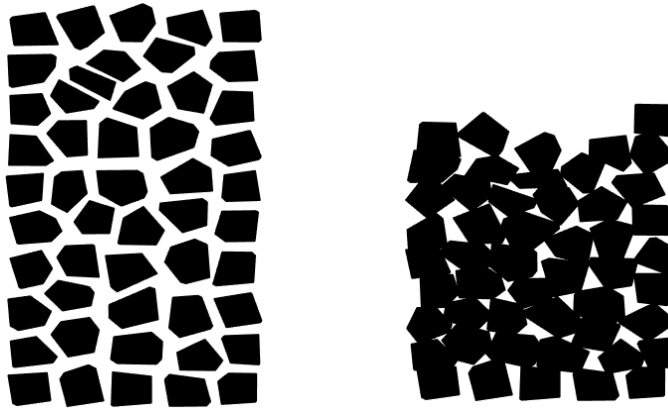

(a) (b)

Figure 3.45: The generated domain in DLEM: (a) re-scaled, and (b) discretized domain with inter-particle pore structure

displacements, the contact matrix does not need to be updated frequently after each time iteration (D'Addetta 2004). This assumption reduces computational costs.

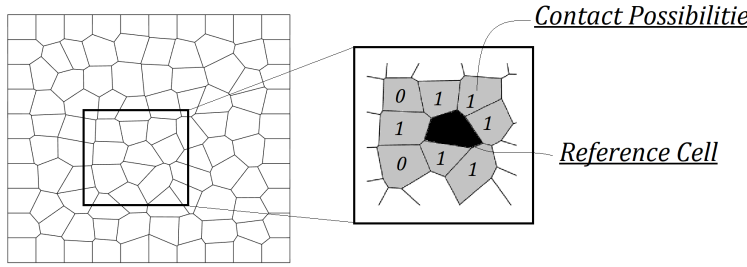

Figure 3.46: The neighboring cells and contact search in DLEM

The material heterogeneity can be assigned at the particle level on each generated cell. Similarly to the lattice approach, the generated Voronoi cell can represent an individual particle or a domain. The generated lattice elements in DLEM, represent the cohesive bond between the Voronoi cells. Therefore, based on the contact matrix, which is assembled when solving the equation of motion, the lattice bonds between the Voronoi cells are generated. Fig.3.47 depicts the generated lattice bonds using the standard VRL model on the inter-particle scale. In DLEM, the lattice elements represent only the cohesive bond. However, in the conventional lattice model described in Sec.3.4, the lattice elements represent the contact quality.

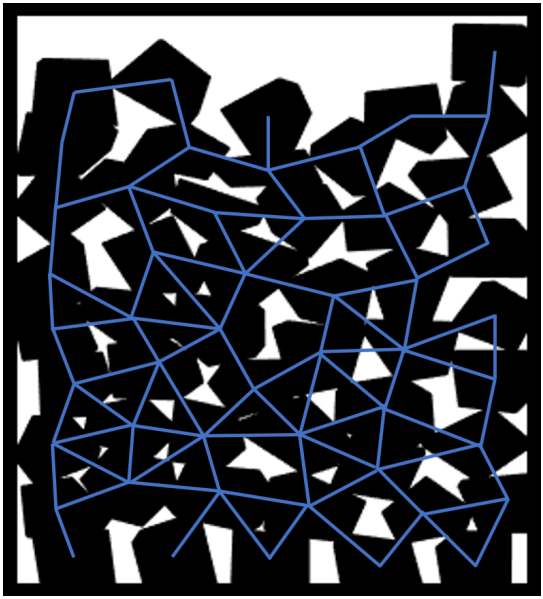

Figure 3.47: DLEM and lattice bonds generated in contact regions

3.8.3 Mathematical formulation of discrete lattice model

The mathematical framework for the DLEM is developed on the basis of Newton's law of motion. Acceleration, velocity, and displacement of Voronoi cells are calculated with regard to the applied external loads, contact forces, bond stiffness, damping factor, as well as the mass of unit cells. The main differences between this formulation and the dynamicLEM, which is explained in Sec.3.7, are the calculated contact forces between two individual cells ($\boldsymbol{f_{con}}$) and the consideration of angular acceleration and rotation of the particle.

$$\boldsymbol{M}\ddot{\boldsymbol{u}}(t_i) + \boldsymbol{C_m}\dot{\boldsymbol{u}}(t_i) + \boldsymbol{K_g}\boldsymbol{u}(t_i) = \boldsymbol{f_{ext}}(t_i) + \boldsymbol{f_{con}}(t_i), \qquad t_i = t_{i-1} + \Delta t, \tag{3.117}$$

where t_i is the time at the iteration step of i. For a single 2D Voronoi cell of (j) at a time iteration of i, the solution is

$$\begin{aligned} &\begin{bmatrix} m_j & 0 & 0 \\ 0 & m_j & 0 \\ 0 & 0 & J_j \end{bmatrix} \begin{bmatrix} \ddot{u}_{X,t_i} \\ \ddot{u}_{Y,t_i} \\ \ddot{\theta}_{t_i} \end{bmatrix} + \begin{bmatrix} c_{m,X} & 0 & 0 \\ 0 & c_{m,Y} & 0 \\ 0 & 0 & c_{I,\phi} \end{bmatrix} \begin{bmatrix} \dot{u}_{X,t_i} \\ \dot{u}_{Y,t_i} \\ \dot{\theta}_{t_i} \end{bmatrix} + \\ &+ \begin{bmatrix} K_{XX} & K_{XY} & K_{X\theta} \\ K_{YX} & K_{YY} & K_{Y\theta} \\ K_{\theta X} & K_{\theta Y} & K_{\theta\theta} \end{bmatrix} \begin{bmatrix} u_{X,t_i} \\ u_{Y,t_i} \\ \theta_{t_i} \end{bmatrix} = \begin{bmatrix} f_{ext,X,t_i} \\ f_{ext,Y,t_i} \\ T_{ext,t_i} \end{bmatrix} + \begin{bmatrix} f_{con,X,t_i} \\ f_{con,Y,t_i} \\ T_{con,t_i} \end{bmatrix}, \end{aligned} \tag{3.118}$$

where $\ddot{\theta}$, $\dot{\theta}$, and θ are angular acceleration, angular velocity, and angular displacement (radian), respectively. The polar moment of inertia for a particle j ($J_{p,j}$) is calculated with

$$J_{p,j} = I_X + I_Y, \qquad I_Y = \frac{1}{12}\sum_{i=1}^{n}(X_i Y_{i+1} - X_{i+1}Y_i)(X_i^2 + X_i X_{i+1} + X_{i+1}^2), \\ I_X = \frac{1}{12}\sum_{i=1}^{n}(X_i Y_{i+1} - X_{i+1}Y_i)(Y_i^2 + Y_i Y_{i+1} + Y_{i+1}^2), \tag{3.119}$$

where n is the number of vertices of each polygon and X and Y are the Cartesian coordinates of the vertices. Torsion (T_r) is determined on the basis of the calculated normal (f_n) and tangential (f_t) contact forces. To calculate the contact forces, the contact penalty method is considered (Tillemans and Herrmann 1995). Fig.3.48 shows the intersection of two Voronoi cells (i and j), where the contact area, length and representative contact point are used for the assessment of the normal and tangential forces.

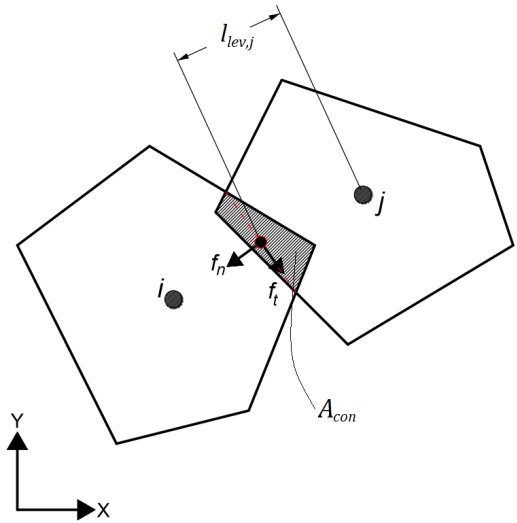

Figure 3.48: The contact penalty method to assess normal and tangential forces between solids

$$f_{con} = f_{con,n} \cdot n + f_{con,t} \cdot t, \qquad f_{con,n} = -\frac{\mathrm{E}_{eff} A_{con}}{D_{eff}} - m_{eff}\gamma_n v_{rel,n}, \\ f_{con,t} = -min(\mu|f_{con,n}|, m_{eff}\gamma_t|v_{rel,t}|), \tag{3.120}$$

where A_{con} is the intersection area, μ is the friction value according to Coulomb's friction law, n and t are normal and tangential directions, γ_n and γ_t are the damping coefficient in the normal and tangential directions, m_{eff} is the effective mass of two Voronoi cells, D_{eff} is the equivalent

effective diameter of two Voronoi cells, and $v_{rel,n}$ and $v_{rel,t}$ are the relative velocity of the cells in the normal and tangential directions, respectively.

$$m_{eff} = \frac{m_i m_j}{m_i + m_j}, \qquad D_{eff} = \frac{D_i D_j}{D_i + D_j}, \qquad v_{rel,n} = v_{j,n} - v_{i,n} \tag{3.121}$$

The contact forces ($f_{con,X,t}$, $f_{con,Y,t}$) at the time step of t are then determined based on the sine and cosine of the angle that builds up between the direction of normal and tangential forces with the X and Y orientations. To determine the contact area between two polygons (A_{con}), the MATLAB functions presented in Tab.3.1 are considered.

Table 3.1: The MATLAB functions used to assess the contact area (A_{con})

Function	Description
polyint = intersect(polygon1,polygon2)	Intersection check
polyint.Vertices	Returns the coordinates of intersection (x,y)
plot(polyint)	Plots the intersection
A_{con}=polyarea(x,y)	Returns the contact area of intersection

The stiffness matrix of the cohesive bond, represented by a lattice element ($\boldsymbol{K_g}$), is calculated and assembled as described in Sec.3.4.2. Contact torsion ($T_{con,i}$) on a Voronoi cell of i is calculated based on the calculated tangential contact forces ($f_{con,t}$) and the respective lever arm (l_{lev}).

$$T_{con,i} = \sum_{j=1}^{n_c} f_{con,t}^{j} \cdot l_{lev}^{j}, \tag{3.122}$$

where n_c is the total number of contacts of cell i. The mass of each cell is calculated with respect to its surface area (2D domain) or volume (3D domain) times the density of the individual cell. The stiffness matrix ($\boldsymbol{K_g}$) represents the cohesive bond between the particles. Separation of the contact stiffness from the cohesive bond is possible with the DLEM. In conventional LEM, the lattice element represents both contact and cohesive bonds. Similar to the LEM, the cohesive bond can be represented with a series of spring elements or a beam element. The mathematical formulation of the stiffness matrix remains identical to the LEM as explained in Sec.3.4. The only difference is the definition of Young's modulus (E), where in LEM it is the combined contact and cohesive bond stiffnesses, and in DLEM it only represents the cohesive bond. The total amount of forces applied on each individual Voronoi cell ($f_{tot,i}$) is a sum of the gravity forces ($f_{g,i}$), external loads ($f_{ext,i}$) as well as contact forces ($f_{con,i}$) calculated based on Eq.3.120.

$$f_{tot,i} = f_{g,i} + f_{ext,i} + \sum_{j=1}^{n_c} f_{con,i}^{j} \tag{3.123}$$

The explicit solution is solved with the Newmark-β method and the incremental formulation explained in Sec.3.7. Similarly, the Newton-Raphson Jacobian is implemented to solve the

system of nonlinear equations with multiple variables. The fracture mechanism discussed in Sec.3.4.4 is adopted. The failure of the cohesive bond represented by the lattice element (spring or beam) allows for frack progression in the domain. The fragmentation of the solids (Voronoi cells) is not captured with the developed model. Therefore, in the developed DLEM, the cracks occur only in the cohesive bonds, and the crashing of the grains is not simulated.

$$\boldsymbol{M}\delta\ddot{\boldsymbol{u}} + \boldsymbol{C_m}\delta\dot{\boldsymbol{u}} + \boldsymbol{K_g}\delta\boldsymbol{u} = \boldsymbol{\delta} f_{tot}. \tag{3.124}$$

3.8.4 Summary

The mathematical formulation of the developed discrete-lattice model is presented in this section. To begin with, the considered domain discretization technique is presented. Afterward, the solution of the equation of motion based on the calculated contact forces at the inter-particle level is discussed. The convergence of the DLEM solution is sensitive to the assigned time step (Δt). Calculating the contact area and the resulting contact force requires small time steps. The selection of time steps can be correlated with the size of Voronoi cells, applied forces, and stiffness of the solids. The objective of DLEM implementation in this work is to illustrate the advantages and disadvantages of the DLEM solution compared to LEM. The main advantages of the mechanical DLEM solver over the conventional lattice model are summarized as:

- ⋆ Effect of particle shape and inter-particle porosity on material behavior could be investigated.
- ⋆ The contact forces between solids could be studied considering the sliding and rolling of the particles.
- ⋆ Due to the defined mass of solids and the solution of the motion equation, simulation of large displacements is possible. The numerical model remains stable when all the cohesive bonds are detached.
- ⋆ The cohesive bond and contact stiffness are defined separately.

On the other hand, the main disadvantages of the mechanical DLEM over the conventional lattice model are:

- ⋆ The convergence of the DLEM is highly sensitive to the defined time step.
- ⋆ The explicit time-integration scheme leads to a computationally more expensive solution.
- ⋆ The effect of Voronoi shape on the effective response of a large-scale domain should be further investigated.

Chapter 4

Numerical verification and parametric studies

4.1 Simulation of geomaterial response with mechanical lattice model

4.1.1 Introduction

The mechanical lattice model is implemented to simulate the initiation and propagation of cracks in the solid bodies. The efficiency and simplicity of the lattice model to simulate the evolution of discontinuities in homogeneous and heterogeneous materials has been widely accepted. However, few works have focused on the analytical validation and parametric study of the irregular lattice structure. Therefore, in this study, initially, the developed lattice model is validated by comparing the lattice results of a debonding of a double cantilever beam with an analytical solution. In addition, the effect of the size of the elements, the randomness factor, and the softening ratio on the mechanical response of the simulated domain is studied. Finally, the comparison of the lattice results with the experimental data is carried out.

4.1.2 Analytical validation: Double Cantilever Beam (DCB)

The mechanical lattice solution is verified by comparing the numerical results with the analytical solution of a Mode I debonding of a double cantilever beam (DCB). The analytical solution of the change in crack opening (2Δ) with crack length (a) is already available in the literature (Song et al. 2006, Dimitri et al. 2017, Waseem and Kumar 2014, Nairn 2011). According to simple beam theory (SBT), for a rectangular beam, the Mode I strain energy release rate (G_{I}) is

$$G_{\mathrm{I}} = \frac{12F^2a^2}{\mathrm{E}t_{\mathrm{b}}^2H^3}, \tag{4.1}$$

where a is the crack length, E is Young's modulus, t_{b} is the beam thickness, H is the single beam height and F is the applied load given as

$$F = \frac{\mathrm{E}\Delta t_{\mathrm{b}} H^3}{4a^3}, \tag{4.2}$$

where Δ is the half of the total crack opening (2Δ) (Dimitri et al. 2017). The crack debonding length (a) is then derived from Eq.4.1 and Eq.4.2 as

$$a = \sqrt[4]{\frac{3\mathrm{E}H^3\Delta^2}{4G_{\mathrm{Ic}}}}, \tag{4.3}$$

where G_{Ic} is the critical strain energy release rate for Mode I fracking process (Song et al. 2006). The debonding load at G_{I}=G_{Ic} can be determined by using

$$F_{\mathrm{c}} = \frac{t_{\mathrm{b}} H}{2a}\sqrt{\frac{G_{\mathrm{Ic}}\mathrm{E}H}{3}}, \qquad \delta_{\mathrm{c}} = \frac{G_{\mathrm{Ic}}}{\sigma_{\mathrm{t}} exp(1)}, \tag{4.4}$$

where δ_{c} is the critical displacement. Furthermore, enhanced beam theory, cohesive crack model (CCM), or finite fracture mechanics (FFM) theories can be implemented to determine the debonding load (Dimitri et al. 2017). Fig.4.1 schematically illustrates the debonding process of the DCB and the development of traction-free and fracture process zones (FPZ). For numerical simulation, the length (L) to height ($2H$) ratio of the DCB is considered equal to five. This ratio should be large enough to ensure the Mode I fracking process and avoid the evolution of shear stresses throughout the beam debonding path. Tab.4.1 presents all the input parameters required for the numerical simulation. The thickness of the beam (t^{b}) is of considerable size to ensure plane deformation condition, where $\varepsilon_{zz} = 0$.

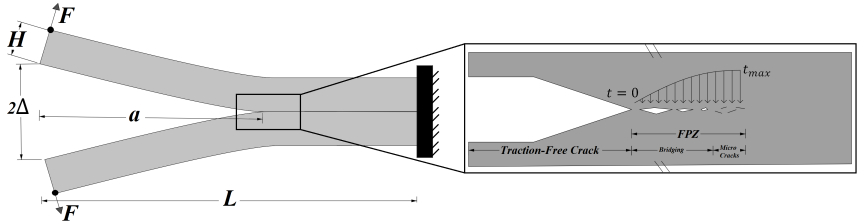

Figure 4.1: Schematic representation of the debonding process of a double cantilever beam (DCB) with a crack opening (Δ), crack length (a), traction-free zone, and fracture process zone (FPZ)

L (mm)	t^{b} (mm)	E (N/mm^2)	σ_{t} (N/mm^2)	G_{c} (N/mm)
10	1000	100	1	0.1

Table 4.1: The input parameters of a DCB for numerical models

According to the input parameters provided in Tab.4.1, the LEM is used to simulate the debonding process of DCB. The discretized domain with VRL and $\alpha_r = 0.1$, has in total 23501 elements. The static solution is implemented to capture the initiation and propagation of the fracture. For a crack length of a, the critical debonding force (F_c) is calculated and adopted to obtain precise and accurate results. The simulated qualitative debonding process of the DCB using LEM is presented in Fig.4.2. The traction free zone and the fracture process zone (FPZ) are clearly visible, where there is crack bridging.

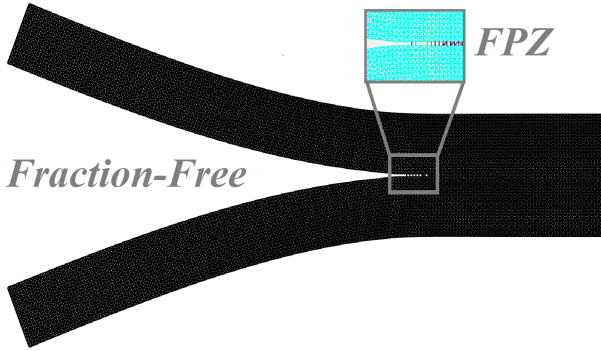

Figure 4.2: Simulated crack propagating and opening mouth of a double cantilever beam (DCB) with LEM

The quantitative result of the fracture model is shown in Fig.4.3. This graph illustrates the ratio of Δ/δ_c vs. a/L. The result of the analytical solution is added to the graph to explore the accuracy of the numerical approach. A great agreement between the analytical and numerical lattice solutions has been found.

4.1.3 Parametric study

Before applying the numerical lattice model to simulate crack initiation and propagation in geomaterials, the mesh size dependence of the results should be evaluated (Borst et al. 2006, Khoei et al. 2014). Therefore, a parametric study is conducted to investigate the effect of the randomness factor, the length of the elements, and the implemented regularization approach on the result of the simulation. First, the effect of the randomness factor on the final stress-strain response of a solid body is studied. A uniaxial tensile failure of a sample is shown in Fig.4.4, where the red line is a cracking path. The quantitative results of the setup under tensile load with brittle material behavior (Sec.3.4.4) are depicted in Fig.4.5. According to the results, without a regularization approach, the mechanical outcomes of the simulation (stiffness, deformation, and strength) depend on the randomness factor (α_r).

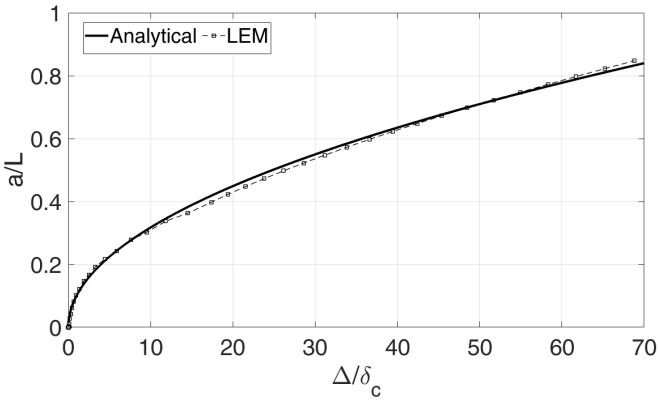

Figure 4.3: Simulated crack propagating and opening mouth of a double cantilever beam (DCB) with LEM

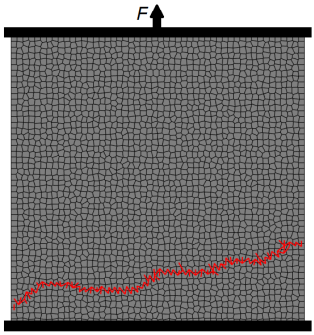

Figure 4.4: Simulation of a uni-axial tensile failure of a discretized domain with the lattice model

Additionally, the effect of the mesh size (element size) on the material response after the regularization process must be validated. This ensures the mesh independence of the numerical results. To do so, a 2D simulation of tensile failure is performed in a square-shaped domain. In four distinct simulations, the domain is discretized with the average length of the elements (l) varying between 0.000279 and 0.2786 [m]. The stress-strain response of the material with a tensile strength of 1.7 [MPa] is shown in Fig.4.6. In all four simulations, the randomness factor is constant and equal to 0.5. The results indicate the mesh independence of pre- and post-failure behavior of the simulated domain.

Next, the effect of the defined softening ratio (S) on the material response is investigated. To simulate the behavior of quasi-brittle materials, a bi-linear softening scheme is introduced

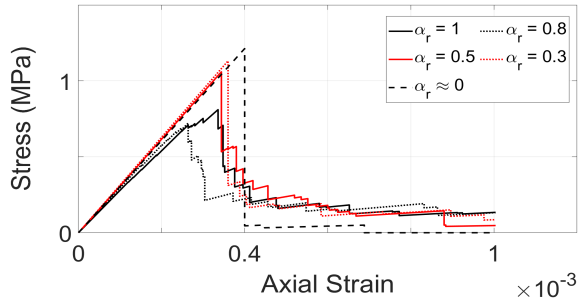

(a)

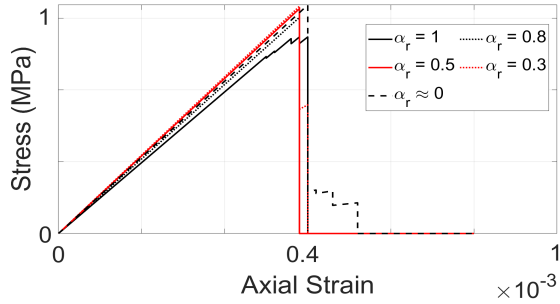

(b)

Figure 4.5: The uniaxial loading model under tension with brittle material behavior: (a) lattice results without regularization, and (b) lattice results after regularization scheme

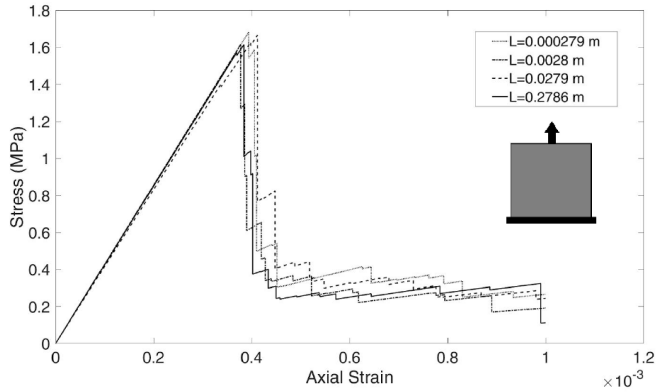

Figure 4.6: The stress-strain response of a discretized domain with four different average element lengths

(Sec.3.4.4). The softening ratio is the ratio of failure strain (ε_f) and peak strain (ε_p), where the peak strain is determined at the peak load. The same uni-axial setup as before is considered for the simulations, and the comparison of the load-displacement response of the sample with three different softening ratios (S) is shown in Fig.4.7. The results indicate that with an increase in the softening ratio, the material becomes more ductile.

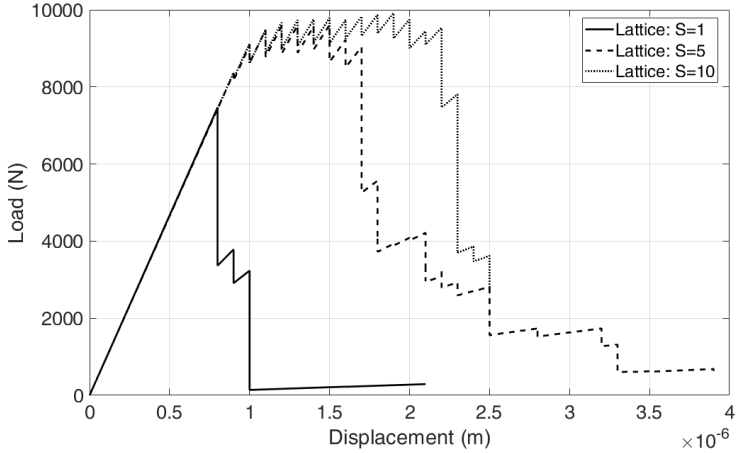

Figure 4.7: The load-displacement response of the sample with an assumption of three softening ratio values

In order to depict the effect of the inherent irregularities/heterogeneities which exist in geomaterials, crack propagation in a compact tension specimen (CTS) is simulated using the proposed static lattice model. Maji and Wang (1992) conducted a series of laboratory tests on CTS and used Electronic Speckle Pattern Interferometry (ESPI) and a Scanning Electron Microscope (SEM) to observe the fracture region and crack mouth opening displacement (CMOD). In the example presented here, the sample dimension is $10 \times 10 \times 1$ [cm] and E=0.3 [GPa]. Mode I failure of the elements is detected as expected, where the tensile strength (σ_t) of a material is set to 1 [MPa]. Here are two simulations with two different randomness factors presented. In the first case, the $\alpha_r \simeq 0$. This case represents a regular mesh that can be expected from a conventional FEM simulation. The emerging crack path and the axial displacement field (Fig.4.8a) indicate a straight crack opening path without crack reorientation. In order to account for the existing irregularities in geomaterials, in the second mesh, $\alpha_r \simeq 1$. This case provides the maximum irregularity that can be achieved using VRL. As depicted in Fig.4.8b the represented fracking path in geomaterials is affected by the shapes of the particles (cell) and the distribution of stress. The total number of generated elements is around 20000, and with the implementation of mesh refinement, the computational cost is reduced.

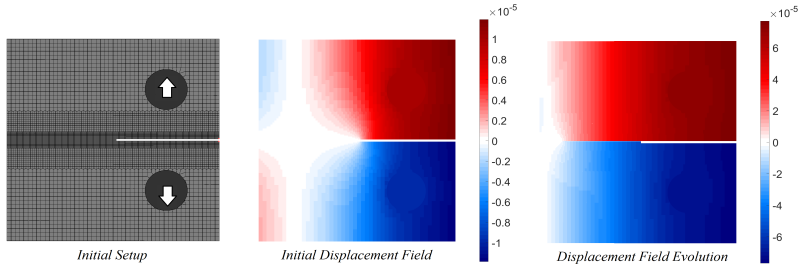

(a)

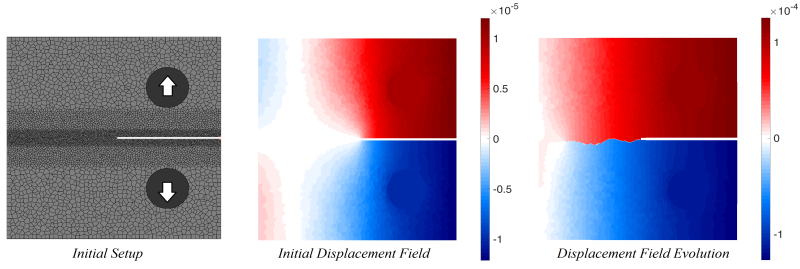

(b)

Figure 4.8: The crack propagation and evolution of displacement fields using static lattice model: (a) regular mesh $\alpha_r \simeq 0$, and (b) irregular mesh $\alpha_r \simeq 1$

4.1.4 Comparison with experimental data

Three-Point Bending Test: In order to study the accuracy of the numerical lattice model, a comparison of the numerical result with the experimental data of the three-point bending test performed on Rockville Granite is carried out (Tarokh et al. 2017). Based on the uni-axial compression test data, Young's modulus and Poisson's ratio of Rockville Granite are equal to E=25-30 [GPa] and $\nu = 0.15 - 0.20$, respectively. The indirect tensile strength (σ_{t}) is equal to 8.1 [MPa] and the uniaxial compressive strength (σ_{UCS}) is 106 [MPa]. The dimension and mechanical properties of a Granite sample used for numerical simulations are given in Tab.4.2. The height (H) to span ratio (s) is equal to 0.4. The ratio of the length of the notch to the height of the sample (a_0/H) is equal to 0.2, and the thickness of the sample (t^{b}) is 30 [mm]. The width of the notch is 1.2 [mm]. During the test procedure, the CMOD and the magnitude of applied load are measured (Tarokh et al. 2017). Schematic representations of the boundary conditions are shown in Fig.4.9.

The 3D discretization of the domain is carried out by refining the mesh around the FPZ. This measure reduces the computational power needed to simulate the progress of the fracture in the lattice model. The total number of elements generated is around 500000, and the refined mesh

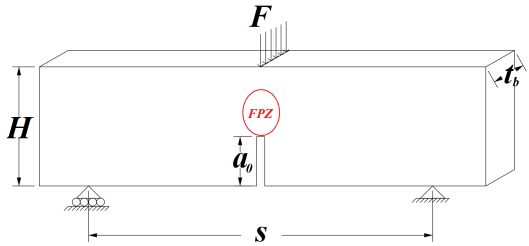

Figure 4.9: Schematic representation of three-point notched bending test with the expected fracture process zone (FPZ)

H [mm]	s [mm]	t^b [mm]	a_0 [mm]	E [GPa]	σ_t [MPa]	ν
50.8	127	30	10.16	25-30	8.1	0.15-0.20

Table 4.2: The dimension and mechanical properties of a Rockville Granite sample used for the numerical simulation

grants the 1.2 [mm] notch width, similar to what is found in the experimental data reported in Tab.4.2. To capture the experimental linear elastic response, the considered Young's modulus for the lattice simulations is modified to 35 [GPa]. The qualitative representation of the CMOD under applied bending load using the lattice model is depicted in Fig.4.10. This figure illustrates the horizontal displacement of the mesh nodes, where in the middle cross-section of the domain, the development of the crack path is visible. The movement of the neighboring nodes in opposite directions depicts the frack propagation path.

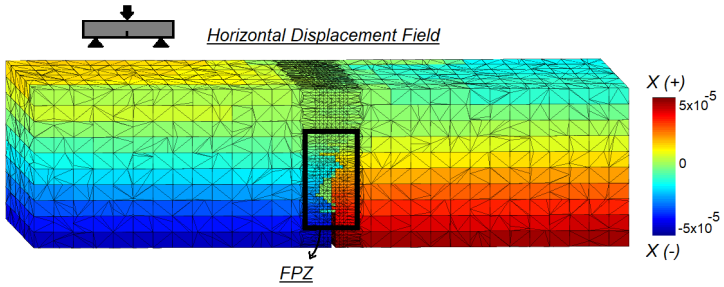

Figure 4.10: The simulated horizontal displacement field and crack propagation path using lattice model (Vowinckel et al. 2021)

The quantitative comparison of the numerical result with the experimental data is presented in Fig.4.11. In this figure, the variation of the crack mouth opening displacement (CMOD) vs. the applied load is plotted. In the numerical simulation, similar to the experimental data, the horizontal displacement at the notch base and the reaction force at the upper boundary are calculated. The lattice model captures the linear elastic response of the Granite sample

(pre-failure path) with great accuracy. The post-failure behavior of the Granite sample shows a softening behavior, which is captured with the quasi-brittle model. In the lattice model, the bi-linear softening scheme is considered to simulate the quasi-brittle post-failure behavior.

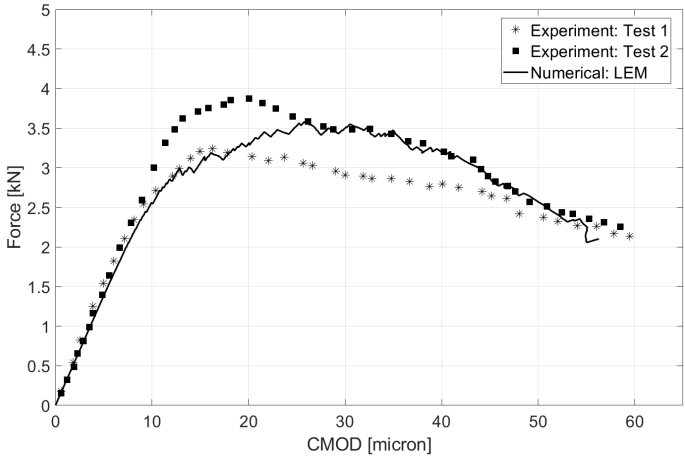

Figure 4.11: Comparison of the numerical results with the experimental data (Tarokh et al. 2017) of a three-point bending test conducted on a Granite sample

Splitting Brazilian Test: The Brazilian test is used to determine the tensile strength of the rock indirectly. In order to validate the lattice model, the experimental data of a glued stone column prepared in the laboratory of CAU Kiel are used. The experimental tests are conducted within the scope of the GeoGlue project. Hydropox Epoxidharz EP1 is used to cement the granular domain and increase the strength of the stone column. From the experimental results, the indirect uniaxial tensile strength is determined to be between 0.72 and 0.79 [MPa]. The 2D lattice simulations are used to generate the circular cross-section where the confinement load is applied from the upper boundary. The porosity is introduced into the medium by randomly assigning properties. Fig.4.12 illustrates the qualitative representation of the failure obtained from experimental and numerical studies. The lattice domain is discretized into 2500 Voronoi cells. The load-displacement response of the experiment and the numerical simulation is plotted in Fig.4.13. The results indicate a great accuracy of the lattice model to capture the material stress-strain response.

Triaxial Test: Finally, a triaxial result of an Opalinus claystone (Kolditz et al. 2021) is used to validate the numerical lattice model. Due to the low water content of the rock sample (less than 2%), the lattice simulations are conducted under dry conditions. The mechanical 3D lattice model is used to simulate the failure of the material under the confinement pressure (σ_3) of

(a) (b)

Figure 4.12: Failure of the glued sand column obtained from (a) experiment (GeoGlue project), and (b) numerical lattice models

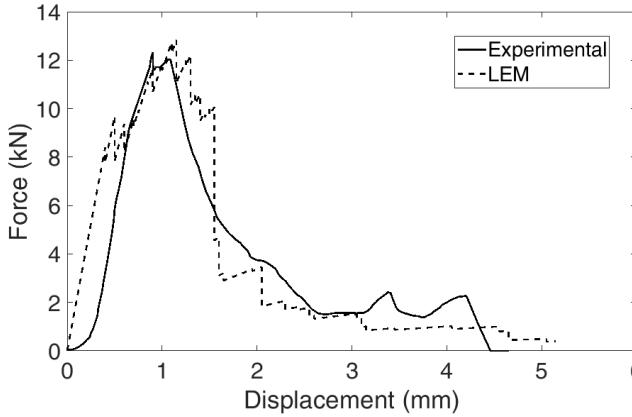

Figure 4.13: The comparison of the load-displacement response of a glued sand column obtained from experimental and numerical results

10 [MPa]. The deviatoric stress is gradually increased until material failure has been detected. The lattice model consists of 16000 Voronoi cells, and the randomness factor is considered to be 0.5. Fig.4.14 shows the test setup, as well as the development of the shear bands after the failure. The comparison of the quantitative results of the deviatoric stress vs. the measured axial strains is illustrated in Fig.4.15. The mixed Mode I and Mode II failure mechanisms are observed during the lattice simulations.

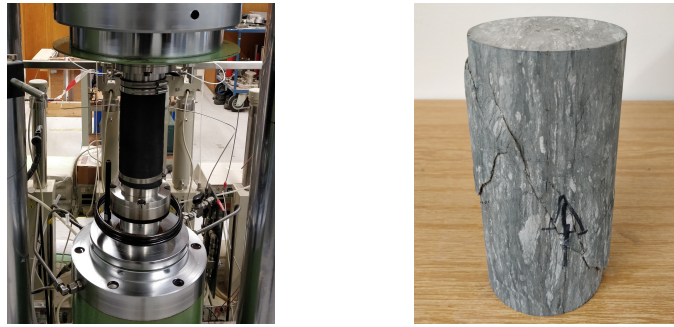

(a) (b)

Figure 4.14: Triaxial test setup: (a) Placement of the sample under the loading frame, and (b) failure of the sample and development of shear failure bands

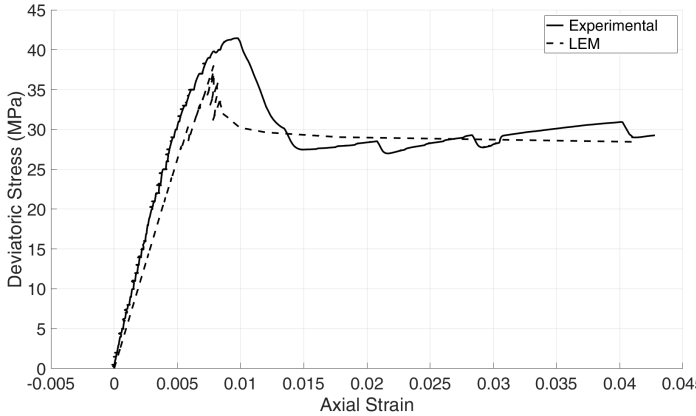

Figure 4.15: The comparison of the stress-strain response of an Opalinus clay under the triaxial confinement pressure of 10 [MPa]

4.1.5 Summary

The application of the mechanical lattice model (Sec.3.4) to simulate the propagation of cracks as well as the change of material response during the failure process is presented. The great precision of the numerical lattice model is realized in comparison with the analytical solution and the experimental data. The stochastic and irregularity of the lattice model results in realistic failure paths for geomaterials, where, due to the arrangement of grains, voids, and stress concentration, irregular crack paths have been observed. The lattice model is able to

- Simulate crack initiation without a predefined imperfection
- Model multiple independent micro-cracks before the evolution of mesoscale crack

- Capture the crack bridging, coalescence, branching and allows multi-crack propagation
- Simulate brittle or quasi-brittle material behavior

The implemented bi-linear softening scheme is essential to capture the cemented geomaterial's post-failure behavior, as shown from a comparison of the experimental data with the numerical results. In the next sections, the developed mechanical lattice model is extended to coupled thermo- and hydro-processes, and additional results are provided.

4.2 Study of the heat transport with the coupled TM lattice model

4.2.1 Introduction

This study investigates the application of LEM for modeling heat transport in cemented geomaterials under coupled thermo-mechanical processes. The proposed method replaces the cemented granular medium with lattice elements for transmission of mechanical and thermal stresses. Contact quality and lengths are assessed with the generation of random lattices using Voronoi tessellation and Delaunay triangulation. In each iteration step, the change of contact surface with applied external mechanical loads, which affects heat transmission and effective thermal conductivity (ETC), is determined. The heterogeneity and porosity are introduced by assigning different material properties to each lattice element. Initially, the heat transfer using LEM is modeled and validated with the solution of FEM. Afterward, a parametric study is performed and the effect of mesh size, randomness factor, porosity, heterogeneity, and applied external mechanical loads on calculated ETC is studied. Finally, the comparison of the LEM results with the experimental data of rock samples tested in the Geomechanical laboratory of Kiel University is carried out. The contents of this section are partially published by Sattari et al. (2017) and Sattari et al. (2019) under the titles *"Meso-scale modeling of heat transport in a heterogeneous cemented geomaterial by lattice element method"*, and *"A new lattice element method (LEM) with integrated interface elements for determining the effective thermal conductivity of rock solids under thermo-mechanical processes"*, respectively.

4.2.2 Parametric study and validation

The heat transfer in a homogeneous medium with three different mesh sizes is modeled and compared to the FEM result obtained from COMSOL Multiphysics. The mesh size can be correlated to the grain size of microscale particles. For a medium of 5x5 [cm], three different mesh sizes of 20×20, 50×50, and 100×100 with $\alpha_r = 0.5$ are modeled (Fig.4.16). In this setup, the properties of the material are given as E=30 [GPa] and $\lambda = 3$ [$\mathrm{Wm^{-1}K^{-1}}$]. The variance of temperature (Var_T) and diameter (Var_d) in the middle cross-section of the medium with

mesh size is calculated and presented in Tab.4.3. The results show that the proposed LEM can represent heat fluctuation due to the granularity of the domain, which depends on α_r and particle sizes. When the size of the mesh is increased, the effect of the granularity of the particles on the heat flow is diminished. It is believed that in 3D simulations the variance of temperature and diameter will be increased.

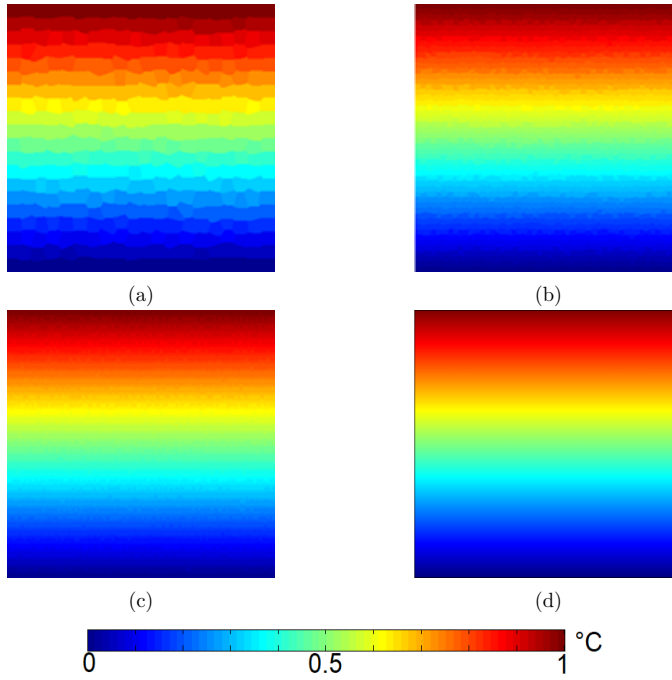

Figure 4.16: The heat transport in a 2D domain with $\alpha_r = 0.5$ and mesh sizes of (a) 20×20, (b) 50×50, (c) 100×100 for a lattice model, and (d) FEM solution (Sattari et al. 2017)

Table 4.3: The effect of mesh size on Var_T, Var_d, and ETC measured in the middle cross-section of the 2D domain

Mesh Size	Var_T	Var_d	ETC
20×20	0.2569	1.68×10^{-8}	3.07
50×50	0.0378	4.73×10^{-9}	3.08
100×100	0.014	9.04×10^{-10}	3.09

Next, the effect of α_r on the variance of the diameters of cells, the temperature, and the ETC is studied. Heterogeneity can be defined by randomly assigning different material properties to each cell, using grain size distribution (GSD), particle packing algorithms, or image processing

method (Sec.3.3), where the particle overlay will define the properties of Voronoi cells. The mesh size considered in this example is 50×50 and the heat transport under three α_r conditions: 0.1, 0.7, and 0.9, is simulated (Fig.4.17). Similarly to the previous setup, in this setup, the material properties are given as E=30 [GPa] and $\lambda = 3$ [$Wm^{-1}K^{-1}$]. With increasing α_r value, the effect of granularity on heat transport is observed. The variance of temperature, diameter, and ETC are presented in Tab.4.4. With decreasing randomness factor, the LEM results match continuum approaches, such as FEM, and the effect of granularity is neglected.

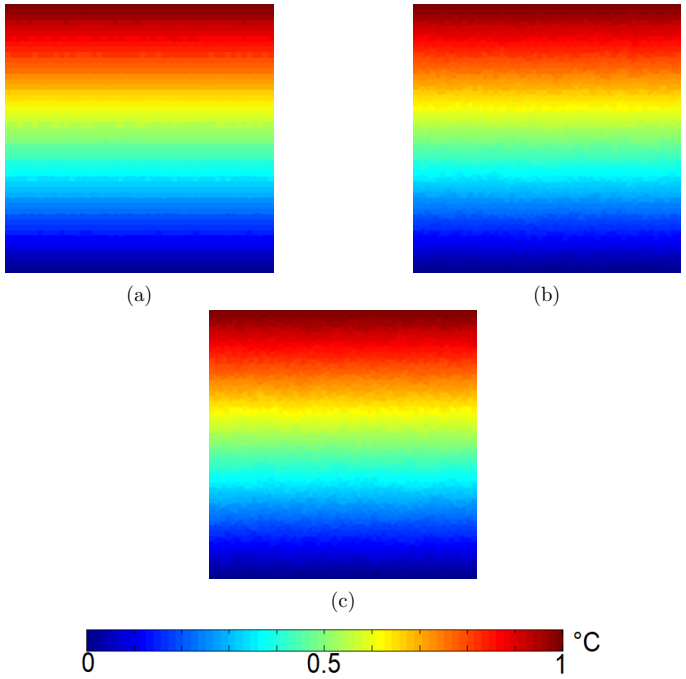

Figure 4.17: The heat transport in a 2D domain with mesh size of 50×50 and α_r = (a) 0.1, (b) 0.7, and (c) 0.9 (Sattari et al. 2017)

Table 4.4: The effect of α_r on Var_T, Var_d, and ETC measured in the middle cross-section of the 2D domain

Randomness Factor (α_r)	Var_T	Var_d	ETC
0.1	0.0017	2.44×10^{-10}	3.05
0.7	0.06	9.09×10^{-9}	3.16
0.9	0.1297	1.35×10^{-8}	3.24

The porosity can also be distributed with a random distribution, particle packing using GSD or image processing method. Here, conduction will govern the heat transfer in the pores, since the

pores are very small and convection can be neglected ($\lambda_{air} = 0.024$ [$Wm^{-1}K^{-1}$]). The medium with a mesh size of 50×50, α_r=0.7 and E=30 [GPa] is modeled (Fig.4.18). The stress concentration around the voids changes the behavior of heat transfer in the geomaterial. According to Tab.4.5, with increasing porosity, the temperature fluctuation increases, and the measured ETC decreases. The variance of temperature in the middle cross-section is highly dependent on the arrangement of the pores in the domain.

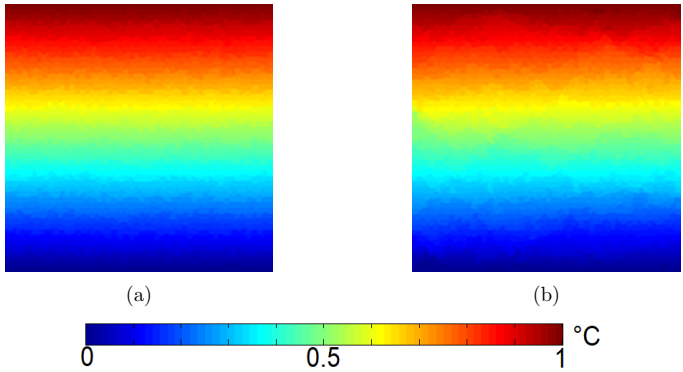

Figure 4.18: The heat flow in a 2D domain (a) without porosity, and (b) with 5% randomly distributed pores (Sattari et al. 2017)

Table 4.5: The effect of porosity on Var_T and ETC measured in the middle cross-section of the 2D domain

Porosity	Var_T	ETC
1%	0.13	3.13
3%	0.21	3.06
5%	0.46	2.97
7%	0.82	2.89
10%	0.98	2.81
15%	2.4	2.67

In FEM simulations, the application of heterogeneity in the mesoscale is tedious, which can be simply introduced in LEM. A microscopic image of a geomaterial composed of two different minerals is used to simulate heat transport and compute the ETC (Fig.4.19). With the use of the source image as the basis for cell discretization, the lattice model is generated. The mesh size is 146×125 and the randomness factor is 0.7. The green cells represent the particles with constant thermal conductivity of $\lambda_p = 3$ [$Wm^{-1}K^{-1}$], while the gray domain represents the matrix with thermal conductivity of λ_m. Taking into account the ratio of λ_p/λ_m as 2, 5, and 10, the heat transfer in a 2D domain is illustrated in Fig.4.20 (λ_p is constant and $E_p = E_m =$

10 [GPa]). The illustrated quantitative results depict the importance of mesoscale parameters, which are the inputs of the lattice model. The resulting ETCs are presented in Tab.4.6.

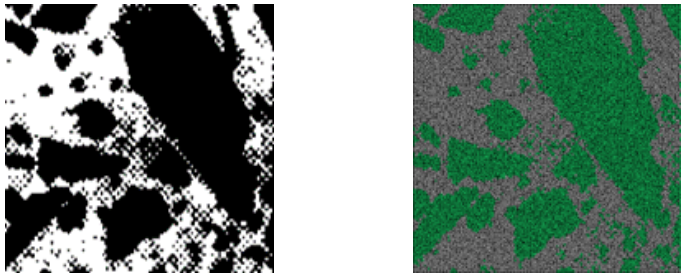

(a) (b)

Figure 4.19: (a) Microscopic image of a heterogeneous geomaterial, and (b) reconstructed lattice setup after image processing (Sattari et al. 2017)

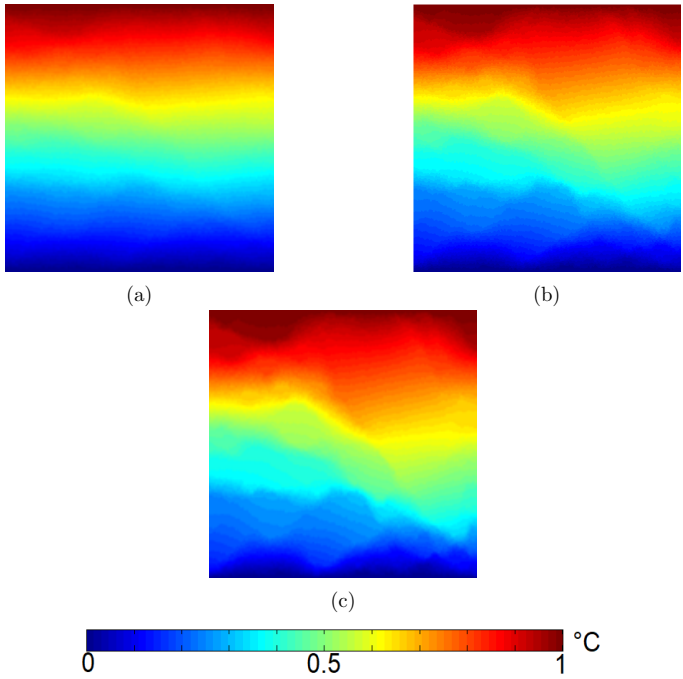

(a) (b)

(c)

Figure 4.20: Heat transfer in a heterogeneous domain with λ_p/λ_m = (a) 2, (b) 5, and (c) 10 (Sattari et al. 2017)

In addition, the effect of applied external loads on ETC is studied. Heat flow in the previous heterogeneous setup is simulated under various mechanical stress conditions. The compressive

Table 4.6: The effect of heterogeneity on the measured ETC

λ_p/λ_m	0.1	0.5	1	2	5	10
ETC	12.24	4.33	3.27	2.71	2.33	2.2

stress (σ_c) is applied to the upper boundary, where the bottom boundary is fixed in all displacement directions. In the simulated setup the $\lambda_p/\lambda_m = 2$ and according to Tab.4.7 with increasing applied stress, the measured ETC is also elevated. This is due to the increase in contact force between the particles, which is considered in Eq.3.44.

Table 4.7: The ETC of the heterogeneous medium under different mechanical stresses

σ_c [MPa]	0	0.5	1	5	10	50	100
ETC	2.71	2.84	2.9	3.11	3.29	3.69	3.95

4.2.3 Heat transfer in 3D domain

The 3D models of steady and transient heat transfer are studied to simulate the change in effective thermal conductivity under TM processes. In the first series of the results, the transient heat transfer in an irregular lattice setup is presented. For a lattice structure, the spring or beam elements transfer mechanical and thermal loads between the adjacent nodes. The cubic domain is discretized into 1728 Voronoi cells with a side dimension of 1 [m]. The thermal loads are applied from the top (1°C) and bottom cap (0°C), under the isolated boundaries. The mechanical load of 1 [kN] is applied from the upper boundary. The heat evolution in the discretized domain is plotted in three different time intervals (Fig.4.21).

In order to determine the 1-directional thermal conductivity of rock samples in the Geomechanical laboratory of the CAU Kiel, the methodology explained in Fig.3.33 is adopted. A reference material with a known thermal conductivity of 2 [$Wm^{-1}K^{-1}$] is placed between the sample and the piston. Eq.3.56 is used to determine the thermal conductivity of the rock sample. This equation is only valid when the 1-D heat flow in the middle cross-section of the cubic sample is present. In order to investigate the effect of non-isolated boundaries on heat evolution, boundary conditions similar to the experimental setup are simulated. The adopted boundary conditions are shown in Fig.4.22, where the rock sample is subjected to Thermo-Mechanical stresses.

The simulated domain is made up of reference material with a height of 2 [cm] and a cubic sample with a side dimension of 43 [cm]. The thermal conductivity of a rock and reference material is considered to be 7 and 2 [$Wm^{-1}K^{-1}$], respectively. The domain is discretized into 61000 Voronoi cells with more than 450000 lattice elements. The lattice solver explained in

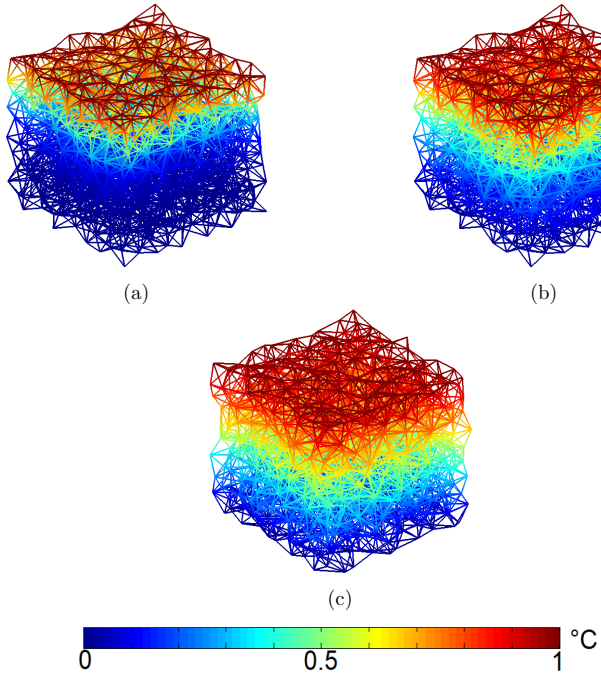

Figure 4.21: The transient heat transfer in a 3D domain with t = (a) 100 [s], (b) 300 [s], and (c) 1000 [s]

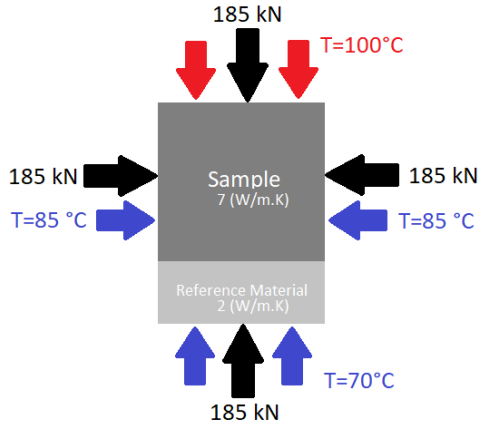

Figure 4.22: Schematic representation of the considered boundary conditions for lattice simulation

Sec.3.5.2 is used to solve the steady heat problem and plot the heat profile as shown in Fig.4.23a. The cross-section (X-Y) of the horizontal heat profile exactly in the rock-reference interface is presented in Fig.4.23b. Eventually, Fig.4.23c depicts the vertical heat profile in the middle cross-section of the sample (X-Z).

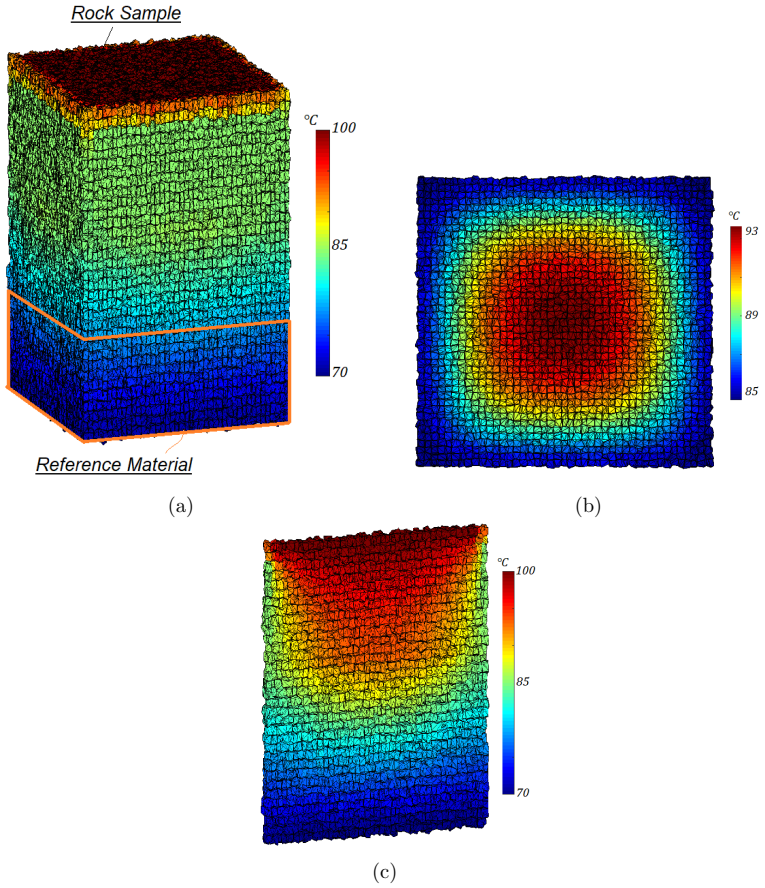

Figure 4.23: The heat profile of (a) the simulated domain, (b) X-Y cross-section on the rock-reference interface, and (c) X-Z cross-section

Based on the qualitative and quantitative visualization of the results, it is concluded that the heat profile in the middle cross-section of the sample is non-linear. The results are also compared with a continuum-based model, FEM, using ABAQUS. The main reason for the non-linearity of the results is due to the large height of the sample and the concentration of the loads on the edges of the cubic sample. In the second approach, a slender rock sample with a height of 1 [cm] and with a circular cross-section is placed on top of the cylindrical

reference material. Similar TM boundary conditions as shown in Fig.4.22 are adopted. Fig.4.24 illustrates the heat profile in the cylindrical rock sample, as well as the vertical heat profile in the middle cross-section of the sample (X-Z).

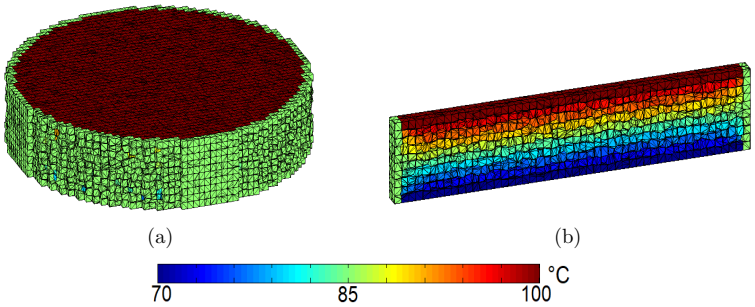

Figure 4.24: The heat profile of (a) the slender cylindrical rock sample, and (b) its X-Z cross-section

The qualitative and quantitative analysis of the results indicate a linear relationship between the temperature and the height of the sample in the middle X-Z cross-section. This grants the 1-dimensional heat flow and application of Eq.3.56 to determine the thermal conductivity of the rock sample. However, more experimental studies should be conducted to further investigate the effect of material isolation, heat loss, cracking, or crack closure of the rock sample on the measured thermal conductivity, which is not covered in this study.

4.2.4 Validation of the model with the experimental data

In the first attempt to compare the experimental results with the numerical lattice simulations, the experimental data of three rock samples under the isotropic confinement pressure are considered. Here, the effect of confinement pressure on the change in ETC is studied. The tests are performed under constant room temperature. The experimental results are based on the calculation of ETC with respect to the measured velocities of P- and S-wave velocities (Almqvist et al. 2013). The true triaxial device in the Geomechanical laboratory of Kiel University is able to apply mechanical pressures and thermal loads to a cubic sample with a side dimension of 43 [mm] up to 600 [MPa] and 600°C, respectively (Motra and Zertani 2018). The applied confinement pressure at room temperature of 20°C is gradually increased and the change in ETC is calculated. To begin with the simulation, a rock sample composed of quartz mineral (Fig. 4.25a), where its mass percentage is greater than 95%, is simulated. For an initial load, the value of λ is considered to be 6.2 [$Wm^{-1}K^{-1}$]. From the experimental data, E=77 [GPa], and Poisson's ratio is 0.071. The domain is considered to be homogeneous and the randomness

factor is considered to be 0.7. Fig.4.25b depicts the thermal conductivities obtained from the experimental test as well as the numerical results.

(a)

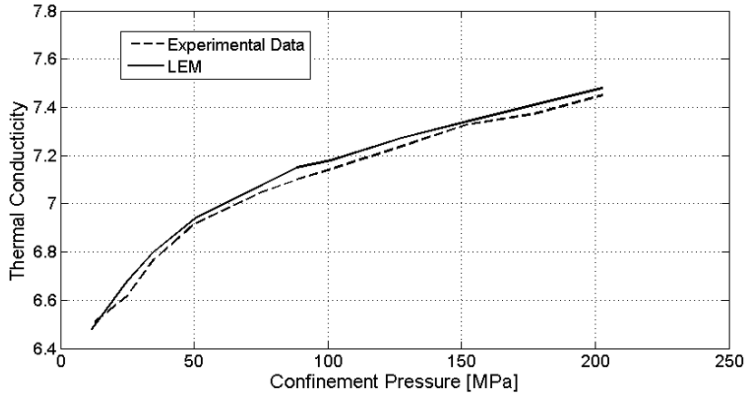

(b)

Figure 4.25: (a) Cubic quartz rock sample, and (b) comparison of experimental and numerical results (Sattari et al. 2017)

The second rock sample is composed of various minerals: Silicon dioxide (SiO_2), Aluminum oxide (Al_2O_3), Calcium oxide (CaO), Magnesium oxide (MgO), Sodium oxide (Na_2O), and Iron oxide (Fe_2O_3). Minerals with mass percentages less than 1% are neglected and porosity is fixed at 1% (Tab.4.8). Due to the lack of microscopic images, the minerals are randomly distributed in the medium (Fig.4.26a). The minerals of SiO_2, Al_2O_3, CaO, MgO, Na_2O, and Fe_2O_3 are shown with gray, green, red, magenta, blue, and yellow cells, respectively. From the experimental data, E=113 [GPa] and Poisson's ratio is 0.21. The randomness factor is assumed to be 0.5. The comparison of the ETC obtained from the experimental data and LEM is illustrated in Fig.4.26b.

Finally, the ETC of the Carboli rock sample (Fig.4.27) mainly composed of quartz, chlorite and muscovite mica minerals is determined (Tab.4.9). Porosity is 1% and microscopic image is used to generate particle overlayer (Fig.4.27b). Quartz, muscovite, and chlorite minerals are

Table 4.8: Mineral properties of simulated rock sample considered for the lattice model

Minerals	SiO_2	Al_2O_3	CaO	MgO	Na_2O	Fe_2O_3
Mass %	53	22	10	6	3	5
E [GPa]	75	300	60	270	110	155
λ [$Wm^{-1}K^{-1}$]	4.1	9	0.05	0.68	0.58	1

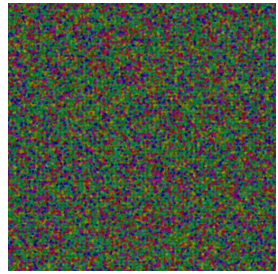

(a)

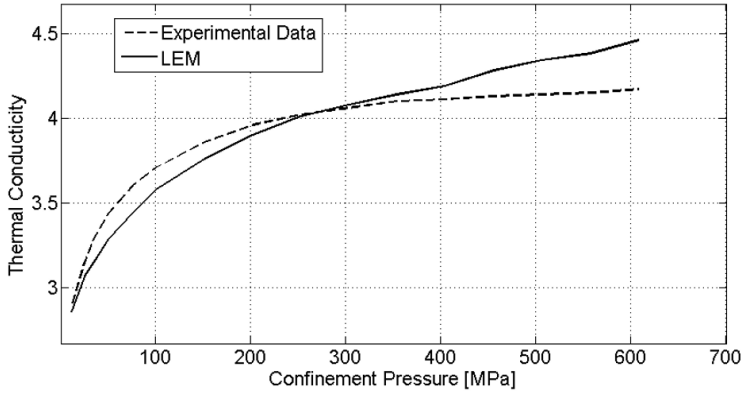

(b)

Figure 4.26: (a) Discretized domain in LEM, and (b) comparison of experimental and numerical results (Sattari et al. 2017)

shown with gray, green, and red cells, respectively. From experimental data, the Poisson's ratio is 0.18 and the randomness factor adopted here is 0.55. Fig.4.28 illustrates the comparison of the ETC obtained from the experimental data and LEM.

According to the results, it can be concluded that with the application of the lattice model the ETC of the heterogeneous rock samples under the confinement pressure can be accurately estimated. However, with increasing heterogeneity and lack of microscopic images the accuracy of the lattice model is decreased. The differences between the numerical and experimental

Table 4.9: Mineral properties of simulated Carboli rock sample considered for the lattice model

Minerals	Quartz	Muscovite	Calcite
E [GPa]	75	30	70
λ [$Wm^{-1}K^{-1}$]	6.2	0.6	4.3

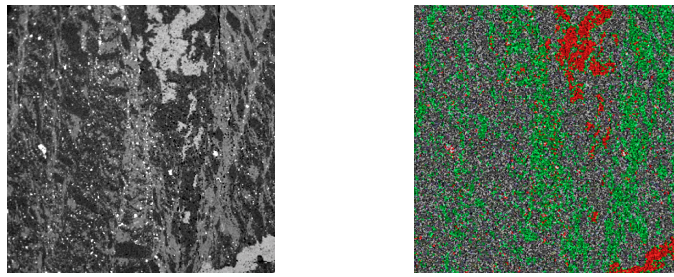

(a) (b)

Figure 4.27: (a) Microscopic image of Carboli rock, and (b) reconstructed domain in LEM using the image processing (Sattari et al. 2017)

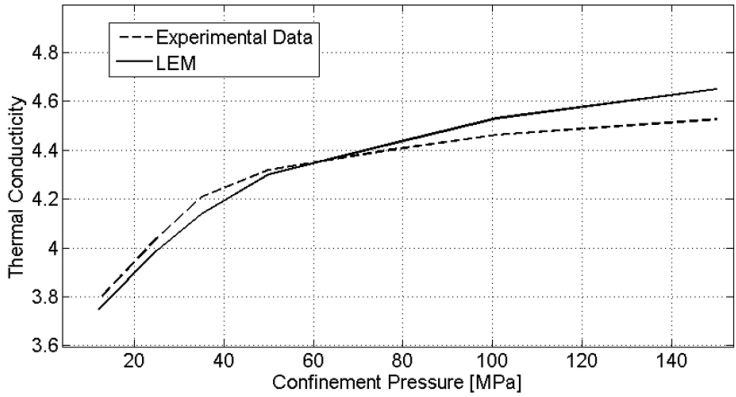

Figure 4.28: Carboli rock: The comparison of ETC obtained from LEM and experiments (Sattari et al. 2017)

results provided in Fig. 4.25b, Fig.4.26b, and Fig.4.28 are believed to be due to: (a) the closure of existing voids and micro-cracks at lower pressures, and (b) the development of new micro cracks at higher pressures.

Similarly, the effect of thermal loading, while keeping the mechanical hydrostatic pressure constant at 200 [MPa], on the initiation and propagation of the fracture, as well as the change in effective thermal conductivity, is studied. The novel interface lattice model discussed in Sec.3.4.2

is considered for the simulations. The rock sample selected for this study is Quartz (Fig.4.25a). In the true triaxial apparatus, the temperature is increased from 20°C to 600°C and the constant confinement pressure (σ_c) is applied from the surroundings. When a lattice element exceeds its strength threshold, the heat conduction between two solid cells is broken, therefore, the thermal conductivity of λ_{air}=0.02 [$Wm^{-1}K^{-1}$] is assigned to the removed elements. According to the results, the effective thermal conductivity decreases with the temperature rise. This is mainly due to the expansion of the medium, re-opening, or initiation of the micro-cracks in the domain. According to Fig.4.29a, it is clear that by increasing the temperature from 400°C to 600°C the generated cracks result in the cooler region in the center of the domain compared to the outer boundaries. The diameter of this cooler region at 600°C is greater than 400°C. According to Fig.4.29b, the main drop in ETC occurred when the temperature was raised to 400°C, which is in agreement with the propagation of fractures developed in the domain.

4.2.5 Summary

In order to study the effect of the confinement pressure on the change in effective thermal conductivity, the experimental data of three rock samples are considered. In these setups, the confinement pressure in the triaxial setup is gradually increased, and the temperature is kept constant at room temperature. In the experimental setup, the ETC is determined based on the calculation of velocities of P- and S-waves. After comparison of the LEM results with the experimental data, the following outcomes are interpreted: (a) In a homogeneous quartz rock, the LEM was able to determine the ETC with high accuracy, (b) increasing the heterogeneity of the medium and assigning the microscale mechanical and thermal properties to lattice elements decreases the accuracy of the method, (c) the lack of microscopic images and use of random distribution of properties increase the simulation error, and (d) at lower pressures, the measured ETC with LEM is underestimated, and at higher pressures, the results are overestimated. The proposed LEM is capable of simulating heat transfer in cemented geomaterials. The results indicate the importance of microscale properties, which are needed for microscale models, such as lattice or discrete element methods.

The developed interface lattice element method was able to predict the change in effective thermal conductivity as a result of coupled TM processes. The interface lattice model is able to capture the stress-strain response of rocks subjected to coupled processes. The simulation results are in great agreement with the experimental results obtained from the multi-anvil apparatus in the laboratory of CAU Kiel. It is shown that, by increasing the temperature and keeping the mechanical pressure constant, the effective thermal conductivity decreases. This is due to the development of microcracks as well as the expansion of volume in the medium. On the contrary, with increasing confinement pressure and keeping the temperature constant at room temperature, the effective thermal conductivity increases. The closure of microcracks

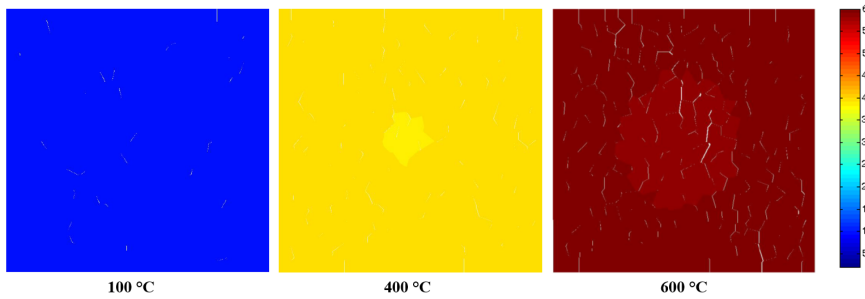

(a)

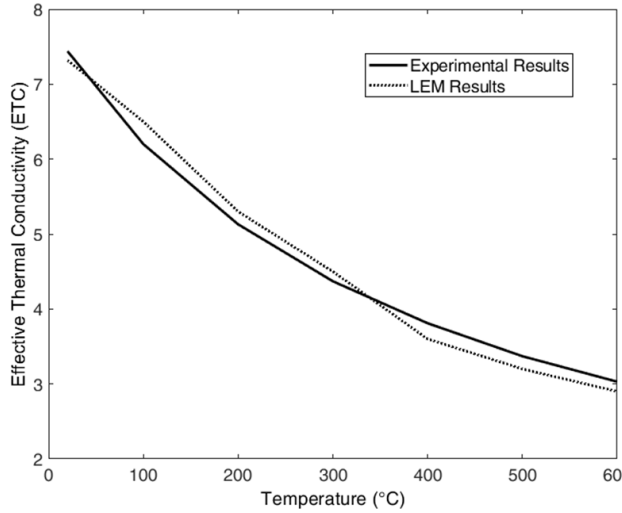

(b)

Figure 4.29: (a) Heat transport and developed fractures under different temperatures (100°C, 400°C, 600°C), and (c) comparison of the ETC obtained from LEM and experiments under the constant confinement pressure of 200 [MPa] (Sattari et al. 2019)

and improved contact quality in the inter-particle domain contributes to this material behavior under TM processes.

4.3 Application of HM lattice model to simulate the fluid transport

4.3.1 Introduction

In this section, the simulation of fluid flow in geomaterial as well as the application of the Hydro-Mechanical lattice model to simulate the crack propagation in solids are presented. First, the developed dual-lattice scheme (Sect.3.6.2) is validated according to analytical solutions that exist in the literature. Here, the planar fluid flow as well as the transient fluid flow through the pre-defined discontinuity, are simulated. Finally, the evolution of effective stresses during the hydraulic fracking process in cemented geomaterial is simulated. The hydraulic fracturing technique introduces fractures that improve the flow of petroleum products from reservoirs (Koplos et al. 2014). To study hydraulic fracking in geomaterials, three case studies with considered different boundary conditions are examined.

4.3.2 Validation of the flow model

The dual-lattice model can simulate the flow through the dedicated conduit elements. The governing parameter to simulate the flow is the defined hydraulic aperture (a_f) as shown in Eq.3.84. The calibration of the hydraulic aperture representing the flow channels (discontinuities) is carried out by simulating the 2D planar flow. The adopted boundary conditions for the simple permeability test are provided in Fig.4.30. The model has a dimension of 0.15×0.04 [m] (LxW), which is discretized with the dual-lattice model. The total number of mechanical lattice elements is 17621. The initial hydraulic aperture (a_0) is assumed to be 0.0001 [m]. The prescribed pressure values on the boundaries are $P_A = 2$ and $P_B = 1$ [MPa]. The simulation is aborted when a steady condition is reached. The qualitative flow profile obtained from the lattice simulation is provided in Fig.4.31a. The results indicate the linear change of the fluid pressure along the domain length. The quantitative development of the change in fluid pressure along the length is presented in Fig.4.31b. The hydraulic properties of the domain are a function of the pre-assumed a_0 value. In contrast to the FDEM simulations, in LEM, the hydraulic aperture is a stand-alone parameter separated from the finite element size (Lisjak et al. 2017). In the second setup, the stationary radial flow developed inside the pressurized hole is simulated for a permeable domain, and the results are compared to the analytical solution (Laplace's equation in 2D (Saudi 2022)). With the assumption of constant pressures at the inner (P_i) and outer boundaries P_o, the fluid pressure distribution is a function of the radial distance (r) from the center of the inner hole.

$$P(r) = P_i + \frac{P_o - P_i}{\ln(\frac{r_o}{r_i})} \ln(\frac{r}{r_i}), \tag{4.5}$$

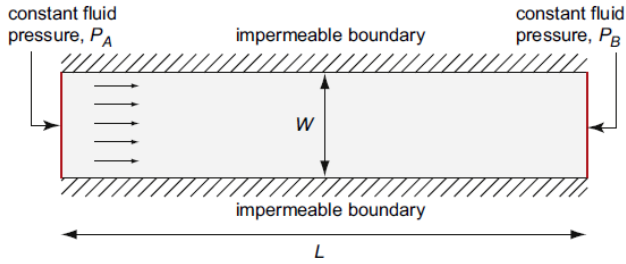

Figure 4.30: Considered boundary conditions and geometry of 2D planar flow (Lisjak et al. 2017)

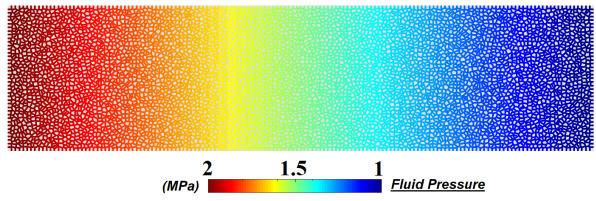

(a)

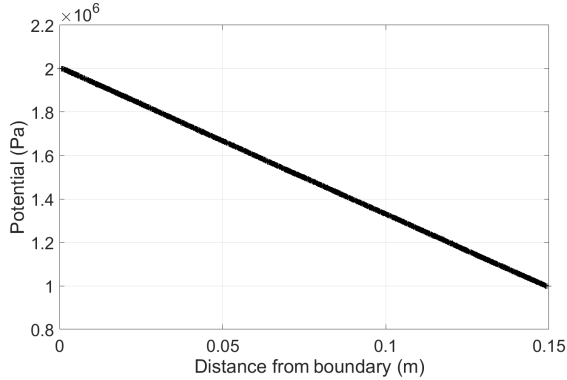

(b)

Figure 4.31: (a) Qualitative linear fluid pressure evolution within the generated conduit elements, and (b) quantitative representation of the results illustrating the fluid potential vs. distance from source

where r_o and r_i are the outer and inner radii, respectively. The geometry and boundary condition of the disc are shown in Fig.4.32. The inner and outer radii are assumed to be 0.05 and 0.5 [m], respectively. The fluid potentials applied at the inner and outer boundaries are 2 and 1 [MPa], respectively. Similarly to the previous setup, the initial hydraulic aperture (a_0) is assumed to be

0.0001 [m]. Fluid viscosity is set to 1.0004×10^{-6}. In this example, the total number of conduit elements generated is 119176.

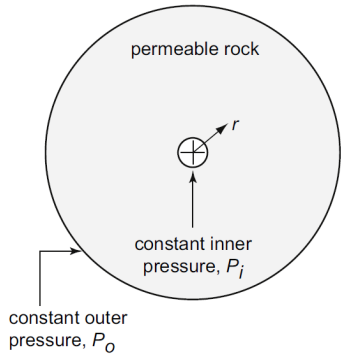

Figure 4.32: Considered boundary conditions and geometry of the pressurized hole with radial flow (Lisjak et al. 2017)

The qualitative result of the dual lattice simulation is depicted in Fig.4.33a. The result projects the radial pressure distribution from the inner hole toward the outer surface. The quantitative comparison between the lattice result and the analytical solution is provided in Fig.4.33b. Once again, the results imply the great accuracy of the lattice model.

The final setup studies the transient fluid flow through the pre-defined discontinuity along the domain length with a constant and uniform hydraulic aperture. Geometry and assigned boundary conditions are provided in Fig.4.34. The left boundary is subjected to a constant fluid pressure of $P_A = 5$ [MPa], where the right boundary is impermeable. The rock is also assumed to be impermeable, allowing the flow only along the pre-defined fracture. The analytical solution to the 1D flow problem with the assigned boundary conditions is (Poirier and Geiger 2016),

$$P = P_A \cdot (1 + \frac{4}{\pi} \sum_{n=0}^{\infty} e^{(-2n+1)^2 \frac{T^d \pi^2}{4}} \cdot cos(\frac{(2n+1)\pi\xi}{2})(\frac{-1^{(n+1)}}{2n+1})), \tag{4.6}$$

where $\xi = \frac{1-x}{L}$ and T^d is a dimensionless time expressed as

$$T^d = \frac{K_f(\frac{a_f^2}{12\mu_f})t}{L^2} \tag{4.7}$$

The hydraulic properties given as input parameters of the model are the fluid bulk modulus ($K_f = 2.2$ [GPa]), dynamic viscosity ($\mu_f = 10^{-3}$ [Pa.s]) and initial hydraulic aperture ($a_0 = 10^{-5}$ [m]). The quantitative comparison between the dual lattice model and the analytical solution is provided in Fig.4.35. The results illustrate the evolution of the fluid pressure at

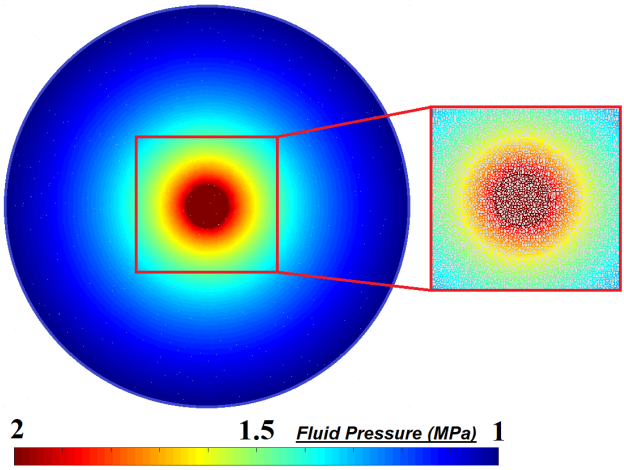

(a)

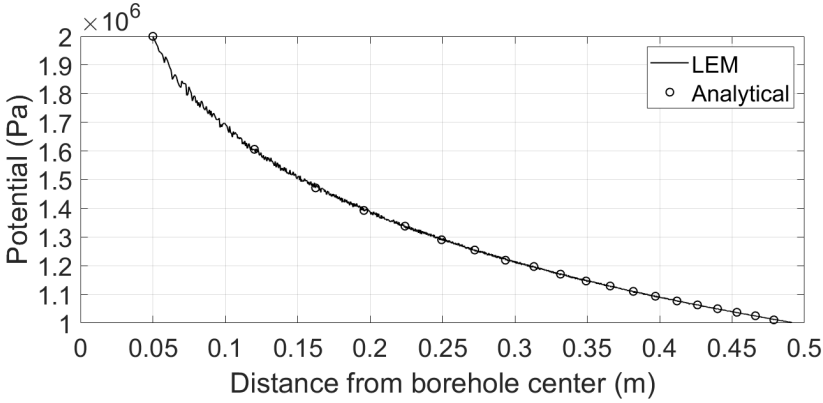

(b)

Figure 4.33: (a) Qualitative pressure distribution along the radius of the disc, and (b) quantitative representation of the results illustrating the fluid potential vs. distance from borehole center

five reference points (A-E) as the fluid flows through the discontinuity. The great agreement between numerical and analytical results has been observed.

4.3.3 Evolution of effective stress during hydraulic fracking

Due to the heterogeneous structure of the rocks, simulation of fracture initiation and propagation is a significantly complicated process, and understanding how these fractures can affect stiffness and eventually alter the stress-strain behavior is indispensable. In many geotechnical

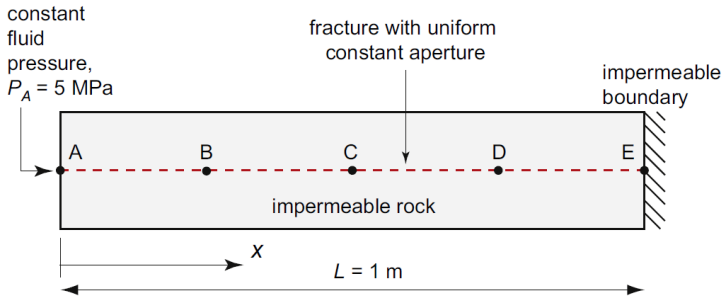

Figure 4.34: Considered boundary conditions and geometry of the impermeable rock with a pre-defined discontinuity (Lisjak et al. 2017)

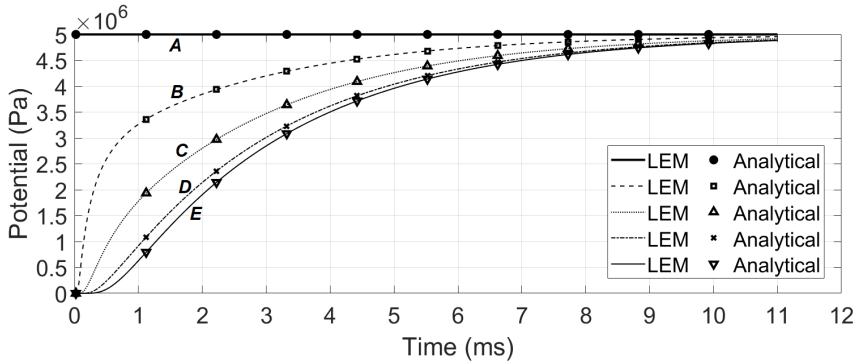

Figure 4.35: The comparison of the numerical and analytical solutions for an impermeable rock with a pre-defined discontinuity

engineering applications, such as rock mining and tunneling, the utilization of natural resources such as enhanced geothermal systems or the execution of hydraulic fracturing with pressurized liquid, the fracture process due to coupled THM stresses can cause severe damage or decrease the efficiency of the designed structure (Bazant 2003). The development of micro-cracks in quasi-brittle rock material leads to a meso- and macroscale crack progression, degrading the overall stiffness and material strength. The failure mechanism of quasi-brittle heterogeneous geomaterials, such as rock, concrete, or ceramics, is associated with complicated failure modes and is biased due to their anisotropic micro-structure characteristic.

This study presents the application of the HM lattice model to model the evolution of effective stress during the hydraulic fracking process. Therefore, hydraulic fracturing in homogeneous porous rock with a porosity of 1% is evaluated. The input parameters for the mechanical and hydraulic properties are given in Tab.4.10. The domain is discretized into 6400 Voronoi cells,

$\alpha_r = 0.6$, and the softening ratio is $S = 2$. The adopted boundary conditions for three different case studies are as follows:

- **Case 1** An isotropic confinement pressure from the boundaries of the domain ($\sigma_V = \sigma_H$) that mimics a hydrostatic stress condition (Fig.4.36a). Fluid pressure (σ_h) is applied at the center in the form of a circular hole in a radially outward direction. The rotation in the boundaries is not modeled and is assumed to be fixed. The initial fluid pressure of 1 [MPa] is applied in the central hole and gradually increases. However, the isotropic confinement pressure at the boundaries is kept constant at 1 [MPa].

- **Case 2** For the second case, the lateral confinement pressure is assumed to be half of the vertical pressure ($\sigma_V = 2\sigma_H$) (Fig.4.36a). The exact boundary conditions as in Case 1 are applied. The lateral confinement pressure is reduced to 0.5 [MPa].

- **Case 3** For the last case, a bedrock is considered. The lateral confinement pressure is assumed to be half the normal pressure ($\sigma_V = 2\sigma_H$), and all displacements in the lower boundary of the domain are prohibited to simulate the rigidity condition of the bedrock (Fig.4.36b). The applied lateral confinement pressure is assumed to be 0.5 [MPa].

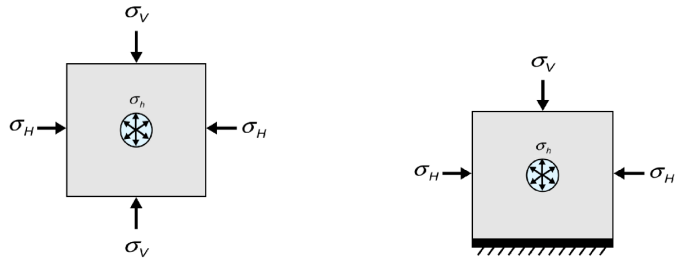

Figure 4.36: The adopted boundary conditions for a) case study 1 and 2, and b) case study 3

Table 4.10: Considered HM properties for the simulation of hydraulic fracking

E [GPa]	ν	σ_t [MPa]	σ_s [MPa]	K_f [GPa]	a_f [m]	ν_f [m/s^2]
30	0.15	18	12.6	2	10^{-5}	1×10^{-6}

The fluid pressure inside the borehole is gradually increased in the radial direction. For the evaluation of stress in the domain, eight lattice elements, as shown in Fig.4.37 are monitored. Air pressure and compression failure (crushing of particles) are both neglected, and failures among elements are predominated by Mode I failure (tensile failure). As an element exceeds

its failure threshold, the element is removed and the deformations are projected onto the hydraulic model. This allows for the percolation of the pressurized fluid inside the porous medium.

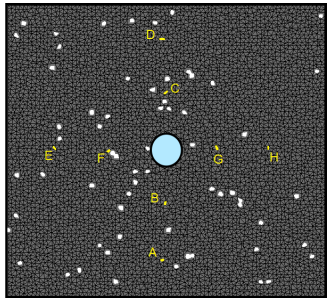

Figure 4.37: The simulated domain with selected eight reference elements (yellow) for data logging

For the 1^{st} case, Fig.4.38 depicts the propagation of the fracture in the discretized domain. Due to the boundary conditions considered, the development of fractures along the X (horizontal) and Z (vertical) axes is observed. Fig.4.39 illustrates the change of the effective stresses on the pre-selected reference elements. The fracture captured in elements H, F, and G is due to the Mode I failure (tensile (-) and compression (+)). On the contrary, Mode II failure in element B is detected.

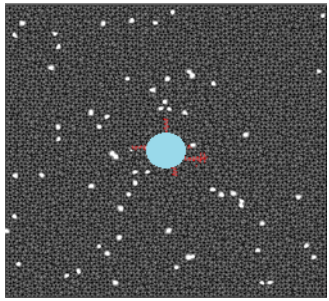

Figure 4.38: Case 1: Fracking of the domain with the increment of the borehole pressure at $\sigma_h = 26$ [MPa]

The fracking of the domain for the 2^{nd} case is shown in Fig.4.40. Due to the boundary condition considered ($\sigma_V = 2\sigma_H$), the development of fractures along the Z (vertical) axis is observed. The propagation of the crack is observed in the direction perpendicular to the minimum principal stress (σ_H) (Sakaue et al. 2007). According to the quantitative data detected in the reference elements (Fig.4.41), the effective stress change in horizontal orientation was negligi-

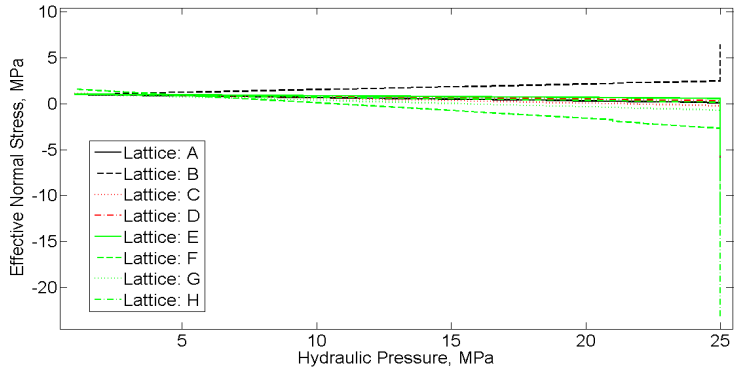

(a)

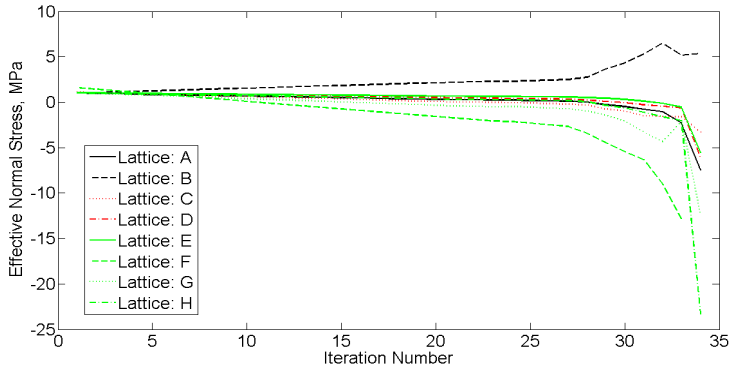

(b)

Figure 4.39: Case 1: The evolution of the effective normal stress vs. (a) borehole pressure, and (b) the model iteration number

ble (green lines). The failure of the element is once again due to the Mode I fracture mechanism.

The result of case study 3 is similar to the frack propagation profile captured in case 2, where the development of fractures along the Z (vertical) axis is observed (Fig.4.42). The bedrock considered in Case 3 allows the crack mouth to open in the perpendicular direction of the applied minimum principal stress (σ_H). Once again, the quantitative data shown in Fig.4.43 depicts the negligible change in the effective stresses along the horizontal axis (green lines). Here, the failure of the element is once again due to the Mode I fracture mechanism.

Fig.4.44 presents the effective normal stresses developed with increasing borehole pressure in the discretized domain (case 3). The location and concentration of stress around the borehole cavity, as well as the fracture tip (FPZ), are distinguishable. With the propagation of the fracture

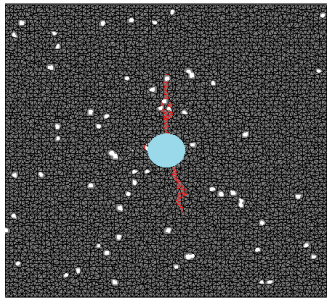

Figure 4.40: Case 2; Fracking of the domain with the increment of the borehole pressure at $\sigma_h = 23$ [MPa]

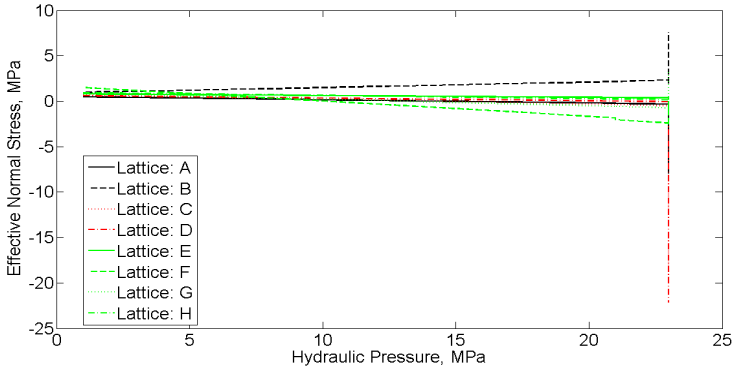

(a)

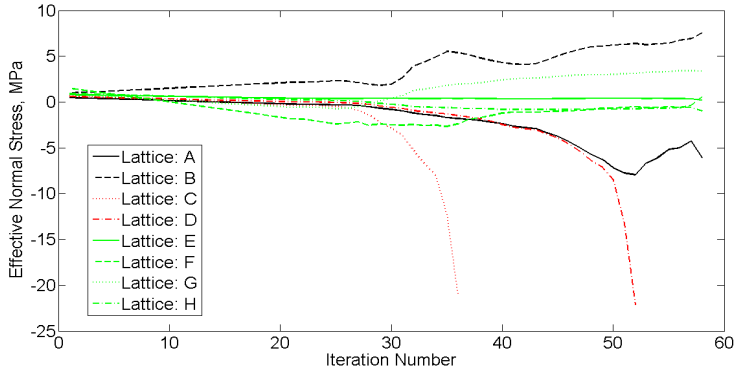

(b)

Figure 4.41: Case 2: The evolution of the effective normal stress vs. (a) borehole pressure, and (b) the model iteration number

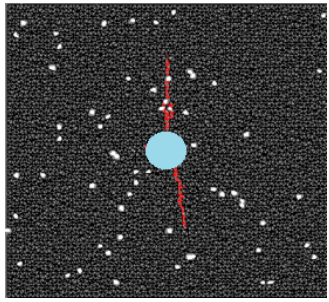

Figure 4.42: Case 3: Fracking of the domain with the increment of the borehole pressure at $\sigma_h = 23$ [MPa]

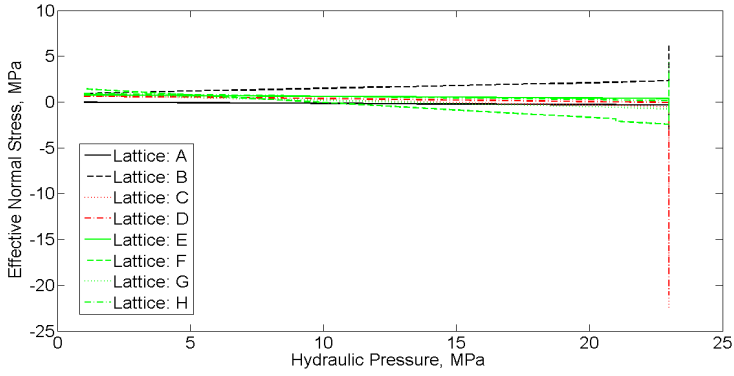

(a)

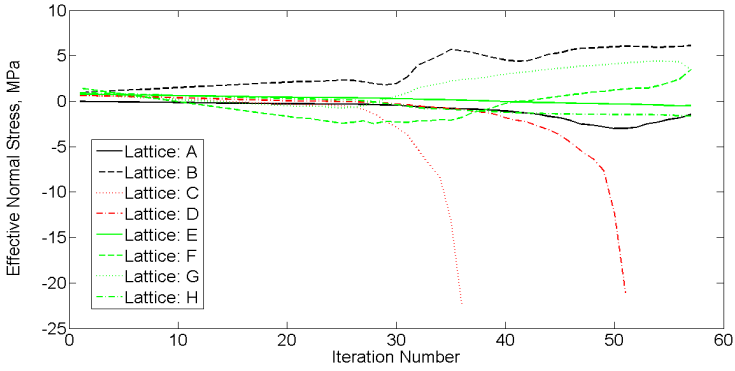

(b)

Figure 4.43: Case 3: The evolution of the effective normal stress vs. (a) borehole pressure, and (b) the model iteration number

and the development of fluid pressure in cracked paths, the effective stress distribution of the structure is distorted. The LEM is able to effectively model crack initiation and propagation, as well as the evolution of effective stress during the fracking process.

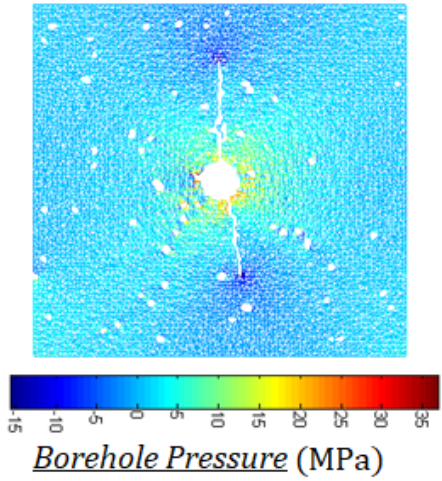

Figure 4.44: Case 3: The stress localization and concentration around the cavities and crack tip $\sigma_h = 23$ [MPa]

4.3.4 Summary

In this study, the developed HM lattice model is used to model the fluid flow in the permeable domain to calibrate the hydraulic aperture. Validation of the numerical model is conducted with comparison of the results with the analytical solutions. The great agreement between the numerical and analytical results has been observed. Moreover, the 2D model is used to simulate the change of effective stresses in the discretized domain under three different boundary conditions. According to the results: (a) the crack opening is observed in the perpendicular direction of the applied minimum principal stress (σ_H), (b) the stress concentration around the cavities and the tip of the fracture is detected, and (c) during hydraulic fracking, the Mode I failure mechanism is dominant. The application of a 3D HM lattice model to simulate pressure-driven percolation in solids is presented in Sec.5.3.

4.4 Simulation of wave propagation in geomaterial using dynamicLEM

4.4.1 Introduction

The application of the lattice element method is extended in dynamic structural analysis to tackle the effect of discontinuities and inherent material heterogeneities on wave field scattering and distortion. The inherent mesh irregularity of the lattice element and accurate fracking process realization make the model suitable for the simulation of discontinuities under expected small deformations. First, the validation benchmark is presented, and the dynamic lattice results for a 2D domain are compared to the analytical and boundary element method (BEM) solutions. Within that benchmark, the dynamic structural behaviors are compared in the frequency domain to demonstrate the method's accuracy. To show the influence of discontinuities, a series of full-wavefield simulations are performed and analyzed. The realization of the wave types, the wave field scattering, and dispersion at heterogeneities, as well as the development of the wave field shadows around discontinuities illustrate the excellent ability of the new dynamic method and its future applications in structural dynamics and structural health monitoring. The contents of this section are published by Sattari et al. (2022) under the title *"Study of wave propagation in discontinuous and heterogeneous media with the dynamic lattice method"*.

4.4.2 Validation benchmark

The validation of the dynamic lattice method is performed by a comparison of the results obtained from the presented dynamic lattice method with the solution of the Boundary Element Method (BEM) for an elastodynamic problem. The benchmark considered here is a plane P-SV-wave propagation within a plane strain domain. The analytical solution for the one-dimensional shear wave propagation problem can be easily obtained (Dominguez 1993). In the example presented, the domain is homogeneous. The BEM is solved according to the boundary integral equation method (BIEM) and with the use of a collocation procedure (Dominguez 1993):

$$c_{lk}u_k(x,\omega) = \int_\Gamma U^*_{lk}(x,\xi,\omega)\ t_k(\xi,\omega)d\Gamma - \int_\Gamma T^*_{lk}(x,\xi,\omega)\ u_k(\xi,\omega)d\Gamma. \tag{4.8}$$

Here, ω is the circular frequency; x, ξ are the coordinates of the source and receiver; U^*, T^* are the elastodynamic fundamental solutions for displacement and traction, respectively; t is the traction acting on the domain boundary Γ; and c is the jump-term which depends on the geometry of the source point. The detailed BEM solution is presented in Sattari et al. (2022). The geometry of the benchmark problem is a square with dimensions of 6×6 [m] (Fig.4.45). The properties of the material are as follows: shear modulus G= 10^6 [N/m^2], density ρ=100 [kg/m^2], damping ratio 5% and Poisson's ratio ν=0.25. The prescribed boundary conditions are defined as: (a) zero perpendicular displacement on the bottom boundary, (b) zero transverse

displacement on the side boundaries, and (c) applied uniform traction of 100 [N/m] on the top boundary. The BEM solution is obtained using quadratic line elements. An analytical solution of the resonance frequencies is given for discrete frequencies as follows:

$$\omega_n = (2n+1)\frac{\pi C_1}{2L}, \tag{4.9}$$

where L is the travel distance, C_1 is the velocity of the P-wave and $n = 0, 1, 2$ ..., which yields $\omega_n \approx 45.40$, 136.20, 227.00, 317.81 ... [rad/s] (Dominguez 1993).

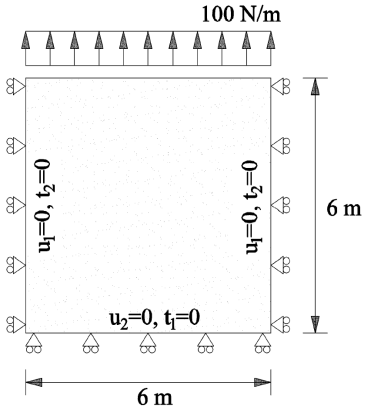

Figure 4.45: The considered plane strain boundary condition for validation of the dynamic lattice model (Sattari et al. 2022)

Using the dynamic lattice method, as described in Sec.3.7, the problem is solved in the time domain using different harmonic $sin(\omega t)$ functions. Ordinary frequencies (f_d) shifted during simulations from 1 to 50 [Hz], where the angular frequencies are equal to $2\pi f_d$. The time step (Δt) is set to $\Delta t = 1.0 \times 10^{-5}$, where the problem is solved for a duration of 1 [s]. The total number of elements generated using LEM is 10561, where the ratio of minimum wavelength (λ_l) at 50 [Hz] to element length (l) is 21. For both the dynamic lattice method and BEM, the structural dynamic responses under different circular frequencies [rad/s] are illustrated in Fig.4.46.

According to the recorded displacements at the midpoint of the upper boundary (u_{mid}) vs. circular frequency results provided in Fig.4.46, it can be concluded that the dynamicLEM solution provides accurate results, similar to the BEM solution as well as the analytical solution found in Dominguez (1993). The results of the analytical solution of the resonance frequencies (45.50, 136.20, 227.0, 317.81 [rad/s]) obtained from Eq.4.9 are also marked in this figure. The main factor that affects the accuracy of the dynamicLEM solution is the wavelength to element length ratio (Langer et al. 2017). In the conducted parametric study, it is found that when the

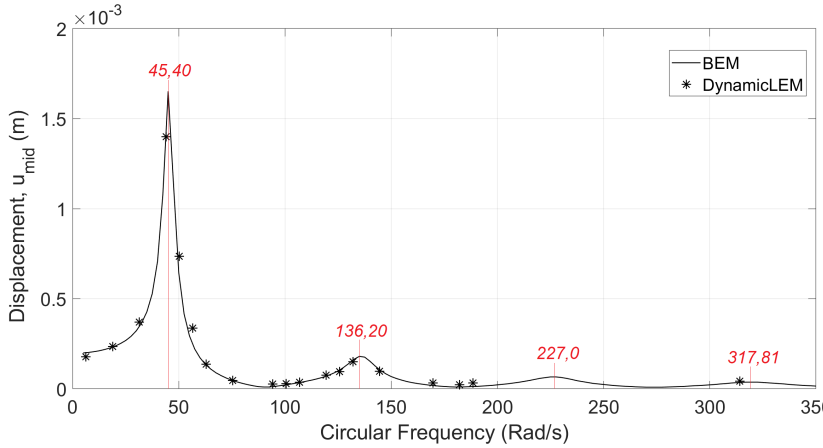

Figure 4.46: The comparison of BEM solution and dynamic lattice method results of displacements in mid-point of upper boundary (u_{mid}) under different circular frequencies (Sattari et al. 2022)

wavelength to element length ratio is kept higher than 10, the dynamicLEM solution provides accurate results.

4.4.3 Simulation framework

For the analysis of wave fields in arbitrarily damaged and heterogeneous materials, it is essential that the wave field be simulated considering all the wave fields that affect perturbations. The following essential factors can be categorized for modeling:

- Crack-dependent criteria: length, thickness, orientation, and location
- Domain-dependent criteria: characteristics and properties, such as stiffness, anisotropy, and heterogeneity factors
- Excitation-dependent criteria: source, wavelength, frequency, and magnitude
- Model dependent criteria: element length size and mesh irregularity

In this study, the following conditions that affect the disturbance of displacement wave fields are investigated: single crack orientation, multiple discontinuities, particle heterogeneity similar to a concrete body, and randomly distributed mineral heterogeneity mimicking rock geomaterials. Fig.4.47 shows the cantilever beam element generated with receiver sensors located on the outer surfaces (boundaries). Dynamic excitation is also carried out through these predefined receiver (reference) sensors. The arrival of the first and second displacement wavefronts can be measured in each receiver sensor, which can be accessed to detect discontinuities (Zima and

Kedra 2020). In all of the simulated results, the frequency considered for a single rectangular pulse is 0.2 [MHz]. Young's modulus of a homogeneous medium is assumed to be equal to 3 [GPa], where Poisson's ratio is equal to 0.2. The randomness factor of the generated mesh is 0.5. The mesh size is kept constant and equal to 800×160, where the total number of generated nodes and lattice elements are equal to 128000 and 382081, respectively. Therefore, the minimum ratio of wavelength to element length is kept as low as 22. The maximum equivalent diameter of polygonal Voronoi cells is equal to 0.125 [mm] and the damping ratio is assumed to be zero. The applied magnitude of the excitation pulse is equal to 10 [N], which is low enough to avoid any frack occurrence and propagation. Here, the Newton-Raphson Jacobian is implemented to solve the system of nonlinear equations with multiple variables as explained in Sec.3.7. Convergence is granted when the maximum error between two subsequent iterations is less than 1.0×10^{-10}. This error margin is mainly achieved after the third iteration. The simulation of the non-linear dynamic frack propagation is not in the scope of this research work.

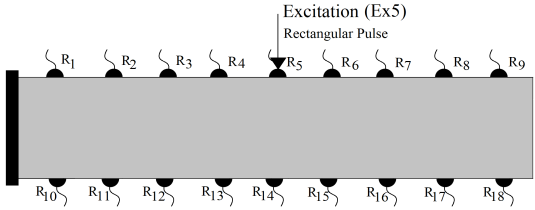

Figure 4.47: The defined excitation source and receiver sensors on a 2D cantilever beam (Sattari et al. 2022)

The natural frequency of a simulated domain depends on the effective stiffness of the continuum and the masses assigned to the Voronoi cells. In each model setup, the same mesh with similar Voronoi masses is simulated. Therefore, the natural frequency of a system (cantilever beam) only varies with the assigned different effective stiffness values.

4.4.4 Propagation of wave fields through the discontinuity

In order to investigate the disturbance of wave fields in fractured materials, a cantilever beam body as shown in Fig.4.47 is considered. Initially, three homogeneous domains with different discontinuity conditions are simulated:

- NC - homogeneous beam element with no damage
- SC1 - homogeneous beam body with predefined single crack, where the crack orientation is perpendicular to the loading direction
- SC2 - homogeneous beam body with predefined single crack, where the crack orientation builds an angle of 45° with the horizon

A single rectangular pulse is excited through receiver sensor R5 (EX5). The simulated results according to dynamicLEM are provided in Fig.4.48 and Fig.4.49. Fig.4.48 illustrates the displacement wave field through the simulated beam body (qualitative results). In these results, the P-wave, SV-wave, and Rayleigh surface waves are clearly visible and detectable. The time history of the displacements in the reference sensors (R_4, R_5, R_6, R_{13}, R_{14}, and R_{15}) are plotted in Fig.4.49 (quantitative results). The disturbance of the wave fields due to the predefined discontinuities in the SC1 and SC2 models is visible when compared to the NC model. Additionally, the arrival of the first and second wavefronts can be used to detect the location, orientation, and length of the discontinuities in the domain. The wave field covers direct, diffracted, and reflected waves around the crack within the domain. In these simulations, the time step is equal to $\Delta t = 1.0 \times 10^{-7}$. The convergence of the dynamic solution depends on the size of the assigned time interval.

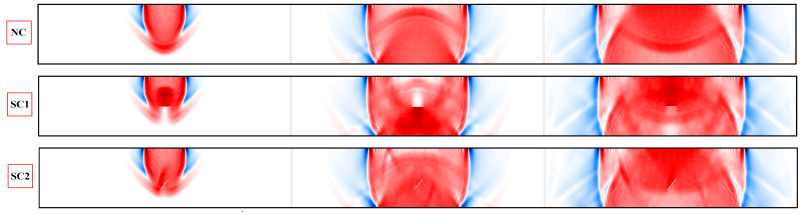

Figure 4.48: Plotted displacement wave fields in different time steps for each generated discontinuity condition: NC, SC1, and SC2 (Sattari et al. 2022)

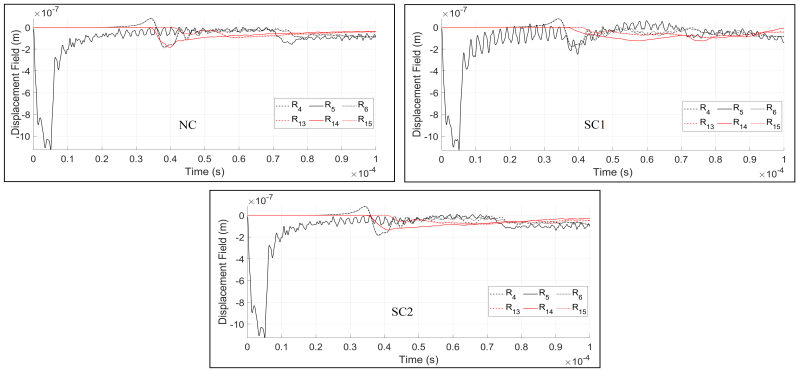

Figure 4.49: The recorded time histories at the receiver sensors under consideration of different crack conditions. Besides the direct wavefronts, the reflected and diffracted wavefronts are clearly visible by studying the different arrival times (Sattari et al. 2022)

In the next series of results, multiple predefined discontinuities are generated within the homogeneous beam element as shown in Fig.4.50. The ability of the proposed dynamic element

method to simulate even complex wave field patterns is investigated here. In the presented setup, five cracks (MC1:MC5) of different locations, lengths, and orientations are randomly generated (Fig.4.50). Three excitation positions, Ex2, Ex5, and Ex8, are used to excite the domain independently, where the wave fields at the receivers can then be analyzed. Similarly to the previous results, the qualitative and quantitative results of the simulations are presented in Fig.4.51 and Fig.4.52. Due to the higher discontinuity of the simulated domain, a greater disturbance of the wavefronts in the recorded time histories of the displacements are observed. To identify multiple discontinuities, analysis of the recorded time histories under multiple excitation sources is required. In the results provided, in addition to the excitation source, the recorded time history on the R_{11}, R_{13}, R_{14}, R_{15}, and R_{17} sensors are plotted.

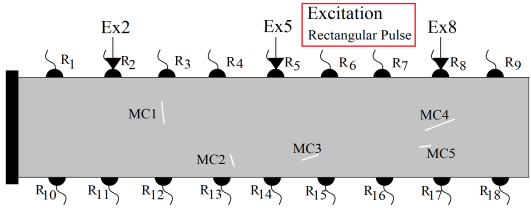

Figure 4.50: The generated random discontinuities and assigned excitation sources in R_2, R_5 and R_8 (Sattari et al. 2022)

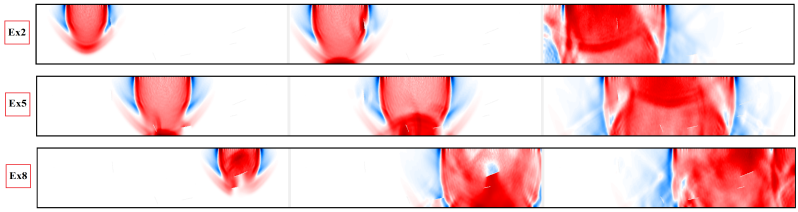

Figure 4.51: Plotted displacement wave fields in different time steps for each dynamic excitation condition: Ex2, Ex5, and Ex8. For better visualization of the wave disturbance and dispersion, the results at different time steps are plotted (Sattari et al. 2022)

4.4.5 Scattering of wave fields in heterogeneous domain

One of the main advantages of the lattice element method over conventional continuum methods is its ability to simulate discontinuities while accounting for the inherent heterogeneity and irregularities in the particle scale. Irregularities, such as shape factors, are already implemented while considering irregular meshes and the defined randomness factor. In solid geomaterials, such as concrete or rock, the domain is composed of granular particles, cement (bond material), and the bond-particle interfaces as shown in Fig.3.9. Here two different heterogeneous domains

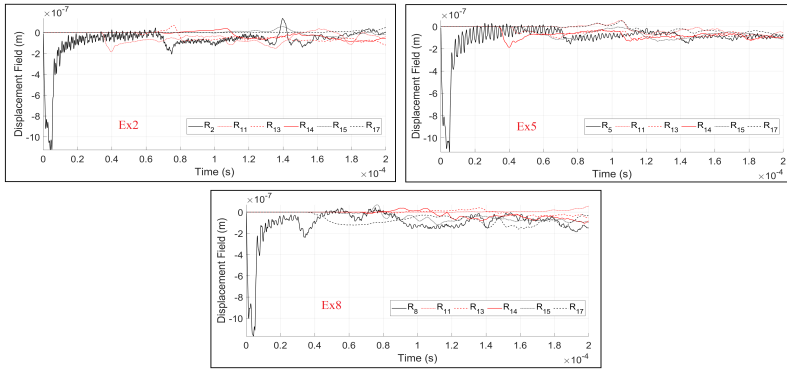

Figure 4.52: The recorded time histories at the receiver sensors (R_i) under consideration of different dynamic excitation sources: Ex2, Ex5 and Ex8 (Sattari et al. 2022)

are simulated, one similar to concrete and the other similar to rock geomaterial, to analyze and study the effect of the heterogeneity ratio on wave disturbance. As a result, not only can the effect of the heterogeneity ratio on the wave disturbance be investigated, but also the mineral cluster effect can be studied. Similar to the concrete composition, a particle packing procedure is implemented here to generate a heterogeneous domain composed of two main components: aggregates and cement matrix. A rectangular beam element with non-uniform packing and particle diameter varying from 0.5∼4 [mm] is generated as shown in Fig.4.53. The exact boundary condition as in previous setups is considered here, and the rectangular pulse with an amplitude of 10 [N] is excited from the R_5 receiver. The stiffness of aggregates (k_p), bond cement (k_b), and aggregate-bond interface (k_i) are then assigned for each corresponding lattice element. Five different heterogeneity (stiffness) ratios are simulated:

- NC - $k_p = k_b = k_i$, where $\mathrm{E}_i = 3$ [GPa]
- CH1 - $k_p = 2 \times k_b = 4 \times k_i$, where $\mathrm{E}_i = 3$ [GPa]
- CH2 - $k_p = 3 \times k_b = 30 \times k_i$, where $\mathrm{E}_i = 3$ [GPa]
- CH3 - $k_p = 5 \times k_b = 50 \times k_i$, where $\mathrm{E}_i = 3$ [GPa]
- CH4 - $k_p = 20 \times k_b = 200 \times k_i$, where $\mathrm{E}_i = 3$ [GPa]

The qualitative and quantitative results of DynamicLEM in a heterogeneous concrete body are presented in Fig.4.54 and Fig.4.55. Under the assumption of different heterogeneity ratios, the natural frequencies of the simulated domains are also affected. According to the results, the wave fields exhibit a larger diffusion and noise with an increase in the heterogeneity ratio in the domain. Due to the increased wave velocity in CH3 and CH4, the simulation time step is reduced to $\Delta t = 1.0 \times 10^{-8}$. However, the frequency is kept constant and equal to 0.2

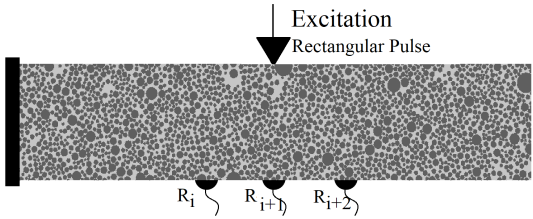

Figure 4.53: The generated concrete beam structure composed of aggregates and cement (Sattari et al. 2022)

[MHz]. The value of the time step is dependent on the domain size, the size of the elements, the frequency, and the property of the material. The assigned Δt ensures the convergence of the iteration method. The higher the difference between the stiffness of the mediums, the greater the magnitude of the reflected wave fronts. Visualization and investigation of particle scale heterogeneity behavior by ordinary continuum-based methods are not possible, which opens a new research field to study these effects in detail by means of dynamicLEM.

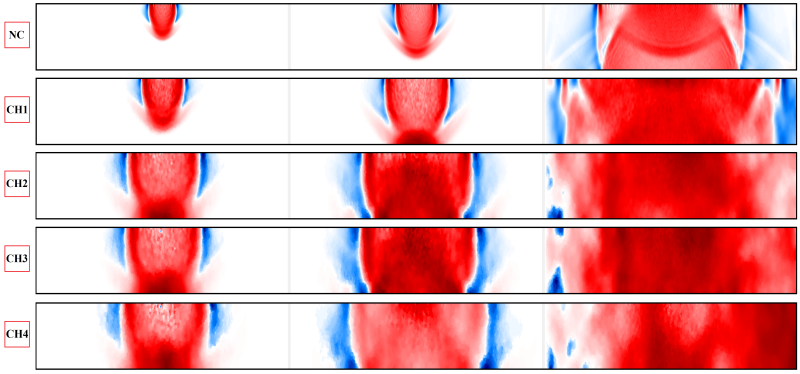

Figure 4.54: Plotted displacement wave fields in the same time steps (2, 3 and 10 $\times 10^{-5}$ [s]) and different heterogeneity ratios in concrete beam body: NC, CH1, CH2, CH3, and CH4 (Sattari et al. 2022)

As a follow-up, qualitative and quantitative analyses of a wave field disturbance under multiple heterogeneity ratios are performed for a medium with randomly distributed heterogeneity. In this setup, a stochastic distribution of heterogeneity in each generated Voronoi cell is carried out. Therefore, instead of a cluster of cells representing a similar component as shown in the previous example, in this example, each Voronoi cell individually represents a unique mineral. The beam body without predefined discontinuities is made up of four different minerals as shown with dark blue (DB), light blue (LB), red (R), and orange (O) cells in Fig.4.56. The interface values between two minerals (i and j) are determined based on the equivalent value:

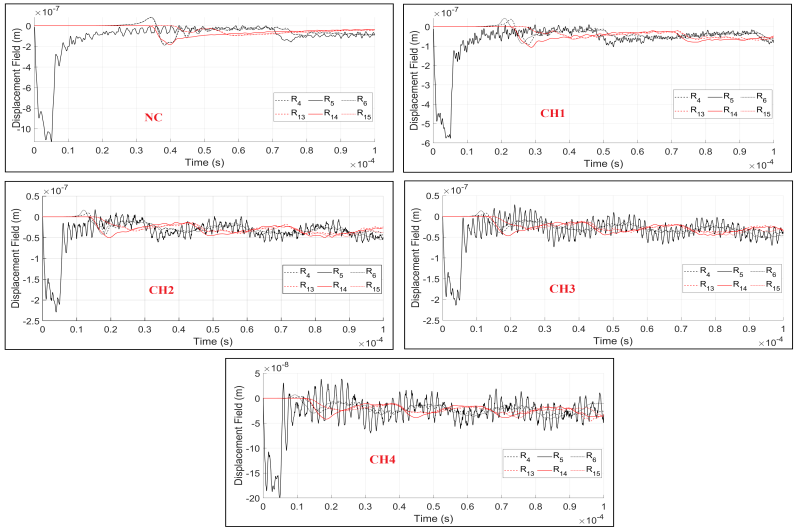

Figure 4.55: The recorded time histories at the receiver sensors (R_i) under consideration of different heterogeneity ratios in concrete beam domain: NC, CH1, CH2, CH3, and CH4 (Sattari et al. 2022)

$$\mathrm{E}_{int} = \frac{2 \times \mathrm{E}_i \times \mathrm{E}_j}{\mathrm{E}_i + \mathrm{E}_j} \tag{4.10}$$

Here, E_{int} is Young's modulus of the interface element between minerals i and j. This also highlights the importance of measuring the micro- and nanoscale THM properties in heterogeneous materials, which requires further investigation.

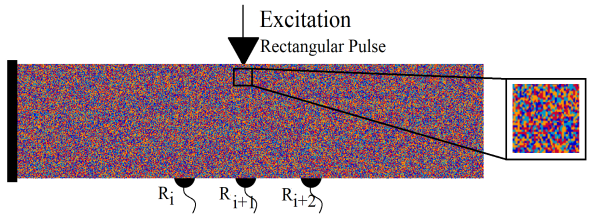

Figure 4.56: The randomly distributed heterogeneity inside the beam body to mimic a rock geomaterial (Sattari et al. 2022)

In order to investigate the effect of a heterogeneity ratio on wave fields and to determine the critical heterogeneity ratio threshold, the following ratios are considered and simulated:

- NC - homogeneous domain, where $k_{DB} = k_{LB} = k_R = k_O$

- RH1 - heterogeneous domain with two distinct minerals, where $k_{DB} = k_{LB} = 2k_R = 2k_O$
- RH2 - heterogeneous domain with two distinct minerals, where $k_{DB} = k_{LB} = 10k_R = 10k_O$
- RH3 - heterogeneous domain with four distinct minerals, where $k_{DB} = 2k_{LB} = 3.4k_R = 10k_O$
- RH4 - heterogeneous domain with two distinct minerals, where $k_{DB} = k_{LB} = 30k_R = 30k_O$
- RH5 - heterogeneous domain with two distinct minerals, where $k_{DB} = k_{LB} = 50k_R = 50k_O$
- RH6 - heterogeneous domain with two distinct minerals, where $k_{DB} = k_{LB} = 80k_R = 80k_O$
- RH7 - heterogeneous domain with four distinct minerals, where $k_{DB} = 2k_{LB} = 10k_R = 100k_O$
- RH8 - heterogeneous domain with two distinct minerals, where $k_{DB} = k_{LB} = 200k_R = 200k_O$
- RH9 - heterogeneous domain with four distinct minerals, where $k_{DB} = 2k_{LB} = 40k_R = 200k_O$

Similarly to the previous setup, a single rectangular pulse is excited through the R5 reference point (Ex5). With increasing wave velocities, the time step is decreased to grant the convergence of the numerical solution. Therefore, the simulation time step is reduced to $\Delta t = 1.0 \times 10^{-8}$, where the frequency is kept constant and equal to 0.2 [MHz]. The quantitative and qualitative recorded displacement time histories in all of the simulation setups are presented in Fig.4.57 and Fig.4.58. In all simulations, a similar setup with the same mesh size (same masses), randomness factor, and stochastic heterogeneity is considered. The adapted effective stiffnesses of the domains result in different natural frequencies in each setup. The simulated damping ratio is equal to zero, which grants continuous vibration of the beam structure.

In addition to simulation of wave propagation under isotropic conditions, the dynamicLEM is able to simulate wave vibrations in anisotropic media. Based on the results presented for both concrete and rock-type geomaterials, it can be concluded that

- Increasing the heterogeneity of the stiffness between the particle, the bond matrix, and the aggregate-cement interface induces excessive disruption on the wavefronts. The magnitude of the reflected wave fronts increases when the stiffness ratio is increased. The recorded and plotted data depend on the natural frequency of a beam structure. In all the setups presented for a concrete body, the assigned masses (generated mesh) on Voronoi cells are constant. With increasing stiffness of a domain, the wave velocity also increases. Although the increase in the heterogeneity ratio produces wave dispersion in the concrete body, the evaluation of the outcomes based on the arrival of P- and SV- waves is still possible.

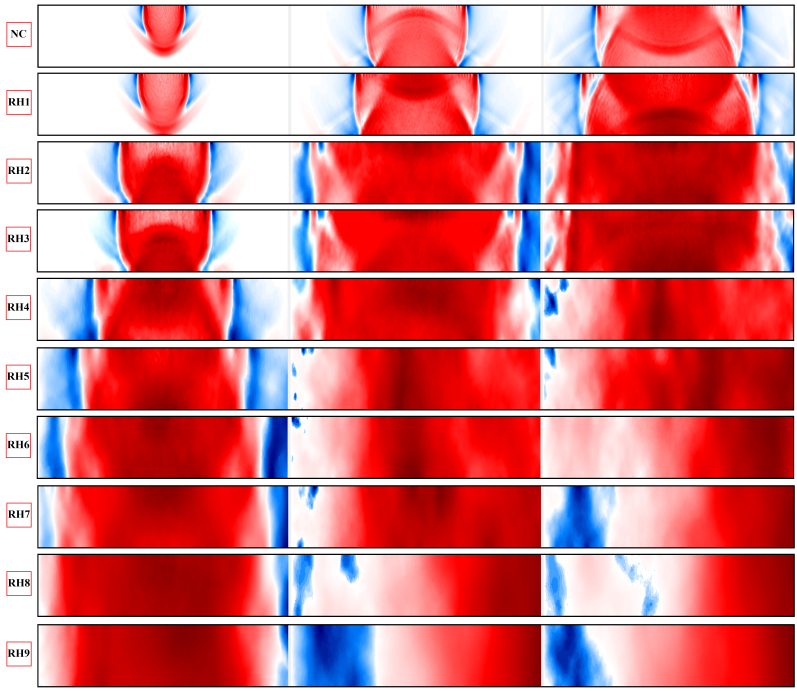

Figure 4.57: Plotted displacement wave fields in the same time steps (3, 7 and 10 $\times 10^{-5}$ [s]) and different heterogeneity ratios in the rock domain: NC, RH1:RH9 (Sattari et al. 2022)

- In a rock domain, the effect of heterogeneity ratios as well as the number of minerals on wave disturbance is analyzed. Similar to the concrete body, increasing the stiffness heterogeneity induces excessive disruption on the wavefronts. In contrast to the concrete body, after a certain stiffness heterogeneity ratio, evaluation of the outcomes based on the arrival of P- and SV- waves is not possible. This is clearly visible from the plotted time histories, starting from RH5, where at around $t = 0.9 \times 10^{-4}$ the accumulated noise disrupts the wavefronts.

- The total number of minerals in a rock domain has an effect on the disturbance of the wavefronts. This is clearly distinguishable when comparing the RH8 and RH9 results, where the maximum stiffness heterogeneity ratio is equal to 200. In RH8, the disturbance of the wave fronts starts at $t = 0.45 \times 10^{-4}$, where in RH9, the wave dispersion begins at $t = 0.4 \times 10^{-4}$. It should be noted that the natural frequencies of these domains are not equal, which can also induce different vibration responses. The results clearly show that increasing the number of minerals induces a larger disturbance on the wavefronts.

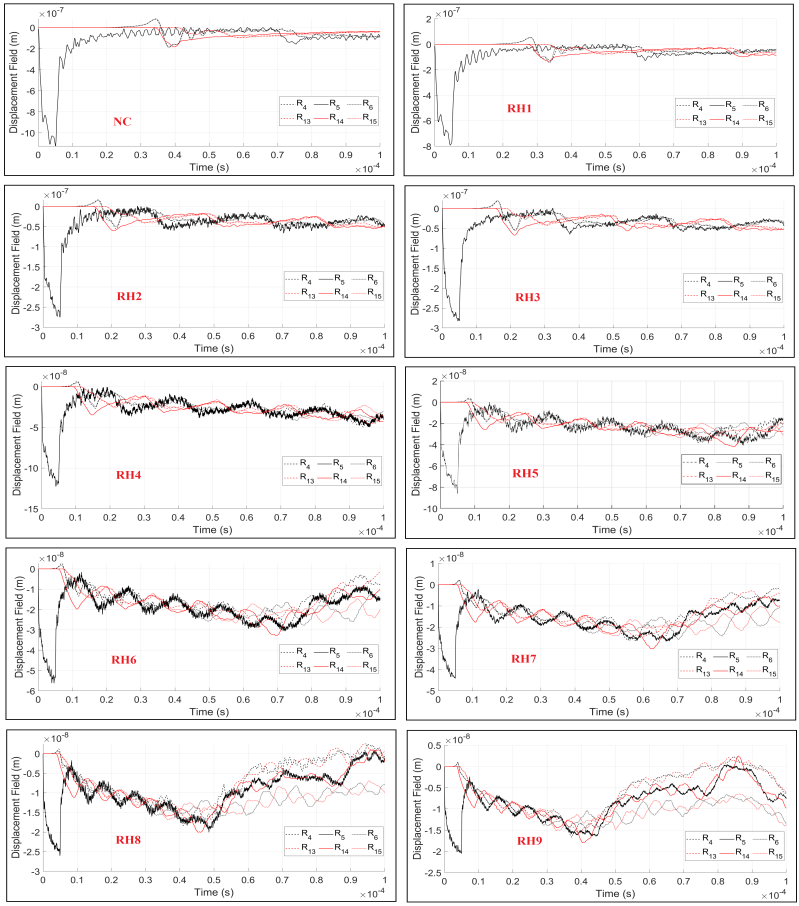

Figure 4.58: The recorded time histories at the receiver sensors (R_i) under consideration of different heterogeneity ratios in rock domain: NC, RH1:RH9 (Sattari et al. 2022)

- When comparing the rock and concrete bodies, it is clear that in a heterogeneous rock body with a similar stiffness heterogeneity ratio, the wave dispersion and scattering are higher. In contrast to CH4, in RH9, where in both setups the maximum stiffness heterogeneity ratio is equal to 200, the evaluation of the arrival of P- and SV- waves is not possible. This again emphasizes the importance of considering the inherent heterogeneity in numerical simulations. The identification of discontinuities based on the arrival of first and second P- and S- waves will then be a challenging task, which requires further investigation.

- A small stiffness transition zone (mineral to mineral) produces a larger variation of P- and S- wave velocities, which leads to larger reflections and dispersion of waves. Increasing the thickness of the transition zone (cluster of minerals) results in a gradual variation of seismic velocities. This also reduces the energy of reflected and diffracted waves, which eventually has less impact on the disturbance of wavefronts.

4.4.6 Summary

The advantage of dynamic lattice in the displacement wave field simulation lies in its embedded irregularity in domain discretization, its ability to define discontinuities and particle heterogeneity, simulate crack initiation and propagation, and the stress redistribution and concentration upon crack propagation. Similar to discrete methods, the lattice method also considers the inherent heterogeneity in the particle scale. Here, the developed dynamicLEM is used to simulate displacement wave fields in heterogeneous concrete and rock geomaterials. The results indicate that, by increasing the maximum heterogeneity ratio (stiffness ratio), the disturbance of wave fields becomes greater. After a certain heterogeneity threshold, the quantitative evaluation of dynamic results with conventional methods is not possible. It is also shown that increasing the number of mineral compositions in a rock body has a considerable effect on wave field disturbance. The comparison of rock and concrete beam bodies indicates the importance of mineral distribution schemes and particle sizes in the dispersion of wavefronts. It is shown that in the same stiffness heterogeneity ratio, the reflection and diffraction of waves in a rock domain (individual mineral distribution) are stronger than in a concrete domain, where a cluster of Voronoi cells represents an individual aggregate. The results cohere with the theory, where a small stiffness transition zone (mineral-to-mineral) produces a larger variety of P- and SV- wave velocities compared to a larger transition zone (cluster of minerals). The simulations are performed on a Desktop-PC with a Xeon processor (2.10 GHz) with a total number of 16 cores, and the computational time for a single simulation is approximately 24 hours. In the developed explicit algorithm, parallel computing is partially implemented. However, the main solver depends on the performance of a single core. For large-scale simulations, parallelization and optimization of the developed algorithm are essential.

The dynamic lattice element is capable of modeling the wave field's disturbance and dispersion when discontinuity and heterogeneity in the domain are present. Identification of discontinuities in heterogeneous materials is a challenging task, where particle-scale models similar to dynamicLEM can provide accurate outcomes. However, the simulation of large domains with high frequencies requires a substantial number of elements not only to model the particle size effect but also to reach a greater wavelength-to-elements length ratio and avoid numerical difficulties. One way to overcome this obstacle is to consider artificial neural networks (ANN) models to predict the location of discontinuities in homogeneous and heterogeneous bodies (Wuttke et al. 2021). The recorded displacement wave fields at each reference point in dynamicLEM are

considered as training data for developing an ANN method to not only decrease the computational costs but also increase the accuracy of the crack predictions. Eventually, for any given wave spectrum that can be obtained from field applications, the ANN method can predict the location, length, and orientation of the existing discontinuities.

Chapter 5

Applications of the developed lattice model in practice

5.1 Framework of engineering applications

This chapter presents the application of the developed Multiphysics lattice model in different research projects. In addition to experimental studies to investigate the geomaterial's behavior on a lab-scale, the developed numerical lattice model simulates and discusses the results from a micro- to mesoscale perspective. The mechanical lattice model, described in Sec.3.4, is used to simulate the mechanical response of geomaterials. The HM lattice model described in Sec.3.6 is implemented to simulate pressure-driven percolation in solids.

To do so, experimental results from conventional geomechanical tests, such as the three-point bending test, the splitting test, or the uniaxial confinement test, are used to calibrate the developed lattice model. Eventually, the material properties obtained from the experimental data, as well as the setup boundary conditions, are considered as the input parameters of the numerical model. The results indicate that the lattice model cannot only simulate and model complex Multiphysics problems but can also be used to evaluate the governing phenomena of such material behavior. The experimental data are used to:

- Study the lab-scale material behavior
- Calibrate the numerical solution
- Provide input properties and boundary conditions to the numerical model

On the other hand, the numerical simulations give insight into the following objectives.

- Ability of the model to simulate complex Multiphysics problems in geomaterials.
- Interpretation of experimental results

- Applicability of lattice model in large-scale simulations with micro- to macroscale transitions

5.2 Simulation of the reinforced masonry shear wall with the lattice model (ShearWall Project)

5.2.1 Introduction

In the presented study, the application of ductile and fabric-reinforced mortar to masonry shear walls under vibration and earthquake loads is studied. To improve the strength of mortar and its interface with bricks, various additives can be added to the mortar mixture (Shah and Naaman 1976, Dawood and Ramli 2011, Sevil et al. 2011). Initially, a series of experimental tests were carried out to determine the effect of different additives on the mechanical properties of the brick-mortar composition. The three-point bending and interface tests on brick and mortar mixtures give insight into the tensile and flexural strength of these materials. In addition to the experimental results, a numerical model is developed that could simulate the initiation and propagation of fractures for masonry walls under static and dynamic loadings. The mechanical lattice model developed in Chapter 3 is implemented to study and simulate fracture propagation in heterogeneous masonry walls. Initially, the back-calculation of tensile strength and Young's modulus of materials is carried out, and later, the final outputs are used to model the behavior of the masonry walls under static and dynamic shear loadings. The results presented in this section are part of a research project with the German title of *"Neuer hochduktiler, gewebeverstärkter Mörtel zur nachhaltigen Erstkonstruktion und nachträglichen Revitalisierung von Ziegel-Scherwänden in schwingungs- und erdbebengefährdeten Gebäuden"*.

5.2.2 Experimental studies and results

In order to determine the behavior of the masonry wall under static or dynamic loadings, the material response of each component of the wall on a microscale is studied. The ductility, brittleness, shear, or tensile strength of a material depends on microscale properties. The initiation and propagation of fractures in the walls of masonry occur in the weakest zone, where the stress concentration is higher. This frail zone is mainly the interface between mortar and bricks, which can be reinforced with the addition of additives, such as fibers. The main objective of conducting experimental tests on brick and mortar mixtures is to determine the material strength of each composition, which not only can provide a better understanding of their behavior under different loading conditions but also provides input parameters for the LEM, where the tensile strength and Young's modulus of materials are required. Therefore, a series of three-point bending tests, as well as an interface setup, have been conducted to determine the bond strength between different mortar mixtures and brick. Initially, the strength

of the mini bricks (Fig.5.1a), which can be obtained from a small lab-scale test, is determined. Afterward, for different mortar mixtures composed of glass fibers (Fig.5.1b) and dispersion powder (Fig.5.1c), the three-point bending test is performed. In these tests, the effect of each additive is investigated on the strength and ductility of the mortar. Finally, for an interface setup (shear test), where the strength of the bond between brick and mortar can be examined, the effect of mortar mixtures on the strength of the interface is studied. The small-scale brick sample with a dimension of 23×11×5 [mm], which is used in these tests, is made of Terracotta.

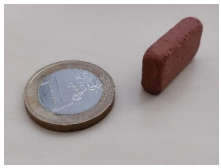

(a)

(b)

(c)

Figure 5.1: Setup compositions: (a) bricks made from Terracotta, (b) fiber glasses (PVA-(Polyvinyl alcohol)-fibers 401/6), and (c) dispersion powder (Polymer dispersion powder VINNAPAS 5010 N (Wacker Chemie))

The experimental tests are carried out using the uniaxial compression device with controlled strain rate loading. The load is gradually increased for a mini brick sample under a three-point bending test until the failure has been observed (Fig.5.2). Five series of tests have been carried out on different mini bricks, and the average load at failure was found to be 998.3 [N]. The failure of the brick sample is brittle, with a sudden loss of strength.

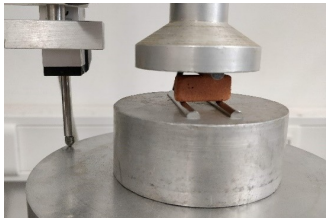

(a)

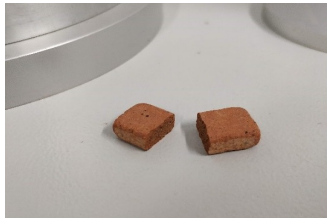

(b)

Figure 5.2: The brick under three-point bending test (a) before, and (b) after failure

The mortar mixture is composed of four components:

- Cement, Portlandkalksteinzement (Dyckerhoff Comfort CEM II/A-LL 42.5)
- Water, with water to cement ratio of 0.2 (W/C=0.2)
- Fiber glasses to increase the strength and ductility of mortar (PVA-(Polyvinylalkohol)-Fasern 401/6)

- Dispersion powder to increase the bond strength (Polymerdispersionspulver VINNAPAS 5010 N (Wacker Chemie))

With the help of Scanning Electron Microscopy (SEM), a picture of the mortar mixture after failure is captured for a three-point bending test with a 1% mass ratio of fiber glasses and is depicted in Fig.5.3a. Mortar mixtures are prepared with different ratios of mass of fiberglass and dispersion powder, ranging from 0 to 3%. Increasing the dispersion powder by more than 2% makes the mixture highly fluid (less viscosity), which makes it difficult to work on a small lab scale. The water-to-cement ratio is 0.2, which results in a strong mortar mixture. The mortar samples are cast inside plastic molds with dimensions of 120×30×15 [mm], where the plastic mold is printed with the 3D printer in the Geotechnical Laboratory of CAU Kiel. After the mortar was poured, it was cured for 28 days to reach its 99% strength. Fig.5.3 illustrates the mortar sample under vertical load applied from the upper middle boundary, as well as the path of fracture resulting after failure.

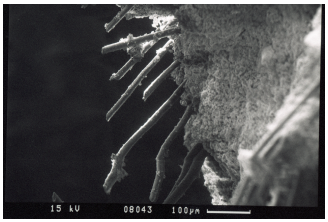

(a)

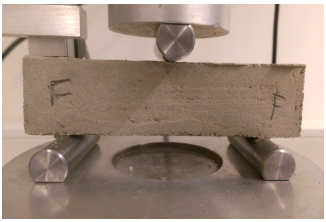

(b)

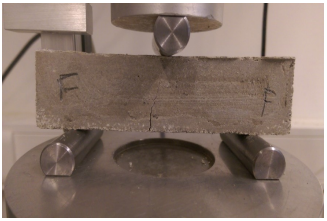

(c)

Figure 5.3: (a) Arrangement of fiber glasses inside mortar mixture after failure under three-point bending test captured with Scanning Electron Microscopy (SEM); The mortar sample under three-point bending test (b) before, and (c) after the failure

Fig.5.4 shows the maximum failure load change in each mortar mixture. For each mortar mixture, the tests are repeated at least three times to minimize the stochastic error in the results. To investigate the effect of additives on mortar ductility, load-displacement graphs for four reference mortar mixtures have been plotted (Fig.5.5). The four mortar mixtures that are further investigated are:

(a) 0% fiberglass and 0% dispersion powder

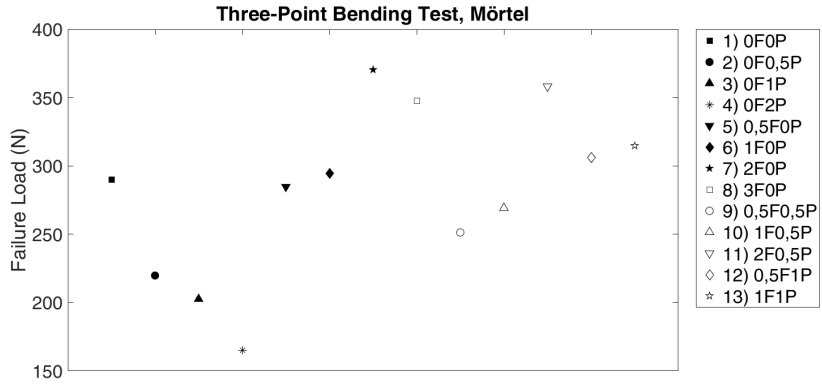

Figure 5.4: The failure load in the three-point bending test for different mortar mixtures. (Example: 1F1P stands for 1% of mass fiberglass and 1% of mass dispersion powder)

(b) 2% fiberglass and 0% dispersion powder

(c) 0% fiberglass and 2% dispersion powder

(d) 2% fiberglass and 0.5% dispersion powder

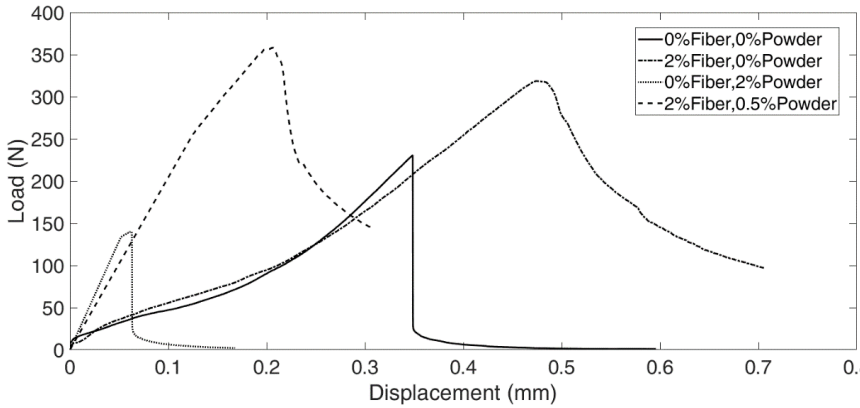

Figure 5.5: The load-displacement curve for four different mortar mixtures (a, b, c and d) under three-point bending test

After individually determining the bending strength of the brick and mortar mixtures, the interface or bond strength between the brick and mortar mixtures is investigated. To determine the strength of the interface, mini bricks are prepared with two layers of mortar mixtures between them (Fig.5.6a). After the preparation of the samples and curing them for 28 days, experimental tests (shearing test) using the uniaxial compression device are carried out (Fig.5.6b).

Fig.5.6c depicts the failed sample after the shearing test. As a result, the interface strength is determined for different bond conditions, depending on the mortar mixture. Similarly to the previous results, each experiment for each mortar mixture is repeated a minimum number of three times. The results of the failure load reached for each composition under the shear test are shown in Fig.5.7. For four reference cases (a, b, c, and d), the load-displacement curves under the shearing test are plotted and illustrated in Fig.5.8.

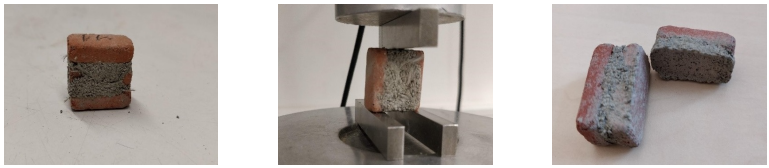

(a) (b) (c)

Figure 5.6: (a) Prepared interface setup with mortar and bricks; The interface setup under vertical load using uniaxial compression device (b) before, and (c) after failure

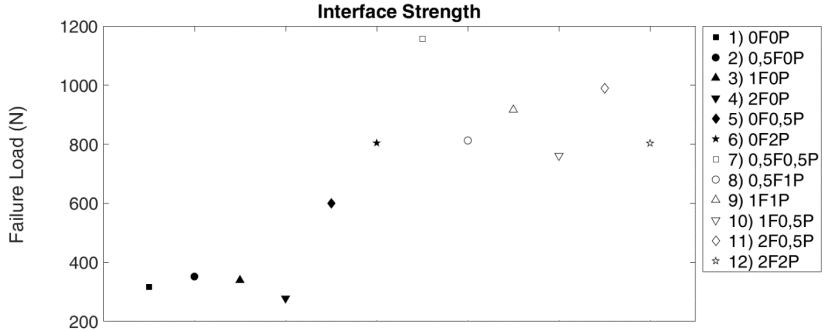

Figure 5.7: The measured failure load in the shear setup for different mortar mixtures (Example: 1F1P stands for 1% of mass fiber and 1% of mass dispersion powder)

According to the results, it is concluded that

- With the addition of dispersion powder, the strength of the mortar decreases. On the contrary, the interface strength increases.
- With the addition of fiberglass, the strength and ductility of the mortar increase. In contrast, the strength of the interface decreases.

5.2.3 Implementation of the lattice model

After the experimental tests are performed and the material properties on a lab-scale are determined, a numerical study using the lattice element method (LEM) is conducted. LEM is

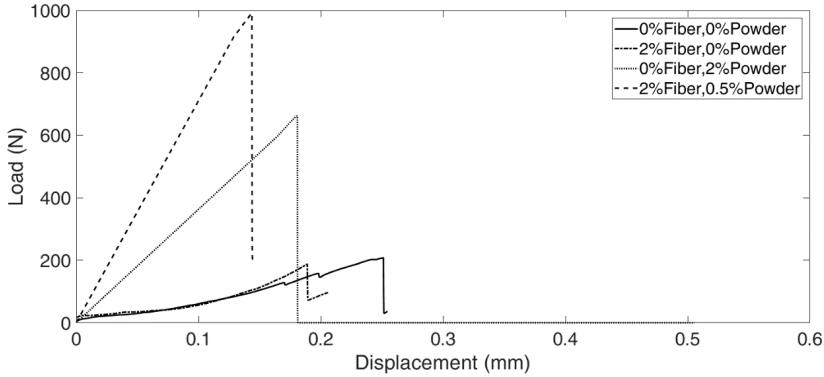

Figure 5.8: The load-displacement curve for four different mortar mixtures (a, b, c, and d) under shear test setup

implemented to back-calculate the tensile strengths and stiffness of bricks, mortar mixtures, and interfaces using the available data from experimental tests. Eventually, these parameters are used to model the behavior of the masonry wall under static normal and dynamic shear loads. With the application of LEM, the medium is discretized into elements that represent the bond between the particles. The discretization of the medium is done using the vectorizable random lattice (VRL) and controlling the randomness factor (α_r), which varies between 0 and 1 (Sect.3.2). Displacements in nodes and stresses in the elements are calculated by minimizing the system's potential energy. The measured stresses in the elements are compared to the defined strength threshold, which is back-calculated from the experimental results. When an element exceeds the threshold, it is removed and the fracture process is initiated. The LEM is able to model brittle and quasi-brittle materials with the application of a bi-linear softening scheme, where the softening ratio (S) is defined. Dynamic simulation is carried out by implementing Newton's second law, where the mass, velocities, and acceleration of cells or particles are determined using the integrated Newmark-β model. The harmonic Sine or Cosine loads can be initiated from any boundaries in time or frequency domains.

According to the experimental results of the three-point bending setup, the LEM simulations are carried out for the mortar mixtures (a, b, c, and d), as well as the brick samples, and the results of failure load (F_f), displacement at failure (d_f), Young's modulus (E) and tensile strengths (σ_t) are given in Tab.5.1. The softening ratio (S) is considered to simulate a quasi-brittle failure, as discussed in Sec.3.4.4. The lattice model of the three-point bending test of a brick sample with the fracture path highlighted in red is illustrated in Fig.5.9a. In this setup, the number of elements is 39041 and $\alpha_r = 0.5$. Fig.5.9b depicts the comparison of the experimental and numerical load-displacement curve for a mini brick with a brittle failure.

Note that the fiberglass and dispersion powder could not be individually simulated due to the computational limitations of micro- and macroscale models.

Table 5.1: The mechanical properties of mortar and brick samples determined from experimental and numerical LEM simulations of the three-point bending test (Mesh Size=220×60, $\alpha_r = 0.5$)

Mortar	F_f [N]	d_f [mm]	σ_t [MPa]	E [GPa]	Failure type
Brick	913.4	0.205	120	11	brittle
Mixture (a)	289.8	0.103	5	5.3	brittle
Mixture (b)	370.3	0.455	5.9	1.6	quasi-brittle (S=2)
Mixture (c)	165	0.094	2.7	3.4	brittle
Mixture (d)	358	0.206	5.7	3.3	quasi-brittle (S=2)

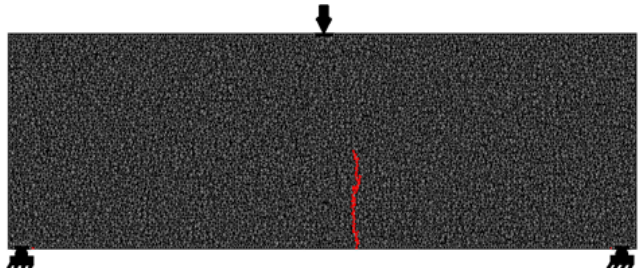

(a)

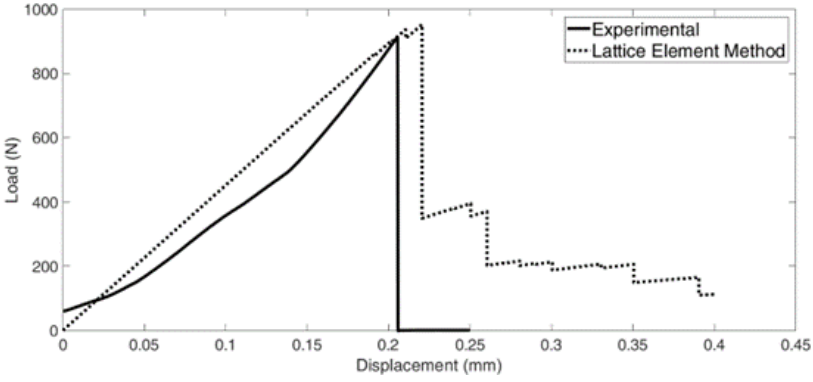

(b)

Figure 5.9: The numerical simulation of the three-point bending test with (a) fracture path highlighted with red, and (b) comparison of the load-displacement response of experimental and numerical results for the brick sample

Similarly to the previous results, the LEM results of an interface setup are given in Tab.5.2. Reference mortar mixtures (a, b, c, and d) are considered for the lattice simulations. The

interface setup is discretized with 34071 elements and $\alpha_r = 0.5$. Each individual brick shown in red has a dimension of 23×5 [mm] and the mortar has a thickness of 2.5 [mm]. Fig.5.10a depicts the interface failure for case (b), where 2% fiber glass and 0% dispersion powder are added to the mortar mixture. Fig.5.10b shows the interface and mortar failure for case (d), where the 2% fiber glass and 0.5% dispersion powder are added to the mortar mixture. The fracture path is highlighted with the green line.

Table 5.2: The evaluation of the interface strength using experimental and LEM results for different mortar mixtures (Mesh Size=100×115, $\alpha_r = 0.5$)

Mortar	F_f [N]	d_f [mm]	σ_t [MPa]	E [MPa]	Failure zone
Mixture (a)	316.15	0.318	2	4.3	Minor mortar and major interface
Mixture (b)	278	0.182	1.3	7.2	Only interface
Mixture (c)	804.2	0.217	3.5	19.6	Major mortar and minor interface
Mixture (d)	990.2	0.143	4.9	47	Mixed mortar and interface

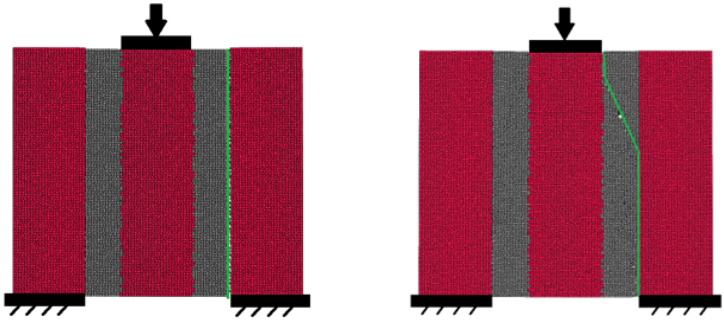

(a) (b)

Figure 5.10: The lattice simulation of interface setup for mortar mixture with (a) 2% fiber glass and 0% dispersion powder, and (b) 2% fiber glass and 0.5% dispersion powder (The red and gray domains represent the brick and mortar, respectively; the fracture path is shown with green line)

After the back-calculation of the stiffness and strength of brick, mortar mixtures and interfaces, a masonry wall under static and dynamic shear loading is simulated. A static normal load of (0.1 and 1 [kN]) is applied from the upper boundary, and the dynamic shear load with a displacement rate of (0.1Sin(t)) is excited from the upper left boundary as shown in Fig.5.11 The total number of elements in this simulation is 41301 and $\alpha_r = 0.5$. The fracture paths developed for three mortar mixtures (a, b and d) are shown in Fig.5.12. In case (a), the failure is due to bending failure, which occurs when the applied vertical load is small (0.1 [kN]). With weak interface strength in case (b), sliding failure occurs. In case (d), the failure resembles a shear failure, with high applied vertical and shear loads (10 [kN]). These failure patterns are consistent with what is found in the literature (Barazza 2012, Mistler 2006).

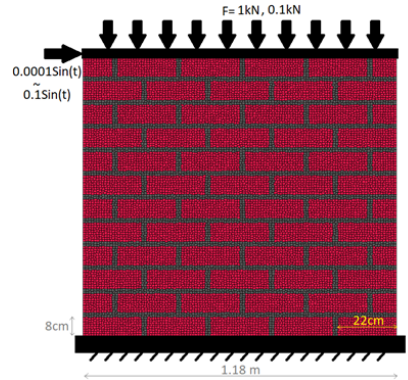

Figure 5.11: The masonry shear wall setup for the numerical study of failure behavior under static normal (building load) and dynamic shear loadings (earthquake)

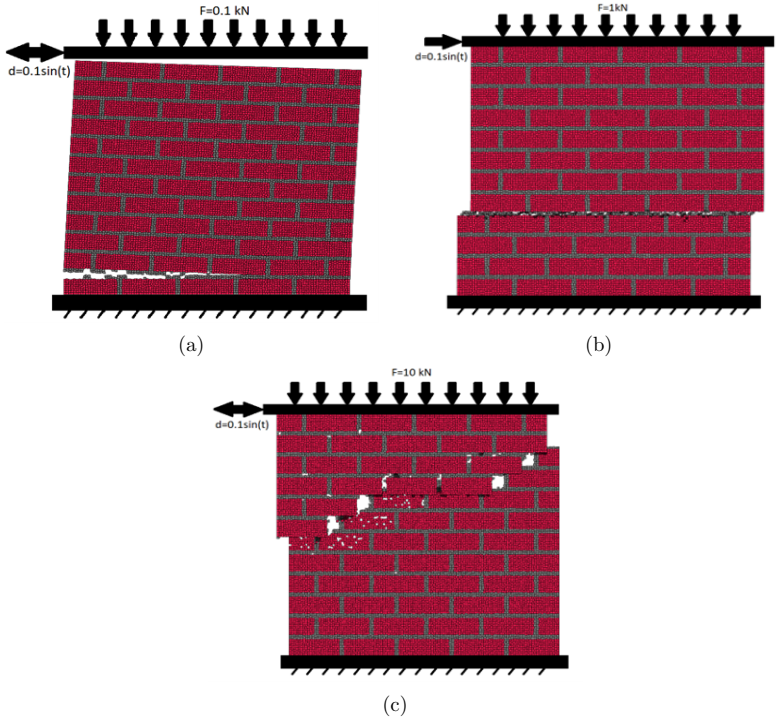

Figure 5.12: Failure pattern for the simulations of a shear wall using the material mixtures (a) no additives, (b) with 2% fiber glass and 0% dispersion powder, and (c) with 2% fiber glass and 0.5% dispersion powder

5.2.4 Summary

According to the experimental results, it is concluded that: (a) fiberglass improves the strength and ductility of the mortar and decreases the interface strength, and (b) dispersion powder improves the interface strength and decreases the strength of the mortar. Finally, with the application of the lattice element method (LEM) and using the experimental data for the back-calculation of the mechanical properties of compositions, the failure processes in masonry walls are simulated under three different conditions:

- Sliding failure with weak interface strength
- Shear failure due to high vertical load
- Bending failure due to low vertical load

It has been shown that by adding only fiber glasses, the fracture pass occurs only in the mortar and brick interfaces. On the other hand, by adding a small portion of dispersion powder up to 0.5%, the interface strength has improved significantly and the fracture path is not limited to interface failure. Therefore, the interface is reinforced. According to experimental studies, the optimal amount of additives is 2% of the mass of fiberglass and 0.5% of the mass of dispersion powder.

5.3 Application of HM lattice model to study the integrity of the geological rock barriers (GeomInt Project)

5.3.1 Introduction

To explore the material response of salt and clay rocks under coupled THM processes, a series of laboratory tests are conducted within the scope of the GeomInt project. Experiments are conducted to investigate the integrity of geological barrier rocks, such as clay and salt rocks, by coupling THM processes. In addition to the experimental tests, numerical simulations are performed to analyze and interpret the results. The developed lattice model is extended to investigate the integrity of the barrier rocks under HM processes. Discontinuities in solid bodies lead to a change in the tightness of geological reservoir-barrier systems. The lattice model is chosen due to its straightforwardness and capability to accurately simulate fracture processes in anisotropic and heterogeneous domains. Sand facies samples of Opalinus clay were extracted from the Mont-Terri underground laboratory in Switzerland, while most salt rock samples were collected from the Springen site in Thuringia, Germany (Kolditz et al. 2021). Opalinus clay has the potential to be a suitable host rock for the safe storage of nuclear waste that produces heat

(Hostettler et al. 2018). Salt rock has been established to be an effective geological barrier for hydrogen and compressed air, similar to the way it has been used to contain natural gas for many years (Schlichtenmayer et al. 2015). The contents of this section are partially published by Sattari et al. (2021) and Vowinckel et al. (2021) under the titles *"GeomInt-Mechanical Integrity of Host Rocks: Experimental Platform"* and *"GeomInt-Mechanical Integrity of Host Rocks: Model-Experiment-Exercises (MEX)"*, respectively.

5.3.2 Fracture toughness of the Opalinus clay: Anisotropy

Initially, the effect of anisotropy on the fracture toughness of Opalinus clay is investigated experimentally and numerically. In linear elastic fracture mechanics, the resistance of a material to fracture propagation is known as fracture toughness. The unit of fracture toughness is [Pa.$\sqrt{\text{m}}$] and the fracture toughness is measured under three different coupled or individual fracture Modes I, II and III. In a three-point bending test, the parameters of flexural strength (σ_{flex}), flexural Young's modulus (E_{flex}) and flexural strain (ϵ_{flex}) are measured. The three-point bending test is used to determine the Mode I fracture toughness (K_{Ic}) of a material (Fig.5.13).

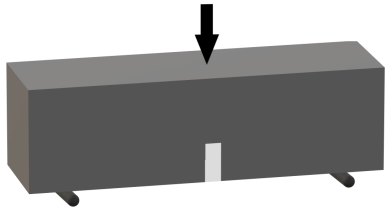

Figure 5.13: Sketch of the three-point bending test setup (Sattari et al. 2021)

The stress intensity factor (K_{I}) at the tip of the crack in the predefined notch is obtained as below (Bower 2009),

$$K_{\text{I}} = \frac{4f_{\text{flex}}}{B_{\text{flex}}}\sqrt{\frac{\pi}{W_{\text{flex}}}}\left(1.6\left(\frac{a_{\text{flex}}}{W_{\text{flex}}}\right)^{\frac{1}{2}} - 2.6\left(\frac{a_{\text{flex}}}{W_{\text{flex}}}\right)^{\frac{3}{2}} + 12.3\left(\frac{a_{\text{flex}}}{W_{\text{flex}}}\right)^{\frac{5}{2}} - 21.2\left(\frac{a_{\text{flex}}}{W_{\text{flex}}}\right)^{\frac{7}{2}} + 21.8\left(\frac{a_{\text{flex}}}{W_{\text{flex}}}\right)^{\frac{9}{2}}\right) \quad (5.1)$$

where f_{flex} is the flexural load, a_{flex} is the length of the pre-defined notch, B_{flex} and W_{flex} are the thickness and height of the sample under the flexural test, respectively. CMOD values are measured and recorded during the test procedure. At the load where the crack starts to spread in the medium, the fracture toughness K_{Ic} is calculated. To perform the fracture toughness test, a loading cell with three rolling supports is considered. However, the in-situ condition can only be reconstructed when the material is under controlled temperature and humidity

conditions. Therefore, a climate chamber in a laboratory of the CAU Kiel has been utilized to reach the desired temperature and humidity. Within the chamber, the temperature can be controlled between 20 to 80 °C, and relative humidity varies from 0 to 100.

The claystone samples are prepared with the dimension of 140×30×30 [mm] and the notch has a height and width of 10 and 2 [mm], respectively. The span length (S_{flex}) is 120 [mm], which is four times the size of its width and thickness. In this setup, the embedded layering is perpendicular to the loading direction. The image processing technique is used to track the reference points, which are predefined prior to the test procedure (Fig.5.14a). The distance between the reference points is measured using the optical microscopic image and is considered an initial reading value (Fig.5.14b). The resolution of the readings from the images is 2 micrometers (pixel size), which is possible by taking 4k video at 30fps.

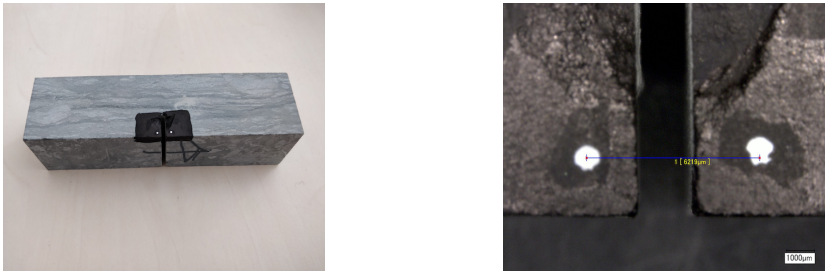

(a) (b)

Figure 5.14: The application of image processing technique with (a) the predefined reference points for measuring the CMOD, and (b) the measured rough distance using an optical microscope (Sattari et al. 2021)

The orientation of the embedded layers in clay rock has a major influence on its anisotropy behavior (Kolditz et al. 2021; 2023, Glaß 2023, Schumann 2019, Bergmann 2019). When the loading direction is perpendicular ($\perp$) to the layering orientation, the strength of the material is highest. On the contrary, the material strength is the lowest when the loading direction is parallel ($\parallel$) to the orientation of the layer. The maximum load obtained from the experimental data ($\perp$) is 598 [N] and the bending stiffness is around 3.3 [GPa] (Fig.5.15). The CMOD at failure load is 24 [μm]. The 4K video with 30fps is used to track the reference points on the claystone. Subsequently, the image analysis technique is implemented to determine the CMOD. The images extracted from the video recordings were not adequate to detect the brittle failure of the sample, and therefore, in the experimental data, the post-failure response is not well represented. The measured fracture toughness ($\perp$) is 0.746 [MPa.$\sqrt{\text{m}}$]. The results indicate an anisotropic behavior of claystone and its dependence of the fracture path on the orientation of the embedded layering (Fig.5.16a and Fig.5.16b). As a result, frack propagation along the layer orientation, where the sample is weakest, is observed. Furthermore, the fracture toughness of

claystone is measured inside a climate chamber at temperatures of 50 and 80 $°C$ and is presented in Tab.5.3.

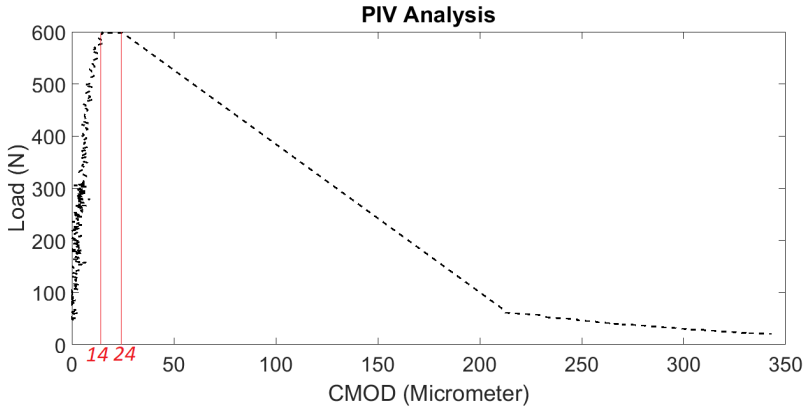

Figure 5.15: The load vs. CMOD for the Opalinus clay sample under the room temperature (Vowinckel et al. 2021)

(a) (b)

Figure 5.16: The anisotropy of the frack progression in claystone: (a) the frack propagation parallel to the loading direction, and (b) the zig-zag frack propagation when loading is perpendicular to the layering orientation (Vowinckel et al. 2021)

Table 5.3: The fracture toughness of Opalinus clay rock under different temperatures

Opalinus clay	20°C	50°C	80°C
Peak Force [N]	559	482	455
Fracture Toughness [MPa.$\sqrt{\text{m}}$]	0.697	0.601	0.582

The lattice model is used to study the anisotropy of claystone in two individual cases, where the loading direction is parallel or perpendicular to the layering orientation. The lattice model

($\perp$) is generated in the 2D domain and the material properties are back-calculated from the results of the fracture toughness and splitting tests. The tensile strength of the material perpendicular to the embedded layers is considered to be five times weaker than when it is parallel to the layering. The fracture paths for both cases ($\perp$ and $\parallel$) are shown in Fig.5.17a and Fig.5.17b, respectively. Fig.5.18 illustrates the comparison between the experimental and numerical data. Camera limitations and low frame rate setup have caused the simulated post-failure behavior to not match the experimental results, as previously discussed.

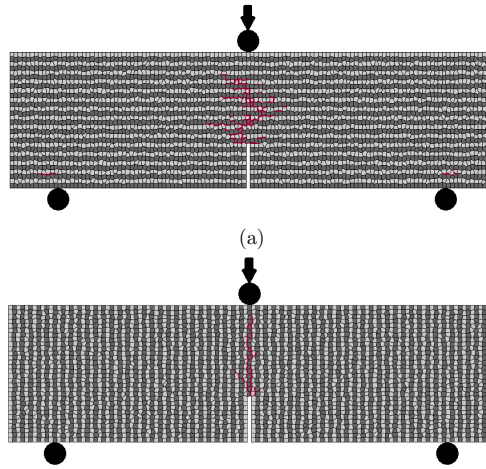

(a)

(b)

Figure 5.17: Simulated fracking path under loading direction (a) perpendicular, and (b) parallel to the layering orientation (Vowinckel et al. 2021)

The influence of the orientation of the embedded layers on the fracking path is demonstrated by both experimental and numerical data. Due to the orientation of the layers and the stress distributions (in the $\perp$ case), the fracking path has a zig-zag pattern following the weakest interface bonds. The lattice model is validated with the experimental data for the $\perp$ case and extended to model the $\parallel$ case, where the loading direction is parallel to the embedded layers. The findings suggest that, in the $\parallel$ case, the frack path is a straight line through the weak interface bond.

5.3.3 Drying and wetting paths of Opalinus clay

This study focuses on the simulation of the drying and wetting processes and the evolution of micro-channels in Opalinus clay. In this regard, experimental data is used to model shrinkage and swelling processes. Additionally, the change in hydraulic conductivity is presented both in

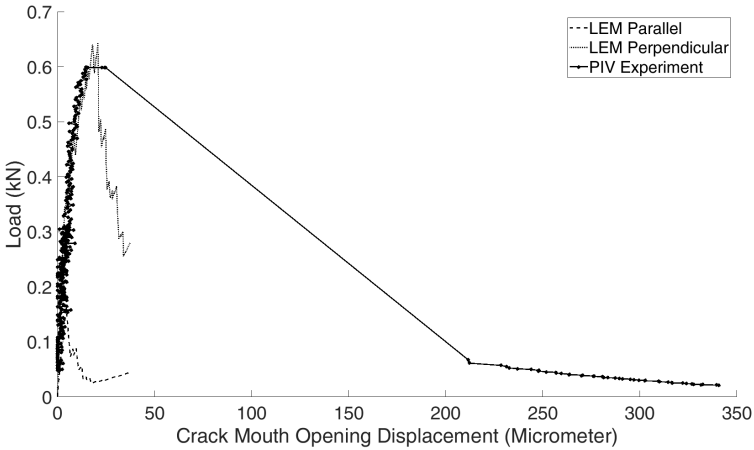

Figure 5.18: Comparison of experimental and numerical data on the effect of anisotropy in Opalinus clay, when the point load is parallel or perpendicular to the embedded layers (Vowinckel et al. 2021)

parallel and perpendicular to the embedded layering orientations. As a result of the inherent anisotropy of claystone material, the evolution of the linear strain of the material in parallel and perpendicular orientations is different.

The shrinkage and swelling of claystone results in micro-fracking and higher permeability values, which in nuclear waste disposal sites can lead to contamination of the environment. Micro-cracks also decrease the strength of the material subjected to THM loading processes. Conventionally, the swelling pressure and heave of claystone are determined using Oedometer tests (Peron et al. 2009), where a constrained or unconstrained sample is subjected to the swelling process (Fig.5.19a). During the test procedure, the swelling pressure and the magnitude of the heave are recorded. The swelling pressure in sandy facies of claystone is observed to be lower than in shaly facies. Compared to swelling tests, shrinkage tests are not as frequent and are challenging to perform on rock materials. Minardi et al. (2016) performed a shrinkage test on claystone with shaly and sandy facies using a desiccator and various salt solutions (Fig.5.19b). During the testing process, the axial strain values obtained from the strain gauges are recorded, and the second sample is periodically weighed.

Two slender cylindrical sections of 100×10 [mm] (DxH) Opalinus clay with sandy facies are used to investigate the inherent material anisotropy during the shrinkage and swelling processes (Fig.5.20a). The mineral composition of claystone and its layered arrangement has a major effect on the anisotropy behavior, which in turn affects the orientation of shrinkage and swelling progression as well as the formation of micro-fractures. The first sample is used to determine

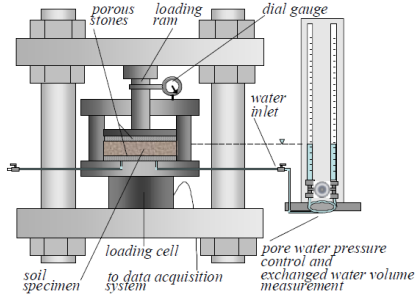

(a)

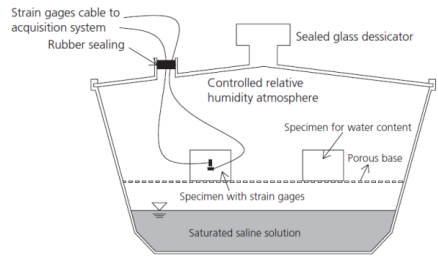

(b)

Figure 5.19: The swelling and shrinkage tests on Opalinus clay (a) the Oedometer test setup for constrained swelling pressure in Opalinus clay samples (Peron et al. 2009), and (b) the measurement of the drying and wetting paths with the help of the desiccator (Minardi et al. 2016)

the axial strains in parallel and perpendicular directions to the layer orientations. The strain gauge strips (HBM, LY 10 [mm]/120 Ω) are glued and attached to the surface of the first sample (Fig.5.20b). The second sample is used to determine the alteration in the water content during the wetting and drying cycles.

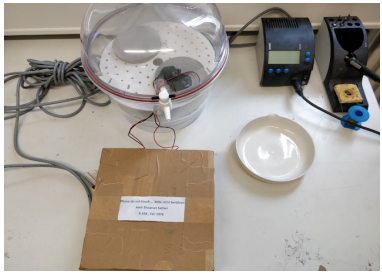

(a)

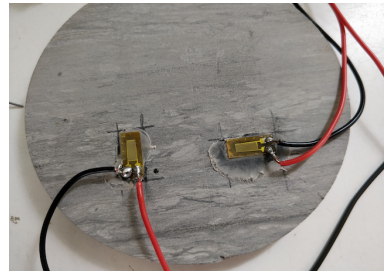

(b)

Figure 5.20: (a) Desiccator setup, and (b) arrangement of the strain gauge strips on the sample surface (Vowinckel et al. 2021)

The saturated salt solutions are used to apply different osmotic suctions. Salt solutions and their values of induced suction and relative humidity at a constant room temperature of 20 °C are listed in Tab.5.4. The suction values range from 3.2 to 367 [MPa], which ensures both the drying and wetting paths. The temperature within the test room remains constant with no significant changes. The total suction (ψ_{total}) value can be measured using the Kelvin relation, which is derived from the ideal gas law:

$$\psi_{\text{total}} = \frac{RT}{V_{\text{mol}}} \ln\left(\frac{P_{\text{vap}}^{cur}}{P_{\text{vap}}^{cur=0}}\right) \tag{5.2}$$

where $\left(\frac{P_{\text{vap}}^{cur}}{P_{\text{vap}}^{cur=0}}\right)$ is the relative humidity, $P_{\text{vap}}^{cur=0}$ is the vapor pressure when the surface curvature is equal to zero (flat surface), R is the universal gas constant, T is the temperature and V_{mol} is the molecular volume of water. The equilibrium in the desiccator is achieved when the strain gauge measurement or the water content of the samples remains the same in two successive readings. The testing process is time-consuming, and, after collecting data for over four months, the suction and water content values are analyzed and graphed.

Table 5.4: The relative humidity and suction values of the saturated salt solutions at 20 °C

Salt solution	Relative humidity (%)	Suction [MPa]
K_2SO_4	97.6	3.2
KNO_3	94.6	7.5
KCl	85.1	21.8
NaCl	75.5	38
$Mg(NO_3)_2$	54	84
$MgCl_2$	33.1	149.5
LiCl	12	286.7
LiBr	6.6	367.5

Fig.5.21a shows the change in suction and linear axial deformations in the parallel and perpendicular directions. Similarly, Fig.5.21b illustrates the change in water content with applied suction using salt solutions. On the drying path, the results indicate higher strains for a strain gauge perpendicular to the embedded layers. When the suction is greater than 150 [MPa], the measured strains in the perpendicular direction are approximately 4.5 times greater than the parallel alignment. The strain gauges show only slight variations in the wetting path. Water content data suggest that the air-entry pressure for the sandy facies of Opalinus clay is approximately 25 [MPa].

The drying and wetting processes of the Opalinus clay can be simulated by using the integrated interface element as outlined in Sect.3.4.2. The results of the experiment are used to determine the linear deformation of the elements. The initial values of hydraulic conductivity (K^f) are estimated based on the technical report, Mont-Terri 2008-04, as follows:

$$K_{\parallel}^{f} = 2 \times 10^{-13} \quad , \quad K_{\perp}^{f} = 0.6 \times 10^{-13} \tag{5.3}$$

Taking into account the cubic law for flow transfer through the porous medium, the hydraulic aperture (a_f) or length of the interface element is calculated as

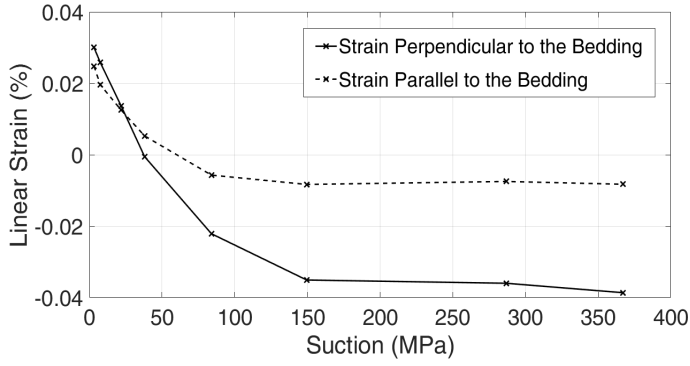

(a)

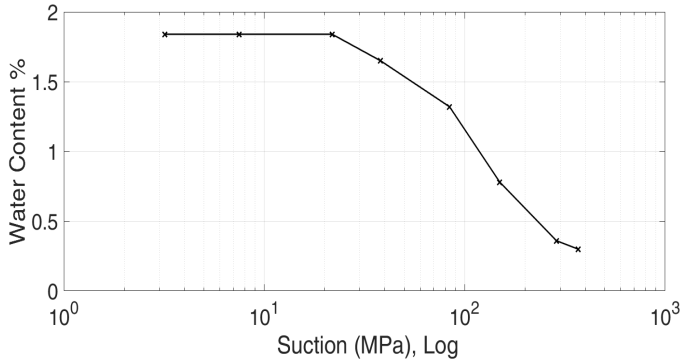

(b)

Figure 5.21: The drying and wetting paths for Opalinus clay: (a) Suction vs. linear strains, and (b) suction vs. the water content (Vowinckel et al. 2021)

$$a_f = \sqrt{\frac{12K^f\nu_f}{\mathbf{g}}} \quad , \quad a_{f,\parallel} = 4.95 \times 10^{-10} \quad , \quad a_{f,\perp} = 2.71 \times 10^{-10} \tag{5.4}$$

where $\nu_f = 1.004 \times 10^{-6}$ [m^2.s^{-1}] and $\mathbf{g} = 9.8$ [m.s^{-2}]. VRL is used to discretize the domain and define the orientation of the embedded layers. As observed from the experimental data, the interface strength between two layers is assumed to be five times weaker than the bond between the same layer. Therefore, fracking is expected along the layers in horizontal (X) and vertical (Z) orientations, resulting in higher hydraulic conductivity values as the wetting and drying process continues (Fig. 5.22b). Fig. 5.23 shows the change in hydraulic conductivity along the three axes of X, Y, and Z. Hydraulic conductivity experienced the least amount of alteration

during the drying process when measured along the Y orientation, where the drying process was perpendicular to the orientation of the embedded layer.

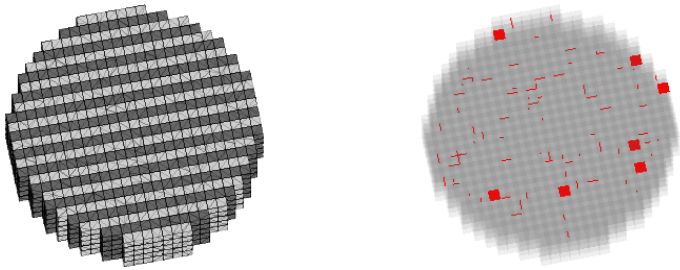

(a) (b)

Figure 5.22: (a) Generated domain for simulation of the drying and wetting processes, and (b) crack surfaces shown with red color (Vowinckel et al. 2021)

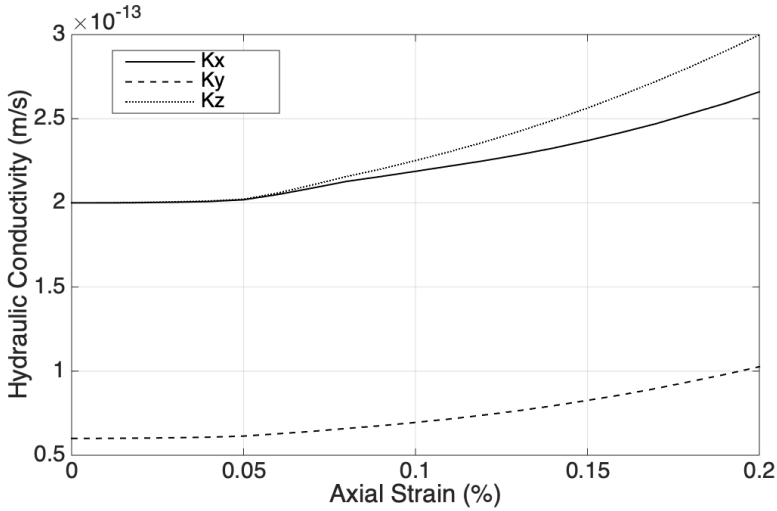

Figure 5.23: The change of hydraulic conductivity along three axes for Opalinus clay under drying process (Vowinckel et al. 2021)

5.3.4 Pressure-driven fluid percolation in geomaterials

The use of pressurized fluid for hydraulic fracking or storage can cause fracturing of the rock barrier and movement of fluid through hydraulic openings and cavities (Yoshioka et al. 2022, Ghanbarzadeh et al. 2015). This can cause a drop in pressure and leakage in the

reservoir, decrease the output and efficiency of the designed system, and eventually lead to contamination of the environment. The application of the HM lattice model is extended to simulate pressure-driven fluid percolation in salt and clay rocks. The effect of anisotropic confinement pressure on the development of the crack path in salt rock is investigated. The main objective of this study is to qualitatively observe the stress-dependent fracking path and to assess the fracking pressure, which, in theory, should be greater than the applied minimum principal stress. Eventually, the impact of the layers embedded in the Oplainus clay rock on the formation of discontinuities is examined.

Salt rock A series of experimental tests was conducted at IfG Leipzig (Kamlot 2009). Cubic samples with a side length dimension of 100 [mm] were prepared and placed in the true triaxial apparatus (Fig.5.24). Cubic samples were prepared with a drilled hole that is 40 [mm] long and 16 [mm] wide. The pressurized fluid was injected through a tube from the top and the fracking process and alteration of the flow rate were monitored. The two applied anisotropic stress configurations and the fracking paths are shown in Fig.5.25a and Fig.5.25b. Fig.5.26a and Fig.5.26b illustrate the change of pressure inside the borehole over time when the flow rate remains constant.

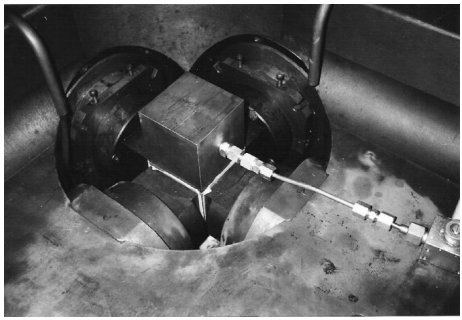

Figure 5.24: Setup configuration of salt rock in the true tri-axial apparatus (Kamlot 2009)

The dual-lattice model, described in Sec.3.6.2, is implemented to simulate fluid-driven percolation in salt rock. The weak coupling scheme is used to transform the applied hydraulic pressures into a mechanical model. Subsequently, the element's failure and change of hydraulic aperture are calculated and transformed back to the hydro model. The mass conservation law leads to the prediction of the flow rate, the alteration of the reservoir pressure, and the flow and fracking paths. These predictions are then compared with the experimental data. The total number of mechanical and conduct lattice elements is approximately 6000 and 45000, respectively (Fig.5.27). The experimental setup shown in Fig.5.25a is simulated using dual LEM and the developed fracture surfaces are shown in Fig.5.28a. Similarly, the fracture surfaces under the second stress configuration (Fig. 5.25b) are illustrated in Fig.5.28b.

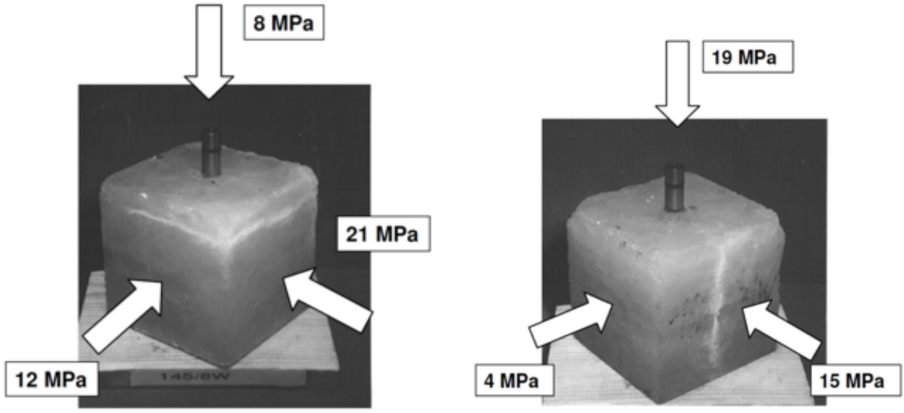

(a) (b)

Figure 5.25: The confining (a) 1^{st} stress, and (b) 2^{nd} stress configuration setup in salt rock (Kamlot 2009)

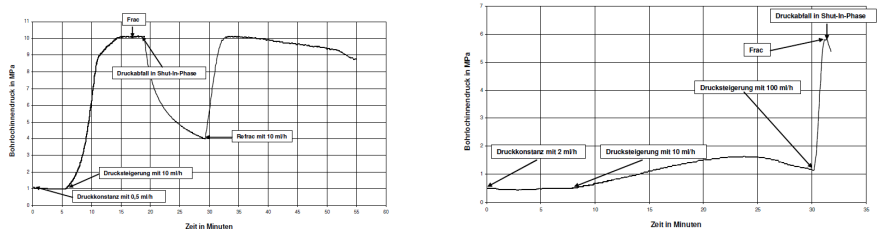

(a) (b)

Figure 5.26: The borehole pressure evolution under constant flow rate sequels for (a) 1^{st} stress, and (b) 2^{nd} stress configurations (Kamlot 2009)

Young's modulus is assumed to be 30 [GPa] in these simulations. During the comparison of the experimental and numerical results, the propagation of the frack along the horizontal axis (visible on the surface frack path) for the 1^{st} stress configuration (Fig.5.28a) is observed. In Fig.5.28b, the propagation of the fracking path is observed in the vertical direction (visible on the surface frack path) similar to the experimental result (Fig.5.25b).

For 1^{st} and 2^{nd} stress configurations, the fracking pressure is found to be 13.2 and 7.1 [MPa], respectively. The fracking pressure found in the literature is slightly lower than the two values obtained here. In both cases, the fracking pressures are higher than the minimum principal stresses. The red surfaces indicate fracking paths that agree with the experimental results. The 1^{st} stress configurations lead to horizontal fracking paths, while the 2^{nd} stress configurations result in vertical fracking paths. The flow pathways are perpendicular to the direction of the

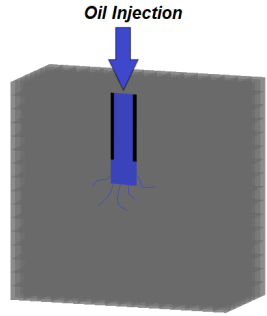

Figure 5.27: Cross-section view of the boundary condition in the lattice model (Vowinckel et al. 2021)

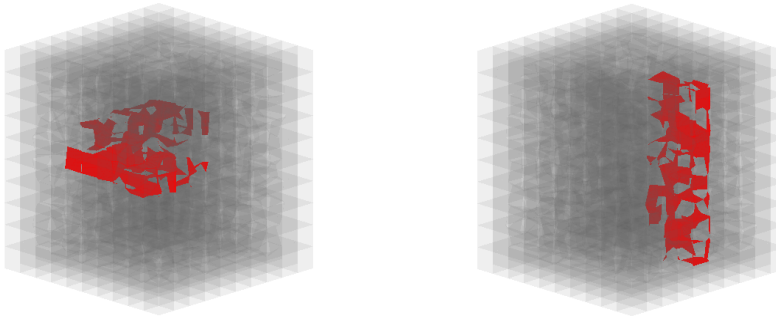

(a) (b)

Figure 5.28: The simulation of the pressure-driven percolation and developed frack surfaces (red) for the (a) 1^{st}, and (b) 2^{nd} stress configurations (Vowinckel et al. 2021)

minimum applied principal stress.

Opalinus clay The cubic Opalinus clay samples are prepared with a side dimension of 43 [mm] and a drilled cavity with a length and diameter of 20 and 8 [mm], respectively (Fig.5.29a). In the CAU Kiel geomechanics laboratory, the true triaxial apparatus with the maximum mechanical pressure of 600 [MPa] and thermal loading up to 600 °C is used to conduct pressure-driven percolation in claystone samples from Mont-Terri. The syringe pump, with a maximum pressure of 517 [bar], is used to pressurize the oil fluid. Finally, cubic samples are attached to pump pipes and sealed with O-rings and epoxy adhesive (Fig.5.29b).

The applied mechanical stress configurations are illustrated in Fig.5.30a and Fig.5.30b. The embedded layering orientations of the samples are shown in Fig.5.31a and Fig.5.31b, where in

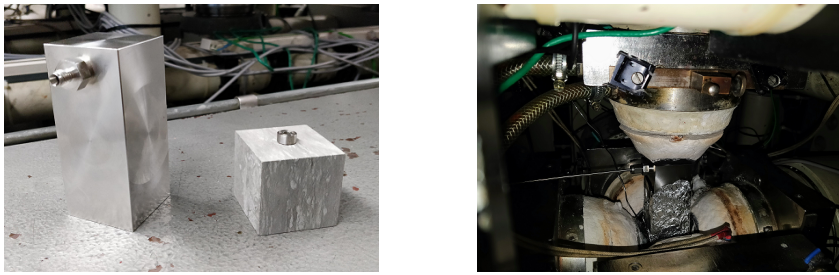

(a) (b)

Figure 5.29: The pressure-driven percolation test preparation (a) the prepared cubic claystone sample and the adapter, and (b) the sample placement inside the true triaxial apparatus (Sattari et al. 2021)

the first case the applied oil pressure is perpendicular to the layering orientations, and in the second case it is parallel to the layering orientations.

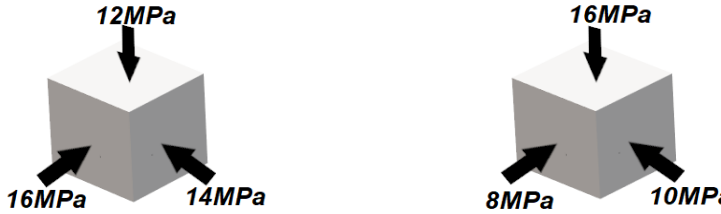

(a) (b)

Figure 5.30: The applied (a) 1^{st}, and (b) the 2^{nd} stress configurations (Vowinckel et al. 2021)

(a) (b)

Figure 5.31: The orientation of the embedded layers (a) perpendicular, and (b) parallel to the direction of the borehole pressure configuration (Vowinckel et al. 2021)

In the first setup, hydraulic fracking starts at 23 [MPa] and clear flow paths are observed through the embedded layering surfaces (Fig.5.32a). Similarly, for the second test setup,

hydraulic fracking is started at 10 [MPa] through the embedded layering surfaces, as shown in Fig.5.32b. Fig.5.33a and Fig.5.33b illustrate the evolution of the borehole pressure with the change in flow volume obtained from the experimental data. The starting volume of the pump is approximately 265 [mL].

(a) (b)

Figure 5.32: The fracking paths through the Opalinus clay (a) 1^{st} stress configuration, and (b) 2^{nd} stress configuration (Vowinckel et al. 2021)

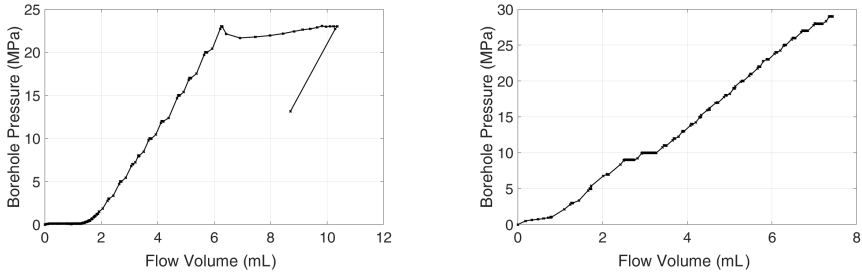

(a) (b)

Figure 5.33: The borehole pressure vs. flow volume for an Opalinus clay (a) 1^{st} stress configuration, and (b) 2^{nd} stress configuration (Vowinckel et al. 2021)

From the experimental data, fracking and leakage through the weak bond along the embedded layers are observed. However, more experimental data is required under different principal stress configurations to detect and analyze the stress distribution and dependence of the frack paths on the anisotropy (Kolditz et al. 2023, Glaß 2023). The fracking stress for both tested samples was greater than the minimum principal stress that was applied. For a 1^{st} stress configuration, the fracking pressure was much higher than the maximum principal stress applied, which can be due to an error in the experimental results and a small sample size (size effect). The lack of a pre-defined notch during the sample preparation can also lead to greater fracking stresses. For the 2^{nd} stress configuration, no pressure drop until the borehole pressure

of 30 [MPa] is recorded. However, the change in flow volume at the borehole pressure of 10 [MPa] is detected. This may be due to the localized frack process around the borehole cavity.

The lattice model was used to explore the influence of the anisotropy of the Opalinus clay on the fracking paths and the fracking pressure. It is assumed that the interface elements bonding two different layers have a strength five times weaker than that of the same layer bond (found from preliminary fracture toughness and splitting tests). The 3D setup generated using the LEM is shown in Fig.5.34a and Fig.5.34b. The total number of mechanical and conduct lattice elements are approximately 28000 and 200000, respectively. The percolation tests are simulated under the two stress configurations and with different embedded layering orientations. Fig.5.35a and Fig.5.35b depict the fracking surfaces (red) for the 1^{st} and 2^{nd} stress configurations, respectively. It is seen that, according to the experimental result, the orientation of the layers has an influence on the development of flow paths in the Opalinus clay samples.

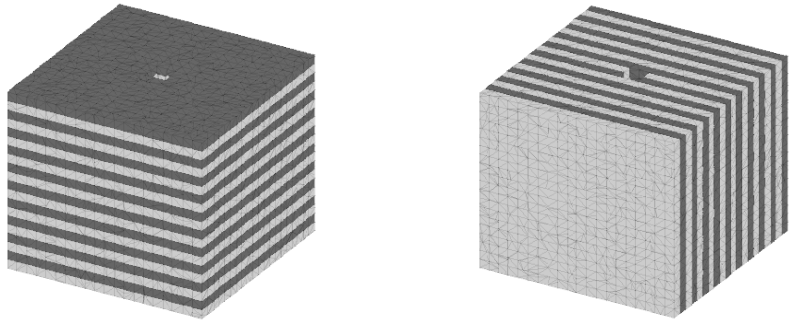

(a) (b)

Figure 5.34: The generated 3D domain in lattice model for the (a) 1^{st} stress configuration, and (b) 2^{nd} stress configuration (Vowinckel et al. 2021)

5.3.5 Summary

The conducted experimental and numerical studies in the scope of the GeomInt project give insight into barrier rock's integrity under the coupled Multiphysics processes. In the scope of the GeomInt project, a series of experimental tests on an Opalinus claystone have been carried out. The experimental results of the three-point bending test, wetting and drying paths, as well as pressure-driven percolation, are presented in this section. The results indicate the effect of anisotropy on the evolution of crack paths in the Opalinus claystone. It has been discovered that the tensile strength of the material when perpendicular to the embedded layers is approximately five times weaker than when it is parallel to the layers. Moreover, the lattice model is implemented to simulate the material anisotropy of the Opalinus claystone. The initiation and

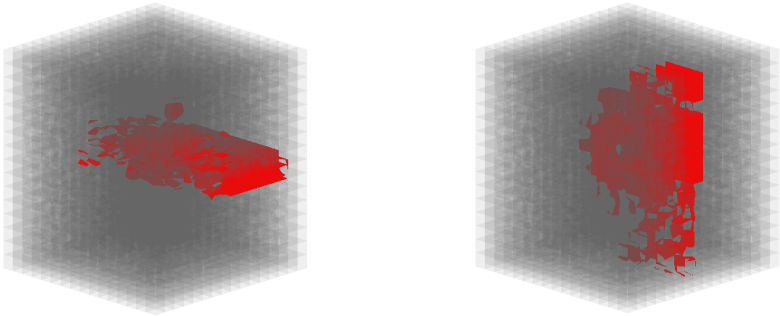

(a) (b)

Figure 5.35: The fracking surfaces (red) for the (a) 1^{st}, and (b) 2^{nd} stress configurations (Vowinckel et al. 2021)

propagation of cracks under shrinkage and swelling processes, as well as pressure-driven percolation, are simulated. The qualitative results reported show the domination of the crack paths along the embedded layers, similar to what is realized from the experimental data. However, more experimental studies are needed to quantitatively validate the developed lattice model.

Chapter 6

Conclusion and Outlook

6.1 Summary

In the scope of this work, the theoretical and mathematical frameworks of the Thermo-Hydro-Mechanical (THM) lattice model to simulate coupled processes in cemented geomaterials are presented. Advances in the discrete lattice model in simulation of material heterogeneity as well as evolution of the discontinuities under the THM processes are highlighted. Initially, the discretization of the domain while accounting for the pre-existing heterogeneity and discontinuities in the 2D and 3D domains is presented. With the definition of a controlled mesh irregularity using the randomness factor, the non-uniform stress distribution in inter-particle scale is captured. This study presents a model framework for a mechanical lattice model, which includes a description of the mesh regularization scheme, the assignment of element properties, and consideration of the fracture mechanisms.

The mechanical framework is then adopted to simulate the coupled Thermo-Mechanical (TM) and Hydro-Mechanical (HM) processes. The mathematical formulation of the TM model is presented where the simulation of steady and transient heat flow through the generated lattice elements is possible. At the particle level, the lattice elements enable heat to be conducted based on the specified cross-sectional length (or area in 3D). The new interface lattice model is presented to simulate the thermal expansion of the generated domain and realize the tensile failure of the interface elements. Eventually, the calculated thermal forces are transformed into the mechanical solver to study the initiation and propagation of fractures in the domain. A novel HM model is developed to address fluid flow and hydraulic fracking processes in cemented geomaterials. In this regard, the dual-lattice scheme is implemented to discretize the flow channels, where the conduit elements and hydraulic nodes are employed to calculate the hydraulic aperture and fluid pressures. At last, the hydraulic forces are transmitted to the mechanical solver to realize the domain deformation and change in the dimension of inter-particle flow channels.

The lattice model is extended to simulate wave propagation in heterogeneous and discontinuous domains. With the dynamicLEM developed on the basis of the equation of motion formulation, the dispersion and reflection of the wavefronts are captured. The discrete lattice model is developed to account for the irregularity of particle shapes and their influence on the mechanical response of the geomaterial. Here, the contact forces are determined based on the contact penalty method.

The validation and parametric study of the developed lattice model is presented in Chapter 4. First, the mechanical solver is validated on the basis of the analytical solution of the fracture propagation in DCB. The effect of model parameters, such as the randomness factor and softening ratio, on the mechanical response is investigated. Next, steady and transient heat flows in the 2D and 3D domains are modeled. A comparison of the numerical solution with the experimental data of different rock samples is carried out to capture the change in thermal conductivity and the evolution of cracks during the coupled TM processes. Analytical solutions of 2D planar fluid flow and flow through a discontinuity are adopted to validate the hydro lattice model. Additionally, the evolution of effective stresses during the hydraulic fracking process is simulated. Eventually, the dynamicLEM is implemented to simulate the wavefront dispersion in concrete and rock-like bodies.

In Chapter 5, the applicability of the discrete lattice model in practical studies is discussed. To do so, two research projects are presented, where the developed lattice model was used to carry out numerical investigations. The application of the lattice model is adopted to simulate crack initiation at the reinforced brick-mortar interface. Moreover, the HM lattice model is considered to study the integrity of the barrier rocks, such as salt and clay rocks. Here, validation of the lattice model with the experimental results of the three-point bending test, shrinkage and swelling processes, as well as pressure-driven fluid percolation in Opalinus claystone, is established.

6.2 Conclusion and discussion

The validation of the discrete lattice model with the experimental data and analytical solutions is provided in Chapters 4 and 5. According to the results, the lattice model can simulate crack initiation and propagation in heterogeneous cemented geomaterials with great precision. The findings of this numerical study are listed below:

- ✓ **Mechanical lattice model** formulation is implemented to solve the fracture evolution in geomaterials. Initially, validation of the mechanical model with an analytical solution of DCB is presented. The results indicate the great accuracy of the model. Next, the parametric study of the model constants grants the mesh independence of the lattice model. Here, the effect of the randomness factor, the size of the elements, and the softening

ratio on the final output of the model is studied. Additionally, the lattice results are compared to the experimental data of a Brazilian test performed on a glued sand column. The comparison of the results once again proves the great accuracy of the quasi-brittle fracture mechanism adopted in the lattice model. Eventually, the lattice model is applied to simulation of crack development in reinforced masonry walls and a three-point bending test on a heterogeneous clay stone. With the consideration of the layered heterogeneity in the lattice, the numerical method is able to accurately simulate the pre- and post-failure behavior of homogeneous and heterogeneous materials. However, the assessment of particle-level properties from the experimental approach should be further investigated.

✓ **Thermo-Mechanical lattice model** is established to simulate steady and transient heat flow in cemented geomaterials. With the consideration of the change of contact quality with the inter-particle forces, the coupling of thermal heat flow with the mechanical solver is carried out. The novel interface lattice model is adopted to simulate thermal strains and calculate contact forces. A parametric study of the effect of porosity, heterogeneity, and mesh irregularity on the final outcome of the heat profile has been provided. It has shown that by increasing the mesh size, the outcome of the lattice model is similar to that of the continuum-based solution. Eventually, the experimental results of different rock samples are considered to validate the TM solution. As a result of the increased mechanical load, the measured and computed thermal conductivity values have increased. On the other hand, with the increase in temperature, it has been shown that the thermal conductivity value decreases, which is due to the generation of micro-cracks and degradation of contact quality at the particle level. The initial thermal properties of any composition, such as thermal conductivity and heat capacity, are input parameters of the TM lattice model. Therefore, an experimental approach to accurately measure these properties will enhance the accuracy of the lattice model.

✓ **Hydro-Mechanical lattice model** is able to simulate fluid flow through cemented geomaterials. The coupling scheme has been reached with the generation of conduit elements and hydro nodal at the circumference of Voronoi cells. With the flow propagation in defined virtual cavities and the adoption of mass conservation theory, the fluid pressures and forces on the hydro nodes are calculated. It is feasible to use a mechanical solver to replicate hydraulic fracking and pressure-driven percolation in geomaterials by transforming fluid forces. The change in hydraulic aperture occurs with deformation of the structure and results in a change in the dimension of the fluid channels. The analytical solution of 2D planar flow and fluid flow through a pre-defined discontinuity has been conducted to analyze the accuracy of the flow model. The results indicate the great precision of the developed lattice model. In three different case studies, the evolution of the effective stresses during hydraulic fracking is modeled. The domination of the Mode I failure of the elements has been observed. Eventually, pressure-driven percolation, as well as shrinkage

and swelling processes, are presented in highly heterogeneous Opalinus claystone. The results indicate the great dependence of the developed crack path on the orientation of the embedded layers. However, to quantitatively validate the HM lattice model, more experimental data are required.

✓ **Dynamic lattice model** is applied in the simulation of wave field dispersion in heterogeneous and discontinuous domains. The lattice model is able to simulate the P-, S-, and surface wavefronts to study dynamic problems in geomaterials. The validation of dynamicLEM with the analytical solution of wave propagation in the homogeneous domain illustrates the accuracy of the numerical method. With the simulation of a homogeneous beam element with pre-defined discontinuity, the scattering and evolution of wavefield shadows have been studied. The introduced heterogeneity (concrete or rock composition) in the beam element increases the dispersion of wavefronts. The results indicate that as the heterogeneity factor (stiffness ratio) increases, the disturbance of the wave fields becomes greater. The dynamicLEM solution is used to train the ANN method to detect and localize defects in a homogeneous domain. However, more studies are needed to detect discontinuities in heterogeneous geomaterials and extend the applicability of the lattice model in the SHM field.

According to the findings of this work, the advantages of discrete lattice model over continuum- or discountiuum-based models are listed below:

- Simplicity and efficiency in simulation of the discontinuities and model single-crack propagation, crack bridging, and multi-crack progression compared to continuum methods
- Capture the inherent material heterogeneity and adoption of stochastic mesh irregularity compared to continuum methods
- Computationally efficient to simulate Multiphysics problems compared to discontinuum methods

However, the application of the lattice model in engineering applications presents its own challenges. The main drawbacks of a lattice model are:

- Difficulties in assessing microscale THM properties, such as stiffness, strength, fracture toughness, and thermal conductivity, using experimental approaches.
- Challenges to simulate large-scale problems with the micro- to macroscale transition.
- Optimization and parallelization of the THM lattice code

6.3 Recommendations for future research

In this contribution, advances in discrete lattice modeling of cemented geomaterial are presented. However, the limitations of the current state-of-the-art could be addressed in future studies. The recommendations to improve and extend the current state of work for the simulation of complex THM processes are listed below:

- Theoretical and mathematical formulation of the anisotropic THM lattice model to simulate the inherent anisotropy of the geomaterials
- Parallel and GPU computation to increase the computational efficiency and simulate large-scale domains
- Multiscale discrete lattice scheme to project the discontinuities from micro- to macroscale and able to model macroscale problems
- Adoption of more complex constitutive models to account for material hardening, plastic flow, and state-dilatancy
- Implementation of the fully implicit discrete lattice formulation
- Development and validation of the TH lattice model to fully couple the THM processes
- Development of strong THM coupling formulation to increase the accuracy of the model
- Qualitatively validate the developed dual-lattice HM model with large-scale experimental and in-situ data
- Extension of the dynamicLEM into the defect localization in the heterogeneous and discontinuous domain in the scope of SHM
- Development of the coupled lattice and continuum-based model (e.g. FEM) to address discontinuities and model coupled THM processes
- Assessment of the microscale THM properties, such as elastic stiffness, fracture toughness, thermal conductivity, and hydraulic aperture, using nano- to microscale laboratory tests, such as nanoindentation technique. These properties can then be imported as input parameters to the lattice model.

Bibliography

Abdel-Fattah, H. and S. A. Hamoush (1997). Variation of the fracture toughness of concrete with temperature. *Construction and Building Materials 11*(2), 105–108.

Abdulhadi, N. O., J. T. Germaine, and A. J. Whittle (2012). Stress-dependent behavior of saturated clay. *Canadian Geotechnical Journal 49*, 907–916.

Aksu, I., E. Bazilevskaya, and Z. Karpyn (2015). Swelling of clay minerals in unconsolidated porous media and its impact on permeability. *GeoResJ 7*, 1–13.

Almqvist, B. S. G., J. P. Burg, J. Berger, and L. Burlini (2013). Seismic properties of the kohistan oceanic arc root: Insights from laboratory measurements and thermodynamic modeling. *Geochemistry, Geophysics, Geosystems 14*(6), 1819–1841.

Anandarajah, A. and P. Amarasinghe (2013). Discrete-element study of the swelling behaviour of na-montmorillonite. *Géotechnique 63*, 674–681.

André, D., I. Iordanoff, J. Charles, and J. Néauport (2012). Discrete element method to simulate continuous material by using the cohesive beam model. *Computer Methods in Applied Mechanics and Engineering 213-216*, 113–125.

Azevedo, N. M., J. V. de Lemos, and J. R. de Almeida (2006). A discrete element model for the fracture analysis of reinforced concrete. In C. A. Motasoares, J. A. C. Martins, H. C. Rodrigues, J. A. C. Ambrósio, C. A. B. Pina, C. M. Motasoares, E. B. R. Pereira, and J. Folgado (Eds.), *III European Conference on Computational Mechanics*, Dordrecht, pp. 104–104. Springer Netherlands.

Azizia, H., H. Siahkoohi, B. Evans, N. Keshavarz Farajkhah, and E. Kazemzadeh (2017). A comparison between estimated shear wave velocity and elastic modulus by empirical equations and that of laboratory measurements at reservoir pressure condition. *Journal of Sustainable Energy Engineering 5*(1), 29–46.

Azmi, M., M. H. Ramli, M. A. Hezmi, S. Mohd Yusoff, and M. N. A. Alel (2019). Estimation of soil water characteristic curves (swcc) of mining sand using soil suction modelling. *IOP Conference Series: Materials Science and Engineering 527*(1).

Bahrami, M., J. R. Culham, M. M. Yananovich, and G. Schneider (2006). Review of thermal joint resistance models for nonconforming rough surfaces. *Applied Mechanics Reviews 59*, 1–12.

Bahrami, M., M. Yovanovich, and J. Culham (2004). Thermal joint resistances of conforming rough surfaces with gas filled caps. *Journal of Thermophysics and Heat Transfer - J THERMOPHYS HEAT TRANSFER 18*, 318–325.

Barazza, J. A. C. (2012). *Numerical Model for Nonlinear Analysis of Masonry Walls*. Ph. D. thesis, RWTH Aachen University.

Basirat, R., K. Goshtasbi, and M. Ahmadi (2019). Discrete element simulation of interaction between hydraulic fracturing and a single natural fracture. *Fluids 4*(2).

Basma, A. A., A. S. Al-Homoud, H. Malkawi, and M. A. Al-Bashabsheh (1996). Swelling-shrinkage behavior of natural expansive clays. *Applied Clay Science 11*(2), 211 – 227.

Bazant, Z. P. (2003). *Scaling of structural strength*. Hermes-Penton, London.

Bergmann, L. R. H. (2019). *Die Anisotropie der Festigkeit und Verformbarkeit von Ton and Salzsteinen unter thermomechanischen Prozessen*. Thesis of bachelor of science, Kiel University.

Berton, S. and J. E. Bolander (2006). Crack band model of fracture in irregular lattices. *Computer Methods in Applied Mechanics and Engineering 195*(52), 7172–7181. Computational Modelling of Concrete.

Bitencourt, L., Y. Trindade, T. Bittencourt, O. L. Manzoli, and E. Rodrigues (2018). *Multiscale modeling of steel fiber reinforced concrete based on the use of coupling finite elements and mesh fragmentation technique*, pp. 877–888. Computational Modelling of Concrete Structures, CRC Press.

Bobet, A., A. Fakhimi, S. Johnson, J. Morris, F. Tonon, and M. Yeung (2009). Numerical models in discontinuous media: Review of advances for rock mechanics applications. *Journal of Geotechnical and Geoenvironmental Engineering - J GEOTECH GEOENVIRON ENG 135*.

Bolander, J., S. Choi, and S. Nair (2008). Fracture of fiber-reinforced cement composites: Effects of fiber dispersion. *International Journal of Fracture 154*, 73–86.

Bolander, J. and Y. Kobashi (1995). Size effect mechanisms in numerical concrete fracture. In *Fracture mechanics of concrete structures*. AEDIFICATIO Publishers.

Bolander, J. and S. Saito (1998). Fracture analyses using spring networks with random geometry. *Engineering Fracture Mechanics 6*, 1569–1591.

Bolander, J. E. and S. Berton (2004). Simulation of shrinkage induced cracking in cement composite overlays. *Cement and Concrete Composites 26*(7), 861–871.

Borst, R., J. Remmers, and A. Needleman (2006). Mesh-independent discrete numerical representations of cohesive-zone models. *Engineering Fracture Mechanics 73*(2), 160–177. Advanced Fracture Mechanincs for Life Safety Assessments.

Bower, A. F. (2009). *Applied mechanics of solids*. CRC Press.

Burt, N. and J. Dougill (1977). Progressive failure in a model heterogeneous medium. *Journal of the Engineering Mechanics Division 103*(3), 365–376.

Cekerevac, C. and L. Laloui (2004). Experimental study of thermal effects on the mechanical behaviour of a clay. *International Journal for Numerical and Analytical Methods in Geomechanics 28*(3), 209–228.

Chang, C. and P. Y. Hicher (2005). An elasto-plastic model for granular materials with microstructural consideration. *International Journal of Solids and Structures 42*(14), 4258–4277.

Chang, S. H., C. Lee, and S. Jeon (2002). Measurement of rock fracture toughness under modes i and ii and mixed-mode conditions by using disc-type specimens. *Engineering Geology 66*(1), 79–97.

Chen, S. X. (2008). Thermal conductivity of sands. *Heat and Mass Transfer 44*.

Choo, L. Q., Z. Zhao, H. Chen, and Q. Tian (2016). Hydraulic fracturing modeling using the discontinuous deformation analysis (dda) method. *Computers and Geotechnics 76*, 12–22.

Cleto, P. R., O. L. Manzoli, M. Sánchez, M. A. Maedo, L. B. S. Beserra, and L. J. N. Guimarães (2020). Hydro-mechanical coupled modeling of hydraulic fracturing using the mesh fragmentation technique. *Computers and Geotechnics 124*, 103591.

Cristescu, N. D. (1994). *Viscoplasticity of Geomaterials*, pp. 103–207. Vienna: Springer Vienna.

Cundall, P. A. and O. D. L. Strack (1979). A discrete numerical model for granular assemblies. *Géotechnique 29*(1), 47–65.

da Silva, G. S., L. E. Kosteski, and I. Iturrioz (2020). Analysis of the failure process by using the lattice discrete element method in the abaqus environment. *Theoretical and Applied Fracture Mechanics 107*.

D'Addetta, G. (2004). *Discrete models for cohesive frictional materials*. Phd thesis, University of Stuttgart.

D'Addetta, G., F. Kun, E. Ramm, and H. Herrmann (2008). *From solids to granulates - Discrete element simulations of fracture and fragmentation processes in geomaterials*, Volume 586, pp. 231–258. Lecture Notes in Physics book series, LNP, V. 568, Springer.

D'Albano, G., T. Lukas, F. Su, T. Korakianitis, and A. Munjiza (2017). Numerical comparison of some contact detection algorithms. *Engineering Computations 34*.

Damjanac, B., C. Detournay, and P. Cundall (2020). *Numerical Simulation of Hydraulically Driven Fractures*, pp. 531–561. Cham: Springer International Publishing.

Dawood, E. T. and M. Ramli (2011). High strength characteristics of cement mortar reinforced with hybrid fibers. *Construction and Building Materials 25*(5), 2240–2247.

Dehdezi, P. (2012). *Enhancing pavements for thermal applications*. Phd thesis, University of Nottingham.

Demırcı, A., K. Görgülü, and Y. Durutürk (2004). Thermal conductivity of rocks and its variation with uniaxial and triaxial stress. *International Journal of Rock Mechanics and Mining Sciences 41*(7), 1133–1138.

Diaz, J. and A. Ezziani (2009). Analytical solution for waves propagation in heterogeneous acoustic/porous media. part ii: The 3d case. *Communications in Computational Physics - COMMUN COMPUT PHYS 7*.

Dimitri, R., P. Cornetti, V. Mantic, M. Trullo, and L. De Lorenzis (2017). Mode-i debonding of a double cantilever beam: A comparison between cohesive crack modeling and finite fracture mechanics. *International Journal of Solids and Structures 124*, 57–72.

Dominguez, J. (1993). *Boundary Elements in Dynamics*. Computational Engineering. Computational Mechanics Publications.

Dong, W., Z. Wu, and X. Zhou (2016). Fracture mechanisms of rock-concrete interface: Experimental and numerical. *Journal of Engineering Mechanics 142*.

Elzohairy, A., H. Hammontree, E. Oh, and P. Moler (2020). Temperature effect on the compressive behavior and constitutive model of plain hardened concrete. *Materials 13*, 1–18.

Feia, S., J. Sulem, J. Canou, S. Ghabezloo, and X. Clain (2016). Changes in permeability of sand during triaxial loading: effect of fine particles production. *Acta Geotech. 11*, 1–19.

Feng, Y. T., K. Han, and D. R. J. Owen (2009). Discrete thermal element modelling of heat conduction in particle systems: Pipe-network model and transient analysis. *Powder Technology 193*(3), 248–256. Special Issue: Discrete Element Methods: The 4th International conference on Discrete Element Methods.

Fern, E., K. Soga, and D. J. Robert (2014). Shear strength and dilatancy of partially saturated sand in direct shear tests. In *Geomechanics from Micro to Macro*. Taylor & Francis Group.

Gautam, T. P. (2018). *Cohesive Soils*, pp. 161–162. Cham: Springer International Publishing.

Ghanbarian, B., A. Liaghat, G. Huang, and M. Van Genuchten (2010). Estimation of the van genuchten soil water retention properties from soil textural data. *Pedosphere 20*(4), 456–465.

Ghanbarzadeh, S., M. A. Hesse, M. Prodanović, and J. Gardner (2015). Deformation-assisted fluid percolation in rock salt. *Science 350*(6264), 1069–1072.

Ghassemi, A., J. Abbaszadeh, and A. Pak (2020). Evaluation of the accuracy of the cubic law for flow through fractures using lattice boltzmann method. *Soils and Rocks 43*, 521–533.

Gimenes, M., E. A. Rodrigues, L. A. G. Bitencourt, and O. L. Manzoli (2023). 2d mesoscale modeling of compressive fracture in concrete using a mesh fragmentation technique. *International Journal of Solids and Structures 260-261*.

Glaß, K. (2023). *Druckgetriebene Perkolation im anisotropen Opalinuston-Gesteinsmaterial*. Thesis of master of science, Kiel University.

Gopalaratnam, V. S., S. P. Shah, G. Batson, M. Criswell, V. Ramakishnan, and M. Wecharatana (1991). Fracture toughness of fiber reinforced concrete. *ACI Materials Journal 88*.

Grassl, P. (2009). A lattice approach to model flow in cracked concrete. *Cement & Concrete Composites 31*, 454–460.

Grassl, P., C. Fahy, D. Gallipoli, and J. Bolander (2013). A lattice model for liquid transport in cracked unsaturated heterogeneous porous materials. *VIII International Conference on Fracture Mechanics of Concrete and Concrete Structures*.

Gudehus, G. (2004). A visco-hypoplastic constitutive relation for soft soils. *Soils and Foundations 44*(4), 11–25.

Hadzalic, E., A. Ibrahimbegovic, and M. Nikolić (2018). Failure mechanisms in coupled poroplastic medium. *Coupled Systems Mechanics 7*, 43–59.

Hamoush, S. A. and H. Abdel-Fattah (1996). The fracture toughness of concrete. *Engineering Fracture Mechanics 53*(3), 425–432.

Hashiguchi, K. (2017). Consistent hypo- and hyper-elastic equations of geomaterials. *The Proceedings of the Materials and Mechanics Conference 2017*.

Herrmann, H. J. and S. Roux (1990). Statistical models for the fracture of disordered media. *Elsevier eBooks*.

Hong, G. and K. Yoshitake (2000). Structural concrete analysis using rigid-body-spring networks. *Computer-aided Civil and Infrastructure Engineering 15*, 120–133.

Hostettler, B., A. Reisdorf, D. Jaeggi, G. Deplazes, H. Bläsi, A. Morard, S. Feist-Burkhardt, A. Waltschew, V. Dietze, and U. Menkveld-Gfeller (2018). *Litho- and biostratigraphy of the Opalinus Clay and bounding formations in the Mont Terri rock laboratory (Switzerland)*, pp. 23–39.

Hrennikoff, A. (1941). Solution of problems of elasticity by the framework method. *Journal of Applied Mechanics 9*.

Humar, J. and E. Wright (2011). Numerical methods in structural dynamics. *Canadian Journal of Civil Engineering 1*, 179–193.

Ibrahim, H., A. Ilinca, and J. Perron (2008). Energy storage systems-characteristics and comparisons. *Renewable and Sustainable Energy Reviews 12*(5), 1221–1250.

Ince, R., A. Arslan, and B. Karihaloo (2003). Lattice modelling of size effect in concrete strength. *Engineering Fracture Mechanics 70*(16), 2307 – 2320. Size-scale effects.

Jafari, A., M. Vahab, P. Broumand, and N. Khalili (2023). An extended finite element method implementation in comsol multiphysics: Thermo-hydro-mechanical modeling of fluid flow in discontinuous porous media. *Computers and Geotechnics 159*.

Jefferson, I. (1994). *Temperature effects on clay soils*. Ph. D. thesis, Loughborough University.

Jenabidehkordi, A. (2018). Computational methods for fracture in rock: a review and recent advances. *Frontiers of Structural and Civil Engineering 13*.

Jing, L. and O. Stephansson (2007). 11 - discrete element methods for granular materials. In L. Jing and O. Stephansson (Eds.), *Fundamentals of Discrete Element Methods for Rock Engineering*, Volume 85 of *Developments in Geotechnical Engineering*, pp. 399 – 444. Elsevier.

Juanes, R. (2005). A variational multiscale finite element method for multiphase flow in porous media. *Finite Elements in Analysis and Design 41*(7), 763–777. The Sixteenth Annual Robert J. Melosh Competition.

Jweeg, M. J., M. Al-Waily, and K. K. Resan (2022). Chapter 13 - higher-order isoparametric formulation. In M. Jweeg, M. Al-Waily, and K. K. Resan (Eds.), *Energy Methods and Finite Element Techniques*, pp. e633–e676. Elsevier.

Kamlot, W. (2009). *Habilitationsschrift: Gebirgsmechanische Bewertung der geologischen Barrierefunktion des Hauptanhydrits in einem Salzbergwerk*. des Instituts für Geotechnik der Technischen Universität Bergakademie Freiberg.

Karihaloo, B., P. Shao, and Q. Xiao (2003). Lattice modelling of the failure of particle composites. *Engineering Fracture Mechanics 70*, 2385–2406.

Keaton, J. R. (2018). *Noncohesive Soils*, pp. 689–690. Cham: Springer International Publishing.

Khazanovich, L. (2012). *A coupled lattice and finite element model for fracture in composite concrete pavements*. Phd thesis, University of Minnesota.

Khoei, A., M. Vahab, E. Haghighat, and S. Moallemi (2014). A mesh-independent finite element formulation for modeling crack growth in saturated porous media based on an enriched-fem technique. *International Journal of Fracture 188*, 79–108.

Kodama, J., T. Goto, Y. Fujii, and P. Hagan (2013). The effects of water content, temperature and loading rate on strength and failure process of frozen rocks. *International Journal of Rock Mechanics and Mining Sciences 62*, 1–13.

Kok, S., A. Ti, B. Huat, J. Noorzaei, and S. Jaafar (2009). A review of basic soil constitutive models for geotechnical application. *Electronic Journal of Geotechnical Engineering 14*.

Kolditz, O., U. J. Görke, H. Konietzky, J. Maßmann, M. Nest, H. Steeb, F. Wuttke, and T. Nagel (2021). *GeomInt-Mechanical Integrity of Host Rocks*. Cham: Springer International Publishing.

Kolditz, O., K. Yoshioka, T. Cajuhi, R. M. Günther, H. Steeb, F. Wuttke, and T. Nagel (2023). *GeomInt-Discontinuities in Geosystems From Lab to Field Scale*. Springer Cham.

Kolymbas, D. and I. Herle (1998). Hypoplasticity: A framework to model granular materials. In B. Cambou (Ed.), *Behaviour of Granular Materials*, Vienna, pp. 239–268. Springer Vienna.

Komatitsch, D. and J. Tromp (2003). A perfectly matched layer absorbing boundary condition for the second-order seismic wave equation. *Geophysical Journal International 154*(1), 146–153.

Koplos, J., M. E. Tuccillo, and B. Ranalli (2014). Hydraulic fracturing overview: How, where, and its role in oil and gas. *Journal - American Water Works Association 106*, 38–56.

Kosteski, L., R. Barrios D'ambra, and I. Iturrioz (2012). Crack propagation in elastic solids using the truss-like discrete element method. *International Journal of Fracture 174*, 139–161.

Kosteski, L., I. Iturrioz, L. Friedrich, and G. Lacidogna (2022). A study by the lattice discrete element method for exploring the fractal nature of scale effects. *Scientific Reports 12*.

Kosteski, L. E., J. D. Riera, I. Iturrioz, R. K. Singh, and T. Kant (2015). Analysis of reinforced concrete plates subjected to impact employing the truss-like discrete element method. *Fatigue & Fracture of Engineering Materials & Structures 38*(3), 276–289.

Krishna, D., R. S. Dr, and S. Narayanan (2021). High temperature effects on different grades of concrete. *Sadhana 46*, 31.

Kunhwi, K. and L. Yun Mook (2011). Simulation of rate dependent fracture in concrete using an irregular lattice model. *Cement and Concrete Composites 33*(9), 949 – 955.

Kuruppu, M. D. (2000). Fracture Toughness Testing Of Geomaterials Using Semicircular Specimen. *ISRM International Symposium*.

Lade, P. and R. Nelson (1987). Modelling the elastic behaviour of granular materials. *International Journal for Numerical and Analytical Methods in Geomechanics 11*, 521–542.

Langer, P., M. Maeder, C. Guist, M. Krause, and S. Marburg (2017). More than six elements per wavelength: The practical use of structural finite element models and their accuracy in comparison with experimental results. *Journal of Computational Acoustics 25*(04).

Lee, D. and B. Schachter (1980). Two algorithms for constructing a delaunay triangulation. *International Journal of Parallel Programming 9*, 219–242.

Lemaitre, J. (2001). Handbook of materials behavior models. Burlington: Academic Press.

Lepillier, B., K. Yoshioka, F. Parisio, R. Bakker, and D. Bruhn (2020). Variational phase-field modeling of hydraulic fracture interaction with natural fractures and application to enhanced geothermal systems. *Journal of Geophysical Research: Solid Earth 125*(7).

Li, C., Y. Hu, T. Meng, C. Zhang, R. Gao, P. Jin, and Y. Hu (2020). Mode-i fracture toughness and mechanisms of salt-rock gypsum interlayers under real-time high-temperature conditions. *Engineering Fracture Mechanics 240*.

Li, C., D. Yang, H. Xie, L. Ren, and J. Wang (2023). Size effect of fracture characteristics for anisotropic quasi-brittle geomaterials. *International Journal of Mining Science and Technology 33*(2), 201–213.

Li, J., S. Wang, K. Dong, S. Meng, Q. Lu, and Z. Li (2023). Effects of in-situ temperature in deep reservoirs on shale fracture properties. *Energy Reports 9*, 73–83.

Li, M. and F. Zhang (2022). *Discrete Element Modeling of Hydraulic Fracturing*, Chapter 12, pp. 141–175. John Wiley & Sons, Ltd.

Li, Y. and Q. Yu (2020). Rock-core scale modeling of initial water saturation effects on co2 breakthrough pressure in co2 geo-sequestration. *Journal of Hydrology 580*.

Lilliu, G. and J. van Mier (2003). 3d lattice type fracture model for concrete. *Engineering Fracture Mechanics 70*(7), 927–941.

Lin, H. and S. Atluri (2001). The meshless local petrov-galerkin (mlpg) method for solving incompressible navier-stokes equations. *CMES - Computer Modeling in Engineering and Sciences 2*.

Lin, Z. Y., Y. Wang, C. S. Tang, Q. Cheng, H. Zeng, C. Liu, and B. Shi (2021). Discrete element modelling of desiccation cracking in thin clay layer under different basal boundary conditions. *Computers and Geotechnics 130*.

Lisjak, A., P. Kaifosh, L. He, B. S. A. Tatone, O. K. Mahabadi, and G. Grasselli (2017). A 2d, fully-coupled, hydro-mechanical, fdem formulation for modelling fracturing processes in discontinuous, porous rock masses. *Computers and Geotechnics 81*, 1–18.

Liu, J., S. Deng, J. Zhang, and N. Liang (2007). Lattice type of fracture model for concrete. *Theoretical and Applied Fracture Mechanics 48*, 269–284.

Liu, J., Z. Zhao, S. Deng, and L. Naigang (2009). Numerical investigation of crack growth in concrete subjected to compression by the generalized beam lattice model. *Computational Mechanics 43*, 277–295.

Liu, W., J. Cheng, H. Yao, L. Zheng, Q. Zhang, Y. Zhang, and F. Yang (2023). A micromechanical thermo-hydro-mechanical coupling model for fractured rocks based on multi-scale structures variations. *International Journal of Rock Mechanics and Mining Sciences 170*.

Liu, X. Y. (2001). *3-D network model and mechanical behaviour simulation of short-fiber reinforced composites*. Phd thesis, Institute of Mechanics, CAS, Beijing, China.

Long, J., G. Wang, X. Feng, and S. Yu (2012). Two-dimensional hertzian contact problem with surface tension. *International Journal of Solids and Structures 49*(13), 1588–1594.

Lu, J. M., C. F. Li, and S. M. Cao, G. C. amd Hu (2022). Simulating fractures with bonded discrete element method. *IEEE Trans Vis Comput Graph. 28*.

Ma, S. K., M. S. Huang, P. Hu, and C. Yang (2013). Soil-water characteristics and shear strength in constant water content triaxial tests on yunnan red clay. *Journal of Central South University 20*, 1412–1419.

Maddalena, F. and M. Ferrari (1995). Viscoelasticity of granular materials. *Mechanics of Materials 20*(3), 241–250.

Mähler, L., M. Ekh, and K. Runesson (2001). A class of thermo-hyperelastic-viscoplastic models for porous materials - theory and numerics. *International Journal of Plasticity 17*(7), 943–969.

Maji, A. and J. Wang (1992). Experimental study of fracture processes in rock. *Rock Mechanics and Rock Engineering 25*, 25–47.

Maßmann, J., G. Ziefle, M. Kohlmeier, and W. Zielke (2011). Thermo-hydro-mechanical modeling of coupled processes in clay materials. In *Modelling, Simulation and Software Concepts for Scientific-Technological Problems*, Volume 57, pp. 266–290. Springer, Berlin, Heidelberg.

Minardi, A., E. Crisci, A. Ferrari, and L. Laloui (2016). Anisotropic volumetric behaviour of opalinus clay shale upon suction variation. *Geotechnique Letters 6, 1-5*.

Mistler, M. (2006). *Verformungsbasiertes seismisches Bemessungskonzept für Mauerwerksbauten*. Ph. D. thesis, RWTH Aachen University.

Mitchell, J. K. and K. Soga (2015). *Fundamentals of soil behavior*. Hoboken, N.J.: John Wiley & Sons.

Motra, H. B., F. Sittig, D. Schwindrofska, A. S. Sattari, and F. Wuttke (2020). Determination of rock thermal conductivity under in-situ conditions: Experimental and numerical investigation. EasyChair Preprint no. 3476.

Motra, H. B. and S. Zertani (2018). Influence of loading and heating processes on elastic and geomechanical properties of eclogites and granulites. *Journal of Rock Mechanics and Geotechnical Engineering 10*(1), 127–137.

Mottaghy, D., H. D. Vosteen, and R. Schellschmidt (2008). Temperature dependence of the relationship of thermal diffusivity versus thermal conductivity for crystalline rocks. *International Journal of Earth Sciences 97*, 435–442.

Moukarzel, C. and H. J. Herrmann (1992). A vectorizable random lattice. *J. Stat. Phys. 68*, 911–923.

Mun, W., T. Teixeira, M. Balci, J. Svoboda, and J. McCartney (2016). Rate effects on the undrained shear strength of compacted clay. *Soils and Foundations 56*(4), 719–731.

Munjiza, A., T. Bangash, and N. W. M. John (2004). The combined finite-discrete element method for structural failure and collapse. *Engineering Fracture Mechanics 71*(4), 469–483. Fracture and Damage Mechanics.

Munjiza, A., E. Knight, and E. Rougier (2011). *Computational Mechanics of Discontinua*. WILEY.

Nairn, J. (2011). Generalized crack closure analysis for elements with arbitrarily-placed side nodes and consistent nodal forces. *International Journal of Fracture 171*, 11–22.

Nayfeh, A. H. and M. S. Hefzy (1978). Continuum modeling of three-dimensional truss-like space structures. *AIAA Journal 16*(8), 779–787.

Nikolić, M., E. Karavelić, A. Ibrahimbegovic, and P. Miščević (2018). Lattice element models and their peculiarities. *Archives of Computational Methods in Engineering 25*, 753–784.

Nikolić, M., X. Nam Do, A. Ibrahimbegovic, and v. Nikolić (2018). Crack propagation in dynamics by embedded strong discontinuity approach: Enhanced solid versus discrete lattice model. *Computer Methods in Applied Mechanics and Engineering 340*, 480 – 499.

Nishimura, S., N. A. Minh, and R. J. Jardine (2007). Shear strength anisotropy of natural london clay. *Géotechnique 57*(1), 49–62.

Niu, C., F. Wang, C. Yongzhen, and S. Deng (2020). Effect of water content on dynamic fracture characteristic of rock under impacts. *KSCE Journal of Civil Engineering 25*.

Ocłoń, P., P. Cisek, M. Pilarczyk, and D. Taler (2015). Numerical simulation of heat dissipation processes in underground power cable system situated in thermal backfill and buried in a multilayered soil. *Energy Conversion and Management 95*, 352 – 370.

Orsi, E. and U. Sanfilippo (2020). Uncertainty in experimental evaluation of chezy-strickler-manning and colebrook-white roughness coefficients in circular pipes. *IGHEM2004*.

Osama, J. K. (2010). *Discrete modeling of heat transfer*. Thesis of master of science, University of Glasgow.

Oschmann, T., M. Schiemann, and H. Kruggel-Emden (2016). Development and verification of a resolved 3d inner particle heat transfer model for the discrete element method (dem). *Powder Technology 291*, 392–407.

Ostoja-Starzewski, M. (2002). Lattice models in micromechanics. *Applied mechanics 55*(1), 35–60.

Paaswell, R. E. (1967). Temperature effects on clay soil consolidation. American Society of Civil Engineers.

Paavilainen, J., J. Tuhkuri, and A. Polojärvi (2009). 2d combined finite-discrete element method to model multi-fracture of beam structures. *Engineering Computations - ENG COMPUTATIONS 26*, 578–598.

Peron, H., J. Y. Delenne, L. Laloui, and M. Youssoufi (2009). Discrete element modelling of drying shrinkage and cracking of soils. *Computers and Geotechnics 36*, 61–69.

Peron, H., S. Salager, M. Nuth, P. Marschall, and L. Laloui (2009). Analysis of the swelling pressure development in opalinus clay - experimental and modelling aspects. *2nd International Conference on Fault and Top Seals*.

Poirier, D. R. and G. H. Geiger (2016). *Conduction of Heat in Solids*, pp. 281–327. Cham: Springer International Publishing.

Pokojski, W. and P. Pokojska (2018). Voronoi diagrams - inventor, method, applications. *Polish Cartographical Review 50*, 141–150.

Prado, E. and J. van Mier (2003). Effect of particle structure on mode i fracture process in concrete. *Engineering Fracture Mechanics 70*, 1793–1807.

Rabczuk, T. and T. Belytschko (2004). Cracking particles: a simplified meshfree method for arbitrary evolving cracks. *International journal for numerical methods in engineering 61*(13), 2316–2343.

Rasmussen, L. L., M. M. de Farias, and A. de Assis (2018). Extended rigid body spring network method for the simulation of brittle rocks. *Computers and Geotechnics 99*, 31–41.

Richard, H. A. and M. Sander (2016). *Fundamentals of Fracture Mechanics*, pp. 55–112. Cham: Springer International Publishing.

Riera, J. (1984). Local effects in impact problems on concrete structures. *Proceedings of the Conference on Structural Analysis and Design of Nuclear Power Plants 3*.

Rizvi, Z. (2019). *Lattice Element Method and its application to Multiphysics*. Phd thesis, Kiel University.

Rizvi, Z., S. Mustafa, A. Sattari, S. Ahmad, P. Furtner, and F. Wuttke (2020). Dynamic lattice element modelling of cemented geomaterials. In *Advances in Computer Methods and Geomechanics*, Singapore, pp. 655–665. Springer Singapore.

Rizvi, Z., M. Nikolić, and F. Wuttke (2019). Lattice element method for simulations of failure in bio-cemented sands. *Granular Matter 21*.

Rizvi, Z., D. Shrestha, A. Sattari, and F. Wuttke (2018). Numerical modelling of effective thermal conductivity for modified geomaterial using lattice element method. *Heat and Mass Transfer 54*(2), 483–499.

Rizvi, Z., F. Wuttke, and A. Sattari (2018). Dynamic analysis by lattice element method simulation. *Springer Series in Geomechanics and Geoengineering*, 405–409.

Rodriguez, J. M., J. M. Carbonell, J. C. Cante, and J. Oliver (2016). The particle finite element method (pfem) in thermo-mechanical problems. *International Journal for Numerical Methods in Engineering 107*(9), 733–785.

Rougier, E., A. Munjiza, Z. Lei, V. T. Chau, E. E. Knight, A. Hunter, and G. Srinivasan (2020). The combined plastic and discrete fracture deformation framework for finite-discrete element methods. *International Journal for Numerical Methods in Engineering 121*(5), 1020–1035.

Sakaue, K., S. Yoneyama, and M. Takashi (2007). Relation between principal stress direction and crack propagation direction in a quenched glass plate. *International Conference on Advanced Technology in Experimental Mechanics: Asian Conference on Experimental Mechanics 6*.

Sánchez, M., O. L. Manzoli, and L. J. N. Guimarães (2014). Modeling 3-d desiccation soil crack networks using a mesh fragmentation technique. *Computers and Geotechnics 62*, 27–39.

Sattari, A., H. Motra, Z. Rizvi, and F. Wuttke (2019). A new lattice element method (lem) with integrated interface elements to determine the effective thermal conductivity of rock solids under thermo-mechanical processes. In *Energy Geotechnics*, Cham, pp. 266–275. Springer International Publishing.

Sattari, A., Z. Rizvi, H. Motra, and F. Wuttke (2017). Meso-scale modeling of heat transport in a heterogeneous cemented geomaterial by lattice element method. *Granular Matter 19*(66).

Sattari, A. S., T. Frühwirt, J. Maßmann, M. Nest, D. Naumann, D. Pötschke, M. Ruf, T. Kneuker, B. Vowinckel, M. Furche, and G. Ziefle (2021). *GeomInt-Mechanical Integrity of Host Rocks: Experimental Platform*, pp. 15–61. Cham: Springer International Publishing.

Sattari, A. S., Z. H. Rizvi, H. D. B. Aji, and F. Wuttke (2022). Study of wave propagation in discontinuous and heterogeneous media with the dynamic lattice method. *Scientific Reports 12*.

Sattari, A. S., M. Siebelist, N. Toker, and F. Wuttke (2020). Simulation of hysteresis in soil-water retention with a correlation between the invading pressure to the governing effective flow area. *Granular Matter 22*.

Sattari, A. S. and N. Toker (2016). Obtaining soil-water characteristic curves by numerical modeling of drainage in particulate media. *Computers and Geotechnics 74*, 196–210.

Saudi, A. (2022). *The Solutions to 2D Laplace's Equation using Iterative Methods*.

Schlangen, E. and E. Garboczi (1997). Fracture simulations of concrete using lattice models: Computational aspects. *Engineering Fracture Mechanics 57*(2), 319–332.

Schlangen, E. and J. Van Mier (1992). Micromechanical analysis of fracture of concrete. *International Journal of Damage Mechanics 1*(4), 435–454.

Schlichtenmayer, M., A. Bannach, M. Amro, and C. Freese (2015). Renewable energy storage in salt caverns - a comparison of thermodynamics and permeability between natural gas, air and hydrogen. *SMRI research report RR2015-1*.

Schumann, N. R. (2019). *Die Analyse der effektiven Materialeigenschaften des Opalinustons unter gekoppelten thermo-mechanischen Belastungen*. Thesis of master of science, Kiel University.

Sedaee, B., M. Mohammadi, L. Esfahanizadeh, and Y. Fathi (2019). Comprehensive modeling and developing a software for salt cavern underground gas storage. *Journal of Energy Storage 25*.

Sevil, T., M. Baran, T. Bilir, and E. Canbay (2011). Use of steel fiber reinforced mortar for seismic strengthening. *CONSTRUCTION AND BUILDING MATERIALS*, 892–899.

Shah, S. and A. Naaman (1976). Mechanical properties of glass and steel fiber reinforced mortar. *J Am Concr Inst 73*(1), 50–53.

Shao, H., P. Hein, A. Sachse, and O. Kolditz (2016). *Geoenergy Modeling II*. Springer, Cham.

Sharafisafa, M., Z. Aliabadian, A. Sato, and L. Shen (2023). Coupled thermo-hydro-mechanical simulation of hydraulic fracturing in deep reservoirs using finite-discrete element method. *Rock Mechanics and Rock Engineering 56*, 5039–5075.

Shrestha, D., Z. Rizvi, and F. Wuttke (2019). Effective thermal conductivity of unsaturated granular geocomposite using lattice element method. *Heat and Mass Transfer 55*(6), 1671–1683.

Shubber, K. and N. K. S. Al-Saoudi (2018). Hydraulic conductivity of granular materials. In *3rd International Conference on New Developments in Soil Mechanics and Geotechnical Engineering*.

Sibilla, S. (2013). Fluid mechanics and the sph method: theory and applications. *Journal of Hydraulic Research 51*.

Sima, J., M. Jiang, and C. Zhou (2014). Numerical simulation of desiccation cracking in a thin clay layer using 3d discrete element modeling. *Computers and Geotechnics 56*, 168–180.

Simoni, A. (2006). The direct shear strength and dilatancy of sand-gravel mixtures. *Geotechnical & Geological Engineering 24*, 523–549.

Snyder, K., E. Garboczi, and A. Day (1993). The elastic moduli of simple two-dimensional isotropic composites: Computer simulation and effective medium theory. *Journal of Applied Physics 72*, 5948–5955.

Sofianos, C. and V. K. Koumousis (2017). Rigid body spring network model for plasticity and fracture. In *Proceedings of the 2nd World Congress on Civil, Structural, and Environmental Engineering (CSEE'17)*.

Song, S. H., G. H. Paulino, and W. G. Buttlar (2006). Simulation of crack propagation in asphalt concrete using an intrinsic cohesive zone model. *Journal of Engineering Mechanics 132*(11), 1215–1223.

Stróżyk, J. and M. Tankiewicz (2014). The undrained shear strength of overconsolidated clays. *Procedia Engineering 91*, 317–321.

Stutz, H., D. Masin, A. S. Sattari, and F. Wuttke (2017). A general approach to model interfaces using existing soil constitutive models application to hypoplasticity. *Computers and Geotechnics 87*, 115–127.

Suchorzewski, J., J. Tejchman, and M. Nitka (2018). Discrete element method simulations of fracture in concrete under uniaxial compression based on its real internal structure. *International Journal of Damage Mechanics 27*.

Sun, Y., L. Xie, B. He, C. Gao, and J. Wang (2016). Effects of effective stress and temperature on permeability of sandstone from co2-plume geothermal reservoir. *Journal of Rock Mechanics and Geotechnical Engineering 8*(6), 819–827.

Tang, A. M., Y. J. Cui, and N. Barnel (2008). Thermo-mechanical behaviour of a compacted swelling clay. *Geotechnique 58*(1), 45–54.

Tanzi, B. N. R., G. Birck, M. Sobczyk, I. Iturrioz, and G. Lacidogna (2023). Truss-like discrete element method applied to damage process simulation in quasi-brittle materials. *Applied Sciences 13*(8).

Tarokh, A., R. Makhnenko, A. Fakhimi, and J. Labuz (2017). Scaling of the fracture process zone in rock. *International Journal of Fracture 204*.

Tian, D. and H. Zheng (2023). The generalized mohr-coulomb failure criterion. *Applied Sciences 13*(9).

Tillemans, H. J. and H. J. Herrmann (1995). Simulating deformations of granular solids under shear. *Physica A: Statistical Mechanics and its Applications 217*(3), 261–288.

Tiskatine, R., A. Eddemani, G. Lahoucine, B. Abnay, A. Ihlal, A. Ahmed, and L. Bouirden (2016). Experimental evaluation of thermo-mechanical performances of candidate rocks for use in high temperature thermal storage. *Applied Energy 171*, 243–255.

Tokoro, T., T. Ishikawa, S. Shirai, and T. Nakamura (2016). Estimation methods for thermal conductivity of sandy soil with electrical characteristics. *Soils and Foundations 56*(5), 927–936. Special Issue on the International Symposium on Geomechanics from Micro to Macro IS-Cambridge 2014.

Topin, V., J. Delenne, F. Radjai, L. Brendel, and F. Mabille (2007). Strength and failure of cemented granular matter. *The European physical journal. E, Soft matter 23*.

Vallejo, L. E. and R. Mawby (2000). Porosity influence on the shear strength of granular material-clay mixtures. *Engineering Geology 58*(2), 125–136.

van Mier, J., M. van Vliet, and K. Wang Tai (2002). Fracture mechanisms in particle composites: statistical aspects in lattice type analysis. *Mechanics of Materials 34*.

van Vliet, M. R. A. (2000). *Size effect in tensile fracture of concrete and rock*. Phd thesis, Delft University of Technology.

Vervoort, R. W. and S. Cattle (2003). Linking hydraulic conductivity and tortuosity parameters to pore space geometry and pore-size distribution. *Journal of Hydrology 272*, 36–49.

Vervuurt, A. (1997). *Interface fracture in concrete*. Phd thesis, Delft University of Technology.

Vo, T. D., A. Pouya, S. Hemmati, and A. M. Tang (2017). Numerical modelling of desiccation cracking of clayey soil using a cohesive fracture method. *Computers and Geotechnics 85*, 15–27.

Vowinckel, B., T. Frühwirt, J. Maßmann, T. Nagel, M. Nest, D. Pötschke, C. Rölke, A. S. Sattari, P. Schmidt, H. Steeb, K. Yoshioka, G. Ziefle, and O. Kolditz (2021). *GeomInt-Mechanical Integrity of Host Rocks: Model-Experiment-Exercises (MEX)*, pp. 97–192. Cham: Springer International Publishing.

Wan, W. and P. Chen (2022). A fully coupled thermomechanical phase field method for modeling cracks with frictional contact. *Mathematics 10*(23).

Wang, H. C., W. H. Zhao, D. S. Sun, and B. B. Guo (2012). Mohr-coulomb yield criterion in rock plastic mechanics. *Chinese Journal of Geophysics 55*(6), 733–741.

Wangen, M. (2018). A 2d model of hydraulic fracturing, damage and microseismicity. *Pure Appl. Geophys. 175*, 813–828.

Waseem, H. S. M. and N. K. Kumar (2014). Finite element modeling for delamination analysis of double cantilever beam specimen. *International Journal of Mechanical Engineering 1*, 6–11.

Wenk, H. R., M. Voltolini, and M. Mazurek (2009). Preferred orientations and anisotropy in shales: Callovo-oxfordian shale (france) and opalinus clay (switzerland). *Clays and Clay Minerals - CLAYS CLAY MINER 56*.

Wolper, J. (2021). *Material Point Methods for Simulating Material Fracture*. Ph. D. thesis, University of Pennsylvania.

Wong, J., K. Soga, X. Xu, and J. Delenne (2015). Modelling fracturing process of geomaterial using lattice element method. *3. International Symposium on Geomechanics from Micro to Macro*.

Wood, M., D. Andrea, D. Andrea, and I. Erdin (2016). Fibres and soils: A route towards modelling of root-soil systems. *Soils and Foundations 56*, 765–778.

Woodside, W. and C. M. A. De Bruyn (1959). Heat transfer in a moist clay. *Soil Science 87*(3), 166–173.

Wu, J. Y., V. P. Nguyen, C. T. Nguyen, D. Sutula, S. Bordas, and S. Sinaie (2019). Phase field modelling of fracture. *Advances in Applied Mechanics 53*, 1–183.

Wuttke, F., H. Lyu, A. S. Sattari, and Z. H. Rizvi (2021). Wave based damage detection in solid structures using spatially asymmetric encoder-decoder network. *Scientific Reports 11*.

Xi, B., Y. Guo, X. Chen, and Z. Zhang (2021). Investigation on swelling behavior of expansive clay by discrete element method. pp. 448–452. IEEE.

Xiao, W., C. Xia, W. Wei, and Y. Bian (2013). Combined effect of tortuosity and surface roughness on estimation of flow rate through a single rough joint. *Journal of Geophysics and Engineering 10*(4), 045015.

Xie, H., C. Li, Z. He, C. Li, Y. Lu, R. Zhang, M. Gao, and F. Gao (2021). Experimental study on rock mechanical behavior retaining the in situ geological conditions at different depths. *International Journal of Rock Mechanics and Mining Sciences 138*.

Xu, F., H. Hajibeygi, and L. J. Sluys (2021). Multiscale extended finite element method for deformable fractured porous media. *Journal of Computational Physics 436*.

Yan, C., T. Wang, W. Ke, and G. Wang (2021). A 2d fdem-based moisture diffusion-fracture coupling model for simulating soil desiccation cracking. *Acta Geotechnica 16*.

Yan, C., H. Zheng, G. Sun, and X. Ge (2016). Combined finite-discrete element method for simulation of hydraulic fracturing. *Rock Mechanics and Rock Engineering 49*, 1389–1410.

Yang, G. and X. Wang (2012). Discrete element modeling for granular materials. *Electronic Journal of Geotechnical Engineering 17*.

Yang, Q., J. M. Zhang, H. Zheng, and Y. Yao (2013). *Constitutive Modeling of Geomaterials*. Springer Berlin, Heidelberg.

Yao, J., T. Wang, and W. Likos (2019). Measuring thermal conductivity of unsaturated sand under different temperatures and stress levels using a suction-controlled thermo-mechanical method. pp. 784–793.

Yoon, J. S., A. Zang, O. Stephansson, H. Hofmann, and G. Zimmermann (2017). Discrete element modelling of hydraulic fracture propagation and dynamic interaction with natural fractures in hard rock. *Procedia Engineering 191*, 1023–1031. ISRM European Rock Mechanics Symposium EUROCK 2017.

Yoshioka, K., A. S. Sattari, M. Nest, R. M. Günther, F. Wuttke, T. Fischer, and T. Nagel (2022). Numerical models of pressure-driven fluid percolation in rock salt: nucleation and propagation of flow pathways under variable stress conditions. *Environmental Earth Sciences 81*.

Yu, S., X. Ren, and J. Zhang (2023). Using an improved sph algorithm to simulate thermo-hydro-mechanical-damage coupling problems in rock masses. *Case Studies in Thermal Engineering 47*.

Yu, S., X. Ren, J. Zhang, H. Wang, and Z. Sun (2021). An improved form of smoothed particle hydrodynamics method for crack propagation simulation applied in rock mechanics. *International Journal of Mining Science and Technology 31*(3), 421–428.

Zeng, Q., J. Yao, and J. Shao (2020). An extended finite element solution for hydraulic fracturing with thermo-hydro-elastic-plastic coupling. *Computer Methods in Applied Mechanics and Engineering 364*.

Zhang, C., Q. Bai, P. Han, L. Wang, X. Wang, and F. Wang (2023). Strength weakening and its micromechanism in water-rock interaction, a short review in laboratory tests. *International Journal of Coal Science & Technology 10*.

Zhang, H., Q. Zhou, H. Xing, and H. Muhlhaus (2011). A dem study on the effective thermal conductivity of granular assemblies. *Powder Technology 205*, 172–183.

Zhang, S., W. Leng, F. Zhang, and Y. Xiong (2012). A simple thermo-elastoplastic model for geomaterials. *International Journal of Plasticity 34*, 93–113.

Zhang, Y., A. Zhou, M. Nazem, and J. Carter (2019). Finite element implementation of a fully coupled hydro-mechanical model and unsaturated soil analysis under hydraulic and mechanical loads. *Computers and Geotechnics 110*, 222–241.

Zhao, G., N. Khalili, J. Fang, and J. Zhao (2012). A coupled distinct lattice spring model for rock failure under dynamic loads. *Computers and Geotechnics 42*, 1–20.

Zheng, T. (2018). *A fully coupled thermo-hydro-mechanical finite element model of freezing in porous media and the application in ground source heat pump system*. Ph. D. thesis, Technische Universität Dresden.

Zhou, H., D. Hu, Z. F., and J. Shao (2011). A thermo-plastic/viscoplastic damage model for geomaterials. *Acta Mechanica Solida Sinica 24*(3), 195–208.

Zima, B. and R. Kedra (2020). Detection and size estimation of crack in plate based on guided wave propagation. *Mechanical Systems and Signal Processing 142*.

In Geo-Engineering applications, understanding the geomaterial's behavior under coupled therm-hydro-mechanical (THM) processes is imperative. The change of geomaterial's THM properties subjected to the coupled processes can lead to a decrease in the efficiency of the designed Geo-Systems (e.g. rock barriers), failure of the Geo-Structures, or even contamination of the environment. With the increase of computational power during the last decades, numerical methods are utilized as engineering tools not only to model large-scale problems but also to better comprehend the physical phenomena governing such a material behavior from micro- to macroscale perspective. In this contribution, the in-house developed discrete lattice method is applied to simulate the geomaterial's behavior under coupled THM processes.

The Lattice Element Method (LEM) is able to simulate a stochastic frack initiation and propagation in brittle or quasi-brittle materials, where small deformations are expected. In this study, the application of the conventional lattice method is extended to simulate complex Multiphysics problems. The developed Thermo-Mechanical lattice model is able to simulate the transient heat flux as well as the change in the effective thermal conductivity in heterogeneous domains under the coupled processes. With the implementation of the dual-lattice network, the Hydro-Mechanical lattice is considered to model the change of permeability and pressure-driven fluid percolation in discountinuum bodies. The dynamic lattice model is presented to investigate wavefield scattering in discontinuous and heterogeneous geomaterials.

The validation of the numerical results is carried out by comparing the lattice results with the analytical solutions and the experimental data. The theoretical developments presented in the field of Multiphysics are extended into practical applications, where the failure of reinforced masonry walls and the integrity of barrier rocks are studied. The LEM has been demonstrated to be an effective means of modeling and analyzing alterations in material behavior, even in complex anisotropic and heterogeneous geomaterials. As computational power increases and a transition from micro- to macroscale is put into practice, the lattice model can be used in large-scale engineering applications.

ISSN: 2365-7162